

NEUTRON SCATTERING STUDIES OF THE FAMILY OF
HIGH TEMPERATURE SUPERCONDUCTING CUPRATES
 $La_{1.6-x}Nd_{0.4}Sr_xCuO_4$

By Qianli Ma, B.Sc., M.Sc.

*A Thesis Submitted to the School of Graduate Studies in the Partial
Fulfillment of the Requirements for the Degree Doctor of Philosophy*

McMaster University © Copyright by Qianli Ma February 23, 2022

McMaster University

Doctor of Philosophy (2022)

Hamilton, Ontario (Department of Physics and Astronomy)

TITLE: Neutron Scattering Studies of the Family of High Temperature Superconducting Cuprates $La_{1.6-x}Nd_{0.4}Sr_xCuO_4$

AUTHOR: Qianli Ma (McMaster University)

SUPERVISOR: Dr. Bruce D.Gaulin

NUMBER OF PAGES: xiv, 119

Abstract

High T_C superconductivity is regarded as one of the most challenging problems in the physical sciences of the 20th century. The ultimate goal is to create room temperature superconductors that have the potential to revolutionize many aspects of modern technology. The La-214 family of the cuprate high T_C superconductors is comprised of single layers of CuO_2 planes, and the original high T_C superconductor was from this family. As such these copper oxides have been of great topical interest for 35 years since their discovery. This family displays a complex phase diagram with magnetism, charge order, an enigmatic pseudogap phase all intertwined with superconductivity. Neutron scattering famously first observed so-called stripe order phases by observing incommensurate elastic peaks centered around (π, π) positions in reciprocal space in the Nd-LSCO member of this family in 1995. Since then, many related studies of stripe ordered phases have been carried out on different branches of the La-214 family, including LBCO, LSCO, and Nd-LSCO.

This thesis presents a comprehensive study of a series of $\text{La}_{1.6-x}\text{Nd}_{0.4}\text{Sr}_x\text{CuO}_4$ (Nd-LSCO) crystals, from their synthesis and single crystal growth, to their advanced characterization using elastic and inelastic neutron scattering techniques. The thesis begins with a detailed description of the methods of materials synthesis and single crystal growth and the related characterization of the materials synthesized. It then moves on to explore the evolution of magnetic order and low energy excitations at various Sr doping levels from $x = 0.12$ to 0.26 in Nd-LSCO single crystals. These data show that spin stripe magnetic order persists beyond the putative quantum critical point associated with the pseudogap phase, and extends at least as far as the end of superconductivity. The behaviour of the associated dynamic spin stripes in these materials is also investigated with modern neutron spectroscopic methods, and these are also found to be pervasive across this range of doping. The implications of these data and their analysis are discussed and a new phase diagram is proposed which shows strong correlations between superconductivity and parallel spin stripe order and fluctuations.

Acknowledgements

I am deeply grateful to my PhD supervisor Prof. Bruce Gaulin. This project has been an ongoing effort for the past five years. It would not have been possible without the guidance from him. Having worked with Bruce for the past six years has been a real pleasure. I can never thank enough to his continuous support and encouragement to push me through difficulties during my PhD. This has been more important in the past two years with pandemic. Bruce is not only a great physicist but also an excellent mentor. I want to particularly thank Bruce for providing me with opportunities to travel around the world to conduct neutron scattering experiments, for the inspiring discussions about physics and finally for all the great memories during my time at McMaster University. I hope to continue collaboration with Bruce after graduation. I also strongly recommend Bruce to future graduate students. I can proudly say Bruce has been the best supervisor I have ever had during my entire school years.

I would like to express my gratitude towards my committee members Prof. Takashi Imai and Prof. Graeme Luke. Thank you for the guidance through out my PhD and the inspiring discussion during my committee meetings to make sure I am on track with the progress. I would also like to thank the scientists at Australian Nuclear Science and Technology and Oak Ridge National Laboratory. Matthew Stone, Alexander I Kolesnikov, Songxue Chi for their support during the experiment. I would like to particularly thank Kirrily Rule at Australian Nuclear Science and Technology for the wonderful collaborations and for trusting me with the equipment and providing great insights during and after the experiment.

I want to thank my colleagues and friends Mirela Dragomir, Evan Smith, Zach Cronkwright, Symphony Huang, Mathew Pula, Connor Buhariwalla, Yipeng Cai, Murray Wilson, Jonathan Gaudet, Alannah Hallas, Pat Clancy and Sean Takahashi for the wonderful times we shared in the office. I hope things are going well with every one of you.

Finally I would like to thank my parents for the never-ending support. Without them I could never be where I am today. Pandemic has created many challenges

for studying abroad, but my family has always encouraged me to chase my dreams and supported my decisions along the way. I am forever grateful to them.

Preface

This thesis consists of three papers two of which has been published and the third one has been accepted but yet published at the time of submission of present thesis. The three papers together provide a comprehensive description from material synthesis to the magnetic order in the Nd-LSCO systems. The surrounding material aims to establish formalism required to understand the research and connects the three papers as a coherent story. The publications are listed below:

Publication 1: Materials preparation, single-crystal growth, and the phase diagram of the cuprate high-temperature superconductor $\text{La}_{1.6-x}\text{Nd}_{0.4}\text{Sr}_x\text{CuO}_4$, Mirela Dragomir, Qianli Ma, J. Patrick Clancy, Amirreza Ataei, Paul A. Dube, Sudarshan Sharma, Ashfia Huq, Hanna A. Dabkowska, Louis Taillefer, and Bruce D. Gaulin. *Phys. Rev. Materials* 4, 114801

Publication 2: Parallel spin stripes and their coexistence with superconducting ground states at optimal and high doping in $\text{La}_{1.6-x}\text{Nd}_{0.4}\text{Sr}_x\text{CuO}_4$, Qianli Ma, Kirrily C. Rule, Zachary W. Cronkwright, Mirela Dragomir, Gabrielle Mitchell, Evan M. Smith, Songxue Chi, Alexander I. Kolesnikov, Matthew B. Stone, and Bruce D. Gaulin. *Phys. Rev. Research* 3, 023151

Publication 3: Dynamic Parallel Spin Stripes from the 1/8 anomaly to the End of Superconductivity in $\text{La}_{1.6-x}\text{Nd}_{0.4}\text{Sr}_x\text{CuO}_4$, Qianli Ma, Evan M Smith, Zachary W Cronkwright, Mirela Dragomir, Gabrielle Mitchell, Alexander I Kolesnikov, Matthew B Stone, Bruce D Gaulin. arXiv:2109.11570

Contents

Abstract	iii
Acknowledgements	iv
1 Introduction	1
1.1 High Temperature Superconductivity in Cuprate Systems	1
1.2 Structure of $\text{La}_{1.6-x}\text{Nd}_{0.4}\text{Sr}_x\text{CuO}_4$	4
1.3 The Phase diagram for $\text{La}_{1.6-x}\text{Nd}_{0.4}\text{Sr}_x\text{Cu}_2\text{O}_4$	7
1.3.1 The Nature of the Pseudogap Phase and Pseudogap Quantum Critical Point in 214 Cuprate Superconductors	7
1.3.2 Magnetic Order Within the Stripe Picture	15
2 Neutron Scattering	20
2.1 The Basics of Neutron Scattering	21
2.2 Nuclear Scattering By a Single Fixed Nucleus	23
2.3 Magnetic Neutron Scattering	27
2.4 The Triple Axis Neutron Spectrometer	29
2.5 Direct Geometry Time-of-Flight Chopper Spectrometers	31
3 The Crystal Growth of the family of $\text{La}_{1.6-x}\text{Nd}_{0.4}\text{Sr}_x\text{CuO}_4$	35
3.1 Preface	35
3.2 Incongruently Melting materials	35
3.3 Single Crystal Growth	37
3.4 Annealing on Post-Grown Single Crystals	42
4 The Material Synthesis and Single Crystal Growth of $\text{La}_{1.6-x}\text{Nd}_{0.4}\text{Sr}_x\text{CuO}_4$	46

4.1 Preface	46
5 Static Parallel Spin Stripe Order in Optimal and Overdoped Nd-LSCO	65
5.1 Preface	65
6 Parallel Spin Stripe Fluctuations in Optimally and Overdoped Nd-LSCO	82
6.1 Preface	82
7 Conclusion	99
7.1 Materials Synthesis, Crystal Growth and the Phase diagram of Nd-LSCO	99
7.2 Parallel Spin Stripes and their co-existence with Superconductivity in Nd-LSCO	101
7.3 The Persistence of Parallel Spin Spin Fluctuations Across the Phase Diagram of Nd-LSCO	105
7.4 Main Conclusions and Future Considerations	109
Bibliography	111

List of Figures

1.1	The determined superconducting temperature vs the time of discovery of various classes of materials. The famous LBCO was discovered in 1986 with a transition temperature of 30K. The images on the right shows representative structures of these superconducting materials. The first one on the upper right corner represents the structure of the cuprate system which are marked as red lines in the T_c vs Year plot. Figure reproduced from Ref.[10] with permission.	3
1.2	The base structure of Nd-LSCO in high temperature tetragonal structure. The CuO_2 form 2D planes sandwiching La, O and Cu atoms. The space between the CuO_2 layers has been described as electronic reservoir. The Cu-O octahedron between the CuO_2 layers exhibits slight tilting in different structures such as low temperature orthorhombic and low temperature tetragonal structures. Reproduced from [29] with permission.	5
1.3	The tilting of the Cu Octahedral with respect to the [100] or [010] axis in the HTT convention.	7
1.4	ARPES measured symmetrized normal-state energy-distribution curves (EDCs) on LSCO and Nd-LSCO. Panel a)-f) Raw symmetrized spectra; g)-i) background subtracted spectra. a), b) compares the symmetrized spectra data between LSCO and Nd-LSCO. c),d) momentum dependence of symmetrized EDCs moving from antinodal to nodal region for Nd-LSCO $x = 0.12$ and 0.2 . e),f) Temperature dependence of antinodal symmetrized EDCs on Nd-LSCO $x = 0.12$ and 0.20 . Each spectra were shifted vertically for clarity. The solid black lines in the bottom panls are fits using a phenomenological Green function. Reproduced from [35] with permission	9

1.5	In-plane electrical resistivity $\rho(T)$ of Nd-LSCO measured as a function of temperature measured in $x = 0.20$ and 0.24 sample. The magnetic field is strong enough to fully suppress superconductivity. The black line is linear fit for the $x = 0.20$ sample. The deviation of the linear T behaviour has been estimated to start at $T^*=80$ K with a minimum at 37 K. Same measurement in the $x = 0.24$ sample shows no upturn down to lowest temperature. Reproduced from [41] with permission.	10
1.6	Hall coefficient $R_H(T)$ measurements of Nd-LSCO $x=0.20$ and 0.24 samples in a magnetic field of 15 T. The dashed blue horizontal line indicates the Hall coefficient calculated from large electronlike Fermi surface enclosing $1+p$ holes. Reproduced from [41] with permission.	11
1.7	Illustration of the Fermi surface of a single-layered cuprate system. The Fermi surface evolves from large hole-like Fermi surface above p^* to small pockets of holes and electrons in a small region below p_0 and p^* . The reconstruction is believed to be due to a new periodicity from the antiferromagnetic modulation of wave vector (π, π) . With further decreased doping the electron pockets eventually shrinks to zero below p_0 and the four nodal hole pockets contain a total of p holes. Reproduced from [43] with permission.	12
1.8	a) Raw data for C/T in Eu/Nd-LSCO measured at different temperatures and magnetic field. b) Normal state electronic specific heat for Eu/Nd-LSCO at 0.5 K Dashed red line marks the pseudogap critical point p^* in Nd-LSCO. Reproduced from Ref.[33]with permission	14
1.9	Theorized illustration of spin stripes in the CuO_2 planes of Nd-LSCO $x = 0.125$ sample. Only the Cu atoms are represented. Arrows indicate the direction of magnetic moments on the Cu atoms. As can be seen they are locally antiferromagnetic. The rows of circles without arrows indicate the presence of holes. The spins experience an 180° shift upon crossing the magnetic domain walls. Reproduced from [11] with permission.	16

1.10	Scans in reciprocal space that reveals the spin and charge orders at proposed positions, in Nd-LSCO $x = 0.125$ at 11K. a) shows diagram of reciprocal space where the the scans were conducted. The open circles indicate Bragg peaks, solid circles denote spin and charger ordering superlattice peaks. Arrows indicate directions of specific scans. b) Scans along the $(\pi, \pi, 0)$ positions vertically with an incident neutron energy of 13.9 meV. The two incommensurate peaks were regarded as the evidence of static parallel spin stripe orders. The small peak width indicates the correlation length is over 150 Å. c) scans through $(0, 2+q, 0)$ using 14.7 meV incident neutron energy. The peak is a result of the spacial modulation due to charge ordering. Reproduced from [11] with permission.	17
1.11	A widely accepted phase diagram of Nd-LSCO with both spin and charge order over-plotted with pseudogap phase and T_c [59]. The situation of spin order was not clear in the overdoped region prior to the current work. The exact boundary of charge order is still under investigation. However it was believed that both ordered phases does not extend beyond the putative quantum critical point p^* which marks the Sr concentration where there is no upturn in the linear resistivity measurements. Reproduced from [59] with permission.	19
2.1	Geometry of a general scattering experiment. The quantities defined here are used to calculate the scattering cross sections. Figure reproduced from [60] with permission.	24
2.2	Diagram of triple axis spectrometer. A white beam of neutrons come out from reactor source onto the monochromator. The monochromator then scatter off neutrons with specific wavelength onto the sample. The scattered neutrons then reach the analyzer and detector which determines the intensity, momentum of the neutrons. . . .	31

2.3	Schematic diagram of a time-of-flight spectrometer at SEQUOIA, ORNL. The ToF spectrometer consists a few choppers to select incident neutron energy as well as avoid interference between different phases of neutrons. The detectors is a bank of ^3He detectors which is produces a pulse when a neutron hit on the detector. The deployment of such set up drastically increased the capacity of neutron scattering experiments as multiple energy and momentum transfer can be measured simultaneously.	34
3.1	The phase diagram of the binary system $\text{LaO}_{1.5}\text{-CuO}$. The upper right region of the phase diagram shows a region with pure liquid. This is the key area to the solvent floating zone crystal growth technique. A target of 22:78 of La:Cu ratio was determined such that when operating $\sim 1100\text{-}1200^\circ$ the solvent is uniformly melted in a homogeneous liquid phase.Courtesy to Dr.Jianshi Zhou.	38
3.2	The feed rod of $x=0.24$ sample. Photo taken after final annealing in flowing oxygen. The rod is about 7cm long and weighs 14.6 grams. Rod of this size can sustain two growths spanning over a time frame of two weeks.	39
3.3	Schematic diagram of the set-up within the mirror stage. Four halogen lamps are mounted on ellipsoidal mirror stage that focuses lights in the molten zone. The feed rod hangs under the upper shaft and the seed rod is mounted on top of the bottom shaft. The seed and feed rod rotates counterclockwise to achieve a homogeneous mixing in the molten zone.	40
3.4	A photo taken at the Crystal System furnace at McMaster University's crystal growth lab.	41
3.5	A comparison of the measured susceptibility of the annealed and un-annealed Nd-LSCO samples. The blue data points indicate field-cooled measurements while the red data points indicating the zero-field-cooled measurements. The applied field is indicated in each figure. The direction of the applied fields are all parallel to the c-axis.	44

3.6	Resistivity measurements on the Nd-LSCO $x = 0.24$ sample before and post annealing. The sample is annealed in flowing oxygen at 900° 1am for a week. The solid black and red line represent data measured in magnetic field at 16T.	45
4.1	A continuous growth of Nd-LSCO $x=0.17$. The growth lasted for more than 250 hours. The crystal is about 13cm long.	48
4.2	A continuous growth of Nd-LSCO $x=0.19$. The crystal is about 9cm long	49
4.3	A continuous growth of Nd-LSCO $x=0.24$. The crystal is about 4.5cm long	49
5.1	Elastic peak measured around $(1/2, 1/2, -0.3)$ at $T = 2K$.The panel a) and b) shows a single peak at $q=0$ but in panel c) the $x = 0.05$ LSCO sample displays two incommensurate peaks "diagonal" to the $(1/2, 1/2)$ position. The inset of panel c) shows the direction of the scans in reciprocal space. Reproduced from [67] with permission. . .	68
6.1	Summarized maximum $\chi''(\omega)$ vs onsite T_c measured by the magnetic susceptibility for LSCO $x = 0.25, 0.27, 0.28$ and 0.30 . The $\chi''(\omega)$ is taken as maximum from 2-10 meV energy range. Figure reproduced from [72] with permission.	85
6.2	Integrated intensity of $S(\omega)$ vs ω in meV. Blue square indicates data from LBCO and the rest are LSCO data with Sr concetration $x = 0.25$ and 0.30 Figure reproduced from [73]with permission.	86
7.1	a) Schematic phase diagram of antiferromagnetic insulating state, superconducting dome, Fermi metal and the pseudogap characterized by the linear T resistivity T^* . b),c) Schematic drawing of the electron like Fermi surface and reconstructed Fermi surface as a result of an order with (π, π) wavevector. Reproduced from [81] with permission.	104

7.2	Fermi surface of LSCO $x = 0.063$. Black solid lines and red open circles are sketched Fermi surface and measured data points. The dotted lines represent the antiferromagnetic zone boundary. There are eight yellow dots marks the intercepts between the AF zone boundary and the Fermi surface. The double headed green arrow is the nesting vector. The inset demonstrates the incommensurate peaks measured by neutron scattering. Reproduced from [83] with permission.	106
7.3	The spectral function $\chi''(\omega)$ calculated from random t-J model averaged over 100 disorder realizations on an 18-site cluster. We interpret the peaks at $\omega \sim 0.1$ with our quasi-elastic neutron scattering data on the static parallel spin strip order up to $x = 0.26$. We also associate the region where $\omega > 0.5$ with our inelastic neutron scattering results suggesting the intensity at different energies do not show strong x - dependence. Reproduced from [74] with permission.	108
7.4	Illustrations of different properties of the spin and charge dynamics in Nd-LSCO. Top row shows static spin and charge distribution in real space. Middle row shows the dynamic spin fluctuations and the bottom row shows the Fermi surfaces at different doping. Reproduced from [89] with modification.	110

Chapter 1

Introduction

1.1 High Temperature Superconductivity in Cuprate Systems

The discovery of high-temperature superconductivity in the copper oxide perovskite system is one of the most significant scientific breakthroughs of the 20th century [1–4]. The T_C in the first discovered cuprate, $\text{Ba}_x\text{La}_{5-x}\text{Cu}_5\text{O}_{5(3-y)}$, reached as high as 30 K which was significantly higher than those previously known from older superconducting materials [1]. The La-214 superconductors are a group of copper oxide materials comprised of a stacking of CuO_2 planes into a “single layer” structure (to contrast it from bilayer or trilayer structures). The parent compound for this family, La_2CuO_4 is a Mott insulator, and upon doping with either holes or electrons it quickly becomes conducting and then superconducting, accompanied by magnetic and charge order.

The Bardeen-Cooper-Schrieffer (BCS) theory [5] was very successful in describing the properties of low temperature superconductors that have been known since the discovery of superconductivity in Hg in 1911 [6]. Within BCS theory, electrons, which are fermions, can pair together to form composite Bosons, known as Cooper pairs, and these can undergo Bose-Einstein condensation into a superfluid states, and thereby move freely in the lattice. This formulation requires a net attractive interaction between the electrons in order to get the electrons to form the

Cooper pairs. One possible mechanism for such a net attractive interaction between electrons, and one that is thought to be relevant for many low temperature superconductors, is for negatively charged electrons to slightly distort the positively-charged lattice, causing the ions to displace from their local equilibrium positions to create a local positive charge density which, in turn, attracts a second electron and bind them into pairs with energies typical of phonon energies. This is a form of an electron-phonon interaction. It also implies that the superconducting transition temperature is not likely to exceed ~ 30 K[7, 8]. The discovery of high cuprate superconductors has challenged the very successful BCS theory as the T_C s involved are now much larger than 30 K. As more studies were carried out on such cuprate systems, it has become clear that much of our understanding of metals and superconductors is not as firmly established as we would like, as much of the phenomenology associated with copper oxides is anomalous.[9, 10].

Fig.1.1 surveys the progress over the years in pushing the upper limit of the superconducting transition temperature[10] in new materials. Sophisticated theories and various independent experimental techniques have been used to investigate the mechanism behind high T_C superconductivity from different perspectives. These experimental techniques, including transport measurements, neutron scattering, ARPES, R(I)XS, and NMR have all made significant discoveries related to the cuprates [11–28], yet an unified understanding of the cuprate superconductors remains elusive. With all these studies over some 35 years, it is not a simple task to synthesize all the theoretical and experimental work that has been done to this point. This thesis makes a modest contribution to this field, by providing new, large and high quality single crystals from one of the cuprate High T_C families, and carrying out advanced characterization of these new materials, primarily informing on their static and dynamic magnetic properties using neutron scattering techniques.

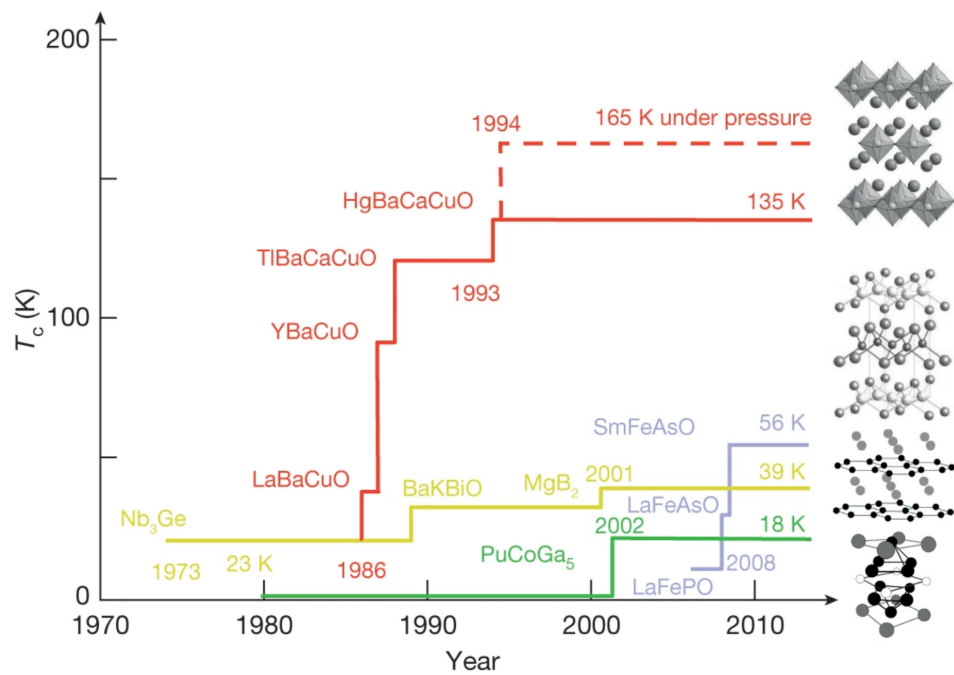


FIGURE 1.1: The determined superconducting temperature vs the time of discovery of various classes of materials. The famous LBCO was discovered in 1986 with a transition temperature of 30K. The images on the right shows representative structures of these superconducting materials. The first one on the upper right corner represents the structure of the cuprate system which are marked as red lines in the T_c vs Year plot. Figure reproduced from Ref.[10] with permission.

1.2 Structure of $\text{La}_{1.6-x}\text{Nd}_{0.4}\text{Sr}_x\text{CuO}_4$

The parent compound of $\text{La}_{1.6-x}\text{Nd}_{0.4}\text{Sr}_x\text{CuO}_4$ (Nd-LSCO) is La_2CuO_4 . It adopts a tetragonal crystal structure (I4/mmm) illustrated in Fig.1.2 [29]. The parent compound has a ratio of La, Cu, O as 2,1,4 and cuprate superconductors derived from La_2CuO_4 are often referred to as the single layer La-214 family. Upon substituting La with Nd and Sr, Nd-LSCO develops a low temperature orthorhombic structure with a space group of Bmab which involves a tilting for the CuO_6 octahedra along the [110] direction. It further develops into a low temperature tetragonal structure when the CuO_6 tilts along the [010] direction. In the tetragonal unit cell, the a and b axes are parallel to the nearest-neighbor copper bonds in the CuO_2 planes. However, in the corresponding orthorhombic structure, the a and b axes runs parallel to the next nearest neighbour copper bonds. This results in difference of $\sqrt{2}$ of the length in a and b axes between the two conventions for the choice of a and b axes. The length of the a,b axes in the orthorhombic structure varies between 5.3-5.4 Å while the c axis is around 13.15 Å. Detailed characterization can be found in Chapter 4 and Ref. [29] where several crystallographic parameters has been plotted vs different Sr doping concentrations.

One of the distinguishing traits of the La-214 family is that it is comprised of a stacking of single-layer two-dimensional CuO_2 planes and the superconductivity is believed to reside in the two dimensional(2D) copper-oxide planes. The La atom has an electronic configuration of $[\text{Xe}]5d^16s^2$. Upon losing three outer shell electrons, it takes on the $[\text{Xe}]$ electronic configuration and enters into the 3+ oxidation state. Similarly, the Nd atoms enters into 3+ oxidation state with electronic configuration of $[\text{Xe}]4f^3$. According to Hund's rule this results in $S=3/2$, $L=6$ and $J=9/2$ ground state for the Nd^{3+} , which is magnetic. The $J=9/2$ allow a maximum of 10 doubly degenerate levels of crystal field states. Two of the excited crystal field states are identified in the thesis at ~ 11 meV and 25 meV, see Chapter 5 and Ref.[30] for more information. Since Nd has the same 3+ oxidation state as La^{3+} , the responsibility for establishing charge neutrality falls onto the CuO_2 units. Cu in its charge neutral state has the electronic configuration of $[\text{Ar}]3d^{10}4s^1$. Assuming that the oxygen maintains a 2- ionic state, doping La^{3+}

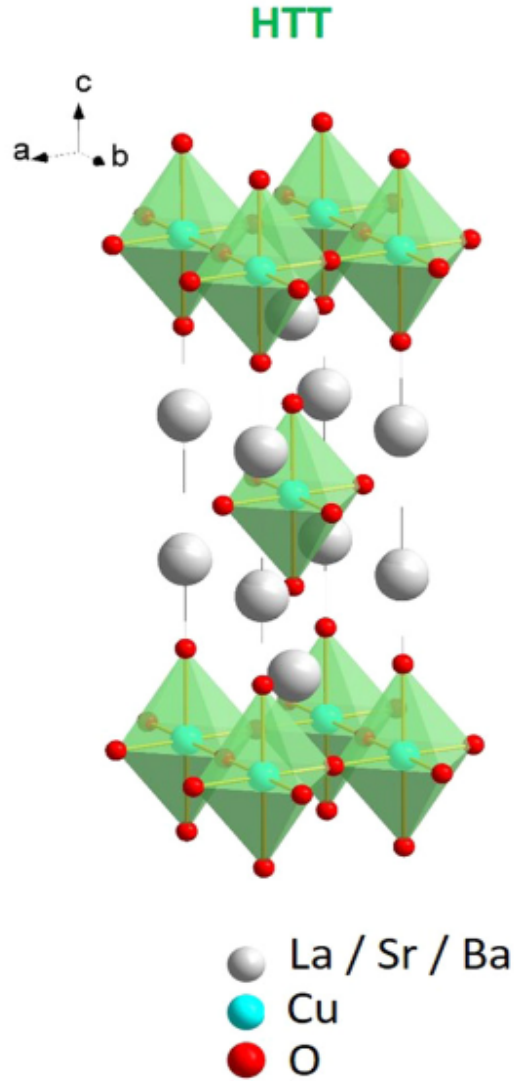


FIGURE 1.2: The base structure of Nd-LSCO in high temperature tetragonal structure. The CuO_2 form 2D planes sandwiching La, O and Cu atoms. The space between the CuO_2 layers has been described as electronic reservoir. The Cu-O octahedron between the CuO_2 layers exhibits slight tilting in different structures such as low temperature orthorhombic and low temperature tetragonal structures. Reproduced from [29] with permission.

with Sr^{2+} would require some Cu ions to change into $3+$ with an electronic configuration of $[\text{Ar}]3d^8$. The rest of the Cu ions then remain in $[\text{Ar}]3d^9$ states with a $2+$ oxidation state. When Cu is in a $2+$ oxidation state, there are 9 electrons in the 3d shell resulting in one unpaired electron. Therefore Cu^{2+} can be associated with a spin $1/2$ magnetic degree of freedom. For an isolated Cu^{2+} ion in vacuum, all 5 of the doubly degenerate 3d orbitals would themselves be degenerate. In the Nd-LSCO system, the Cu^{2+} finds itself in an octahedral local structure. The crystal electric field effect arising from the surrounding oxygen ions splits the 5 3d orbitals into two subsets, e_g and t_{2g} orbitals. The doubly degenerate e_g orbitals have a higher energy than the triply degenerate t_{2g} orbitals, and 6 of the 9 Cu^{2+} electrons will fill the t_{2g} orbitals. The remaining 3 electrons fill the e_g orbitals at higher energy. The spin-only magnetic moment for Cu^{2+} ion can be calculated from the formula $\mu_{Cu} = \sqrt{n(n+2)} = \sqrt{4S(S+1)} = \sqrt{3} = 1.73\mu_B$ where $n = 1$, or $S=1/2$ for one unpaired electron. As discussed above, doping La^{3+} with Sr^{2+} in the parent compound implies that mobile holes are being introduced into the copper-oxide planes. The doped holes are known to actually reside on the oxygen site [31]. However, these have been postulated to form Zhang-Rice singlets [32] with nearby Cu^{2+} ions, and via this mechanism it is possible to imagine the holes being associated with the Cu sites. Within a naive spin and charge order picture, it is often the case that the CuO_2 plane is abstracted to an approximately square Cu lattice with a single electron per site. At half-filling, the case of the parent compound La_2CuO_4 , each Cu site has a single electron, but as holes are doped into this structure, one can think of these electrons being systematically removed. The holes are mobile, so the distribution of holes can occur inhomogeneously so as to lower the overall energy of the system. Within the stripe picture this results in a spin and charge ordered state depending on the hole concentration and the temperature.

Nd^{3+} acts as an isovalent dopant in the Nd-LSCO system. One can then ask, what is the role of Nd^{3+} ? The role is subtle as it does not change the valence states associated with any ions, but induces an additional crystalline structure, known as the low temperature tetragonal structure (LTT) in the materials phase diagram, compared with LSCO. The crystalline structures, HTT, LTO or LTT differ by the tilting of the Cu octahedra between the CuO_2 layers. The tilting of Cu octahedral

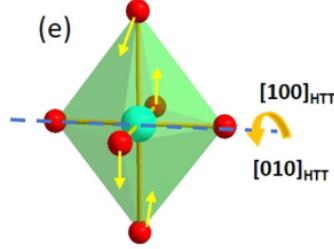


FIGURE 1.3: The tilting of the Cu Octahedral with respect to the $[100]$ or $[010]$ axis in the HTT convention.

is shown in Fig.1.3 as an example. This LTT structure is not found in LSCO however it is seen in both Eu-LSCO and LBCO. The LTT structure is believed to be energetically favorable for the formation of static spin stripes in Eu-LSCO, LBCO and Nd-LSCO. The spin stripe order is the focus of this PhD research where I explored the relationship between both spin stripe order and fluctuations and the superconductivity that this family displays, especially at relatively high hole doping. Now let's discuss briefly the formation of spin stripe order.

1.3 The Phase diagram for $\text{La}_{1.6-x}\text{Nd}_{0.4}\text{Sr}_x\text{Cu}_2\text{O}_4$

1.3.1 The Nature of the Pseudogap Phase and Pseudogap Quantum Critical Point in 214 Cuprate Superconductors

The enigmatic pseudogap phase is now central to the discussion of the low temperature properties of cuprate superconductors, as it is now apparent that this is a universal feature for the hole-doped cuprates [33]. Although the origin of pseudogap remains under debate, it manifests itself through a variety of measurements including NMR, ARPES and transport measurements[34–36]. In ARPES, the pseudogap manifests itself literally as a gap in the electronic energy spectrum for certain directions on the Fermi surface, in particular, in the antinodal regions. ARPES has famously measured a series of LSCO and Nd-LSCO samples by C.E.Matt [35]. Panel h) in Fig.1.4 shows such gapless spectrum for $x = 0.24$

Nd-LSCO. At lower dopings (value of x), a gap around zero energy clearly develops and gets larger for low temperatures and lower doping.

Resistivity measurements have also provided evidence for a pseudogap, consistent with the ARPES data. These measurements require that superconductivity be suppressed by rather large magnetic fields, such that a finite resistivity can be measured down to the lowest temperatures. This evidence was first provided for LSCO $x = 0.08$ and 0.13 by using pulsed fields up to 61 T [37, 38]. An upturn in $\rho(T)$ at low T was first observed for the LSCO sample with hole concentration ~ 0.16 . Later, Hussey *et al.* found that $\rho(T)$ decreases linearly as T approaches 0 from $p = 0.18$ up to $p = 0.23$ in LSCO[39]. The T^* , which is a characterization of the pseudogap phase, is defined as the temperature when the resistivity deviates from the linear fit, shown as an example in Fig.1.5. Samples with doping above the quantum critical point shows no upturn in the resistivity measurements. The p^* in LSCO was later determined to be at $p=0.19$ [40] in similar fashion. The work connecting resistivity and pseudogap came from Daou *et al.*'s work on Nd-LSCO as they attributed the upturn in $\rho(T)$ at 80 K [41] in the $x = 0.20$ Nd-LSCO sample to the opening of the pseudogap. This is in good agreement with the ARPES results shown in Fig.1.4 panel f). ARPES does not observe any opening of pseudogap by $p=0.24$, which is consistent with resistivity measurements in Ref.[41] where a linear relationship was observed down to the lowest temperature. Hall coefficient measurements also shows a change in Hall number over p^* in Fig.1.6[41].

It has been suggested for some time that a putative quantum critical point exists in Nd-LSCO at $x = 0.235$ [33, 41, 42]. One key signature corresponding to the quantum critical point is the change in carrier density from $n=1+p$ above p^* to $n=p$ below p^* . This is summarized in Ref.[43]. An explanation for this behaviour has been proposed by the presence of electron-like carriers at the Fermi surface below p^* for a narrow range of hole doping concentrations. One of the explanations for the drop in carrier density from $1+p$ to p is a quantum phase transition due to the antiferromagnetic order for doping levels below the quantum critical point with a wavevector of (π, π) . Symmetry breaking occurs from the new periodicity imposed by the spin modulation. As a result the large hole-like Fermi surface above p^* transforms into small hole and electron pockets at nodal

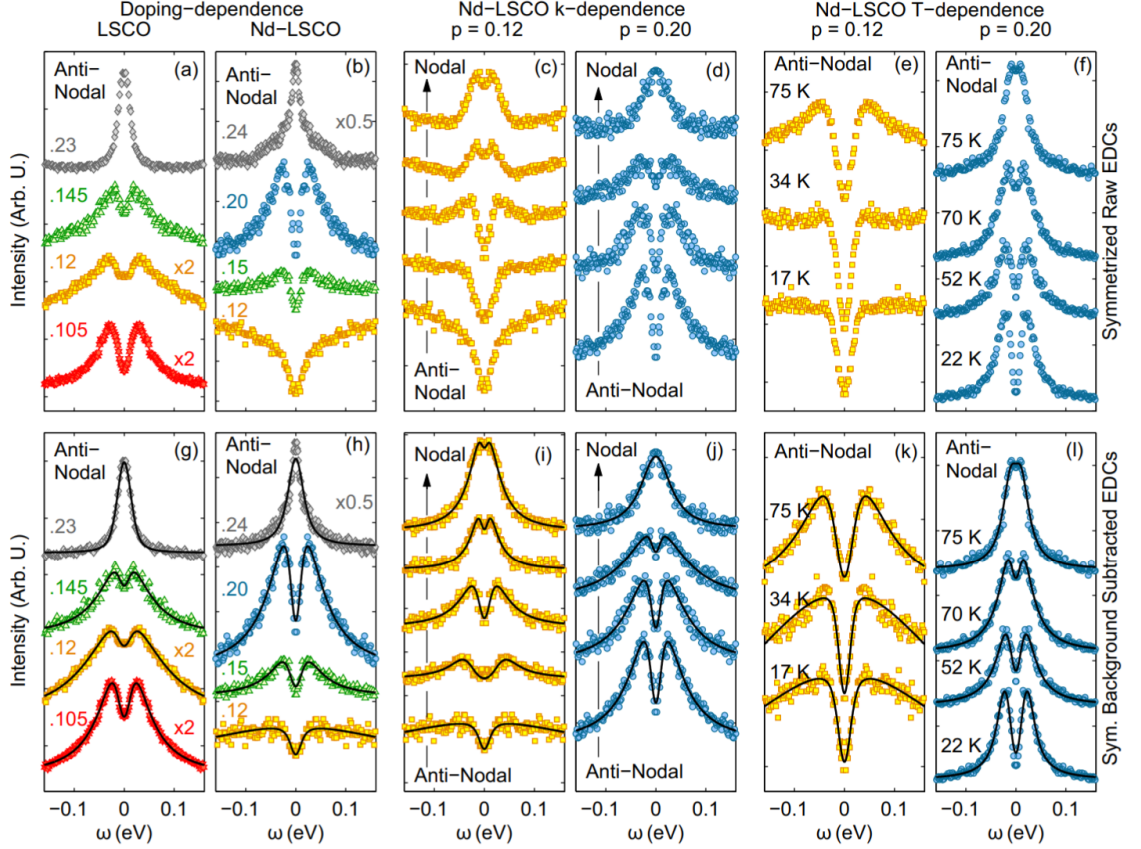


FIGURE 1.4: ARPES measured symmetrized normal-state energy-distribution curves (EDCs) on LSCO and Nd-LSCO. Panel a)-f) Raw symmetrized spectra; g)-i) background subtracted spectra. a), b) compares the symmetrized spectra data between LSCO and Nd-LSCO. c), d) momentum dependence of symmetrized EDCs moving from antinodal to nodal region for Nd-LSCO $x = 0.12$ and 0.2 . e), f) Temperature dependence of antinodal symmetrized EDCs on Nd-LSCO $x = 0.12$ and 0.20 . Each spectra were shifted vertically for clarity. The solid black lines in the bottom panels are fits using a phenomenological Green function. Reproduced from [35] with permission

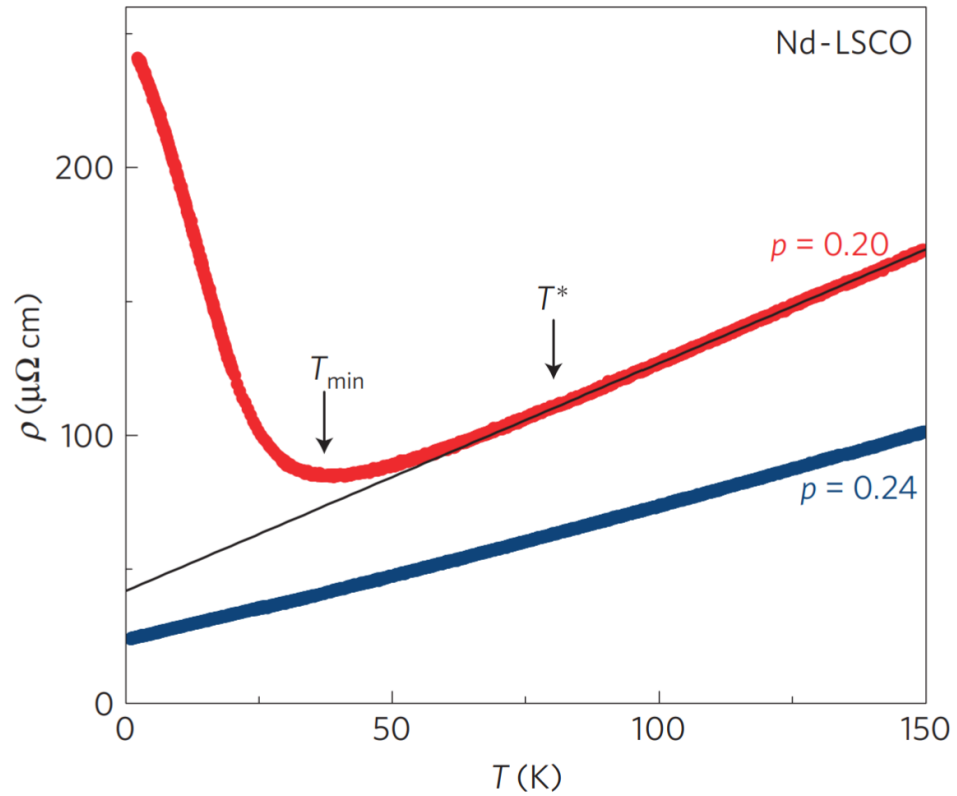


FIGURE 1.5: In-plane electrical resistivity $\rho(T)$ of Nd-LSCO measured as a function of temperature measured in $x = 0.20$ and 0.24 sample. The magnetic field is strong enough to fully suppress superconductivity. The black line is linear fit for the $x = 0.20$ sample. The deviation of the linear T behaviour has been estimated to start at $T^* = 80$ K with a minimum at 37 K. Same measurement in the $x = 0.24$ sample shows no upturn down to lowest temperature. Reproduced from [41] with permission.

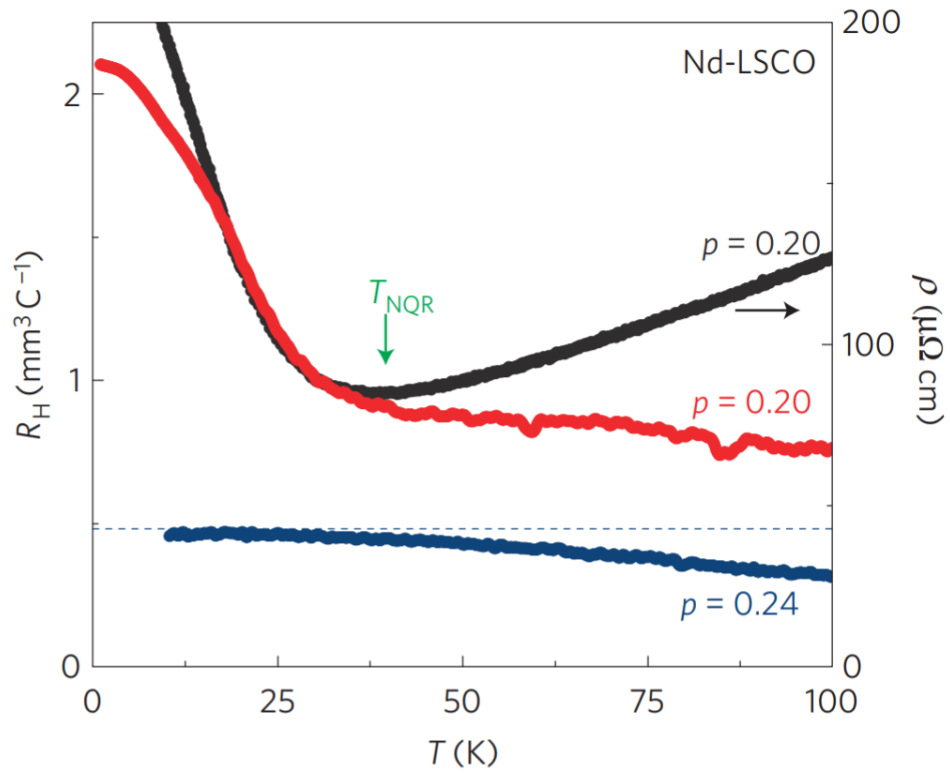


FIGURE 1.6: Hall coefficient $R_H(T)$ measurements of Nd-LSCO $x=0.20$ and 0.24 samples in a magnetic field of 15 T. The dashed blue horizontal line indicates the Hall coefficient calculated from large electronlike Fermi surface enclosing $1+p$ holes. Reproduced from [41] with permission.

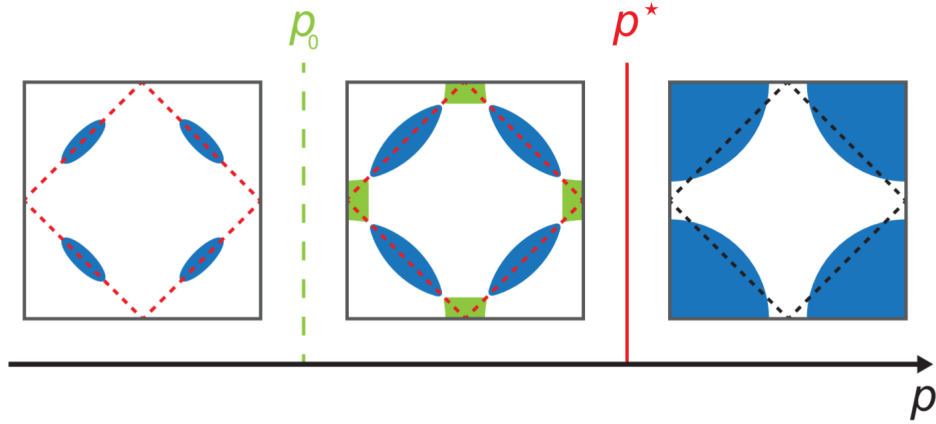


FIGURE 1.7: Illustration of the Fermi surface of a single-layered cuprate system. The Fermi surface evolves from large hole-like Fermi surface above p^* to small pockets of holes and electrons in a small region below p_0 and p^* . The reconstruction is believed to be due to a new periodicity from the antiferromagnetic modulation of wave vector (π, π) . With further decreased doping the electron pockets eventually shrinks to zero below p_0 and the four nodal hole pockets contain a total of p holes. Reproduced from [43] with permission.

and anti-nodal positions respectively. The electron pockets eventually disappear with increased antiferromagnetic moment and decreases $x \sim p$. By Luttinger's theorem [44, 45], the large hole-like Fermi surface above p^* contains $1+p$ hole and the four hole pocket's below some doping concentration p_0 contains p holes illustrated in Fig.1.7. Prior to the work in this thesis, antiferromagnetic modulations has been detected in Nd-LSCO in the form of incommensurate magnetic Bragg peaks by neutron scattering up to $x = 0.20$ by Tranquada *et al.* [12]. The onset T_{SDW} was extrapolated linearly to zero $\sim p^*$ shown in Fig.3.1. One question that remains is that the spin density wave vector is not exactly at (π, π) but rather it is centered around it, at $(\pi \pm \delta, \pi)$ or $(\pi, \pi \pm \delta)$ where $\delta \sim x$ follows the so-called Yamada relation [46]. It is unclear how the incommensurability would affect the results on charge carrier density. However we will see in the following chapters of the thesis that clear evidence exists that parallel spin stripe orders persists beyond p^* .

The other strong evidence in favour of a quantum critical point at $p^* \sim 0.235$ is thermodynamic in origin. Michon *et al* reported a divergence in the Sommerfeld

constant as measured in the electronic C_P , with a form for $C_P(T)$ at p^* that is consistent with earlier work on quantum criticality in other correlated electron systems [33]. Fig.1.8 shows measured C/T and C_{el}/T vs p on a series of Nd/Eu-LSCO samples. By taking advantage from the material synthesis done in this thesis, the heat capacity of three insulating Nd-LSCO samples $x = 0.27, 0.36$ and 0.4 produced at McMaster University along with other dopings of Nd/Eu-LSCO were measured. A huge cusp-like peak in C_{el}/T vs p with $C/T \propto \log(1/|x - x^*|)$ was shown in both panels of Fig.1.8. This cusp-like peak was compared with that seen in iron-based superconductors at their antiferromagnetic p^* [47, 48] and is suggestive of a quantum critical point in both Eu-LSCO and Nd-LSCO.

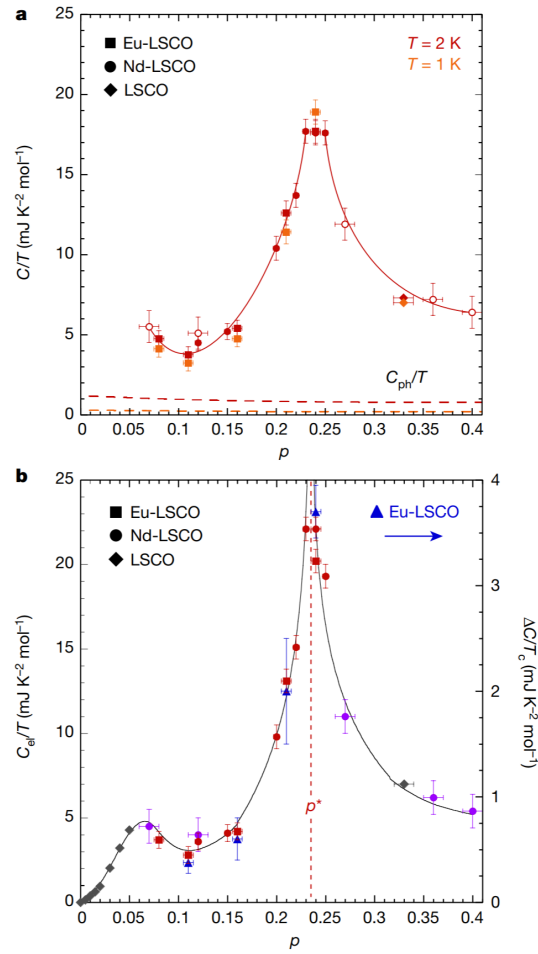


FIGURE 1.8: a) Raw data for C/T in Eu/Nd-LSCO measured at different temperatures and magnetic field. b) Normal state electronic specific heat for Eu/Nd-LSCO at 0.5 K . Dashed red line marks the pseudogap critical point ρ^* in Nd-LSCO. Reproduced from Ref.[33]with permission

1.3.2 Magnetic Order Within the Stripe Picture

The static spin and charge stripe ordered phase in Nd-LSCO was famously first observed by Tranquada and co-workers using triple axis neutron spectroscopy in 1995 [11]. Ever since this measurement of stripe order by neutron scattering, it has been at the center of discussion on cuprate superconductors, now over more than two decades. Many theories have been proposed to explain its relation with superconductivity and how it can manifest itself within the pseudogap phase. It has also long been debated whether the stripe order enhances or suppresses superconductivity due to the fact that $x = 0.12$ corresponds to the maximum in spin stripe order and a minimum of superconducting T_C on the superconducting dome for example in the Nd-LSCO systems. Ref.[49–51] give good summaries on some of these matters. The most recent studies of magnetism in the Nd-LSCO system reported here have shown that incommensurate magnetic order consistent with the stripe picture exists beyond p^* well into the overdoped region of the phase diagram.

The nature of stripe order can be understood within simple stripe picture of Fig.1.9. When Sr^{2+} is introduced into the system by substitution for La^{3+} holes are introduced into the CuO_2 planes. In the presence of holes, the Cu ions can be thought of as made of a mixture of 2+ and 3+ oxidation states. The 3+ Cu ion has an electronic configuration of $[\text{Ar}]3d^8$, and a net spin 0. The Cu ions with or without spins arrange inhomogeneously in the periodic pattern shown in Fig.1.9. For a more accurate description of the proposed distribution of holes within the CuO_2 planes, readers are encouraged to read Ref.[31, 32] about the nature of Zhang-Rice singlets. The local antiferromagnetic structure at low temperatures is indicated by the arrows within circles in the figure. The Cu sites without moments are associated with holes in the figure. Fig.1.9 indicates a hole concentration of $1/8$ which happens to be the Sr concentration at which superconductivity is maximally suppressed. As can be seen, the mobile holes are arranged into quasi-one dimensional stripes, with regions of local (π, π) antiferromagnetism in between. There is a π phase shift in the antiferromagnetic structure across the holes, giving rise to incommensurate magnetic, and charge order.

Fig.1.10 shows the earliest neutron scattering evidence for static spin and charge

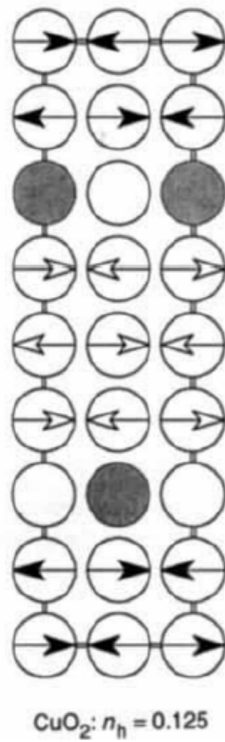


FIGURE 1.9: Theorized illustration of spin stripes in the CuO_2 planes of Nd-LSCO $x = 0.125$ sample. Only the Cu atoms are represented. Arrows indicate the direction of magnetic moments on the Cu atoms. As can be seen they are locally antiferromagnetic. The rows of circles without arrows indicate the presence of holes. The spins experience a 180° shift upon crossing the magnetic domain walls. Reproduced from [11] with permission.

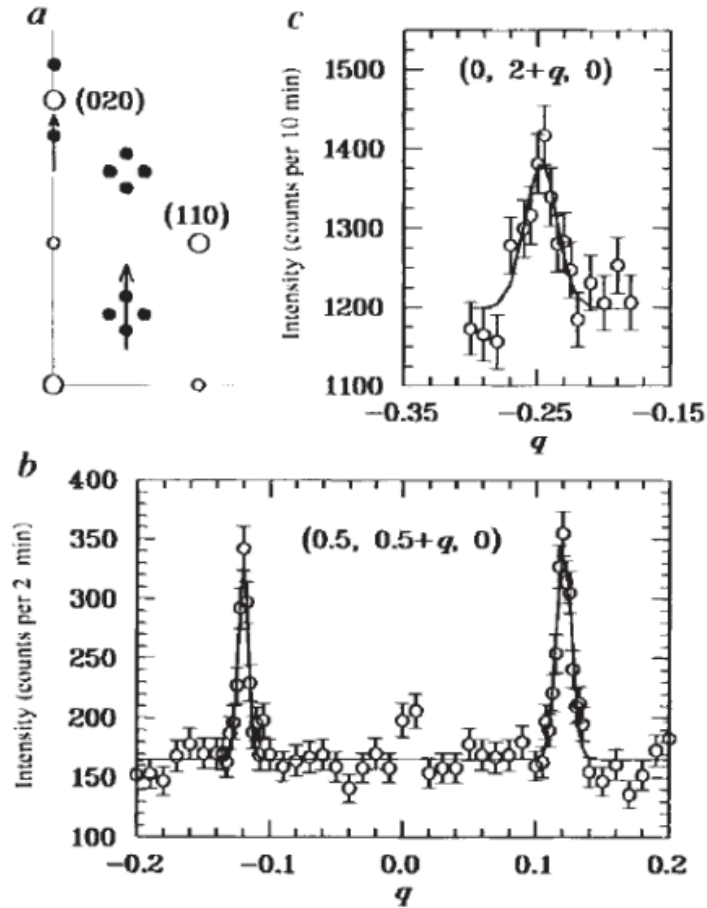


FIGURE 1.10: Scans in reciprocal space that reveals the spin and charge orders at proposed positions, in Nd-LSCO $x = 0.125$ at 11K. a) shows diagram of reciprocal space where the the scans were conducted. The open circles indicate Bragg peaks, solid circles denote spin and charger ordering superlattice peaks. Arrows indicate directions of specific scans. b) Scans along the $(\pi, \pi, 0)$ positions vertically with an incident neutron energy of 13.9 meV. The two incommensurate peaks were regarded as the evidence of static parallel spin stripe orders. The small peak width indicates the correlation length is over 150 Å. c) scans through $(0, 2+q, 0)$ using 14.7 meV incident neutron energy. The peak is a result of the spacial modulation due to charge ordering. Reproduced from [11] with permission.

stripes, taken from triple axis spectroscopy in Nd-LSCO $x = 0.125$ [11]. The experiment was performed with the crystal aligned such that the (001) axis was vertical. The scans were performed by doing line scans in specific reciprocal space directions. Panel a) indicates the predicted positions of the spin and charge stripe order. Panel b) shows that the spin stripes result in incommensurate magnetic peaks at $(\frac{1}{2} \pm q, \frac{1}{2}, 0)$ and $(\frac{1}{2}, \frac{1}{2} \pm q, 0)$ positions, the wavevector q roughly follows Yamada relation where $\delta \sim x$ at small dopings [46]. The charge order is due to the mobile holes, but presumably these also affect the positions of the atoms so as to produce superlattice peaks around (020) and symmetry related positions as shown in panel c) of Fig.1.10.

The evolution of stripe and charge orders at different dopings in different cuprates have been extensively studied with both neutron and X-Ray scattering [11, 52–56]. Charge stripe order has generally been observed to onset at higher temperature than spin order [57]. The end point of charge order in cuprate phase diagrams is still unclear with a recent study observing CDW order at $x = 0.12, 0.17$ but not 0.19 in Nd-LSCO [56]. In LSCO there has been studies reporting the observation of CDW order as high as $x = 0.21$ [58]. Fig.1.11 displays a common understanding of the interrelation between spin stripe and charge stripe order as well as superconductivity [59]. It presents a picture consistent with pre-existing transport data, where no indirect evidence for magnetism exists beyond p^* . However in this thesis, a focal point will be the presentation of experimental evidence which updates the role of spin stripe order within the phase diagram of Nd-LSCO, and its relation to the pseudogap and superconducting states in this family of materials. This allows us to conclude that parallel spin stripe magnetic order and fluctuations are considerably more persistent through the high T_C phase diagram, at least in the Nd-LSCO family, than previously thought.

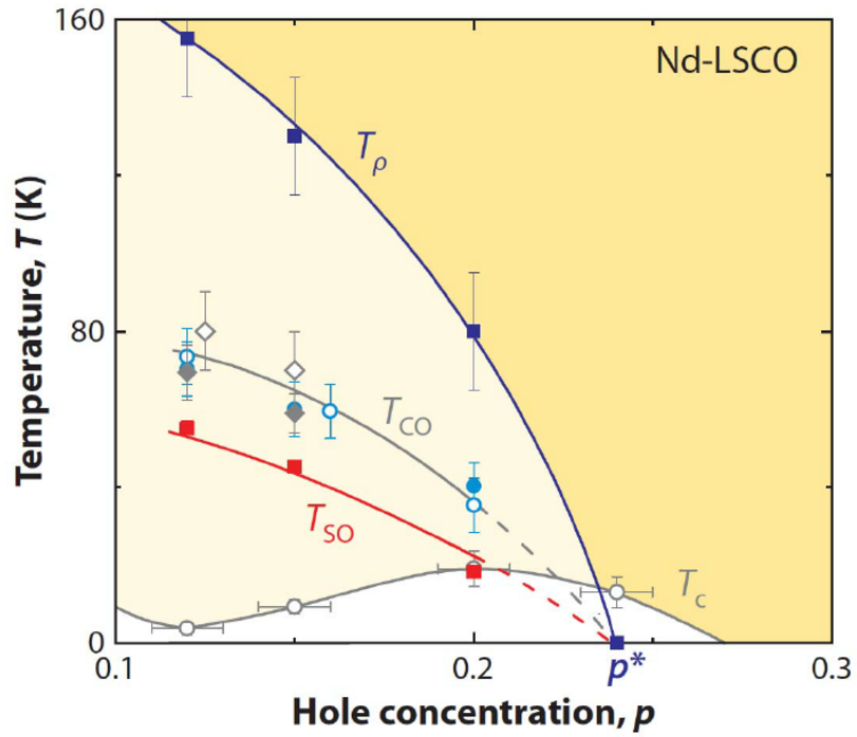


FIGURE 1.11: A widely accepted phase diagram of Nd-LSCO with both spin and charge order over-plotted with pseudogap phase and T_c [59]. The situation of spin order was not clear in the overdoped region prior to the current work. The exact boundary of charge order is still under investigation. However it was believed that both ordered phases does not extend beyond the putative quantum critical point p^* which marks the Sr concentration where there is no upturn in the linear resistivity measurements. Reproduced from [59] with permission.

Chapter 2

Neutron Scattering

Neutrons can scatter from materials both elastically or inelastically. Neutrons which have come into equilibrium at room temperature have de Broglie wavelengths typical of interatomic distances and energies typical of magnetic and lattice excitations in materials. These properties make neutron scattering a powerful probe of materials and very suitable for the study of various magnetic systems.

There are two common technologies used to produce neutrons for a scattering experiment. The first method is via nuclear reactions in a nuclear reactor, while the second is via proton accelerators and the spallation process. These two production methods both require large infrastructure at national laboratories such as Oak Ridge National Laboratory or National Institute of Standards and Technology. The fission production of neutrons in nuclear reactors involves using one low energy neutron being absorbed by a fissile nuclei, typically ^{235}U . This splits ^{235}U into (typically) two heavy nuclei and produces two to three neutrons in the process. The neutrons so produced then go on to repeat this process to create a chain reaction. Fission therefore provides a continuous neutron source, as there is no natural time scale to the process. In contrast, spallation involves having a relativistic high energy proton hit onto a heavy target material, for example mercury. The heavy nucleus absorbs the proton and becomes unstable, "boiling" off (mostly) neutrons and protons in the process. Spallation neutrons are more difficult to bring to equilibrium in a moderating material, and a spallation source typically provides access to higher energy neutrons than a reactor based source. These high energy neutrons can be used in scattering experiments to probe excitations in materials

up to several eV in energy, where they can be used to study crystal field and intermultiplet excitations in magnetic materials.

In this chapter, we will focus on the formalism of neutron scattering following Squire’s Introduction to the Theory of Thermal Neutron Scattering [60]. This chapter introduces basics of neutron scattering and how it is applied to magnetic scattering. With a foundation to this formalism established, we will discuss two specific experimental neutron scattering techniques, triple axis neutron scattering techniques and direct geometry time-of-flight chopper techniques, which are the main neutron scattering techniques employed in this thesis.

2.1 The Basics of Neutron Scattering

The neutron is an uncharged Fermi particle with magnetic dipole moment. There are different types of neutron scattering experiments, which include elastic, inelastic and polarized neutron scattering. Table 2.1 lists some of the basic properties of neutrons. From the mass of neutron, $m=1.675\times 10^{-27}\text{kg}$, one can calculate the average kinetic energy of neutron is around 25meV with a de Broglie wavelength 1.8Å for neutrons in equilibrium at room temperature. This wavelength is comparable to the distance between atoms in materials therefore allowing diffraction between the neutrons and the atomic lattices. Most typical condensed matter excitations fall within same orders of meV range. These numbers imply that inelastic neutron scattering is a suitable candidate to probe the elementary excitations in a material

As Fermions, neutrons are spin- $\frac{1}{2}$ particles with a magnetic dipole moment of $-1.913\mu_N$. This allows neutrons to directly couple with magnetic moments in materials. This feature underlies the study of magnetic structures and excitations with neutrons as well as polarization analysis experiments.

Basic properties of neutron

mass	$m = 1.675 \times 10^{-27} kg$
charge	0
spin	1/2
magnetic dipole moment	$\mu_n = -1.913\mu_N$

Values of physical constants

elementary charge	$e = 1.602 \times 10^{-19} C$
mass of electron	$m_e = 9.109 \times 10^{-31} kg$
Planck constant	$\hbar = 6.626 \times 10^{-34} J s$
Boltzmann constant	$k_B = 1.381 \times 10^{-23} J K^{-1}$
Avogadro constant	$N_A = 6.022 \times 10^{23} mol^{-1}$
Bohr magneton	$\mu_B = 9.274 \times 10^{-24} J T^{-1}$
nuclear magneton	$\mu_N = 5.051 \times 10^{-27} J T^{-1}$

The quantity measured in a neutron scattering experiment is the intensity of neutrons scattered off from the scattering system, and collected with a given solid angle, a given energy window, within a given time. This normalized intensity is related to a quantity known as the cross section for a particular neutron scattering experiment. Suppose the flux of neutrons scattered in a given direction is measured as a function of their energy E' . We use polar coordinates to express the geometry of the scattering process and define a small solid angle for scattering $d\Omega$ shown in Fig.2.1. Let the direction of the scattered neutrons be θ, ϕ . The partial differential cross-section is defined by the equation:

$$\frac{d^2\sigma}{d\Omega dE'} = (\text{number of neutrons scattered per second into a small solid angle } d\omega \text{ in the direction } \theta, \phi \text{ with final energy between } E' \text{ and } E'+dE') / \Phi d\Omega dE' \quad (2.1)$$

where Φ is the flux of the incident neutrons passing through a unit area perpendicular to the direction of the neutron beam per second.

Now if we do not analyse the energy of the scattered neutrons scattered into

solid angle $d\Omega$ in the direction θ, ϕ , then the cross-section corresponding to these measurements is known as the differential cross-section, defined by

$$\frac{d\sigma}{d\Omega} = (\text{number of neutrons scattered per second into a small solid angle } d\Omega \text{ in the direction } \theta, \phi) / \Phi d\Omega. \quad (2.2)$$

Following the Equations 2.1 and 2.2, the total scattering cross-section is defined by

$$\sigma_{tot} = (\text{total number of neutrons scattered per second}) / \Phi. \quad (2.3)$$

The three different cross sections can be connected following their definition by the equations below:

$$\frac{d\sigma}{d\Omega} = \int_0^\infty \left(\frac{d^2\sigma}{d\Omega dE'} \right) dE' \quad (2.4)$$

$$\sigma_{tot} = \int_{\text{all directions}} \left(\frac{d\sigma}{d\Omega} \right) d\Omega \quad (2.5)$$

The cross-sections are often expressed experimentally as per atom or per molecule. The goal for the rest of the chapter is then to derive theoretical expressions and establish formalism for these quantities.

2.2 Nuclear Scattering By a Single Fixed Nucleus

We now consider a simple form of neutron scattering - nuclear scattering of a neutron by a single nucleus fixed in position. We employ the Born approximation and express our incident and outgoing neutrons as plane waves. We further assume that the nuclei is a point source and the scattered neutrons are scattered with

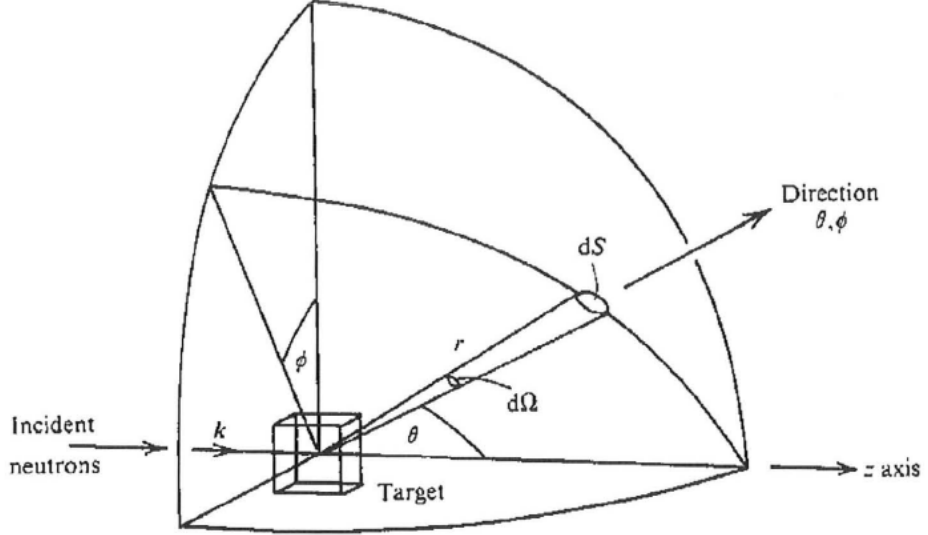


FIGURE 2.1: Geometry of a general scattering experiment. The quantities defined here are used to calculate the scattering cross sections. Figure reproduced from [60] with permission.

spherical symmetry. We set the origin to be at the nucleus itself, and the z axis is along the direction of the incident neutron wavevector \mathbf{k} illustrated in Fig.2.1.. The wavefunction of the incident neutrons can be expressed as

$$\psi_{inc} = \exp(i\mathbf{k}z). \quad (2.6)$$

In a similar fashion we can express the wavefunction of the scattered neutrons at point \mathbf{r} to be

$$\psi_{sc} = -\frac{b}{r}\exp(i\mathbf{k}\mathbf{r}). \quad (2.7)$$

b in this expression is a constant known as the scattering length, which is a characteristic of the nucleus. The negative sign in front of b is arbitrary and corresponds to a repulsive potential for now. The scattering length can take on complex or real form. When the scattering length is complex, it varies rapidly with the energy of the neutrons. The imaginary part of scattering length b corresponds to neutron absorption, and such a nucleus strongly absorb neutrons. However the majority of nuclei, at most energies, are not of this type. Therefore the imaginary part of the scattering length is typically small and we shall confine the discussion

to take the scattering length, b , as a real quantity.

We now calculate the cross-section $d\sigma/d\Omega$ for scattering from a single fixed nucleus using the expression we obtained above. If v is the velocity of the neutrons, then the number of neutrons passing through the area dS per second is

$$vdS|\psi_{sc}|^2 = vdS\frac{b^2}{r^2} = vb^2d\Omega \quad (2.8)$$

The flux of incident neutrons is

$$\Phi = v|\psi_{inc}|^2 = v \quad (2.9)$$

Therefore

$$\frac{d\sigma}{d\Omega} = \frac{vb^2d\Omega}{\Phi d\Omega} = b^2 \quad (2.10)$$

If we take the integral over all space, then we can see that

$$\sigma_{tot} = 4\pi b^2. \quad (2.11)$$

The equations represent a specific case of neutron scattering off a single nuclei. We now derive more general expressions of nuclear scattering by considering a scattering system for which the neutron can induce transitions from one state to another. We will ignore the spin of the neutron for now and come back to this in the section of the thesis on magnetic neutron scattering.

We begin with Fermi's Golden rule, and consider the differential scattering cross function below,

$$\left(\frac{d\sigma}{d\Omega}\right) = \frac{1}{\Phi d\Omega} \sum_{\mathbf{k}'in} W_{\mathbf{k},\lambda,\rightarrow,\mathbf{k}',\lambda'} \quad (2.12)$$

where $W_{\mathbf{k},\lambda,\rightarrow,\mathbf{k}',\lambda'}$ is the number of transitions per second from the state k, λ to the state k', λ' , and Φ is the flux of incident neutrons.

The expression on the right side of Eq.2.12 can be calculated using Fermi's golden rule.

$$\sum_{\mathbf{k}'in} W_{\mathbf{k},\lambda,\rightarrow,\mathbf{k}',\lambda'} = \frac{2\pi}{\hbar} \rho_{\mathbf{k}'} |\langle \mathbf{k}'\lambda' | V | \mathbf{k}\lambda \rangle|^2. \quad (2.13)$$

$\rho_{\mathbf{k}'}$ denotes the number of momentum states in $d\Omega$ per unit energy range for neutrons in the state \mathbf{k}' . We can simplify Eq.2.12 in reciprocal space as

$$\left(\frac{d\sigma}{d\Omega} \right)_{\lambda \rightarrow \lambda'} = \frac{\mathbf{k}'}{\mathbf{k}} \left(\frac{m}{2\pi\hbar^2} \right)^2 |\langle \mathbf{k}'\lambda' | V | \mathbf{k}\lambda \rangle|^2 \quad (2.14)$$

Now, we require that energy be conserved in the equation above, so the partial differential cross-section becomes,

$$\left(\frac{d^2\sigma}{d\Omega dE'} \right)_{\lambda \rightarrow \lambda'} = \frac{\mathbf{k}'}{\mathbf{k}} \left(\frac{m}{2\pi\hbar^2} \right)^2 |\langle \mathbf{k}'\lambda' | V | \mathbf{k}\lambda \rangle|^2 \delta(E_\lambda - E_{\lambda'} + E - E') \quad (2.15)$$

where E and E' are the initial and final energies of the neutron and E_λ and $E_{\lambda'}$ are the initial and final energies of the crystal. That is, the cross section requires that the change of energy between the incident and scattered neutrons are accounted for in the energy change of the scattering system such that the total energy is conserved between neutrons and the scattering system.

We now perform Fourier transformations of the potential V and make a few simplifications to skip to the results. For the details about this derivation, please seek Chapter 2 in Ref.[60]. We eventually arrive at the following expression for coherent and incoherent scattering cross-sections.

$$\left(\frac{d^2\sigma}{d\Omega dE'}\right)_{coh} = \frac{\sigma_{coh}}{4\pi} \frac{\mathbf{k}'}{\mathbf{k}} \frac{1}{2\pi\hbar} \sum_{jj'} \int_{-\infty}^{\infty} \langle \mathbf{exp}\{-i\boldsymbol{\kappa} \cdot \mathbf{R}_{j'}(\mathbf{0})\} \mathbf{exp}\{i\boldsymbol{\kappa} \cdot \mathbf{R}_j(\mathbf{t})\} \rangle \times \mathbf{exp}(-i\omega t) dt \quad (2.16)$$

$$\left(\frac{d^2\sigma}{d\Omega dE'}\right)_{inc} = \frac{\sigma_{inc}}{4\pi} \frac{\mathbf{k}'}{\mathbf{k}} \frac{1}{2\pi\hbar} \sum_j \int_{-\infty}^{\infty} \langle \mathbf{exp}\{-i\boldsymbol{\kappa} \cdot \mathbf{R}_j(\mathbf{0})\} \mathbf{exp}\{i\boldsymbol{\kappa} \cdot \mathbf{R}_j(\mathbf{t})\} \rangle \times \mathbf{exp}(-i\omega t) dt \quad (2.17)$$

where $\sigma_{coh} = 4\pi(\bar{b})^2$ and $\sigma_{inc} = 4\pi\{\bar{b}^2\} - (\bar{b}^2)$. Although we have skipped a few steps to arrive at Eq. 2.16 and 2.17, it does not prevent us from making several interpretations about them. In an actual scattering system there are different nuclei which can be associated with different scattering lengths. By observing the subscripts and the component of Eq.2.16, we can see that the coherent scattering equation suggests that coherent scattering depends on the correlation between different nuclei at different times. The result is that coherent scattering occurs due to interference effects over both space and time. In contrast, the expression for the incoherent scattering in Eq.2.17 shows that it depends on the correlation between the same nucleus at different times. Therefore incoherent scattering provides information primarily on self-correlations as a function of time.

2.3 Magnetic Neutron Scattering

As mentioned previously, neutrons are spin $\frac{1}{2}$ particles which can couple to the magnetic moments in a condensed matter system to inform on magnetic structures and spin dynamics. In this chapter we look specifically at the magnetic scattering of neutrons.

The operator corresponding to the magnetic dipole moment of the neutron is

$$\boldsymbol{\mu}_n = -\gamma\mu_N\boldsymbol{\sigma} \quad (2.18)$$

where $\mu_N = \frac{e\hbar}{2m_p}$ as m_p is the mass of the proton and e its charge. $\gamma = 1.913$ is a constant. σ is the Pauli spin operator for the neutron. The magnetic dipole momentum of electrons can be expressed as

$$\boldsymbol{\mu}_e = -2\mu_B \mathbf{s} \quad (2.19)$$

where $\mu_B = \frac{2\hbar}{2m_e}$ is the Bohr magneton, \mathbf{s} is the spin operator for electron.

Recall Eq.2.15, and we can generalize the $|\langle \mathbf{k}'\boldsymbol{\lambda}' | V | \mathbf{k}\boldsymbol{\lambda} \rangle|^2$, by consider that the neutrons change their state from \mathbf{k}, σ to \mathbf{k}', σ' , due to dipole-dipole interaction, where σ denotes the spin state of the neutrons. We would also consider the potential between neutrons and all the electrons in the scattering system. This leads to

$$\left(\frac{d\sigma}{d\Omega} \right)_{\sigma\lambda \rightarrow \sigma'\lambda'} = \frac{\mathbf{k}'}{\mathbf{k}} \left(\frac{m}{2\pi\hbar^2} \right)^2 |\langle \mathbf{k}'\boldsymbol{\sigma}'\boldsymbol{\lambda}' | V_m | \mathbf{k}\boldsymbol{\sigma}\boldsymbol{\lambda} \rangle|^2 \delta(E_\lambda + E_{\lambda'} + E - E'). \quad (2.20)$$

Evaluation of the $\langle \mathbf{k}' | V_m | \mathbf{k} \rangle$ expression is somewhat complex, and we refer readers to Chapter 7 of Ref.[60] for details. The final result of the cross-fraction for magnetic scattering is given below,

$$\left(\frac{d^2\sigma}{d\Omega dE'} \right)_{\sigma\lambda \rightarrow \sigma'\lambda'} = (\gamma r_0)^2 \frac{\mathbf{k}'}{\mathbf{k}} |\langle \boldsymbol{\sigma}'\boldsymbol{\lambda}' | \boldsymbol{\sigma} \cdot \mathbf{Q}_\perp | \mathbf{k}\boldsymbol{\sigma}\boldsymbol{\lambda} \rangle|^2 \delta(E_\lambda - E_{\lambda'} + \hbar\omega). \quad (2.21)$$

By evaluating the operator $\boldsymbol{\sigma} \cdot \mathbf{Q}_\perp$ we can further express the scattering cross function as

$$\begin{aligned} \left(\frac{d^2\sigma}{d\Omega dE'} \right) &= (\gamma r_0)^2 \frac{\mathbf{k}'}{\mathbf{k}} \sum_{\lambda\lambda'} \rho_\sigma \sum_\alpha \langle \lambda | \mathbf{Q}_{\perp\alpha}^+ | \lambda' \rangle \langle \lambda' | \mathbf{Q}_{\perp\alpha} | \lambda \rangle \delta(E_\lambda - E_{\lambda'} + \hbar\omega) \\ &= (\gamma r_0)^2 \frac{\mathbf{k}'}{\mathbf{k}} \sum_{\alpha\beta} (\delta_{\alpha\beta} - \hat{\kappa}_\alpha \hat{\kappa}_\beta) \times \sum_{\lambda\lambda'} \rho_\lambda \langle \lambda | \mathbf{Q}_\alpha^+ | \lambda' \rangle \langle \lambda' | \mathbf{Q}_\beta | \lambda \rangle \delta(E_\lambda - E_{\lambda'} + \hbar\omega) \end{aligned} \quad (2.22)$$

The cross-section for spin-only scattering by ions with localised electrons can also be derived,

$$\begin{aligned} \left(\frac{d^2\sigma}{d\Omega dE'} \right) &= (\gamma r_0)^2 \frac{\mathbf{k}'}{\mathbf{k}} \sum_{\lambda\lambda'} (\delta_{\alpha\beta} - \hat{\kappa}_\alpha \hat{\kappa}_\beta) \sum_{l'd'} \sum_{ld} F_{d'}^*(\boldsymbol{\kappa}) F_d(\boldsymbol{\kappa}) \\ &\quad \times \sum_{\lambda\lambda'} p_\lambda \langle \lambda | \mathbf{exp}(-\boldsymbol{\kappa} \cdot \mathbf{R}_{l'd'}) S_{l'd'}^\alpha | \lambda' \rangle \\ &\quad \times \langle \lambda' | \mathbf{exp}(-\boldsymbol{\kappa} \cdot \mathbf{R}_{ld}) S_{ld}^\alpha | \lambda \rangle \delta(E_\lambda - E_{\lambda'} + \hbar\omega) \end{aligned} \quad (2.23)$$

where $F_d(\boldsymbol{\kappa}) = \int \delta_d(\mathbf{r}) \mathbf{exp}(i\boldsymbol{\kappa} \cdot \mathbf{r}) d\mathbf{r}$ is the magnetic structural factor. $\delta_d(\mathbf{r})$ is the normalized density of the unpaired electrons in the ion d .

From Eq.2.20, 2.22 and 2.23, we can summarize properties of the magnetic neutron scattering cross section. Firstly, we can see that the cross section is only related to the components of moment that lie within a perpendicular plane to \mathbf{Q} . Secondly, the magnetic scattering is sensitive to the square of magnetic form factor and is typically strongest at small \mathbf{Q} . Lastly, the cross-section of magnetic and nuclear scattering are comparable, so that the intensity of both scattering can produce peaks of similar intensity.

2.4 The Triple Axis Neutron Spectrometer

The triple axis neutron spectrometer(TAS) was pioneered by Canadian physicist Bertram Brockhouse who worked at McMaster University and Chalk River Laboratory. The work by Dr.Brockhouse on the TAS was recognized with the Nobel Prize in physics in 1994, along with Dr.Clifford Shull. The invention of the TAS revolutionized the area of material science research by providing a systematic method to study different types of elementary excitations of a condensed matter system. Fig.2.2 is a schematic diagram of a triple axis spectrometer. The key components of a triple axis spectrometer are three single crystals mounted on three axes shown in the figure. A white beam of neutron coming out of the reactor will reach the first axis where a monochromator is mounted. The monochromator is a single crystal oriented in a specific direction with a known d-spacing. From Bragg's Law, this will only allow neutrons with certain wavelength to be Bragg

reflected by the monochromator. This selection process is configured before the experiment to select the desired incident neutron energy or wavelength. The incident monochromatic neutrons then arrive at the sample, and scatter off it, in general in all directions. The secondary spectrometer is then set up with an analyzer crystal, which is another single crystal with known d-spacing. The analyzer crystal then Bragg reflects the neutrons scattered off the sample in a particular direction, and these neutrons of known energy are reflected into the detector. This set up allows measurements of the scattering intensity at specific \mathbf{Q} as well as $\hbar\omega = E' - E$ positions. In other words, the monochromator controls the incident energy of neutrons and the analyzer controls the final energy of neutrons reaching the detector. For example, the TAS data measured in this thesis are centered around $(1/2, 1/2, 0)$ and repeated positions in reciprocal space of Nd-LSCO samples to capture the evolution of intensities of incommensurate peaks at different Sr doping concentration.

One key experimental component of the triple axis spectrometer is the collimation. Well collimated neutrons produces good energy and momentum resolution. However, in a real world setting, neutrons are never perfectly collimated. Collimators are comprised of a series of parallel plates of neutron absorbing materials that only allows neutrons whose trajectories lie to within a certain angles of desired direction to pass through. However, due to the absorbing feature of the collimators, collimation reduces the flux of neutrons that will reach the sample. This leads to a classical trade-off problem during an neutron scattering experiment - resolution vs flux. To conduct a successful neutron scattering experiment, it is important to understand the goal of the experiment and the characteristics of the instrument so that one can find the right balance such that there is good enough resolution to capture the essential features of the sample, with the maximum allowed flux of neutrons so the measurements can be done within a reasonable time. This is especially important for inelastic neutron scattering experiment due to the inherent nature of magnetic scattering produce weaker signals compared to elastic scattering.

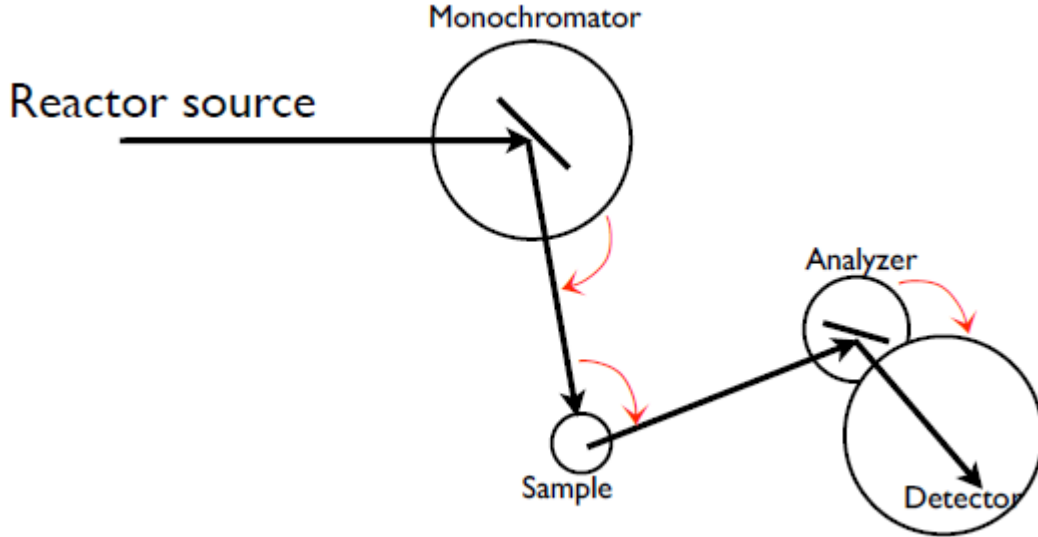


FIGURE 2.2: Diagram of triple axis spectrometer. A white beam of neutrons come out from reactor source onto the monochromator. The monochromator then scatter off neutrons with specific wavelength onto the sample. The scattered neutrons then reach the analyzer and detector which determines the intensity, momentum of the neutrons.

2.5 Direct Geometry Time-of-Flight Chopper Spectrometers

Time-of-flight(TOF) chopper spectrometers allow another powerful approach to elastic and inelastic neutron scattering, and these have been particularly successful following the development of spallation neutron sources, large neutron area detectors and efficient computation. Direct geometry chopper spectrometers possess a monochromating element in the incident beam, typically either a Fermi or Disk chopper. After the sample, a large position sensitive detector with timing resolution identifies both the angle of deflection and time of arrival of the individual scattered neutrons. Using kinematic relationships, these information can be used to calculate changes in the energy of the incoming neutrons on scattering, as well as their corresponding change in momentum. A schematic diagram of the Disk Chopper Spectrometer SEQUOIA at ORNL is shown in Fig.2.3. For detailed information about SEQUOIA, readers are referred to read Ref.[61].

As demonstrated in Fig.2.3, a typical ToF spectrometer deploys a series of "choppers" to produce a monochromatic beam with desired incident neutron energy and flux. The choppers are made of series of rotating disks with slits on them. Highly neutron absorbing material, usually gadolinium, is used as the coating of the choppers. These choppers are configured to rotate with specific frequencies to allow a narrow range of neutrons whose wavelengths are centered on the desired wavelength to pass through. The selected neutrons then scatter off the sample onto a bank of Helium 3 detectors.

From the discussion above, it should be clear that once the knowledge of detector positions and the neutron energy are known, one is able to define \mathbf{Q} related to the scattering system. By taking advantage of multi-array detectors, ToF can produce a large data set sampling a wide region of reciprocal space simultaneously. This is equivalent to conducting multiple triple axis measurements using point detectors at the same time. Due to the nature of ToF measurements, data generated this way are four dimensional in nature which includes three dimensions in reciprocal space and a fourth dimension in energy transfer between incident neutrons and the sample.

In order to visualize four dimensional data sets, data integration is at the core of analyzing ToF neutron scattering data. The data integration can be performed using well developed software packages such as Mantid or DAVE. A common way of data visualization is integrating data over specific ranges in the four dimensional reciprocal-energy phase space. There are generally four ways of data integration, volume integration, "slice", "cut", and point integration. Two of the four methods are routinely deployed when analysing ToF data in this thesis. However for completeness of the thesis we will briefly describe all four methods.

Volume integration requires only integrating 1 direction in the 4D phase space and projecting data in the remaining three dimensions. This method generates a holistic 3D view of the data. However the downside of this method is its high computation cost. Even modern computers could take excessive time to process the necessary calculations. The second way of data visualization is creating slices of data. This method involves integrating data in two of the four dimensions and projecting data in the remaining two dimensions on an intensity map. This method

is more balanced between the cost of computations and speed. The result of this method is a 2D color contour plot. Most of the single crystal data described in this thesis are conducted in an HHL orientation where two reciprocal space directions $HH0$ and $H\bar{H}0$ are oriented in the scattering plane while the $00L$ is perpendicular to the incident neutron beam. Chapter 5 utilizes this method where a large part of the data are plotted in E vs HH plane with integration in L and $H\bar{H}$ as a result of slicing the four dimensional data set. The third method is making a cut of the two dimensional data. Once a 2D color contour plot is made, regions of interest can be identified on the plot. To quantitatively study the intensity of such area, one need to make a cut from the 2D data by integrating an addition dimension and plotting the intensity vs the remaining one dimension. The methods of "slice" and "cut" will be demonstrated through out the thesis in especially in Chapter 5. The last method is point integration, this method simply integrate along all four directions in the energy-reciprocal space. This method can be useful when determining background or compare data points of at different temperatures or in different magnetic fields. It can also be used when normalizing data between different samples and/or different experiments.

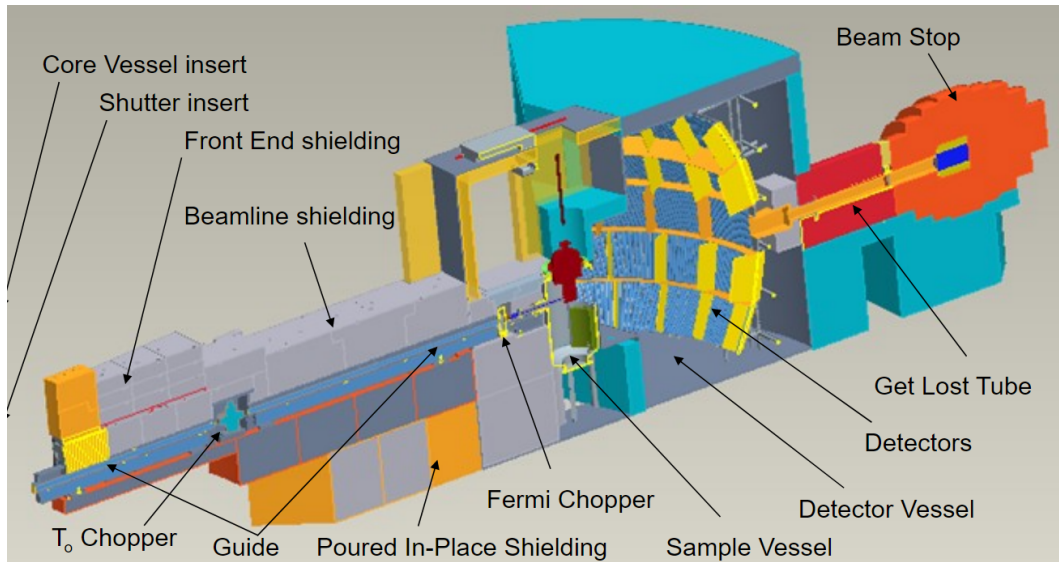


FIGURE 2.3: Schematic diagram of a time-of-flight spectrometer at SEQUOIA, ORNL. The ToF spectrometer consists a few choppers to select incident neutron energy as well as avoid interference between different phases of neutrons. The detectors is a bank of ^3He detectors which is produces a pulse when a neutron hit on the detector. The deployment of such set up drastically increased the capacity of neutron scattering experiments as multiple energy and momentum transfer can be measured simultaneously.

Chapter 3

The Crystal Growth of the family of $\text{La}_{1.6-x}\text{Nd}_{0.4}\text{Sr}_x\text{CuO}_4$

3.1 Preface

Material synthesis is the foundation and first step of material science research. In this chapter, we introduce the process of obtaining high quality powder and single crystal samples of Nd-LSCO through solid state reaction and traveling solvent floating zone technique (TSFZ). Growing Nd-LSCO and other copper oxide superconductors in general has proven to be challenging. This is largely due to its slow growth rate and high sensitivity to the growth conditions. The cause of strict growth condition originates from the fact that Nd-LSCO is a type of incongruently melting material which requires the traveling solvent floating zone techniques to grow. This technique has very slow growth rate (less than 1mm per hour) compared with other methods, therefore the zone is more prone to external turbulence and minimal changes in the rod's movement. I had the pleasure working with Dr. Jianshi Zhou at University of Texas, Austin where I was trained by his former PhD student Zongyao li on this technique.

3.2 Incongruently Melting materials

Incongruently melting materials refer to those that do not melt uniformly. These materials, once being heated to high temperatures, decompose into a mixture of

liquid and solid form. Crystals can not grow if the molten zone created from the before-grown material is inhomogeneously mixed with liquid and solid substances. The solid materials in the molten zone would create instability when the feed and seed rods grind on each other. Therefore, to create a uniformly melted liquid zone, a small amount of solvent is added during the growth between the feed and seed rod. The solvent is specifically designed to have a composition of La and Cu based on the binary phase diagram in Fig.3.1. The goal is to allow solvent to melt uniformly around 1100-1200 °C which is the a common region of operating temperatures for the floating zone furnace at McMaster University.

The molten zone can be considered as a reservoir of the to-be-grown single crystals where crystallization occurs. During the crystal growth, the feed rod continues to supply the reservoir with the desired composition of the target crystal and eventually induces saturation within the molten zone. Readers can take reference of the process of sodium chloride crystallization in water to have a good understanding of the role the solvent in Nd-LSCO crystal growth.

The melting temperature of the solvent plays an important role in determining the quality of crystals. As the liquid zone is essentially held up by surface tension between feed and seed rod only, it must be high enough to create an uniformly melted liquid phase of the solvent but low enough to maintain enough surface tension for the molten zone to be stable. To determine the right melting temperature, we start with the phase diagram of the La_2O_3 - CuO binary system shown in Fig.3.1. The horizontal axis in the phase diagram indicates the amount (in percentage) of CuO (or $\text{CuO}_{1.5}$) in the system. Based on the phase diagram, heating up the system with less than 32% CuO in the solvent will create either $\text{La}_2\text{O}_3 + \text{La}_2\text{CuO}_4$ or $\text{La}_2\text{O}_3 + \text{Liquid}$ which is a solid or a mixture of solid/liquid. Similarly, other regions with less than 60% or more than 90% CuO will produce either solid or solid + liquid mixture as well. Therefore in order to completely melt the solvent, the target temperature is to reach a region within which the CuO takes between 60% and 90% of the whole solvent in order to produce a homogeneous liquid phase. The ideal ratio of La_2O_3 vs CuO was chosen to be 22:78 after many trials. The reason for settling on this La:Cu ratio is not only because at around 1200 °C the rod does not overheat which can absorb the liquid solvent into it, but

also due to the amount of CuO evaporation can be well controlled at roughly 3% molar mass of the Nd-LSCO crystal during an 100-hour growth. The evaporation of CuO is compensated during the powder synthesis process by adding 3% molar mass in the pre-annealed powder.

Solvent and pure-phased powder samples of Nd-LSCO are usually made in parallel for time saving. The powder samples are made with a mixture La_2O_3 , SrCO_3 , Nd_2O_3 and CuO. The details of the chemical reaction can be found in [29]. The solvent and the powder samples are grinded manually and mechanically to achieve best homogeneity. The powder samples are then annealed in air at 1000 °C for a prolonged time. The annealing time is proportional to the Sr doping concentration such that the overdoped samples were annealed much longer comparing to the underdoped samples. For example, for $x = 0.12$ the sample was annealed for 72 hours while for $x = 0.26$ the sample is annealed for over 125 hours with intermittent manual grinding. The color of the powder sample can be used as a rough indication of reaction to determine if the temperature is high enough. The pre-annealed powder sample appears to be in light grey. The post annealed powder sample should be dark black with no grey patches when broken up as an indication that the different materials in the sample have reacted to each other to form Nd-LSCO. The polycrystalline sample is then ground into finer powders. The phase purity of these Nd-LSCO powder samples was examined using the Panalytical XRD instrument. Fig.3.2 shows an image of a 7cm feed rod for the $x = 0.24$ Nd-LSCO sample before the crystal growth as an example.

3.3 Single Crystal Growth

The set up inside the optical furnace for single crystal growth is demonstrated in Fig.3.3. The main part of the furnace is made up (from top to bottom) of rotating upper shaft, ellipsoidal mirror, halogen lamps, bottom shafts. The feed rod hangs below the upper shaft while the seed rod is mounted on the lower shaft. The feed and seed rods are connected by the molten zone formed by melting the solvent while they rotate in opposite directions for homogeneous mixing of the molten zone. The sustainability of the growth relies heavily on the stability of the molten

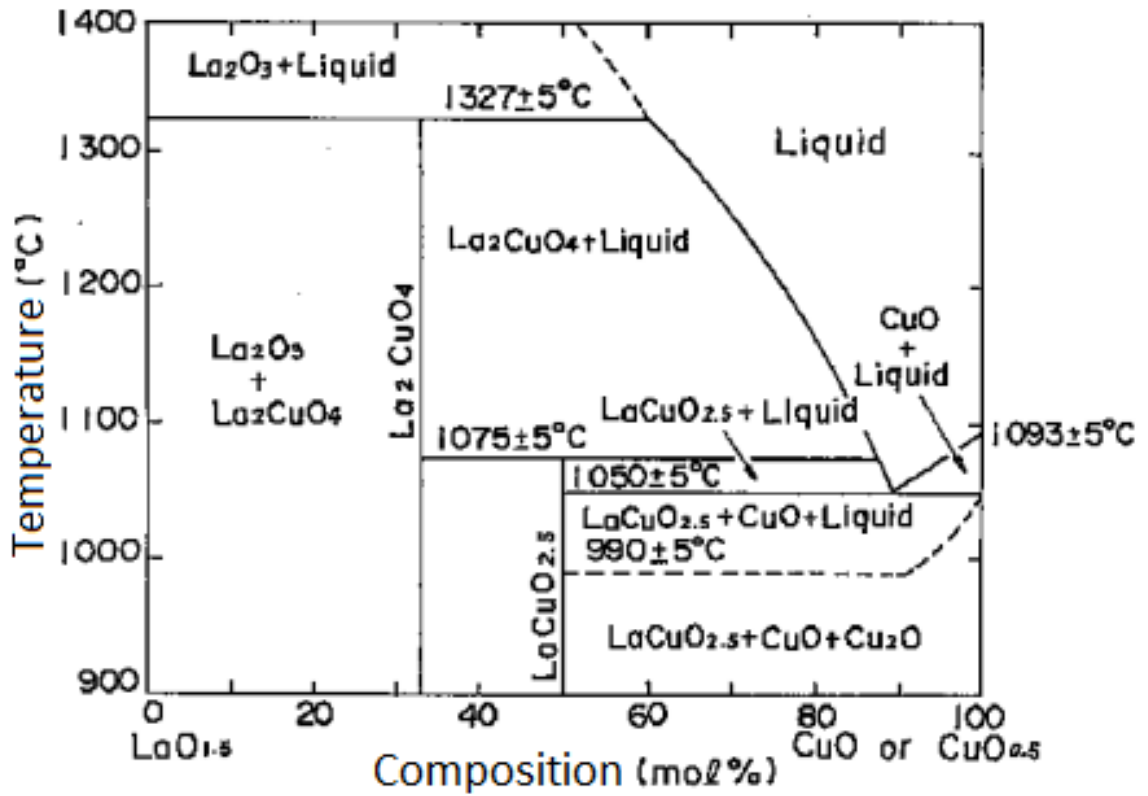


FIGURE 3.1: The phase diagram of the binary system LaO_{1.5}-CuO. The upper right region of the phase diagram shows a region with pure liquid. This is the key area to the solvent floating zone crystal growth technique. A target of 22:78 of La:Cu ratio was determined such that when operating ~ 1100-1200° the solvent is uniformly melted in a homogeneous liquid phase. Courtesy to Dr. Jianshi Zhou.



FIGURE 3.2: The feed rod of $x=0.24$ sample. Photo taken after final annealing in flowing oxygen. The rod is about 7cm long and weighs 14.6 grams. Rod of this size can sustain two growths spanning over a time frame of two weeks.

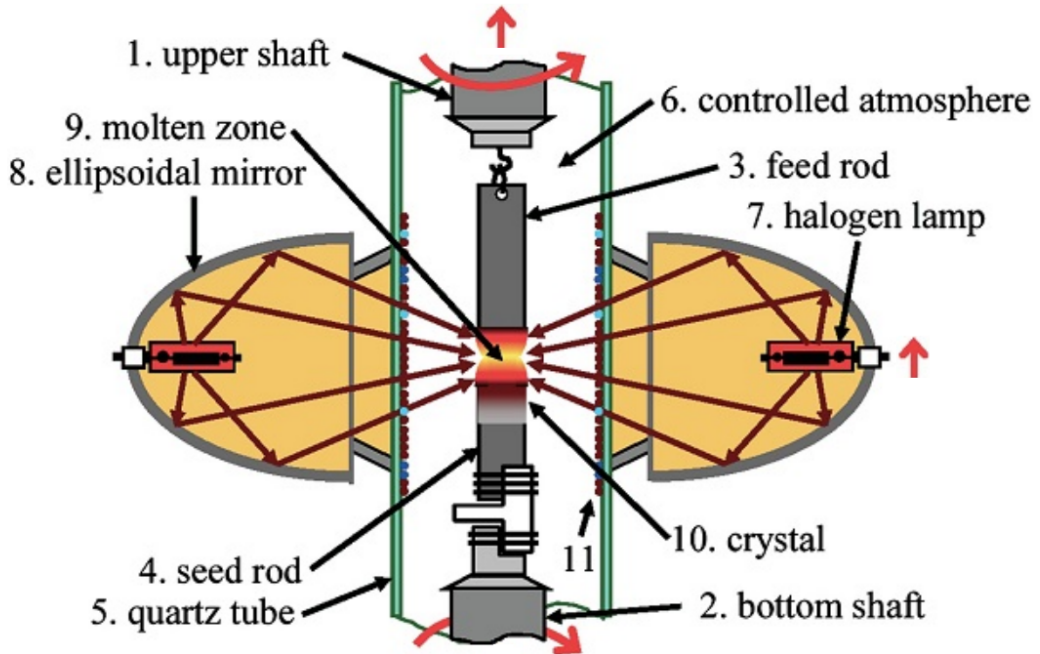


FIGURE 3.3: Schematic diagram of the set-up within the mirror stage. Four halogen lamps are mounted on ellipsoidal mirror stage that focuses lights in the molten zone. The feed rod hangs under the upper shaft and the seed rod is mounted on top of the bottom shaft. The seed and feed rod rotates counterclockwise to achieve a homogeneous mixing in the molten zone.

zone. Subtle changes, such as adjusting the positions of feed/seed rod, would create extra mosaic or even break the molten zone. Therefore adjustment to the growth after the initial 12 hours is not encouraged. The crystals in this thesis are grown by an image furnace using ellipsoidal mirrors that focus the lights from two 400W halogen light bulbs on a small region to melt the solvent. There are two ways to control the growth, one is fixing the position of mirror stage and translating feed and seed rod through the focal area, or fixing seed rod and translating both the mirror stage and feed rod relative to each other and allow the crystal grow on top of the seed rod. At McMaster University, the image furnace (Crystal Systems Inc.) uses the latter movement pattern indicated by the red arrows shown in Fig. 3.3.

A total of over 50 combined attempts were made to optimize the growth conditions of Nd-LSCO single crystals. The ultimate goal during the growth is to achieve an equilibrium state for the molten zone in order to produce high quality



FIGURE 3.4: A photo taken at the Crystal System furnace at McMaster University's crystal growth lab.

single crystals. There are three major factors that controls the stability of the molten zone, the melted material from feed rod as intake of the molten zone, the crystal grown on the seed rod as output of the molten zone, and the temperature which controls the viscosity of the molten zone. As mentioned before, the optical furnace at McMaster University is set up such that the mirror stage and the feed rod travels upwards in the same direction. The seed rod is fixed with no movement during the growth. Therefore feed rod and mirror stage's movements together determine the net intake of material melted into the molten zone. The speed of the mirror stage controls the growth speed directly. In order to create ideal condition for crystallization, the maximum growth speed should not exceed 1mm/hr. The crystals mentioned in this thesis were grown with a speed of 0.65 mm/hr at around 1100 °C which roughly translate into 65-70% of the overall power produced by the halogen lamps in the furnace. The detailed information of the crystal growth can be found in Chapter 4 and Ref.[29].

3.4 Annealing on Post-Grown Single Crystals

A total of 7 Nd-LSCO single crystals were grown using the traveling solvent floating zone technique mentioned in previous section. These crystals are doped with a wide range of Sr concentration from $x = 0.07$ to 0.26 and exhibits different superconducting profiles. It has been known that the oxygen content plays an important role in determining the superconducting transition temperature T_{CS} in various cuprate superconductors. The T_{CS} associated with samples in the overdoped region of the cuprate phase diagram is particularly sensitive to their oxygen content. Therefore it is important to carry out post annealing procedures on the single crystals in an oxygen rich environment to avoid oxygen deficiency.

We have studied the oxygen annealing effect on the superconducting transition temperatures by measuring the susceptibility for Nd-LSCO single crystals $x = 0.17, 0.19, 0.225, 0.24$ and 0.26. Small pellets of 1mm thick and 6mm wide in diameter were carefully cut by a rotating disk diamond saw from the mother single crystals. These pellets were annealed in a quartz tube furnace with flowing oxygen at 900 ° under 1 atm. The duration of the annealing process varies depending on the

Sr concentration. In general, the higher the Sr concentration is the longer it is needed to anneal the samples. The $x = 0.17, 0.19$ samples were annealed for a total of 72 hours while the $x = 0.225, 0.24$ and 0.26 samples were annealed for about a week. The time of anneal was determined when the estimated T_C s no longer change between two anneals from SQUID measurements. Fig.3.5 shows the measured χ normalized to emu/cm^3 of the measured samples. As can be seen, the annealing process is most significant in the overdoped Nd-LSCO samples at $x = 0.24$ and 0.26 . By annealing in flowing oxygen for ~ 168 hours(a week), the superconducting volume increased by $\sim 50\%$ in the $x = 0.24$ sample.

Resistivity measurement can directly measure T_C . By taking advantage of the collaboration with Dr.Louis Taillefer at University of Sherbrooke, we were able to obtain resistivity data on the $x = 0.24$ Nd-LSCO sample before and after annealing. Fig.3.6 shows a comparison of the resistivity on the Nd-LSCO $x = 0.24$ sample before and after annealing under the same procedure discussed above. The solid black and red line are the resistivity measurements conducted within a 16 T applied field. By observing Fig. 3.6, the main effect of annealing the Nd-LSCO samples is that it reduced the residual resistivity by a factor of 3.5 at high doping of the Nd-LSCO samples. Superconducting T_C s are sharpened by annealing and enhanced by $\sim 0.5K$ at high dopings. It will be beneficial to further study if annealing the sample in oxygen alters magnetic properties of the single crystals. However, due to the risk associated with thermal quenching and the logistics with scheduling the neutron scattering experiments, the large single crystals measured in Chapter 5 and 6 were not annealed. Chapter 4 contains detailed information on the structural and superconducting characterizations on these single crystals.

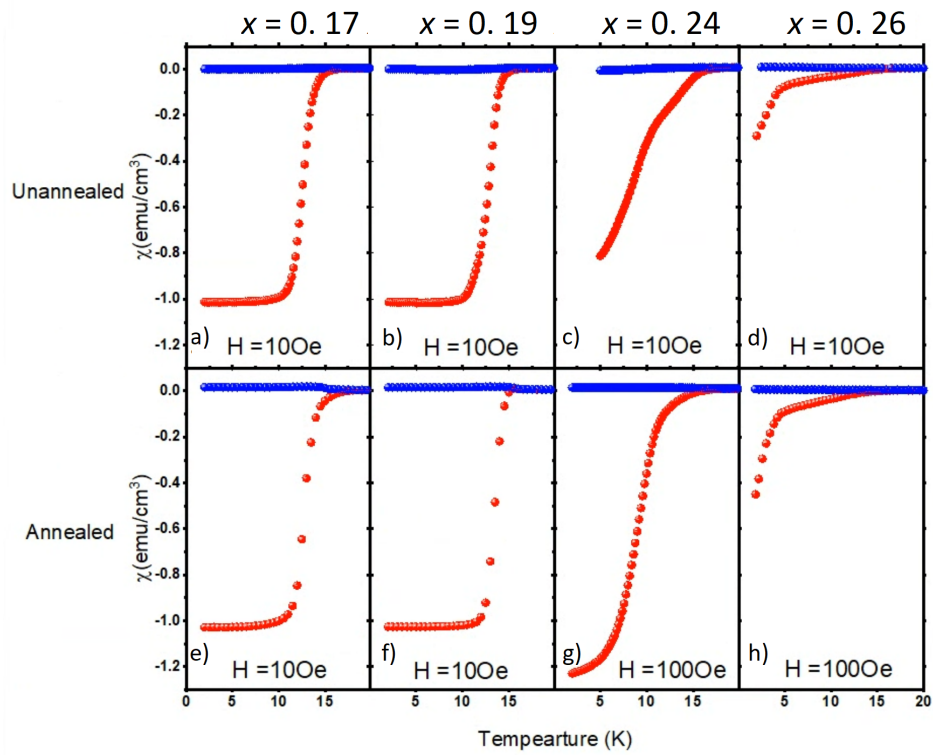


FIGURE 3.5: A comparison of the measured susceptibility of the annealed and un-annealed Nd-LSCO samples. The blue data points indicate field-cooled measurements while the red data points indicating the zero-field-cooled measurements. The applied field is indicated in each figure. The direction of the applied fields are all parallel to the c-axis.

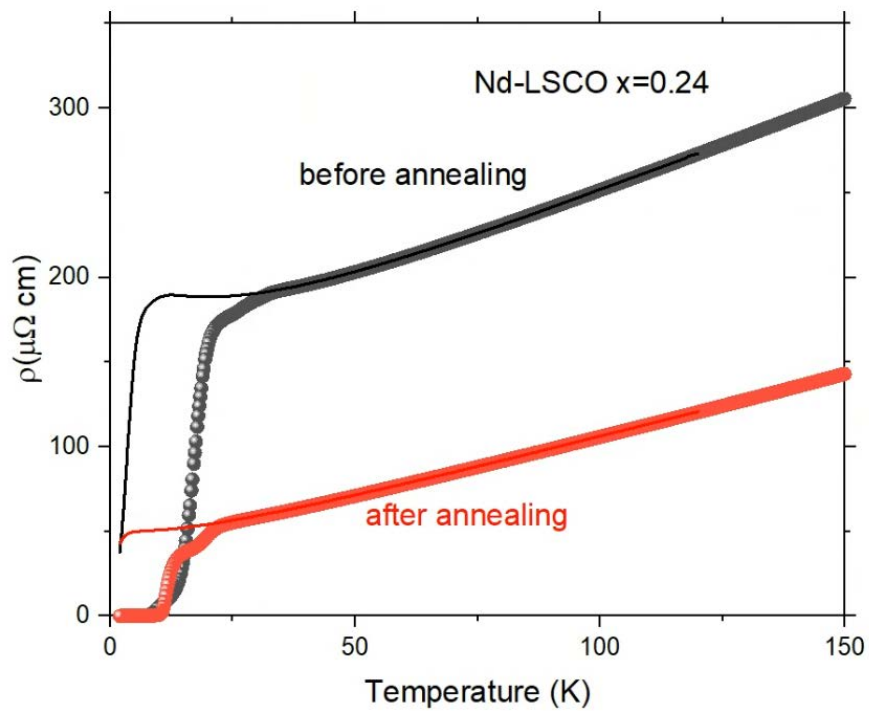


FIGURE 3.6: Resistivity measurements on the Nd-LSCO $x = 0.24$ sample before and post annealing. The sample is annealed in flowing oxygen at 900°C for a week. The solid black and red line represent data measured in magnetic field at 16T.

Chapter 4

The Material Synthesis and Single Crystal Growth of $\text{La}_{1.6-x}\text{Nd}_{0.4}\text{Sr}_x\text{CuO}_4$

4.1 Preface

This Chapter describes the process of material synthesis and single crystal growth of $\text{La}_{1.6-x}\text{Nd}_{0.4}\text{Sr}_x\text{CuO}_4$ as well as the corresponding characterization of the materials so prepared. Material synthesis is at the foundation of most material science. The quality and volume of materials available for study is important in every field of research but it has played a key role in the progress of our understanding of high T_C cuprate superconductors.

Due to the nature of intertwined spin stripe order, charge stripe order, the pseudogap phase and superconductivity, properties of Nd-LSCO samples are very sensitive to their Sr or hole-doping concentration. Therefore, it is important to describe the crystal growth and sample characterization of the new materials produced, so that they can be benchmarked and placed into context of those previously studied. In this regard, it is fortunate that La-214 materials display a rich phase diagram with several distinctive structural phase transitions. In particular Nd-LSCO displays additional low temperature tetragonal structure that is not present in LSCO. This structural richness is very beneficial in estimating Sr concentrations through the measurement of the transition temperatures.

Neutron and X-Ray powder diffraction experiments were conducted on a series of Nd-LSCO polycrystalline samples from $x = 0.02$ to 0.4 to check the phase purity and to help estimate stoichiometry. The neutron diffraction experiments were carried out using POWGEN diffractometer at the Spallation Neutron Source of Oak Ridge National Laboratory. The powder samples were packed into sealed aluminum cans mounted in closed cycle cryostats at POWGEN. The Nd-LSCO powder samples were measured at both room temperature and 10 K. The X-Ray diffraction measurements were conducted at McMaster University using the Panalytical X-Ray diffractometer at room temperature. Supperlattice peaks, as well as peak splittings of (1,1,0) Bragg peaks, were observed in the neutron diffraction experiments as the samples go through LTO1 to HTT structures in Fig.2 of [29]. Both neutron and X-ray diffraction data was refined using the Rietveld method and the analysis was uniformly consistent with no detectable contamination of un-reacted materials.

In our case, the goal of making various powder samples is to understand them and eventually grow high quality single crystals of Nd-LSCO using these as starting materials. Several high quality single crystal samples of Nd-LSCO ranging in Sr concentration from $x = 0.12$ to 0.26 were eventually made. The difficulty of growing large crystals suitable for neutron scattering study increases with x . Possible reasons for the increased difficulty in growing overdoped Nd-LSCO have been suggested as being due to high Sr concentrations in this system creates local inhomogeneity, making it harder to obtain the correct stoichiometry during single crystal growth. During my PhD study, much effort was devoted to attempting to push the boundary of the highest-Sr-doped Nd-LSCO samples, with the goal of enabling the study on magnetism at the end of superconducting dome and beyond. Some examples of the successfully grown single crystals from this thesis for $x = 0.17$, 0.19 and 0.24 are shown below in Fig.4.1, 4.2 and 4.3. The photos are taken immediately after the growth. Overtime, part of these (and other) single crystals decomposed in air, presumably due to an incomplete chemical reaction which tends to break the single crystals into smaller segments. Nonetheless, some of these smaller segments were in fact reasonably large, and we were able to select out suitable single crystals from a subset of all the growths attempted, which then became the basis for our single crystal neutron scattering studies.

In the remaining part of this chapter, we guide the readership through the procedures of synthesizing the polycrystalline materials and the single crystal growth of Nd-LSCO samples. We also describe the characterization of these materials, by neutron powder diffraction, four circle single crystal X-Ray diffraction, susceptibility and transport measurement data to provide a holistic and systematic view of our samples' characteristics. This work performed in collaboration with Dr. Mirela Dragomir, and we shared the first authorship for this publication. My role in this project was material synthesis of the powders, the single crystal growths using floating zone techniques, conducting the powder X-ray diffraction measurements using the Panalytical XRD instrument, collaborated with Dr. Patrick Clancy on conducting four-circle X-ray measurements on single crystal Nd-LSCO $x = 0.12$, 0.17, 0.19, 0.24 and 0.26, and I assisted and performed the susceptibility measurements on all the single crystal and powder samples. I also performed or assisted in data analysis on all the experiments mentioned above. We thank valuable discussions throughout this phase of the project with Dr.Louis Taillefer and Amirreza Ataei from University of Sherbrooke. We also appreciate the training provided by Dr.Janshi Zhou, Zongyao Li at University of Texas, Austin, who hosted me for an extended stay, where I learned from their experience on the single crystal growth of Nd-LSCO.



FIGURE 4.1: A continuous growth of Nd-LSCO $x=0.17$. The growth lasted for more than 250 hours. The crystal is about 13cm long.

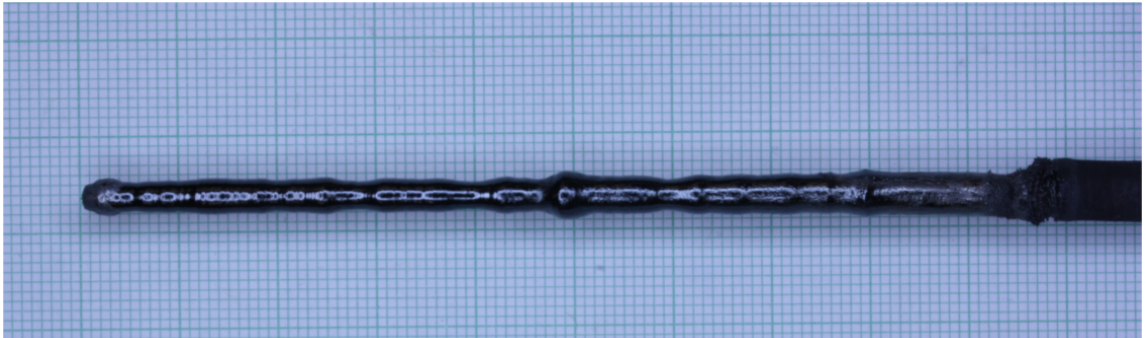


FIGURE 4.2: A continuous growth of Nd-LSCO $x=0.19$. The crystal is about 9cm long

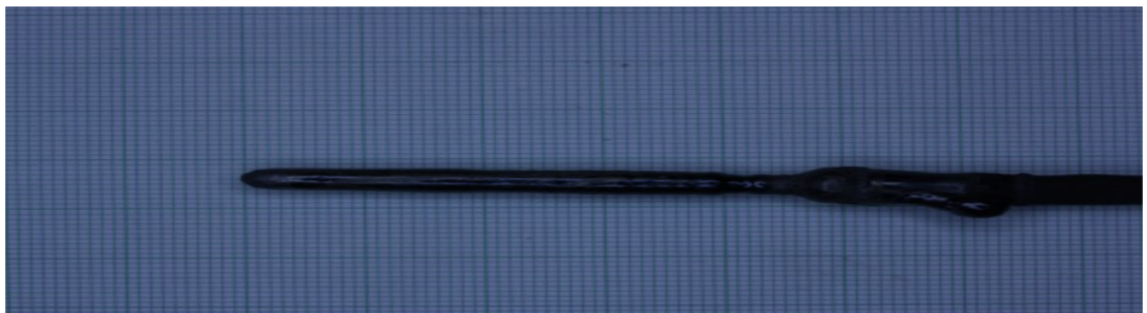


FIGURE 4.3: A continuous growth of Nd-LSCO $x=0.24$. The crystal is about 4.5cm long

Materials preparation, single-crystal growth, and the phase diagram of the cuprate high-temperature superconductor $\text{La}_{1.6-x}\text{Nd}_{0.4}\text{Sr}_x\text{CuO}_4$

Mirela Dragomir ^{1,2,3,*}, Qianli Ma ^{4,*}, J. Patrick Clancy,^{2,4} Amirreza Ataei,⁵ Paul A. Dube ², Sudarshan Sharma ⁴, Ashfia Huq,⁶ Hanna A. Dabkowska ², Louis Taillefer ^{5,7} and Bruce D. Gaulin^{2,4,7}

¹Department of Chemistry and Chemical Biology, McMaster University, Hamilton, ON, Canada, L8S 4M1

²Brockhouse Institute for Materials Research, Hamilton, ON, Canada, L8S 4M1

³Electronic Ceramics Department, Jožef Stefan Institute, Ljubljana 1000, Slovenia

⁴Department of Physics and Astronomy, McMaster University, Hamilton, ON, Canada, L8S 4M1

⁵Institut Quantique, Département de Physique & RQMP, Université de Sherbrooke, Sherbrooke, QC, Canada, J1K 2R1

⁶Neutron Scattering Division, Oak Ridge National Laboratory, Oak Ridge, Tennessee 37831, USA

⁷Canadian Institute for Advanced Research, Toronto, ON, Canada, M5G 1M1



(Received 12 August 2020; accepted 28 September 2020; published 4 November 2020)

One branch of the La-214 family of cuprate superconductors, $\text{La}_{1.6-x}\text{Nd}_{0.4}\text{Sr}_x\text{CuO}_4$ (Nd-LSCO), has been of significant and sustained interest, in large part because it displays the full complexity of the phase diagram for canonical hole-doped, high- T_C superconductivity, while also displaying relatively low superconducting critical temperatures. The low-superconducting T_C s imply that experimentally accessible magnetic fields can suppress the superconductivity to zero temperature. In particular, this has enabled various transport and thermodynamic studies of the $T = 0$ ground state in Nd-LSCO, free of superconductivity, across the critical doping $p^* = 0.23$ where the pseudogap phase ends. The strong dependence of its superconducting properties on its crystal symmetry has itself motivated careful studies of the Nd-LSCO structural phase diagram. This paper provides a systematic study and summary of the materials preparation and characterization of both single-crystal and polycrystalline samples of Nd-LSCO. Single-phase polycrystalline samples with x spanning the range from 0.01 to 0.40 have been synthesized, and large single crystals of $\text{La}_{1.6-x}\text{Nd}_{0.4}\text{Sr}_x\text{CuO}_4$ for select x across the region (0.07, 0.12, 0.17, 0.19, 0.225, 0.24, and 0.26) were grown by the optical floating-zone method. Systematic neutron and x-ray-diffraction studies on these samples were performed at both low and room temperatures, 10 and 300 K, respectively. These studies allowed us to follow the various structural phase transitions and propose an updated structural phase diagram for Nd-LSCO. In particular, we found that the low-temperature tetragonal (LTT) phase ends at a critical doping $p_{\text{LTT}} = 0.255 \pm 0.005$, clearly separated from p^* .

DOI: [10.1103/PhysRevMaterials.4.114801](https://doi.org/10.1103/PhysRevMaterials.4.114801)

I. INTRODUCTION

The discovery of high-temperature superconductivity in Ba-doped La_2CuO_4 (LBCO) by Bednorz and Müller in 1986 [1] represented a major step forward towards achieving room-temperature superconductivity and sparked huge interest in the copper oxide-based materials referred to as “cuprates.” The parent compound of LBCO is La_2CuO_4 (LCO), which is composed of perovskite layers of CuO_6 octahedra and rocksalt layers of LaO structural units located above the CuO_2 planes. By substituting La^{3+} with a aliovalent cation, such as Ba^{2+} or Sr^{2+} , holes are introduced into oxygen levels, and Zhang-Rice singlets formed between the oxygen and copper ions introduce “hole doping” into the insulating state that characterizes LCO. Consequently, the electronic properties of LBCO and Sr-doped LCO (LSCO) change dramatically as a function of Ba^{2+} or Sr^{2+} concentration, and a rich electronic phase diagram results which features both three- and two-dimensional quantum antiferromagnetism and superconductivity.

Soon after the discovery of high-temperature superconductivity in LBCO, it was found that by varying the number of CuO_2 layers (defined by the $\text{Cu } 3d_{x^2-y^2}$ orbital bonding to the $\text{O } 2p_\sigma$ orbitals), the superconducting T_C s of the cuprates could be greatly increased [2,3]. In this way, record superconducting T_C s were achieved in the layered cuprate systems $\text{Bi}_2\text{Sr}_2\text{Ca}_2\text{Cu}_3\text{O}_{10}$ [3] and $\text{Bi}_2\text{Sr}_2\text{CaCu}_2\text{O}_8$ (BSCCO or Bi-2212) [4] and $\text{YBa}_2\text{Cu}_3\text{O}_{7-x}$ (YBCO or 123) [5] with T_C approaching 100 K. Clearly, the superconductivity in these systems originates from the CuO_2 planes, but the mechanism underlying the superconductivity is enigmatic, and has remained so more than 30 years after its original discovery. Thereafter, a myriad of studies was carried out, fueled by the need to understand the relationships among the collective states characterizing this rich phase diagram; that is, between the magnetism, charge ordering, metallic, and superconducting states, as well as the crystallographic structures that these materials exhibit.

The structures of the single-layer cuprates, LBCO and LSCO, are relatively simple compared with those adopted by the multilayered compounds, which, among other things,

*These authors contributed equally to this work.

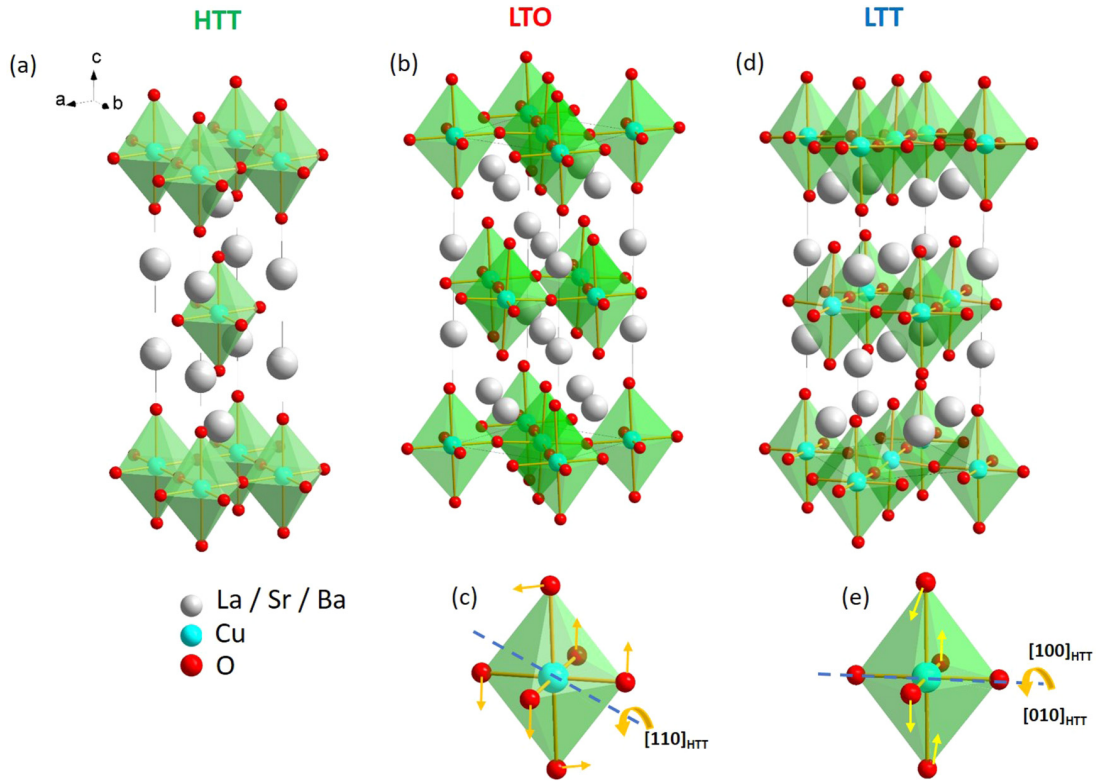


FIG. 1. Schematic views of the crystal structures of LCO and hole-doped LCO: (a) HTT; (b) LTO. (c) The rotations or tilting of the CuO_6 octahedra within the LTO phase relative to the HTT phase; (d) LTT, phase. (e) The rotations or tilting of the CuO_6 octahedra within the LTT phase relative to the HTT phase.

can exhibit incommensurate structures [6]. From this point of view, the LCO-based cuprates are more amenable to a comprehensive characterization of their structures and phase diagrams.

The structures adopted by LCO and hole-doped LCO are presented in Figs. 1(a)–1(e). LSCO undergoes a second-order phase transition from a high-temperature tetragonal structure with the $I4/mmm$ space group (HTT) illustrated in Fig. 1(a), to a low-temperature orthorhombic structure, LTO, with the $Bmab$ space group, illustrated in Fig. 1(b). This transition is relatively subtle and involves a cooperative tilting of the CuO_6 octahedra along the $[110]$ axes of the HTT structure [7] and an elastic deformation of their basal planes, as shown in Fig. 1(c). As a consequence, the space group changes and the unit cell of the LTO phase is rotated by 45° and expanded by $\sqrt{2}$, such that superlattice reflections appear whose intensity is proportional to the square of the tilt angle. Therefore, this tilting is the primary order parameter of the transition. In addition, splitting of the main reflections arises from the twinned orthorhombic domains that are present.

The hole-doped LCO structure in LBCO or LSCO changes with both temperature and hole-doping concentration, x [8]. For a given hole doping, and as a function of decreasing temperature, a sequence of structural transitions occurs in LCO materials: $T(\text{HTT}) > T(\text{LTO}) > T(\text{LTT})$, where HTT represents the tetragonal, high-temperature nontilted structure, while LTO and LTT are the two, low-temperature, tilted structures [7,9]. Although the LTT designation stands for “low-temperature tetragonal,” this structure is in fact

orthorhombic with space group ($P4_2/nmz$), and is illustrated in Fig. 1(d). The LTO to LTT transition is first order (discontinuous) in nature and involves tilts about the $[100]$ axes of the HTT structure [Fig. 1(e)]. The LTT structure is therefore not a subgroup of the LTO structure, which displays tilts about $[110]$ relative to the HTT structure, as illustrated in Fig. 1(c). The discontinuous nature of the structural phase transition between the LTO and LTT phases is thus expected.

The phase diagram of $\text{La}_{1.6-x}\text{Nd}_{0.4}\text{Sr}_x\text{CuO}_4$ (Nd-LSCO) is very similar to that of the other single-layer hole-doped cuprates and as a function of hole doping $p(=x)$, it moves from a three-dimensional commensurate antiferromagnet ($x=0$), to a region of static two-dimensional spin stripe order, to spin and charge stripes coexisting with superconductivity at low temperatures, and finally to a conventional nonsuperconducting Fermi liquid beyond $x \sim 0.26$ [10–12]. The maximum superconducting T_C is ~ 15 K at $x \sim 0.19$. Below a crossover temperature T^* there exists an enigmatic part of the phase diagram referred to as the “pseudogap phase,” characterized by a gapped electronic density of states [13,14]. In Nd-LSCO, angle-resolved photoemission spectroscopy measurements reveal that an antinodal pseudogap is present at dopings up to $p=0.20$, but is absent at $p=0.24$ [15]. Very recent work [16] has shown thermodynamic evidence for a *quantum critical point* at $p^* = 0.23 \pm 0.005$ in Nd-LSCO, associated with the end of this line of phase transitions [$T^*(p)$] [17]. The relatively low maximum T_C exhibited by the Nd-LSCO system was crucial for this study, as it allowed the suppression of superconductivity by practical

magnetic fields ($H \leq 18$ T), so that the thermodynamic properties of the normal state at these doping levels, p , could be studied. The electronic heat capacity of the Nd-LSCO system could then be measured over a range of hole concentrations spanning the underdoped, optimally doped, and overdoped regions, and as a function of temperature. Michon *et al.* [16] found that the C_{el}/T is strongly peaked at p^* and that at p^* it follows a $\log(1/T)$ dependence as T tends to zero. These findings are typical thermodynamic signatures of a quantum critical point, as previously observed, for example, in iron pnictide superconductors [18] and heavy-fermion metals [19].

In Nd-LSCO, a number of transport properties are seen to change abruptly across $p^* = 0.23$, in the $T = 0$ limit and without superconductivity. The carrier density drops from $n \sim 1 + p$ above p^* to $n \sim p$ below p^* , as measured by the Hall coefficient [20–22], the electrical resistivity [20,21], and the thermal conductivity [23]. A contribution to the thermal Hall conductivity from neutral excitations appears below p^* [24], and the Fermi surface changes topology below p^* , as seen by angle-dependent magnetoresistance [25].

According to the structural phase diagram of Nd-LSCO first reported in the literature by Axe and Crawford [9], as well as in other studies [2,3,26], the following structural hierarchy is observed at constant hole concentration for $x \leq 0.15$: $T(\text{HTT}) > T(\text{LTO1}) > T(\text{LTO2}) > T(\text{LTT})$. Note that relative to both LBCO and LSCO, an additional low-temperature orthorhombic phase, LTO2 (*Pccn* space group), is observed in the Nd-LSCO system, which seems to separate the LTO1 and LTT structural phases at low hole-doping concentrations [27,28]. The LTO2 structure is obtained by simultaneous and unequal tilts about the [110] and [1–10] axes of the HTT structure [29].

Among the key questions that ensue then, is what role do the structural symmetries of these crystalline phases play on the superconducting and pseudogap properties of Nd-LSCO? The preexisting phase diagram for Nd-LSCO covers only Sr concentrations up to $x = 0.25$, where superconductivity seems to end, but information near these concentrations and at higher doping is lacking. This is likely due to the difficulty associated with synthesizing samples with $x \geq 0.2$ including overdoped samples of this and other high-temperature T_C superconductors [30].

In this study, we report the synthesis and characterization of both polycrystalline and large single crystals of Nd-LSCO, appropriate for neutron-scattering studies, for example. Our group has synthesized single-phase, polycrystalline Nd-LSCO samples with x spanning from 0.01 to 0.40, and have grown large single crystals (~ 5 grams and larger) of $\text{La}_{1.6-x}\text{Nd}_{0.4}\text{Sr}_x\text{CuO}_4$ for select nominal $x = 0.07, 0.12, 0.17, 0.19, 0.225, 0.24, \text{ and } 0.26$. This work thus extends our understanding of the structural phase diagram of Nd-LSCO at both low and high hole doping, and in particular provides greater detail in the regime around the end of the pseudogap phase, at $p^* = 0.23$, and the end of superconductivity, at $p_c \sim 0.27$. We describe the synthesis of single-phase powder samples as well as the single crystals, and report systematic neutron and x-ray diffraction studies characterizing these samples at both low and high temperatures. These analyses allow us to ascertain the stoichiometries of the samples we have synthesized, and benchmark them against the results of earlier

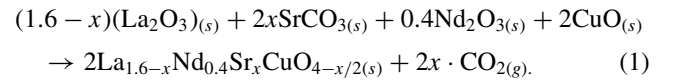
studies. These samples have been, and will be, the subject of further experimental studies. They also allow us to propose an updated phase diagram for Nd-LSCO that now covers Sr doping concentrations up to $x = 0.40$, and make comparisons to the corresponding phase diagram for LSCO.

II. EXPERIMENT SECTION

A. Materials preparation

1. Polycrystalline samples

The chemical reaction that led to the formation of the $\text{La}_{1.6-x}\text{Nd}_{0.4}\text{Sr}_x\text{CuO}_4$ ($x = 0.01, 0.02, 0.04, 0.05, 0.07, 0.12, 0.17, 0.19, 0.225, 0.24, 0.26, 0.27, 0.36, \text{ and } 0.40$) compounds can be written as



The starting materials used in the synthesis of $\text{La}_{1.6-x}\text{Nd}_{0.4}\text{Sr}_x\text{CuO}_4$ were La_2O_3 (Cerac, 99.99%), Nd_2O_3 (REO, Inframat Adv. Mat., 99.9%), CuO (Cerac, 99.999%), and SrCO_3 (Cerac, 99.994%). The lanthanides, La_2O_3 and Nd_2O_3 , were first preannealed at 1000°C to remove any residual water. An appropriate stoichiometric mixture of the oxides was homogenized in a planetary mill, dried, followed by homogenization by hand, in an agate mortar, for about 1 h. The as-obtained homogenized powder was annealed several times at 1000°C , in air, with intermittent grinding. Samples with higher Sr concentration, x , required longer annealing times of up to 1 week. The resulting powder samples were of black color with a grayish shine.

2. Single-crystal growth

Polycrystalline $\text{La}_{1.6-x}\text{Nd}_{0.4}\text{Sr}_x\text{CuO}_4$ with $x = 0.07, 0.12, 0.17, 0.19, 0.225, 0.24, \text{ and } 0.26$ were pressed into rods ~ 80 mm long and with a diameter of 8 mm. A stable single-crystal growth requires dense, single-phase rods. For this purpose, the polycrystalline rods were then annealed for 48 h at temperatures around 1200°C (the temperature slightly varied and was adjusted for each composition), under an oxygen flow of ~ 15 mL/min. The heating and cooling rates were 100° per hour. To compensate for the loss of CuO during annealing and crystal growth, an excess of 3 at.% CuO was used.

The Nd-LSCO materials melt incongruently which implies that instead of producing a melt with the same composition as the prepared polycrystalline material, the melt has a different composition from the solid material feeding it. Therefore, in order to be able to grow large single crystals of these incongruently melting materials, the traveling solvent floating-zone (TSFZ) technique needs to be employed. In contrast to congruent bulk crystal growth techniques, the TSFZ technique involves dissolving a small portion of the material into the created solvent. The solvent is designed in such a way that it melts well below the melting point of the crystal and creates a liquid reservoir. During the crystal growth, the feed rod continues to supply the reservoir with the desired composition of the target crystal and eventually induces saturation within the solvent. Finding the right solvent is never an easy task and to determine the appropriate solvent for Nd-LSCO, the phase

diagram of the $\text{La}_2\text{O}_3\text{-CuO}$ binary system was considered [31]. After many different trials, an ideal ratio of 22:78 for La_2O_3 vs CuO was chosen as the solvent. However, adding Sr and Nd to the solvent with the ratio of the elements being similar to what they are in the desired crystal was also found to be important for a stable crystal growth.

The single-crystal growths were performed on a four-mirror optical floating zone (OFZ) furnace (Crystal Systems, Inc.). The growth of Nd-LSCO single crystals has proven to be challenging due to the relatively low growth rate and their high sensitivity to the growth conditions. To maintain a stable growth, a steady length of the molten zone is desirable and it requires careful control. This can be achieved by maintaining a constant growth speed. For this system, the growth speed should be less than 1 mm/h, as faster growth speeds will dramatically affect the crystal quality. To achieve relatively large single crystals, we determined 0.65 mm/h as an optimal growth speed for Nd-LSCO using the four-mirror floating-zone image furnace at McMaster University. During the growth, both the feed and the seed rods were coaxially counter-rotated at a rate of 30 rpm.

The resulting single crystals, which were typically 8 mm in diameter and about 30 up to 60 mm long, were used in several different experiments, but the large size of the single crystals was driven by the needs of neutron experiments. The crystals were grown in air, and were later annealed in flowing oxygen, as described in the next sections.

B. Characterization

1. X-ray powder diffraction

Laboratory x-ray powder diffraction analysis was carried out on a zero-background plate, at room temperature, using a PANalytical X'Pert PRO (PANalytical, Almelo, Netherlands) with $\text{Cu K}\alpha_1$ radiation ($\lambda = 1.54056 \text{ \AA}$) and X'Celerator detector. A 2θ step of 0.0167° was used for data collection in the $15\text{--}80^\circ 2\theta$ range. The phase identification was performed using the PDF-2 database and the X'Pert HighScore software.

2. Neutron powder diffraction

Time of flight (TOF) powder neutron diffraction experiments were collected on the powder Nd-LSCO samples using the POWGEN instrument [32] (BL-11A) at the Spallation Neutron Source (SNS), Oak Ridge National Laboratory, Oak Ridge, Tennessee, USA. Two sets of measurements were performed at temperatures of 300 and 10 K using neutron beams with a wavelength centered on 1.5 \AA and covering a d -spacing range of $0.5\text{--}13 \text{ \AA}$. Roughly 500 mg of each sample was loaded in a vanadium can (6-mm inner diameter) for the measurements. The Rietveld refinements of the acquired data were performed with the GSAS-II program [33].

3. Single-crystal x-ray diffraction

White beam (Laue) x-ray diffraction was performed on all of our single-crystal samples to assess the surface quality of the as-grown crystals and to determine the orientation of the single-crystal pieces. The Laue measurements were performed using a tungsten tube source powered by a Spellman power supply at a voltage of 10 kV and current of 10 mA. The

diffracted x rays were detected with a Multiwire Laboratories detector, while the data were collected with NORTH STAR software. The orientation of the crystals was determined by fitting the collected patterns using ORIENT EXPRESS.

High-resolution single-crystal x-ray scattering measurements were performed using $\text{Cu K}\alpha$ radiation ($\lambda = 1.54 \text{ \AA}$) produced by an 18-kW rotating anode source with a pyrolytic graphite monochromator [PG-(0,0,2)]. Samples with a size of $\sim 3\text{--}5 \text{ mm}$ (cross section) and $\sim 0.5\text{--}1 \text{ mm}$ (thickness) were mounted on the cold finger of a closed-cycle cryostat, and were aligned using a Huber 4-Circle diffractometer. The accessible temperature range for the cryostat was from $T = 4 \text{ K}$ up to $T = 310 \text{ K}$. The Nd-LSCO single crystals were characterized by measuring the temperature dependence of several Bragg peaks which differ appreciably in each of the HTT, LTO, and LTT crystallographic phases. For example, the HTT to LTO structural phase transition is relatively easily identified from the splitting of $(H, H, 0)_{\text{HTT}}$ -type peaks into $(2H, 0, 0)_{\text{LTO}}$ and $(0, 2H, 0)_{\text{LTO}}$ peaks. Similarly, the phase transitions from LTO to low-temperature tetragonal or to low-temperature less orthorhombic (LTO2) phases can be identified based on the appearance of superlattice Bragg peaks at the $(H, 0, 0)_{\text{HTT}}$, $H = \text{odd}$ or $(0, K, 0)_{\text{HTT}}$, $K = \text{odd}$ positions.

4. Elastic neutron-scattering measurements on single crystals

Elastic neutron-scattering measurements were performed on large single crystals as part of a study of their full inelastic neutron-scattering spectra. The results from the elastic measurements are very useful in their own right, as they permit a comprehensive check of the single-crystal nature of these relatively large samples. As neutrons are deeply penetrating, such measurements are sensitive to single-crystal grains throughout the material. These measurements were performed using the SEQUOIA Time of Flight Chopper Spectrometer at the SNS at Oak Ridge National Laboratory [34]. These measurements were carried out on large $x = 0.12, 0.19,$ and 0.24 single crystals of Nd-LSCO, and were displayed and analyzed using MANTID software [35].

5. Magnetic susceptibility and resistivity measurements

Magnetic susceptibility measurements were carried out on single crystals of Nd-LSCO using a Quantum Design MPMS superconducting quantum interference device magnetometer. The direct current zero-field-cooled and field-cooled data were collected in the temperature range from 2 to 30 K and an applied magnetic field ranging from 10 to 1000 Oe. The single crystals were mounted on a quartz sample holder and the magnetic fields were applied along the c axis.

Samples for resistivity measurements were cut in the shape of rectangular platelets with a cross-section size of typically 2mm^2 and thickness of 0.2 mm. The a and c axes of the samples were along its largest and smallest dimensions. The longitudinal and transverse current pairs of contacts were made using silver paste epoxy H20E EpoTek and silver wires with a diameter of 0.025 mm. The contacts were diffused in the sample by annealing in an oxygen atmosphere at 500°C for 1 h. The resistivity was measured longitudinally with the

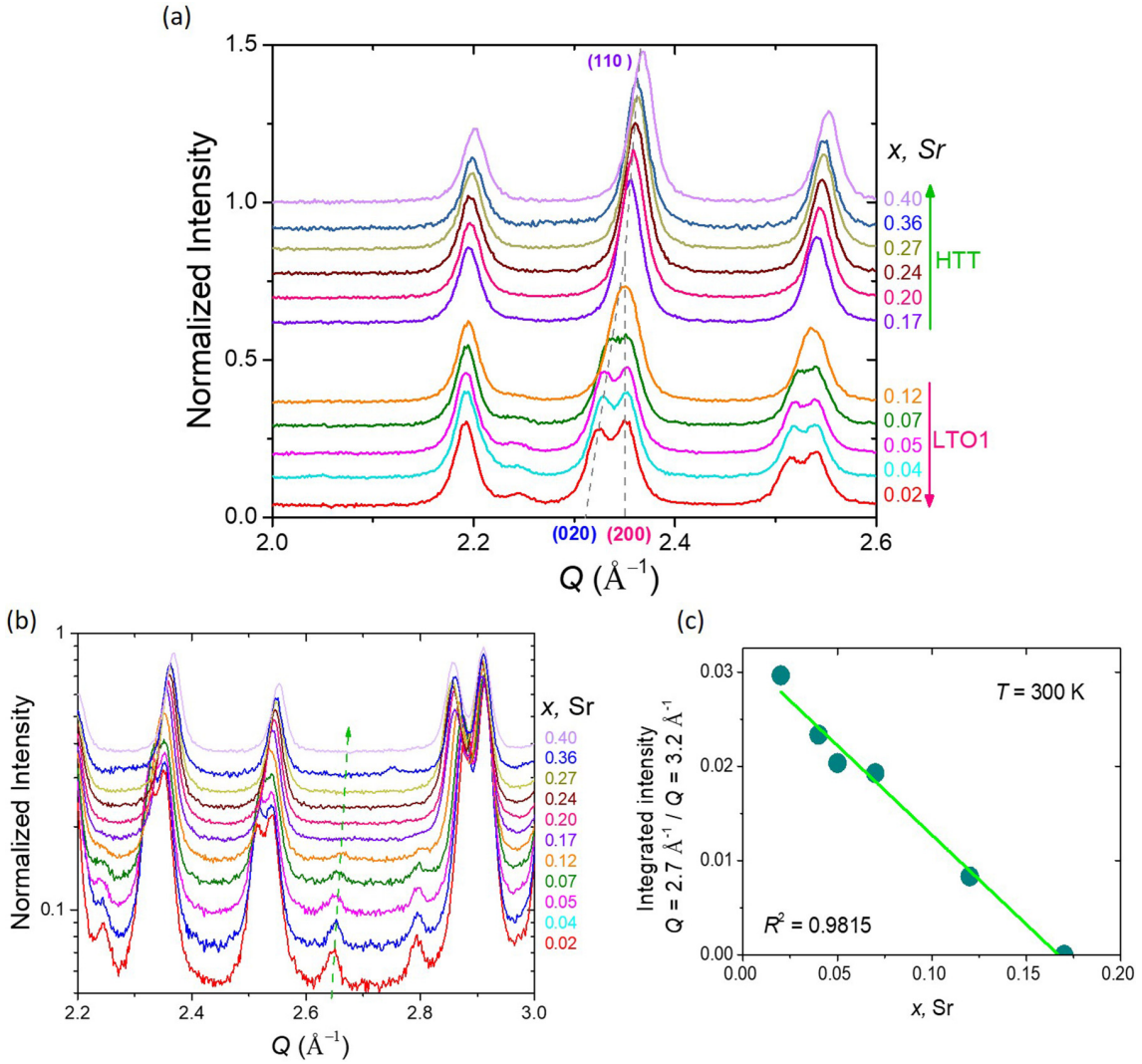


FIG. 2. (a) The evolution of the neutron-diffraction profiles for Nd-LSCO as a function of x , at room temperature, $T = 300 \text{ K}$. The phase transition from HTT to LTO (or LTO1) can be followed either by the splitting of the (110) reflection to (020) and (200) as in (a), or by the evolution of the intensities of the superlattice reflections as a function of x , which is more easily seen on the logarithmic intensity scale (b). (c) The plot of the relative intensity of the superlattice intensity as a function of x , showing the disappearance of the superlattice intensity at $x = 0.16 \pm 0.01$.

standard four-probe technique. In all the measurements, the current was applied along the length of the samples.

III. RESULTS AND DISCUSSION

A. Polycrystalline samples

1. Neutron powder diffraction and x-ray diffraction at 300 K

Examination of the Nd-LSCO powder samples performed with our lab-based Cu $K\text{-}\alpha_1$ x-ray source at room temperature confirmed the phase purity and crystalline nature of the synthesized powders. Room-temperature neutron-diffraction measurements were also carried out. Both room-temperature x-ray and neutron powder diffraction measurements were analyzed in a LTO1, space group $Bmab$, for $x \leq 0.12$, and a HTT with the $I4/mmm$ space group for $x > 0.12$.

Figure 2 presents the neutron powder diffraction profiles obtained at room temperature for the entire powder series, $0.01 \leq x \leq 0.40$. At 300 K, the evolution of the phase transition from the HTT ($I4/mmm$) to LTO1 ($Bmab$) in the powder samples can be observed by the splitting of the (110)_{HTT} reflection into the (020) and (200) reflections appropriate to $Bmab$ symmetry, as x varies from 0.02 to 0.4, as shown in Fig. 2(a). The primary difference between the LTO and HTT structures is the tilt of the CuO_6 octahedra about the [110] axes of the HTT structure. Due to this tilt, the unit cell rotates by 45° and increases by $\sqrt{2}$ and superlattice reflections appear with intensities proportional to square of the tilt angle, which increases with lowering the temperature, but decreases with increasing x . Therefore, this phase transition can also be followed by monitoring the evolution of the superlattice reflection as shown in Fig. 2(b). Here, we can see that there is a continuous decrease in the intensity of this reflection as

TABLE I. Results of the Rietveld neutron refinement for Nd-LSCO with $x = 0.12$ and 0.40 , $T = 300$ K: lattice parameters, positional, and thermal parameters are displayed together with the tilt angle.

$x = 0.12$								
Atom	Space group	Wyckoff site	x	y	z	U_{iso}	Occ	
La	<i>Bmab</i>	$8f$	0	0.0043(3)	0.3606(1)	0.005(3)	0.742(1)	
Nd		$8f$	0	0.0043(3)	0.3606(1)	0.006(2)	0.202(2)	
Sr		$8f$	0	0.0043(3)	0.3606(1)	0.006(1)	0.059(2)	
Cu		$4a$	0	0	0	0.003(2)	0.984(4)	
O1		$8e$	0.25	0.25	0.0073(1)	0.008(2)	0.977(4)	
O2		$8f$	0	-0.0304(3)	0.1825(1)	0.0146(1)	0.988(4)	
Tilt angle ($^{\circ}$)						5.7		
R_{wp} (%)					2.97			
a (\AA)					5.3289(7)			
b (\AA)					5.3625(8)			
c (\AA)					13.1421(2)			
V (\AA^3)					375.557(6)			
$x = 0.40$								
Atom	Space group	Wyckoff site	x	y	z	U_{iso}	Occ	
La	<i>I4/mmm</i>	$4e$	0	0	0.3593(1)	0.018(5)	0.589(7)	
Nd		$4e$	0	0	0.3593(1)	0.030(5)	0.221(7)	
Sr		$4e$	0	0	0.3593(1)	0.024(5)	0.190(3)	
Cu		$2a$	0	0	0	0.003(1)	0.969(6)	
O1		$4c$	0	0.5	0	0.009(1)	0.968(5)	
O2		$4e$	0	0	0	0.1804(2)	0.017(1)	0.980(8)
Tilt angle ($^{\circ}$)						0		
R_{wp} (%)					3.06			
a (\AA)					3.7523(1)			
b (\AA)					3.7523(1)			
c (\AA)					13.1932(4)			
V (\AA^3)					185.761(1)			

the orthorhombicity decreases, characteristic of a continuous, second-order phase transition.

By integrating the relative intensity of the superlattice reflection as a function of Sr composition, x , as shown in Fig. 2(c), we can accurately estimate the critical concentration for which the LTO structure exists to be $x = 0.16 \pm 0.01$. These results are in good agreement with the previous report by Axe and Crawford [9] which covered compositions in powder samples from $x = 0.05$ up to 0.25.

A plot comparing the refined lattice parameters vs composition for Nd-LSCO at 300 K, for both x-ray- and neutron-diffraction data, is presented in Fig. 3. For comparison purposes, \sqrt{a} is plotted for the tetragonal cell. Nearly identical refined lattice parameters were obtained from the refinement of these two sets of data (x ray and neutron). The c -lattice parameter slowly increases with x while the b -lattice parameter shows a large initial decrease with x . No anomalous behavior in these parameters as a function of x is observed, giving further confidence that these polycrystalline samples are single phase and thus confirming the stoichiometry of our samples. The evolution of the a -, b -, and c -lattice parameters in Nd-LSCO as a function of x , resulting from the Rietveld refinement of the neutron powder diffraction data at 300 K and compared to the data at 10 K, is plotted in Fig. 3(c).

The building blocks of the $\text{La}_{1.6-x}\text{Nd}_{0.4}\text{Sr}_x\text{CuO}_4$ structure are the CuO_6 octahedra where the Cu atoms are bonded with

4 planar oxygen atoms (O1) and 2 apical oxygen atoms (O2). Due to the Jahn-Teller effect, the octahedra are distorted and there is a strong overlap of the Cu–O orbitals.

The evolution of the Cu–O bond lengths as a function of x at $T = 300$ K is plotted in Fig. 4. It can be seen that the apical Cu–O bond increases up to $x = 0.07$ after which it experiences a slow decrease, while the planar Cu–O bond lengths decrease almost linearly with x . The evolution of these bond lengths is related not only with the structural changes, but also with the increase in the hole concentration.

Figure 5 shows representative examples of the Rietveld neutron refinement profiles for the powder samples with $x = 0.12$ and 0.40 , while Table I summarizes the structural parameters resulting from these room-temperature refinements. The room-temperature structure for $x = 0.12$ is orthorhombic with the *Bmab* space group. During the refinement, other structural models, such as *PA₂/ncmz* and *Pccn*, were also considered to fit the experimental neutron powder diffraction data, but were ruled out by the indexing and refinement analysis. The structure of the sample with $x = 0.40$ easily refines in the *I4/mmm* space group.

These refinements of the powder diffraction data show that the quality of the diffraction patterns and their refinements are very similar across the full spectrum of hole doping studied, from $x = 0.01$ to $x = 0.4$. In addition, we can estimate the uncertainty associated with the stoichiometries of the

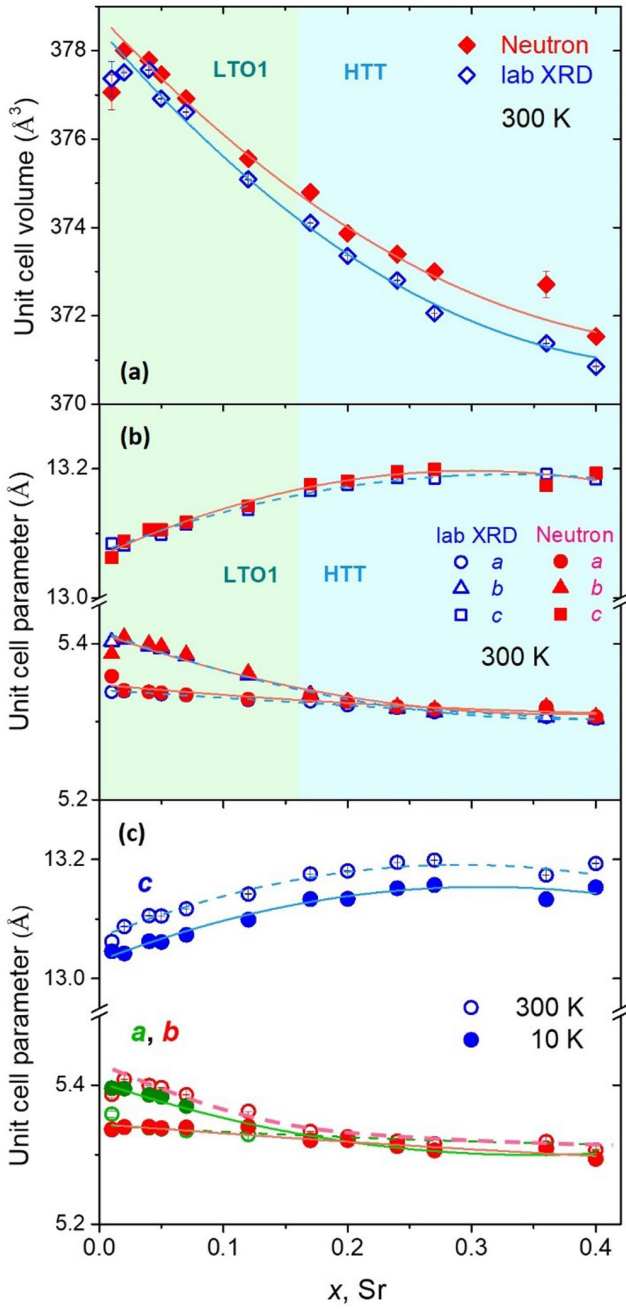


FIG. 3. The refined unit-cell volume, (a), and lattice parameters, (b), vs composition for Nd-LSCO at 300 K with the $Bmab$ and $I4/mmm$ space groups, obtained from Rietveld refinement analysis of both x-ray and TOF-NPD data. \sqrt{a} is plotted for those samples displaying HTT structures. (c) Lattice parameters, a , b , and c of Nd-LSCO at 300 and 10 K as function of Sr concentration, x , as obtained from the refinement of the neutron powder diffraction data.

synthesized materials on the basis of these refinements. We see that the oxygen occupations are stoichiometric at the $\pm 2\%$ level, while the Sr and Nd concentrations are appropriate to the target for the synthesis at the $\pm 1\%$ level or better.

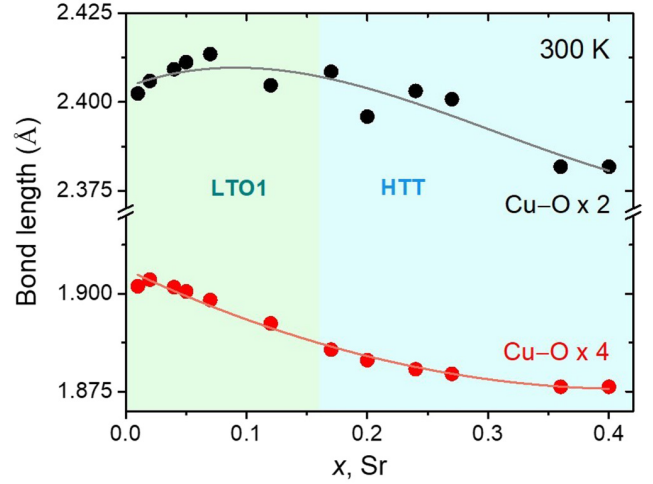


FIG. 4. Cu-O bond lengths for both planar (Cu-O \times 4) and apical (Cu-O \times 2) oxygen ions of $\text{La}_{1.6-x}\text{Nd}_{0.4}\text{Sr}_x\text{CuO}_4$ as a function of x , obtained from Rietveld refinement of the NPD data at 300 K.

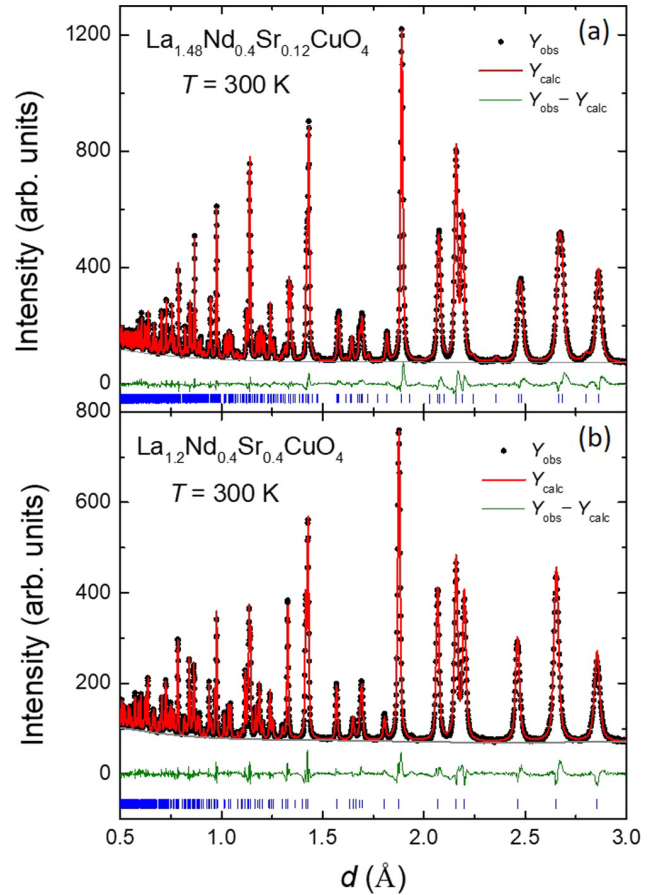


FIG. 5. Rietveld refinement profiles of the neutron diffraction data obtained at room temperature for $x = 0.12$ (a) and $x = 0.40$ (b). The measured pattern is shown in black, the calculated profile in red, difference in green, while tick marks represent the allowed Bragg peaks.

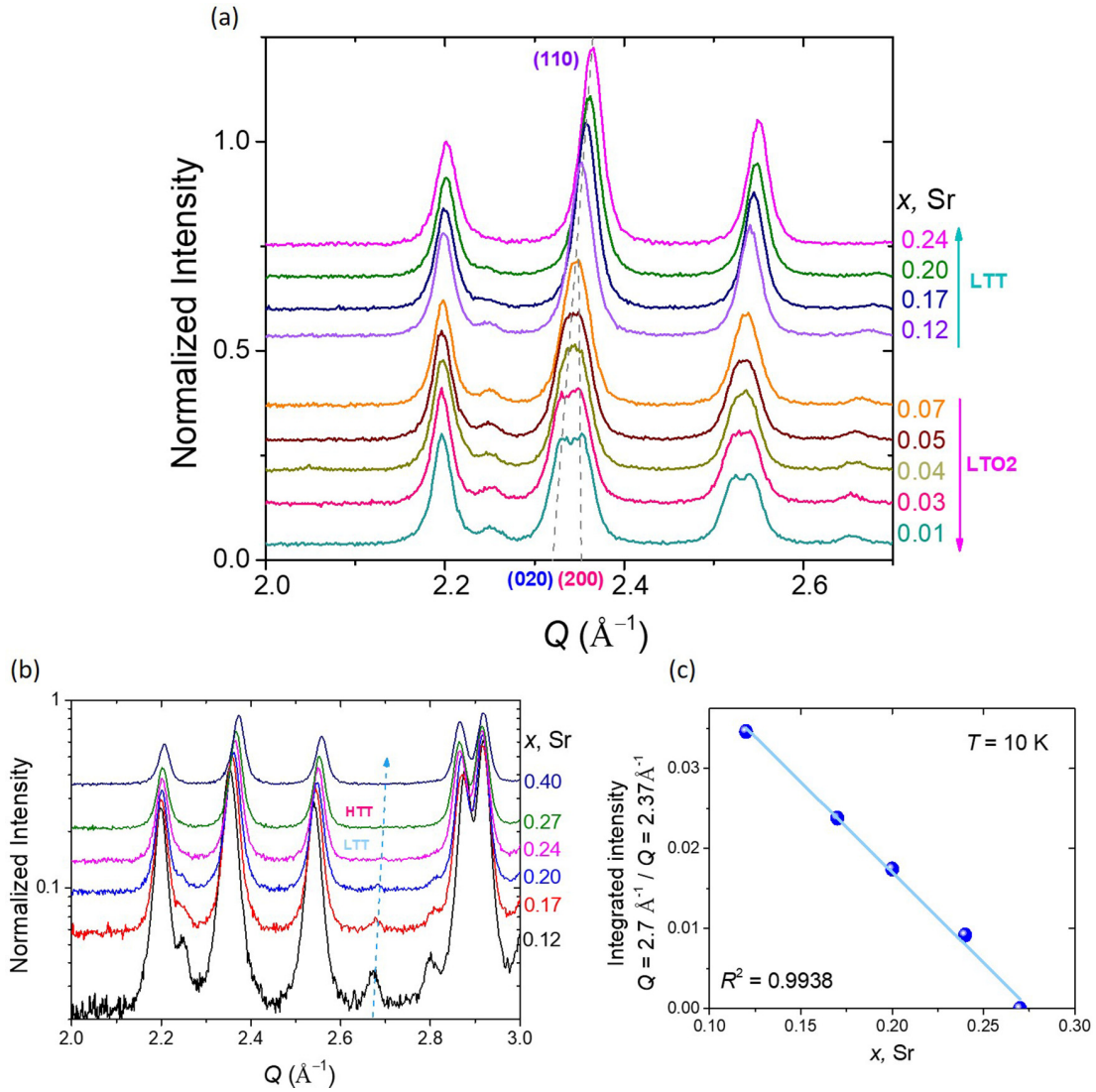


FIG. 6. (a) The evolution of the neutron-diffraction profiles for Nd-LSCO as a function of x , at 10 K. The phase transition from LTT to HTT was followed by the evolution of the superlattice reflection intensity as a function of x , which is more easily observed with intensity on a logarithmic scale (b). The plot of the relative intensity of the superlattice reflection as a function of x shows the disappearance of the superlattice reflection between $x = 0.24$ and $x = 0.27$. (c) A plot of the integrated intensity extrapolates the critical concentration for the end of the LTT phase to be $x_{\text{LTT}} \sim 0.27(1)$.

2. Neutron powder diffraction at 10 K

Our $T = 10 \text{ K}$ neutron powder diffraction (NPD) data reveal that the Nd-LSCO phase diagram becomes more complex at low temperatures, consistent with earlier studies, encountering three structural phase transitions with increasing Sr concentration, x , as shown in Figs. 6(a) and 6(b). These data were analyzed using the LTO2- $Bmab$ orthorhombic space group for $0.01 \leq x \leq 0.07$, the LTT space group, $P4_2/ncmz$ for $0.12 \leq x \leq 0.24$, and the high-temperature tetragonal, HTT - $I4/mmm$ space group for $0.27 \leq x \leq 0.40$.

The CuO_6 octahedra tilt about different directions within the HTT structure, with tilts about the [110] direction for the LTO structure and about the [100] and [010] for the LTT structure, respectively. Studies have shown that the tilts displayed by the LTT structure play an important role in stabilizing spin

and charge stripe order [36]. This induces C_4 intraunit-cell symmetry breaking which stabilizes stripes whose orientation rotates by 90° between neighboring CuO_2 planes.

The evolution of the Cu–O bond lengths as a function of x at 10 K is shown in Fig. 7. Note that for the LTT structure, there are two sets of Cu–O planar bonds due to the tilting of the CuO_6 octahedra within the LTT phase, although the difference between them is very small, only 0.28%. With increasing Sr concentration from $x = 0.01$ to 0.40, and consequently increasing the hole doping, both the planar and apical Cu–O bonds experience a decrease, the latter ones decreasing from 2.406(2) to 2.375(2) \AA . It seems that there is no compression of the CuO_6 octahedra with x since the Cu–O apical bonds do not experience any lengthening, but rather follow the same trend as the planar bonds. The decrease in Cu–O planar bonds can be correlated with the decrease of the a and b lattice

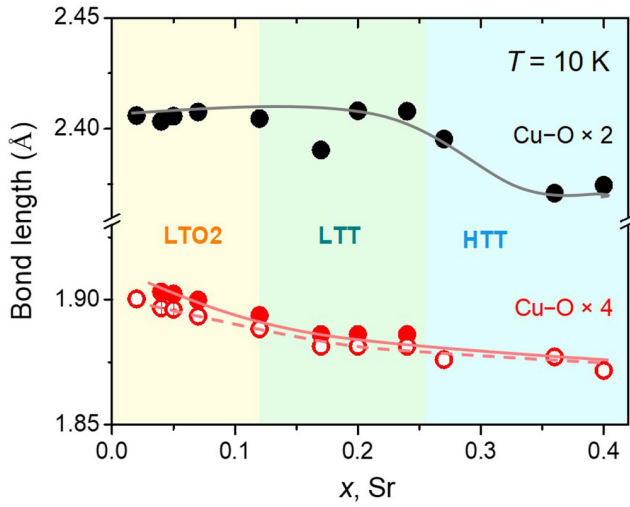


FIG. 7. The Cu–O bond lengths for both planar (Cu–O \times 4) and apical (Cu–O \times 2) oxygen ions of $\text{La}_{1.6-x}\text{Nd}_{0.4}\text{Sr}_x\text{CuO}_4$ as a function of x , as obtained from Rietveld refinement of the neutron powder diffraction data at $T = 10$ K.

parameters; see Fig. 3(c). However, the decrease in the axial bonds is not correlated directly with the c -lattice parameter which slightly increases with x . This is believed to be associated with the increase of the hole concentration of the system [37]. For samples with $x > 0.27$ there is no significant change in either of the Cu–O bond lengths. We therefore conclude that the decrease in the bond lengths as x increases is likely a result of the structural changes.

A summary of the results of the structural refinements of the Nd-LSCO polycrystalline samples using NPD (at 300 and 10 K) and XRD data (300 K) is presented in Table II.

B. Single crystals

1. Single-crystal characterization

Images relevant to the growth of the Nd-LSCO single crystals where $x = 0.19$ are shown in Fig. 8. An image of an

annealed polycrystalline rod of Nd-LSCO prior to its use in a single-crystal growth using a four-mirror optical floating-zone furnace is shown in Fig. 8(a), while Fig. 8(b) shows the single crystal resulting from the growth. To identify the single-crystalline nature and the crystal-growth habit, Laue diffraction was performed perpendicular to the growth axis, on different regions of the crystal. Figure 8(c) shows a typical Laue x-ray-diffraction pattern obtained. All the observed black spots were indexed assuming the growth direction was along the [001]. It can be seen that all spots were sharp within the instrumental resolution, without splitting or broadening that would indicate twinning, thus confirming its single-crystal nature. Based on this analysis, we can state that the Nd-LSCO crystals grown in this study are large single grains. However, neutron-scattering characterization needs to be employed to confirm this and we do so in the next section.

2. Elastic neutron scattering from large single crystals of Nd-LSCO

While x-ray diffraction can be very useful in refining powder structures, examining the crystallography of small single crystals, and for orienting known single crystals, the structure of large volumes of materials such as Nd-LSCO, either single crystals or otherwise, must be carried out with neutron scattering, so that the full volume of the growth can be sampled and characterized. We carried out elastic neutron-scattering measurements on three single crystals of Nd-LSCO, $x = 0.12$, 0.19, and 0.24, resulting from these growths. These measurements were part of a larger program of elastic and inelastic neutron-scattering characterization of these materials. In what follows, we describe only the elastic neutron scattering and how it informs on the single-crystal nature of the large samples grown.

Figure 9 shows maps of the elastic neutron scattering ($-4 \text{ meV} < E < +4 \text{ meV}$) within the $(H, 0, L)$ plane of reciprocal space taken at $T = 5$ K. There is also an integration required in Q space to produce such a two-dimensional map, and this is an integration in K of the form $(0, K, 0)$ from $-0.75 < K < +0.75$. Such maps should only show Bragg intensity at integer positions within the $(H, 0, L)$ plane presented

TABLE II. Summary of the structural refinements of the neutron powder diffraction data at 300 and 10 K and x-ray powder diffraction data at 300 K.

300 K			10 K		
Sample/ x (Sr)	Space group	Abbreviation	Sample/ x (Sr)	Space group	Abbreviation
0.40	$I4/mmm$	HTT	0.40	$I4/mmm$	HTT
0.36	$I4/mmm$	HTT	0.36	$I4/mmm$	HTT
0.27	$I4/mmm$	HTT	0.27	$I4/mmm$	HTT
0.24	$I4/mmm$	HTT	0.24	$P4_2/ncmz$	LTT
0.20	$I4/mmm$	HTT	0.20	$P4_2/ncmz$	LTT
0.17	$I4/mmm$	HTT	0.17	$P4_2/ncmz$	LTT
0.12	$Bmab$	LTO1	0.12	$P4_2/ncmz$	LTT
0.07	$Bmab$	LTO1	0.07	$Pccn$	LTO2
0.05	$Bmab$	LTO1	0.05	$Pccn$	LTO2
0.04	$Bmab$	LTO1	0.04	$Pccn$	LTO2
0.02	$Bmab$	LTO1	0.02	$Pccn$	LTO2
0.01	$Bmab$	LTO1	0.01	$Pccn$	LTO2

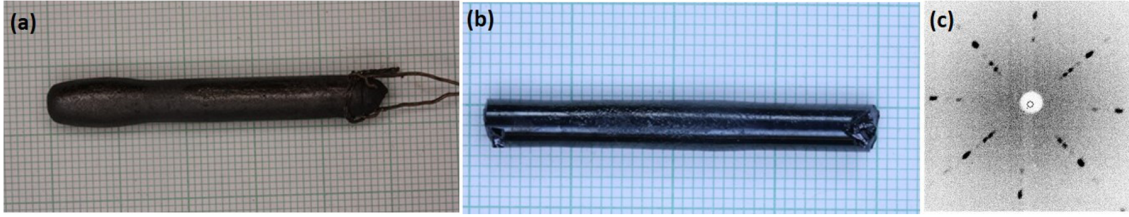


FIG. 8. Photographs of the Nd-LSCO ($x = 0.19$) samples: (a) the ceramic rod used for the crystal growth, (b) the as-grown single crystal from the OFZ furnace growth, (c) Laue diffraction pattern performed on surface of the as-grown single crystal, along the growth direction, [001]. The black spots mark the intensity from the backscattered Bragg peaks, while the white circle shows the center of the beam.

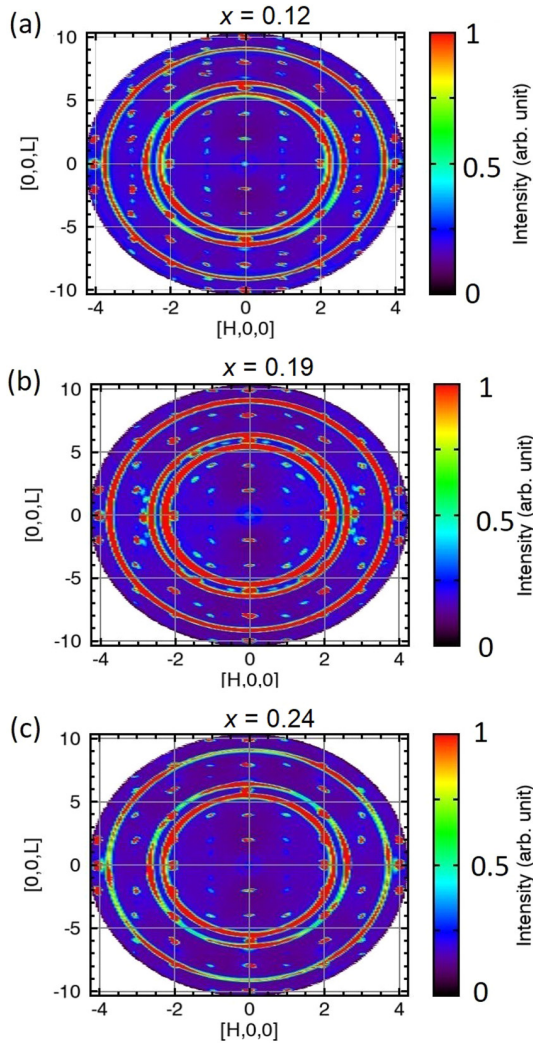


FIG. 9. The elastic Bragg scattering within the $(H, 0, L)$ scattering plane, integrated in K along $(0, K, 0)$ for $-0.75 < K < 0.75$, and in energy for $-4 \text{ meV} < E < +4 \text{ meV}$ are shown at $T = 5 \text{ K}$ for the three single crystals of $x = 0.12$ (a), 0.19 (b), and 0.24 (c). The data were collected using the SEQUOIA time-of-flight direct geometry chopper spectrometer. It can be seen that the Bragg peak positions align well with integer positions. The rings of scattering are due to Debye-Scherrer cones of elastic scattering from polycrystalline Al in the windows of the low-temperature cryostats and the sample holders.

in this way, if the sample is a single crystal, and that indeed is what we observed for the large single crystals of Nd-LSCO $x = 0.12$ in Fig. 9(a), $x = 0.19$ in Fig. 9(b), and $x = 0.24$ in Fig. 9(c). Note that the rings of elastic scattering observed in all three data sets are due to Bragg scattering from the aluminum cryostat windows and sample holders, and this is clearly polycrystalline in nature. We therefore conclude that our large single crystals are predominantly single grains of Nd-LSCO.

3. High-resolution single-crystal x-ray diffraction

The structural phase transitions associated with the single crystals of Nd-LSCO which we grew were studied using high-resolution x-ray diffraction. High resolution is required to characterize the small splitting of several of the HTT Bragg peaks once the materials enter orthorhombic structures, such as the LTO and LTT structures. This experiment employed a four-circle x-ray diffractometer and relatively tight collimation to produce the high angular or Q resolution. In the case of the data on the $x = 0.24$ single crystal shown in Fig. 10(b), $\text{Cu } K_{\alpha 1}$ radiation is not completely separated from $\text{Cu } K_{\alpha 2}$ radiation, and a “ghost” of the diffraction signal from residual $\text{Cu } K_{\alpha 2}$ radiation can be seen in the experimental results. Figure 10 shows the temperature dependence of longitudinal scans through the $(330)_{\text{HTT}}$ Bragg peak for single crystals with $x = 0.12, 0.24,$ and 0.26 , for the 40–200 K temperature interval.

From the neutron powder diffraction experiments we found that at room temperature, the $x = 0.12$ sample adopts the orthorhombic LTO1 structure. Our single-crystal x-ray-diffraction studies of this sample in Fig. 10(a) show that it undergoes a transition to the LTO2 structure at $T \sim 68(4) \text{ K}$.

The $x = 0.17$ sample (not shown here) is orthorhombic at room temperature, with the LTO1 structure and a much larger orthorhombic splitting of the $(330)_{\text{HTT}}$ Bragg peak than for the $x = 0.24$ sample shown in Fig. 10(b). A first-order phase transition to the LTT phase was observed at $75(3) \text{ K}$ for the $x = 0.17$, sample, only slightly above that displayed by the 0.24 single crystal. As Fig. 10(b) illustrates, at room temperature, the $x = 0.24$ sample adopts the tetragonal HTT structure with the $I4/mmm$ space group. The $(330)_{\text{HTT}}$ peak continuously splits into (600) and (060) below $150(3) \text{ K}$, as the crystal structure lowers its symmetry to orthorhombic LTO1 ($Bmab$ space group) due to the tilting or rotation of the CuO_6 octahedra. A second phase transition to the tetragonal

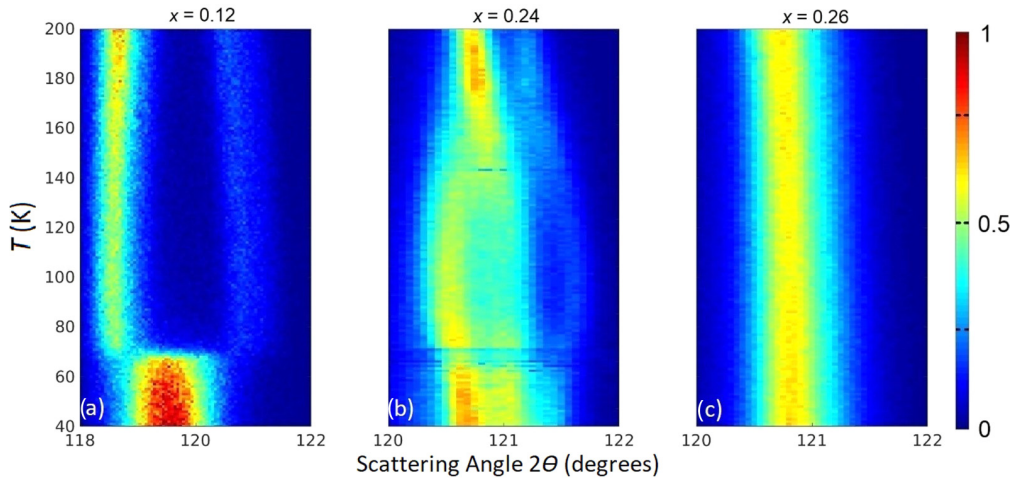


FIG. 10. The temperature dependence of $(3, 3, 0)_{\text{HTT}}$ Bragg peaks monitored via longitudinal x-ray scattering scans for representative Nd-LSCO single crystals with (a) $x = 0.12$, (b) $x = 0.24$, and (c) $x = 0.26$.

LTT ($P4_2/nmz$) structure occurs at a temperature of about 65(5) K, as is evidenced by a change in the splitting of this set of Bragg peaks. Note that while the longitudinal scans show a narrower profile for the LTT phase than for the LTO1 phase, the LTT phase profile remains clearly broadened compared to that in the HTT phase, consistent with the fact that the LTT phase is in fact orthorhombic.

Figure 10(c) shows very similar longitudinal scans for the $x = 0.26$ single-crystal sample, and at this concentration no evidence for any orthorhombic splitting is observed at any temperature between 300 and ~ 4 K. We therefore conclude that the structure of the $x = 0.26$ sample is HTT at all temperatures above 4 K.

The structural transition temperatures identified in our studies are all in excellent agreement with those reported earlier by Axe and Crawford [9]. In particular, our values of $T_1 \sim 150$ K for the HTT to LTO1 transition and $T_2 \sim 60$ K for the LTO1 to LTT transition at $x = 0.24$, are nicely consistent with their values of $T_1 \sim 130$ K and $T_2 \sim 50$ K at $x = 0.25$. Combining our data with theirs, we arrive at the following value for the critical doping at which the LTT phase ends, at $T = 0$: $p_{\text{LTT}} = 0.255 \pm 0.005$ (and also consistent with our polycrystal data above; Fig. 6).

A summary of the results of the high-resolution x-ray scattering study of single crystals of Nd-LSCO is presented in Table III below.

C. Characterization of the superconducting transition temperatures

A key feature of the high- T_C phase diagram is the hole-doping p , or x , dependence of the superconducting transition

temperatures across the Nd-LSCO series. These have been estimated by magnetic susceptibility measurements of our single-crystal samples. The susceptibility measurements were performed with the magnetic field applied along the c direction, that is normal to the ab basal plane of the crystals, and two sets of temperature-dependent measurements were performed, following both zero-field-cooled (ZFC) and field-cooled (FC) protocols. The ZFC data show an abrupt and large drop-off in the susceptibility at superconducting T_C . The FC data, which show the Meissner signal, tend to display a much smaller diamagnetic anomaly, which can nonetheless be useful in obtaining a consistent estimate for T_C , especially at high doping. The superconducting T_C can then be determined by the temperature at which the ZFC data splits from the FC data, and develops a large diamagnetic signal, as shown in Fig. 11.

Difficulties associated with measurements of the diamagnetic susceptibility in Nd-LSCO have been previously noted and discussed [38]. Of course, these will be more pronounced for samples with relatively weak superconductivity, and the data for underdoped $x = 0.07$ and 0.12 Nd-LSCO in Fig. 11 show paramagnetic susceptibilities at all temperatures measured. Nonetheless, the ZFC susceptibility splits below the FC susceptibility below T_C , and the T_C s so identified are consistent with previous determinations from the literature [9,16].

Portions of the single-crystal samples with $x \geq 0.17$ were subjected to annealing in flowing oxygen gas, to optimize their oxygen stoichiometry and the sharpness of the superconducting T_C s, and the data in Fig. 11 for $x \geq 0.17$ are all postannealing. This can be quite important as the condition that the hole concentration equals the Sr stoichiometry, $p = x$, requires that the oxygen content be stoichiometric. The

TABLE III. Summary of the structural transition temperatures as derived from x-ray single-crystal diffraction measurements performed on the Nd-LSCO single crystals.

x, Sr	0.12	0.17		0.19		0.24		0.26
T_1	68(4)	290(2)	75(3)	275(5)	70(2)	150(3)	65(5)	<4 K
T_2 (K)								
Transition	LTO1 to LTO2	HTT to LTO1	LTO1 to LTT	HTT to LTO1	LTO1 to LTT	HTT to LTO1	LTO1 to LTT	

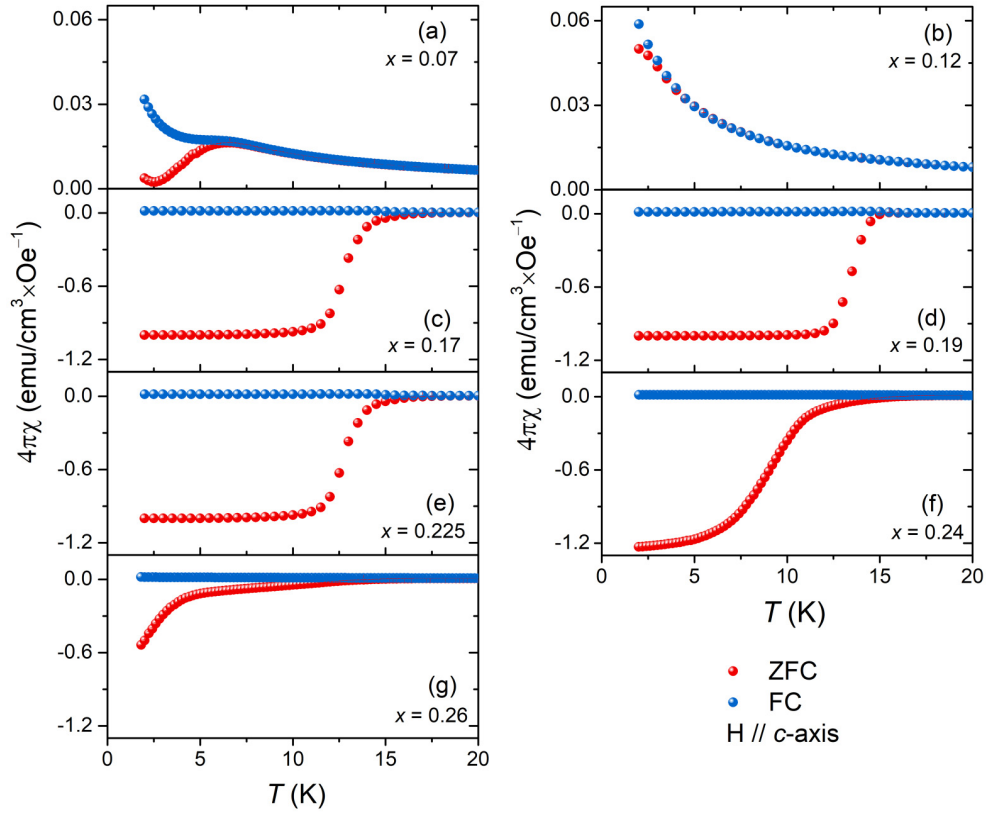


FIG. 11. Magnetic susceptibility data measured on the Nd-LSCO single crystals with $x = 0.07, 0.12, 0.17, 0.19, 0.225, 0.24,$ and 0.26 . The latter measurements for $x \geq 0.17$ were performed on samples that had been subjected to an annealing protocol (see text). The magnetic field, H , was applied \parallel to the c axis, $H = 10$ Oe for $0.17, 0.19, 0.225$ and $H = 100$ Oe for 0.24 and 0.26 samples.

annealing protocol was as follows: the samples were annealed in an oxygen flow of ~ 15 mL/min under 1 atmosphere, at 950°C , for 48 h. The heating and cooling rate was 100° per h to prevent thermal shock to the crystal. The annealing protocol slightly increased T_C , by ≤ 1 K and sharpened the superconducting transitions in all the samples. A similar tendency was observed in the studies on the LSCO system by Lorenz *et al.* [39] and Lee *et al.* [40,41].

The superconducting T_C tends to be more rounded at higher dopings, i.e., $x \geq 0.24$. The widths of the superconducting transitions, as estimated from the temperature interval for 20 to 80% diamagnetic signal, is ~ 1 K for samples near optimal doping and ~ 2 K for $x = 0.24$. For that reason, we examined several experimental measurements in order to provide a robust estimate for T_C . Figure 12(a) shows the FC magnetic susceptibility in our Nd-LSCO $x = 0.24$ single crystal measured with $H \parallel c$ at a range of magnetic field strengths between 10 and 250 Oe, while Fig. 12(b) shows the corresponding ZFC and FC magnetic susceptibility taken with $H = 100$ Oe for $H \parallel c$. We correlate these measurements with a measurement of the in-plane resistivity in zero magnetic field on a piece of the same single crystal, where we see that zero resistance is achieved for 11 K. The FC susceptibilities are all actually paramagnetic (i.e., positive), but clear diamagnetic cusps are observed just at and above 11 K, depending on the strength of the applied magnetic field. The ZFC magnetic susceptibility shows its strongest diamagnetic downturn at 11 K, as well. As a result, we assign $T_C = 11 \pm 1$ K for our $x = 0.24$ Nd-LSCO

sample, as marked by the vertical dashed lines in Fig. 12, consistent with all three of the resistivity as well as FC and ZFC susceptibility measurements (and with previous data [16]).

D. The superconducting phase diagram in $\text{La}_{1.6-x}\text{Nd}_{0.4}\text{Sr}_x\text{CuO}_4$

The superconducting T_C s as a function of doping, x , for the seven single crystals of Nd-LSCO we have grown and characterized are plotted in Fig. 13, along with those determined for single-crystal samples of Nd-LSCO (from Michon *et al.* [16] for $0.12 \leq x \leq 0.25$) and for polycrystalline samples of Nd-LSCO (from Axe and Crawford [9] for $x < 0.12$). One sees very good consistency between the measured T_C s on our large single crystals and those previously determined from both single-crystal and powder samples available in the literature, with a relatively flat $T_C(x) \sim 15$ K between $x \sim 0.15$ and $x \sim 0.22$. As expected, the overall shape of the superconducting phase diagram is similar to other hole-doped cuprates, with a very pronounced $1/8$ anomaly at $x = 0.125$.

E. The structural phase diagram of $\text{La}_{1.6-x}\text{Nd}_{0.4}\text{Sr}_x\text{CuO}_4$

The structural phase transitions as measured in the present study with single-crystal x-ray diffraction on seven Nd-LSCO samples are summarized in Fig. 14 along with the corresponding transitions determined earlier for polycrystalline samples. This plot therefore summarizes the key results from the present study, and illustrates the level of consistency in the

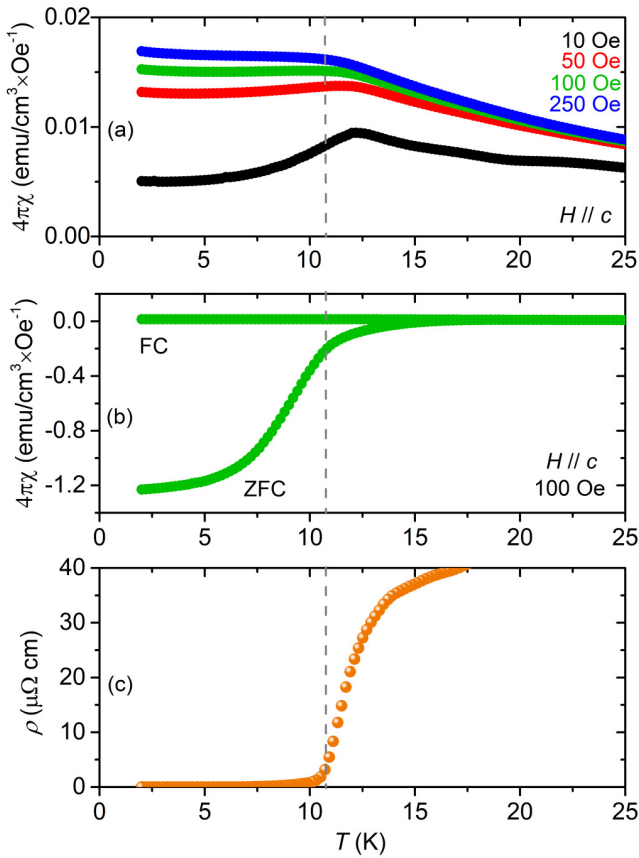


FIG. 12. (a) FC magnetic susceptibility data on $x = 0.24$ single crystal with the magnetic field applied parallel to c axis for 10, 50, 100, and 250 Oe. (b) ZFC-FC magnetic susceptibility data on the $x = 0.24$ sample with a field of 100 Oe applied parallel to c axis. (c) In-plane resistivity measurements on $x = 0.24$ sample. All data are consistent with a bulk superconducting $T_C = 11 \pm 1$ K.

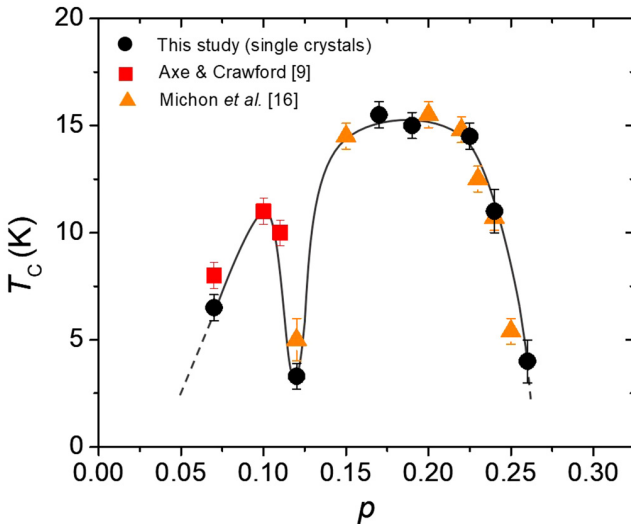


FIG. 13. Superconducting T_C vs p (or x) for several sets of Nd-LSCO samples. The present study shows the T_C from the seven single-crystal samples considered (black circles), while the remaining data are from single-crystal samples (orange triangles [16]) and polycrystalline samples (red squares [9]) in the literature.

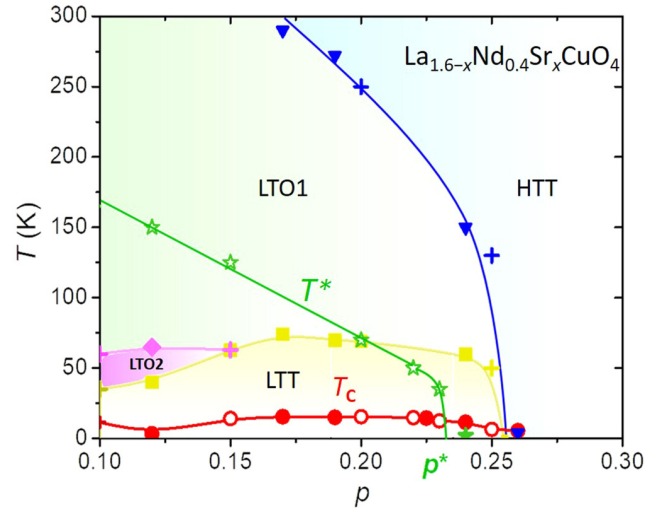


FIG. 14. Proposed Nd-LSCO phase diagram as a function of nominal hole concentration, p , or Sr doping, x , and temperature, T . The filled symbols are results obtained in this study, the crosses are from Axe and Crawford [9], while the open red circles (T_C) are reproduced from Michon *et al.* [16]. The pseudogap temperature, T^* (green stars), is taken from Cyr-Choinière *et al.* [17]. The critical doping p^* where the pseudogap phase ends at $T = 0$ is $p^* = 0.23$ [21].

measured phase transition temperatures between our work on single crystals of Nd-LSCO out to relatively high doping, and earlier measurements on polycrystalline samples. Superposed on the same plot are the measured superconducting T_C s, as shown in Fig. 13, as well as the values of the pseudogap transition temperature, T^* , taken from Cyr-Choinière *et al.* [17], and the associated pseudogap critical point $p^* = 0.23 \pm 0.005$

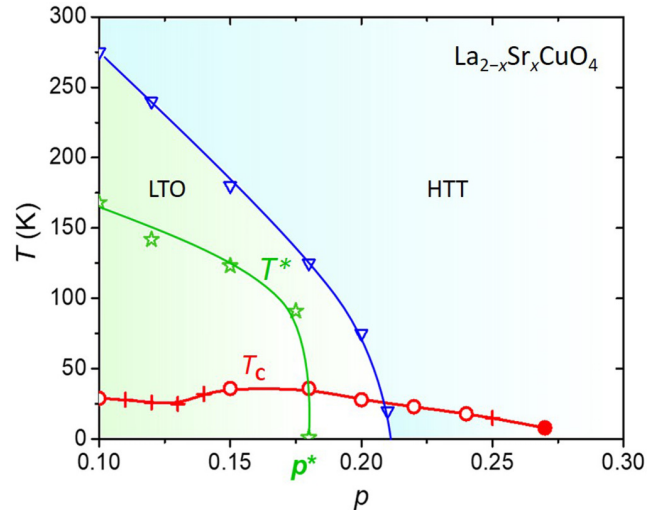


FIG. 15. The LSCO phase diagram, plotted for comparison to that of Nd-LSCO in Fig. 14. Empty symbols are from Yamada *et al.* [42], crosses are from Takagi *et al.* [45], and filled symbols from Lipscombe *et al.* [46]. The pseudogap temperature, T^* (green stars), is taken from Cyr-Choinière *et al.* [17]. The critical doping p^* where the pseudogap phase ends at $T = 0$ is $p^* \sim 0.18$ [17].

[16,20,21,23]. We see that p^* is distinctly below the $T = 0$ structural transition at $p_{\text{LTT}} = 0.255 \pm 0.005$. This means that one can investigate the effect of the pseudogap phase *within the same structural phase* by comparing Nd-LSCO samples with $p = 0.24$ or $p = 0.25$ on the one hand, to samples with $p = 0.22$ or lower, on the other hand.

The corresponding phase diagram for the $\text{La}_{2-x}\text{Sr}_x\text{CuO}_4$ is shown for comparison in Fig. 15. This plot uses earlier data from Yamada *et al.* [42], and again overplots the line of T^* vs x transitions to the pseudogap phase [17]. A striking feature of this plot is that T^* vs x is very similar between $\text{La}_{1.6-x}\text{Nd}_{0.4}\text{Sr}_x\text{CuO}_4$ and $\text{La}_{2-x}\text{Sr}_x\text{CuO}_4$ for $x \leq 0.15$, but then drops more precipitously to 0 at $p^* \sim 0.18$ in $\text{La}_{2-x}\text{Sr}_x\text{CuO}_4$.

The fact that $p^*(\text{LSCO}) < p^*(\text{Nd-LSCO})$ also correlates with the lower p occurrence of the HTT phase at $T = 0$ in LSCO compared to Nd-LSCO, as well as the lower p occurrence of the van Hove singularity point (p^*vHs) in LSCO, which may have some impact on the physics of the pseudogap [43,44].

IV. CONCLUSIONS

A comprehensive series of $\text{La}_{1.6-x}\text{Nd}_{0.4}\text{Sr}_x\text{CuO}_4$ samples, both polycrystalline and single crystals, has been synthesized with x spanning from 0.01 to 0.40, and their structural properties and superconducting T_C s have been investigated by a variety of experimental techniques including x-ray powder and single-crystal diffraction, neutron powder diffraction, neutron elastic scattering, as well as by magnetic susceptibility and resistivity measurements. These measurements and their analyses have allowed us to map the structural and superconducting phase transitions that take place as a function of temperature and Sr concentration, x , or hole doping, p , and to propose an updated temperature-doping phase diagram for Nd-LSCO, presented in Fig. 14, which now covers both

underdoped ($x < 0.15$) and overdoped ($x > 0.25$) regions. This work allows us to compare the phase transitions displayed by large single crystals of Nd-LSCO to those from the literature on both single-crystal and polycrystalline samples, and excellent consistency is seen. We conclude that the stoichiometry of our single crystals is well understood. We find that the critical doping for the end of the LTT structural phase at $T = 0$ is $p_{\text{LTT}} = 0.255 \pm 0.005$, above which doping the material appears only in the HTT phase. This means that the onset of the pseudogap phase, at $p^* = 0.23 \pm 0.005$ [16,21], occurs well within the LTT structural phase ($p^* < p_{\text{LTT}}$). In other words, the structural and pseudogap critical points are well separated in Nd-LSCO, as they are in LSCO (Fig. 15), where $p_{\text{LTO}} = 0.215 \pm 0.005$ [42].

ACKNOWLEDGMENTS

We wish to thank Jianshi Zhou and Zongyao Li for valuable insights into the crystal growth of Nd-LSCO, as well as Graeme M. Luke and John E. Greedan for discussions and other helpful contributions. This work was supported by the Natural Sciences and Engineering Research Council of Canada and by the Slovenian Research Agency (research programme P2-0105). B.D.G. and L.T. acknowledge support from the Canadian Institute for Advanced Research (CIFAR) as Fellows and from the Canada Foundation for Innovation (CFI). L.T. acknowledges support from the Fonds de recherche du Québec – Nature et Technologies (FRQNT), and the Canada Research Chair program. We are grateful for the instrument and sample environment support provided during our neutron-scattering measurements at the Spallation Neutron Source at Oak Ridge National Laboratory. This part of the research was sponsored by the U.S. Department of Energy, Office of the Basic Energy Sciences, Scientific User Facilities Division.

-
- [1] J. G. Bednorz and K. A. Müller, *Z. Phys. B: Condens. Matter* **64**, 189 (1986).
 - [2] J. L. Tallon, R. G. Buckley, P. W. Gilbert, M. R. Presland, I. W. Brown, M. E. Bowden, L. A. Christian, and R. Goguel, *Nature (London)* **333**, 153 (1988).
 - [3] M. Azuma, Z. Hiroi, M. Takano, Y. Bando, and Y. Takeda, *Nature (London)* **356**, 775 (1992).
 - [4] S. A. Sunshine, T. Siegrist, L. F. Schneemeyer, D. W. Murphy, R. J. Cava, B. Batlogg, R. B. van Dover, R. M. Fleming, S. H. Glarum, S. Nakahara *et al.*, *Phys. Rev. B* **38**, 893(R) (1988).
 - [5] J. D. Jorgensen, H. Shaked, D. G. Hinks, B. Dabrowski, B. W. Veal, A. P. Paulikas, L. J. Nowicki, G. W. Crabtree, W. K. Kwok, and L. H. Nunez, *Physica C* **153**, 578 (1988).
 - [6] J. P. Castellan, B. D. Gaulin, H. A. Dabkowska, A. Nabialek, G. Gu, X. Liu, and Z. Islam, *Phys. Rev. B* **73**, 174505 (2006).
 - [7] V. B. Grande, H. Müller-Buschbaum, and M. Schweizer, *Z. Anorg. Allg. Chem.* **428**, 120 (1977).
 - [8] Y. Maeno, M. Nohara, F. Nakamura, T. Suzuki, and T. Fujita, *J. Supercond.* **7**, 39 (1994).
 - [9] J. D. Axe and M. K. Crawford, *J. Low Temp. Phys.* **95**, 271 (1994).
 - [10] M. A. Kastner, R. J. Birgeneau, G. Shirane, and Y. Endoh, *Rev. Mod. Phys.* **70**, 897 (1998).
 - [11] J. M. Tranquada, AIP Conf. Proc. **1550**, 114 (2013).
 - [12] Q. Ma, K. C. Rule, Z. W. Cronkwright, M. Dragomir, G. Mitchell, E. M. Smith *et al.*, [arXiv:2009.04627](https://arxiv.org/abs/2009.04627).
 - [13] M. R. Norman, D. Pines, and C. Kallin, *Adv. Phys.* **54**, 715 (2005).
 - [14] C. Proust and L. Taillefer, *Annu. Rev. Condens. Matter Phys.* **10**, 409 (2019).
 - [15] C. E. Matt, C. G. Fatuzzo, Y. Sassa, M. Månsson, S. Fatale, V. Bitetta, X. Shi, S. Pailhès, M. H. Berntsen, T. Kurosawa *et al.*, *Phys. Rev. B* **92**, 134524 (2015).
 - [16] B. Michon, C. Girod, S. Badoux, J. Kačmarčík, Q. Ma, M. Dragomir *et al.*, *Nature (London)* **567**, 218 (2019).
 - [17] O. Cyr-Choinière, R. Daou, F. Laliberté, C. Collignon, S. Badoux, D. LeBoeuf, J. Chang, B. J. Ramshaw, D. A. Bonn, W. N. Hardy *et al.*, *Phys. Rev. B* **97**, 064502 (2018).

- [18] T. Shibauchi, A. Carrington, and Y. Matsuda, *Annu. Rev. Condens. Matter Phys.* **5**, 113 (2014).
- [19] H. V. Löhneysen, T. Pietrus, G. Portisch, H. G. Schlager, A. Schröder, M. Sieck, and T. Trappmann, *Phys. Rev. Lett.* **72**, 3262 (1994).
- [20] R. Daou, N. Doiron-Leyraud, D. LeBoeuf, S. Y. Li, F. Laliberté, O. Cyr-Choinière *et al.*, *Nat. Phys.* **5**, 31 (2009).
- [21] C. Collignon, S. Badoux, S. A. A. Afshar, B. Michon, F. Laliberté, O. Cyr-Choinière *et al.*, *Phys. Rev. B* **95**, 224517 (2017).
- [22] S. Badoux, W. Tabis, F. Laliberté, G. Grissonnanche, B. Vignolle, D. Vignolles *et al.*, *Nature (London)* **531**, 210 (2016).
- [23] B. Michon, A. Ataei, P. Bourgeois-Hope, C. Collignon, S. Y. Li, S. Badoux *et al.*, *Phys. Rev. X* **8**, 041010 (2018).
- [24] G. Grissonnanche, A. Legros, S. Badoux, E. Lefrançois, V. Zatzko, M. Lizaire *et al.*, *Nature (London)* **571**, 376 (2019).
- [25] Y. Fang, G. Grissonnanche, A. Legros, S. Verret, F. Laliberté, C. Collignon *et al.*, [arXiv:2004.01725](https://arxiv.org/abs/2004.01725).
- [26] B. Büchner, M. Braden, M. Cramm, W. Schlabitz, W. Schnelle, O. Hoffels, W. Braunisch, R. Müller, G. Heger, and D. Wohlleben, *Physica C* **188**, 903 (1991).
- [27] M. K. Crawford, R. L. Harlow, E. M. McCarron, W. E. Farneth, J. D. Axe, H. Chou, and Q. Huang, *Phys. Rev. B* **44**, 7749 (1991).
- [28] S. Shamoto, T. Kiyokura, M. Sato, K. Kakurai, Y. Nakamura, and S. Uchida, *Physica C* **203**, 7 (1992).
- [29] M. K. Crawford, R. L. Harlow, S. Deemyad, V. Tissen, J. S. Schilling, E. M. McCarron *et al.*, *Phys. Rev. B* **71**, 104513 (2005).
- [30] I. K. Drozdov, I. Pletikosić, C.-K. Kim, K. Fujita, G. D. Gu, J. C. Séamus Davis, P. D. Johnson, I. Božović, and T. Valla, *Nat. Commun.* **9**, 5210 (2018).
- [31] G. C. Che, J. K. Liang, W. Chen, S. S. Xie, Y. Yu, H. Li, Q. S. Yang, Y. M. Ni, G. R. Liu, and G. H. Chen, *Sci. Sin., Ser. A (Engl. Ed.)* **31**, 1079 (1988).
- [32] A. Huq, M. J. Kirkham, P. F. Peterson, J. P. Hodges, P. Whitfield, K. Page, T. Huegle, E. B. Iverson, A. Parizzi, and G. Q. Rennich, *J. Appl. Crystallogr.* **52**, 1189 (2013).
- [33] B. H. Toby and R. B. Von Dreele, *J. Appl. Crystallogr.* **46**, 544 (2013).
- [34] G. E. Granroth, A. I. Kolesnikov, T. E. Sherline, J. P. Clancy, K. A. Ross, J. P. C. Ruff, B. D. Gaulin, and S. E. Nagler, *J. Phys.: Conf. Ser.* **251**, 012058 (2010).
- [35] O. Arnold, J. C. Bilheux, J. M. Borreguero, A. Buts, S. I. Campbell, L. Chapon *et al.*, *Nucl. Instrum. Methods Phys. Res., Sect. A* **764**, 156 (2014).
- [36] J. M. Tranquada, B. J. Sternlieb, J. D. Axe, Y. Nakamura, and S. Uchida, *Nature (London)* **375**, 561 (1995).
- [37] S. Katano, J. A. Fernandez-Baca, S. Funahashi, N. Môri, Y. Ueda, and K. Koga, *Physica C* **214**, 64 (1993).
- [38] J. M. Tranquada, J. D. Axe, N. Ichikawa, A. R. Moodenbaugh, Y. Nakamura, and S. Uchida, *Phys. Rev. Lett.* **78**, 338 (1997).
- [39] B. Lorenz, Z. G. Li, T. Honma, and P.-H. Hor, *Phys. Rev. B* **65**, 144522 (2002).
- [40] Y. S. Lee, F. C. Chou, A. Tewary, M. A. Kastner, S. H. Lee, and R. J. Birgeneau, *Phys. Rev. B* **69**, 020502(R) (2004).
- [41] B. O. Wells, Y. S. Lee, M. A. Kastner, R. J. Christianson, R. J. Birgeneau, K. Yamada, Y. Endoh, and G. Shirane, *Science* **277**, 1067 (1997).
- [42] K. Yamada, C. H. Lee, K. Kurahashi, J. Wada, S. Wakimoto, S. Ueki *et al.*, *Phys. Rev. B* **57**, 6165 (1998).
- [43] N. Doiron-Leyraud, O. Cyr-Choinière, S. Badoux, A. Ataei, C. Collignon, A. Gourgout *et al.*, *Nat. Commun.* **8**, 2044 (2017).
- [44] S. Benhabib, A. Sacuto, M. Civelli, I. Paul, M. Cazayous *et al.*, *Phys. Rev. Lett.* **114**, 147001 (2015).
- [45] H. Takagi, R. J. Cava, M. Marezio, B. Batlogg, J. J. Krajewski, W. F. Peck Jr., P. Bordet, and D. E. Cox, *Phys. Rev. Lett.* **68**, 3777 (1992).
- [46] O. J. Lipscombe, S. M. Hayden, B. Vignolle, D. F. McMorrow, and T. G. Perring, *Phys. Rev. Lett.* **99**, 067002 (2007).

Chapter 5

Static Parallel Spin Stripe Order in Optimal and Overdoped Nd-LSCO

5.1 Preface

This chapter discusses the evolution of static parallel spin stripe order from the optimal to the overdoped region of the Nd-LSCO phase diagram. Following the successful crystal growth of Nd-LSCO crystals described in Chapter 4, three high quality Nd-LSCO single crystals with $x = 0.19, 0.24$ and 0.26 were chosen as good candidates for neutron scattering experiments. This was done primarily on the basis of their single crystallinity and the relatively large volume of the crystals. Their single crystal nature and Sr concentration were carefully characterized using the methods described in Chapter 4 [29]. Two triple-axis neutron scattering experiments were conducted on these samples using the TAIPAN instrument at the Australian Nuclear Science and Technology (ANSTO) and one using the HB3 triple axis spectrometer at Oak Ridge National Laboratory (ORNL) respectively. Both experiments employed similar instrumental set ups, with an incident neutron energy of 14.7 meV, and horizontal beam collimation of open-40'-40'-open for TAIPAN and 48'-40'-40'-120' for HB3. The single crystals were loaded in pumped ^4He cryostats with a base temperature of 1.5 K for both experiments.

The undoped parent compound La_2CuO_4 is a Mott insulator with three dimensional antiferromagnetic order below ~ 300 K. Sr doping quickly destroys the 3D AF order and replaces it by 2D incommensurate spin stripe order with much lower transition temperatures[62–66]. There are two types of incommensurate magnetic stripe order in the LSCO system following the destruction of 3D AF phase. They are known as parallel and diagonal spin stripe orders.

We begin by discussing diagonal spin stripe order as this is the incommensurate order displayed at relatively low Sr doping, $x \leq 0.06$, before the parallel spin stripe structure appears. Wakimoto *et al* famously first observed diagonal spin stripe order in $\text{La}_{2-x}\text{Sr}_x\text{CuO}_4$, $x = 0.05$ [67]. Fig. 5.1 shows the TAS data collected on the SPINS cold neutron triple axis spectrometer at NIST [67]. Fig 5.1 panel a) and b) shows the scans in reciprocal space when the sample is mounted in the HHL scattering plane. A single elastic commensurate peak can be observed in the insulating LSCO samples at $x = 0.03$ and 0.04 likely indicating diagonal stripe order with a small incommensurate ordering wavevector co-existing with antiferromagnetic order at these Sr dopings. However, the peak profile dramatically changes at $x = 0.05$ where clear incommensurate peaks were observed. This arrangement of the incommensurate peaks are referred to as diagonal stripe order demonstrated in Fig.5.1. For LSCO, superconductivity also onsets at $x \sim 0.06$ accompanied by a 45° rotation of the incommensurate peaks around the (π, π) position to the so-called parallel spin stripe pattern. This shows that parallel spin stripe order may have a more intimate relationship with superconductivity, as both ordered states onset at approximately the same hole-doping. The present chapter particularly focuses on parallel spin stripe order at $x = 0.19, 0.24, 0.26$ in Nd-LSCO single crystal using triple-axis neutron spectroscopy.

The pseudogap phase has figured prominently in the discussion of the phase diagram for cuprate systems. The pseudogap phase has been studied by resistivity, thermodynamic and ARPES measurements in Nd-LSCO[41, 68]. It is best studied in the underdoped region of cuprate superconductors [14, 15, 30, 67]. However, due to the difficulty in obtaining large and high quality single crystals, little is known about static parallel spin stripe order and its relationship with the pseudogap phase and with superconductivity at higher doping. A commonly held view

is that the pseudogap quantum critical point p^* also marks the end of the regime where well defined spin and charge stripes exist - but many fewer neutron scattering studies exist for hole doping levels that correspond to p^* and higher doping. For example, in Nd-LSCO, prior neutron scattering studies investigating parallel spin stripe order was only able to measure up to $x = 0.20$, and that relatively low intensity measurement was interpreted in terms of an onset to parallel spin stripe order at ~ 20 K [12]. However, this chapter shows new neutron scattering data clearly indicating that the static parallel spin stripe exists beyond p^* , and extends until the end of the superconducting dome at $x = 0.26$ in Nd-LSCO. We also provide analysis that compares our measured square of the sublattice magnetization at 1.5 K and 5 K with pre-existing data from Ref.[12] normalized on the same scale. The analysis reveals a significantly diminished intensity in the strength of the elastic incommensurate scattering for $x=0.24$ and 0.26 compared with the $x = 0.125$ measured by Tranquada *et al* [12]. Additionally, the peak width of the elastic incommensurate peaks measured by scanning the h and k direction in reciprocal space, presented in the form of Half Width at Half Max(HWHM), increases systematically among all measured samples. We show that the incommensurate elastic peak broadens $\sim 50\%$ in $x = 0.26$ sample when compared to that in $x = 0.125$ Nd-LSCO sample. We argue that the diminished intensity, combined with the broadening of the peak, made it a challenge to even observe, let alone to characterize the nature of parallel static spin stripes in optimally and overdoped Nd-LSCO ~ 20 years ago. Therefore our data presented in this chapter provides an updated picture with new insights into the parallel spin stripe order at these relatively high hole doping levels in Nd-LSCO.

One interest question raised by the new neutron data presented in current chapter below, is how it compares with other measurements on other 214 cuprates using complementary techniques such as NMR. A recent NMR study on LSCO up to $x=0.19$ in a magnetic field found indications of strong antiferromagnetism persisting up $x = 0.19$. Although this study does not directly suggest magnetic order exists beyond p^* in LSCO, it does provide evidence for static magnetism at hole doping levels that are higher than previously believed limit [69]. In making these comparisons, it is however important to consider that these different techniques

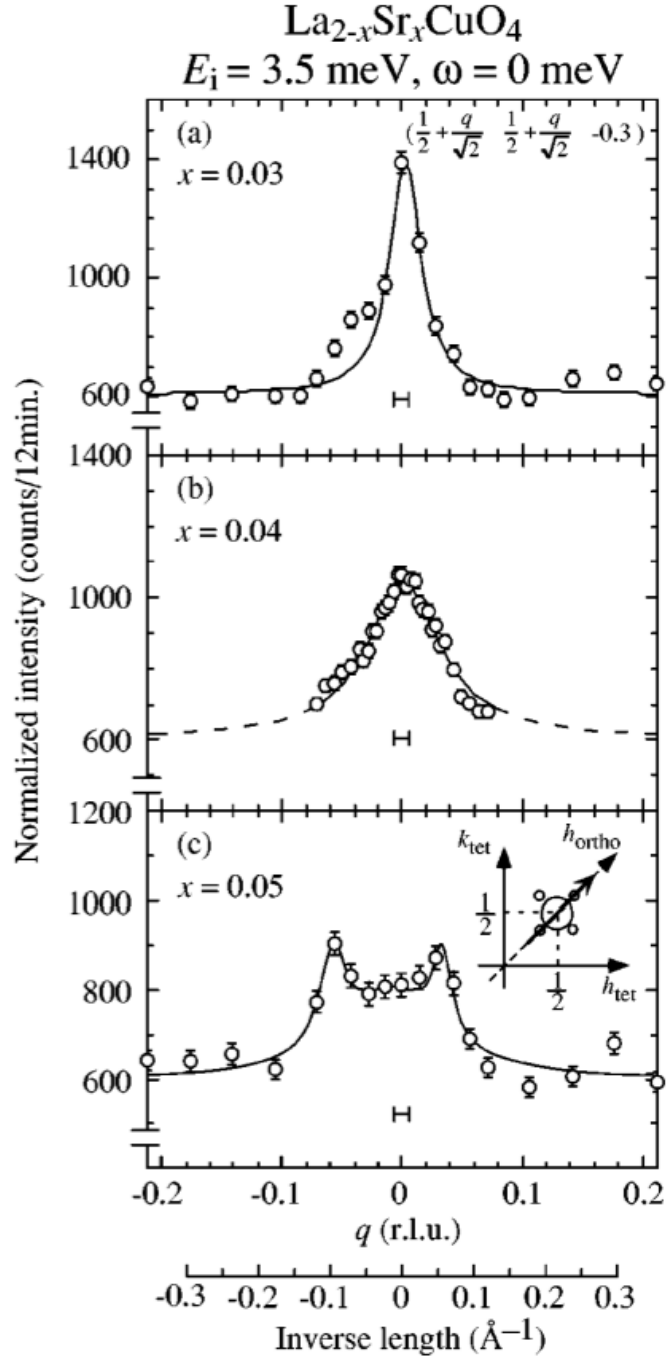


FIGURE 5.1: Elastic peak measured around $(1/2, 1/2, -0.3)$ at $T = 2\text{K}$. The panel a) and b) shows a single peak at $q=0$ but in panel c) the $x = 0.05$ LSCO sample displays two incommensurate peaks "diagonal" to the $(1/2, 1/2)$ position. The inset of panel c) shows the direction of the scans in reciprocal space. Reproduced from [67] with permission.

measure magnetism on different time scales. That associated with NMR is relatively slow, on a time scale of 10^{-6} seconds. Neutron scattering typically measure spin correlations on a maximum time scale of 10^{-10} seconds. Therefore spin fluctuations could appear static to a neutron scattering experiment but dynamic to NMR measurements.

Our new observations of static parallel spin stripe order in the $x=0.24$ and 0.26 Nd-LSCO samples seems to clearly decouple parallel spin stripes from p^* . This leads to another important question - what role does the 2D antiferromagnetism play on superconductivity in Nd-LSCO in the light of this new data? The measured order parameter of the incommensurate spin stripe peaks in our \sim optimally doped $x = 0.19$ sample reveals a plateau in the order parameter with an inflection point in intensity at superconducting T_C . A related effect was observed long time ago in other correlated electron superconductors, UPt₃ [70, 71]

To conclude our results for this chapter, parallel spin stripe order appears to envelope superconducting ground states in Nd-LSCO, while this incommensurate magnetism is not strongly correlated with the pseudogap quantum critical point at p^* . By synthesizing the data from our new neutron scattering experiments with pre-existing data, we propose a new phase diagram for Nd-LSCO in which the parallel spin stripe order envelopes the entirety of the superconducting dome thus making static parallel spin stripe a precursor for superconductivity. We refer readers to the remaining of this chapter for detailed analysis and discussions.

My role in this project was to grow the large single crystal samples required for the neutron scattering studies, to collect and analyzing the experimental data, to facilitating the logistics of collaborations between different groups who took part in the collaboration, and assisting to write the manuscript. Three triple axis neutron experiments and a series of time-of-flight neutron scattering experiments were conducted at ORNL and ANSTO. We thank the valuable contribution of Kirrily C. Rule, Songxue Chi, Alexander I. Kolesnikov, Matthew B. Stone as local scientists. We also appreciate the help within the group from Zachary W. Cronkwright, Evan M. Smith during the experiment. Bruce D. Gaulin, as supervisor, contributed in discussion and writing of the manuscript. Bruce D. Gaulin also conceived and oversaw the entire project.

Parallel spin stripes and their coexistence with superconducting ground states at optimal and high doping in $\text{La}_{1.6-x}\text{Nd}_{0.4}\text{Sr}_x\text{CuO}_4$

Qianli Ma^{1,*}, Kirrily C. Rule², Zachary W. Cronkwright,¹ Mirela Dragomir^{3,4}, Gabrielle Mitchell,¹ Evan M. Smith¹, Songxue Chi,⁵ Alexander I. Kolesnikov⁵, Matthew B. Stone⁵ and Bruce D. Gaulin^{1,4,6}

¹*Department of Physics and Astronomy, McMaster University, Hamilton, Ontario, Canada L8S 4M1*

²*Australian Nuclear Science and Technology Organisation, Locked Bag 2001, Kirrawee DC, New South Wales 2232, Australia*

³*Department of Chemistry and Chemical Biology, McMaster University, Hamilton, Ontario, Canada, L8S 4M1*

⁴*Brockhouse Institute for Materials Research, Hamilton, Ontario, Canada L8S 4M1*

⁵*Neutron Scattering Division, Oak Ridge National Laboratory, Oak Ridge, Tennessee 37830, USA*

⁶*Canadian Institute for Advanced Research, MaRS Centre, West Tower, 661 University Avenue, Suite 505, Toronto, Ontario, Canada M5G 1M1*



(Received 2 September 2020; revised 12 March 2021; accepted 29 April 2021; published 27 May 2021)

Three-dimensional, commensurate long-range magnetic order in La_2CuO_4 quickly evolves to quasi-two-dimensional, incommensurate correlations upon doping with mobile holes, and superconductivity follows for x as small as 0.05 in the $\text{La}_{2-x}\text{Sr}_x/\text{Ba}_x\text{CuO}_4$ family of superconductors. The onset of superconductivity in these systems is known to be coincident with a remarkable rotation of the incommensurate spin order from “diagonal stripes” below $x = 0.05$ to “parallel stripes” above. However, little is known about the spin correlations at optimal and high doping levels, around and beyond the proposed quantum critical point for the pseudogap phase, p^* . Here, we present elastic and inelastic neutron scattering measurements on single crystals of $\text{La}_{1.6-x}\text{Nd}_{0.4}\text{Sr}_x\text{CuO}_4$ with $x = 0.125, 0.19, 0.24,$ and 0.26 and show that two-dimensional, quasistatic, parallel spin stripes have an onset at temperatures such that the parallel spin stripe phase extends beyond p^* and envelops the entirety of superconducting ground states in this system. We also show that the elastic order parameter for parallel spin stripes at optimum doping, $x = 0.19$, displays an inflection point at superconducting T_c , while the low-energy dynamic spectral weight of parallel stripe fluctuations grows with decreasing temperature and saturates below T_c .

DOI: [10.1103/PhysRevResearch.3.023151](https://doi.org/10.1103/PhysRevResearch.3.023151)

I. INTRODUCTION

The microscopic mechanism underlying high-temperature superconductivity in copper oxide materials has been hotly debated since its original discovery in 1986 [1,2], through to the present day [3–16]. The magnetism associated with an approximately two dimensional square lattice of CuO_2 has figured prominently in this debate, both as a mechanism for superconducting pairing between electrons [10,12,14,17] and as a possible competing ground state [18,19].

Hole-doped high- T_c cuprates, such as $\text{La}_{2-x}\text{Sr}_x\text{CuO}_4$ (LSCO), $\text{La}_{2-x}\text{Ba}_x\text{CuO}_4$ (LBCO), and $\text{La}_{1.6-x}\text{Nd}_{0.4}\text{Sr}_x\text{CuO}_4$ (Nd-LSCO), are in some ways the ultimate quantum materials [20]. They display bulk superconductivity, and their parent compound, La_2CuO_4 , is a stacked, two-dimensional quantum magnetic insulator, based on $S = 1/2$ Cu^{2+} spin degrees of freedom. La_2CuO_4 orders near 300 K into a three-dimensional (3D) commensurate (C) antiferromagnetic (AF)

structure [21,22]. However, this 3D C AF order is very unstable in the presence of mobile holes, such as are introduced either by substitution of Sr^{2+} for La^{3+} in LSCO and Nd-LSCO or by substitution of Ba^{2+} for La^{3+} in LBCO. The 3D C AF order is destroyed by $x \sim 0.02$, replaced by quasi-2D incommensurate (IC) order with much lower onset temperatures [21,21–25].

At low dopings, for $x < 0.05$, the quasi-2D IC structure corresponds to “diagonal stripes” wherein local regions of π - π antiferromagnetism are partitioned into domains which are finite along $(1, 1, 0)_{\text{tetragonal}}$ directions, which is at an angle of 45° to the Cu-O bonds within the 2D plane [22,26]. These domains are separated by domain walls running along these diagonal directions, where the excess holes reside. The domain walls introduce a π phase shift into the AF structure, thereby giving rise to IC antiferromagnetism. While such magnetic structures do not display true long-range order, they do possess in-plane correlation lengths over tens of unit cells and are quasistatic, such that Bragg-peak-like features, well defined in \mathbf{Q} and elastic on the time scale of neutron scattering ($\sim 10^{-10}$ s), are easily observed.

Wakimoto *et al.* made the remarkable observation in LSCO that the 2D IC AF structure rotates by 45° at $x = 0.05$ [27], exactly where superconducting ground states are first observed as a function of x . The same rotation [28] of the spin stripe structure was later observed in LBCO at the same

*maq1@mcmaster.ca

Published by the American Physical Society under the terms of the [Creative Commons Attribution 4.0 International license](https://creativecommons.org/licenses/by/4.0/). Further distribution of this work must maintain attribution to the author(s) and the published article’s title, journal citation, and DOI.

doping level, x , indicating that such a rotation of the 2D IC AF structure is a general feature of these single-layer cuprate systems. The rotated stripes are referred to as “parallel” spin stripes, as the hole-bearing domain walls are oriented along (100)_{tetragonal} directions, along Cu-O bonds [29].

On increasing the hole doping, the IC wave vector associated with the spin stripe structure increases $\propto x$, following what is known as the Yamada relation [30]. This has the physical interpretation that the quasi-1D hole-bearing domain walls get closer together to allow for an increased hole density. The onset temperature of this 2D IC AF order also rises strongly to a maximum near $x = 0.125$ [31,32]. However, what happens at dopings beyond $x = 0.125$ is less clear. This is the case for at least two reasons: First, the large single crystals necessary for definitive neutron scattering experiments are progressively more difficult to grow with increasing x . Second, the 2D magnetic signal becomes progressively weaker and spread out in Q , due to smaller ordered moments and shorter correlation lengths associated with the increased hole density.

This paper focuses on neutron scattering studies of the Nd-LSCO system. Muon-spin rotation (μ SR) and nuclear magnetic resonance (NMR) techniques are sensitive to local magnetism on time scales much longer than those of neutron scattering ($\sim 10^{-8}$ s for μ SR and $\sim 10^{-6}$ s for NMR), and such studies have also been carried out on Nd-LSCO and other single-layer, hole-doped cuprates [33–35]. While the energy scale for typical neutron diffraction (~ 1 meV) implies a time scale which is dynamic compared with both μ SR and NMR, this elastic energy scale remains $\sim \frac{1}{2}\%$ or less of the full spin excitation bandwidth of these systems. We henceforth refer to the corresponding magnetism elucidated by neutron scattering as static or quasistatic, but this proviso should be kept in mind, especially when comparing between different techniques.

Nd-LSCO has played a special role within this field, as Nd-LSCO $x = 0.125$ was the first cuprate in which *both* parallel static spin stripe order and charge stripe order were observed [36]. Charge stripe order, with an incommensurate ordering wave vector twice that of the spin stripe order, is a natural consequence of the stripe picture, as it is the charge stripes that introduce a π phase shift into the local π - π antiferromagnetism. At the $x = 0.125$ doping level, superconductivity is suppressed in Nd-LSCO to very low temperatures, with $T_c \sim 3$ K [37,38]. This phenomenon is known as the “ $\frac{1}{8}$ anomaly.” Nd-LSCO is also of interest as its maximum superconducting T_c is relatively low, ~ 15 K [39], compared with either LSCO, ~ 40 K [40], or LBCO, ~ 35 K [32]. This makes it easier to quench superconductivity with practical magnetic field strengths in Nd-LSCO and to thereby explore the normal state properties at doping levels that would give rise to superconductivity at zero field.

Such a deep suppression in superconducting T_c also occurs in LBCO, and coexisting static, parallel spin and charge stripes were later observed in this system around $x = 0.125$, with static, parallel spin stripes observed to $x \sim 0.135$ [32]. In contrast, LSCO displays a much milder suppression of T_c at $x = 0.125$. Both static parallel spin stripes and parallel charge stripes have been observed in LSCO, with static spin stripes observed to $x = 0.15$ [41] and parallel charge stripes observed in the vicinity of $x = 0.125$ [42]. A very recent study suggests

that charge-density waves (CDWs) can be observed at doping levels as high as $x = 0.21$ [43]. The combination of the relatively high onset temperature for charge stripes and an only modestly suppressed superconducting T_c at the $\frac{1}{8}$ anomaly in LSCO has allowed the interaction between parallel charge stripes and superconductivity to be well studied. The x-ray scattering intensity associated with the parallel charge stripes in LSCO around $x = 0.125$ clearly diminishes on entering the superconducting state, providing compelling evidence for competition between superconductivity and charge stripes [42].

This body of work shows clearly that, while $x = 0.05$ is a well-defined minimum doping level for the appearance of static, parallel spin stripes in each of Nd-LSCO, LBCO, and LSCO, the extent of this parallel spin stripe phase and how it ends is much less clear. Various phase diagrams for single-layer, hole-doped cuprates show the *static*, parallel spin stripe phase to fade away by $x \sim 0.135$ for LBCO [32] and $x \sim 0.15$ for Nd-LSCO, with more limited data to $x \sim 0.2$ [37].

In this paper, we present elastic and inelastic neutron scattering measurements on four single crystals of Nd-LSCO with $x = 0.125, 0.19, 0.24,$ and 0.26 . The $x = 0.26$ doping level is close to the end of superconductivity in Nd-LSCO [44], while the $x = 0.24$ sample is close to the proposed quantum critical point, $p^* = 0.23 \pm 0.005$, associated with the pseudogap phase in Nd-LSCO [45]. These measurements show well-defined, but non-resolution-limited magnetic Bragg peaks to appear at low temperatures in all of these samples, significantly extending the range of concentrations over which static, parallel spin stripes have been observed in Nd-LSCO and challenging the notion that static magnetism ends at or before p^* [39]. We report that the effective Cu ordered moment within the spin stripe structure at low temperatures drops off monotonically and steeply from $x = 0.125$ to higher dopings, with a concomitant decrease in the in-plane correlation length. This provides a reasonable explanation for why this signal has been so difficult to observe until now. On the basis of these measurements we propose a phase diagram for parallel spin stripes in Nd-LSCO that uncouples the connection between static magnetism and the pseudogap phase. Instead we show that the static magnetic order spans the entirety of the superconducting dome, $0.05 \leq x \leq 0.26$. Consequently, the superconducting state at any x in Nd-LSCO is entered from a state with extensive static, parallel spin stripe order. We conclude that this parallel spin stripe state, in contrast with the parallel charge stripe state, does not compete with superconductivity in Nd-LSCO, but is a prerequisite for it.

II. METHODS

Crystal growth. High-quality single crystals of Nd-LSCO with $x = 0.125, 0.19, 0.24,$ and 0.26 were grown using the traveling solvent floating zone technique at McMaster University with each resulting single-crystal sample weighing between 3.5 and 5 g. The single crystals were produced using a four-mirror Crystal Systems halogen lamp image furnace at approximate growth speeds of 0.68 mm/h, and growths lasting for approximately 1 week each. The Sr concentration of each single crystal was determined by careful correlation of the structural phase transition temperatures with preexisting

phase diagrams, as described in Ref. [44]. Further details regarding the material preparation and single-crystal growth of these samples, as well as determination of their stoichiometry, are reported in Ref. [44]. The Nd-LSCO sample with $x = 0.19$ was composed of two coaligned single crystals. All single crystals were scanned using a backscattering Laue instrument to assess their single-crystal nature. Neutron diffraction measurements showed mosaic spreads of less than 0.5° in all crystals, attesting to their high-quality, single crystallinity.

Triple-axis neutron scattering experiment. Nd-LSCO single crystals with $x = 0.19, 0.26$ were studied using the triple-axis neutron spectrometer (TAS) Taipan at the Australian Centre for Neutron Scattering (ACNS), Australian Nuclear Science and Technology Organisation (ANSTO), while the TAS experiment for the $x = 0.24$ sample was conducted using the HB3 TAS instrument at the High Flux Isotope Reactor (HFIR) at Oak Ridge National Laboratory. Experiments using both Taipan and HB3 employed pyrolytic graphite monochromators, analyzers, and filters and employed the same fixed final neutron energies: $E_f = 14.7$ meV. Horizontal beam collimations of open-40'-40'-open for Taipan and 48'-40'-40'-120' for HB3 were used. The resulting energy resolution of the two sets of measurements was therefore similar, ~ 0.9 meV. For all TAS measurements the crystals were loaded in pumped ^4He cryostats with a base temperature of 1.5 K.

Time-of-flight neutron scattering experiment. Time-of-flight (TOF) neutron chopper spectrometer measurements were also carried out on the $x = 0.125, 0.19,$ and 0.24 single crystals using the direct geometry spectrometer SE-QUOIA at the Spallation Neutron Source, Oak Ridge National Laboratory [46]. These measurements were performed using $E_i = 60$ meV neutrons, which gave an energy resolution of ~ 1.2 meV at the elastic position. For all TOF measurements, the crystals were loaded in closed-cycle refrigerators with a base temperature of 5 K.

III. RESULTS

A. Elastic neutron scattering

Elastic neutron scattering scans of the form $(H, 1/2, 0)$ and $(1/2, K, 0)$ (using tetragonal notation where the a, b axes are ~ 3.76 Å at room temperature) were carried out for the Nd-LSCO single-crystal samples with $x = 0.19, 0.24,$ and 0.26 with a base temperature $T = 1.5$ K. These elastic scattering data are shown in Fig. 1. Four IC AF $(\frac{1}{2} \pm \delta, \frac{1}{2}, 0)$ and $(\frac{1}{2}, \frac{1}{2} \pm \delta, 0)$ quasi-Bragg peaks are observed, as expected for twinned orthorhombic structures. Schematic trajectories of these scans in reciprocal space are shown in the insets of Figs. 1(a) and 1(b). All the IC AF scattering is non-resolution-limited in Q space, which is why we refer to these sharp diffraction features as quasi-Bragg peaks.

These results show that static IC AF order exists at $T = 1.5$ K in all three single crystals: one at optimal doping and below p^* , and two above p^* . The intensity for the $x = 0.19$ sample is considerably stronger than that of $x = 0.24$ or $x = 0.26$, but the signals are otherwise qualitatively similar to each other. They are also qualitatively similar to earlier elastic neutron scattering results on an $x = 0.125$ sample by Tranquada

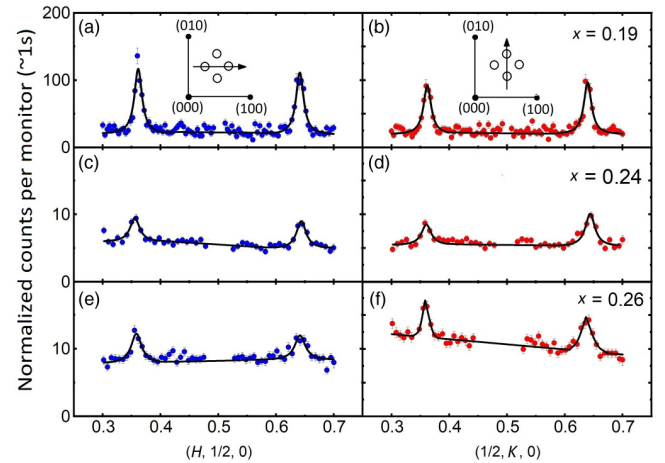


FIG. 1. Elastic TAS neutron scattering scans in reciprocal space for (a) and (b) $x = 0.19$, (c) and (d) $x = 0.24$, and (e) and (f) $x = 0.26$ single crystals of Nd-LSCO at $T = 1.5$ K. The IC peaks can be observed in all three samples at reciprocal space positions $(\frac{1}{2} \pm \delta, \frac{1}{2}, 0)$ and $(\frac{1}{2}, \frac{1}{2} \pm \delta, 0)$, $\delta \approx 0.14$. The insets in (a) and (b) illustrate the H and K scans employed in reciprocal space. The vertical axis displays neutron intensity, counts per monitor for approximately 1 s. The black lines going through the data points are fits to the data described by Eq. (1). Data have been normalized to $(1,1,0)$ Bragg peak intensities to account for differences in effective volume between the three samples.

and co-workers [36,37,47,48]. We therefore conclude that all Nd-LSCO single-crystal samples with $0.125 \leq x \leq 0.26$ display quasi-Bragg peaks at $T = 1.5$ K, which corresponds to IC AF order that is well defined in Q and static on the time scale of the neutron scattering measurements ($\sim 10^{-10}$ s).

The order parameters, or the temperature dependence of the Bragg intensities, were measured at the IC AF position $(0.5, 0.64, 0)$, which is $(\frac{1}{2}, \frac{1}{2} + \delta, 0)$ with $\delta = 0.14$, with careful thermal equilibration of the samples. These order parameter measurements were performed for the Nd-LSCO single crystals with $x = 0.19, 0.24,$ and 0.26 , as shown in Figs. 2(a)–2(c), respectively. All three samples display a pronounced upturn in their intensity below ~ 4 K, which is marked with a vertical fiducial in Fig. 2. Similar behavior was also observed in the corresponding order parameter measurement of Nd-LSCO with $x = 0.125$ by Tranquada *et al.* [37]. There, this upturn was successfully modeled as arising from the coupling between Cu^{2+} and Nd^{3+} moments and the onset of Nd^{3+} magnetic correlations at low temperatures.

This Cu^{2+} - Nd^{3+} coupling leads to the development of pronounced 3D correlations which peak at ordering wave vectors $(\frac{1}{2} \pm \delta, \frac{1}{2}, 0)$ and $(\frac{1}{2}, \frac{1}{2} \pm \delta, 0)$, which is with $L = 0$ [48]. At temperatures above ~ 4 K, the IC AF Bragg scattering takes on a progressively more 2D nature, with scattering extended along L in reciprocal space [48]. The 3D to 2D nature of the IC AF elastic scattering from low to high temperature has been previously discussed for Nd-LSCO with $x = 0.125$ in Ref. [48]. It has also been studied in other 214 cuprates such as LBCO in Ref. [49], for example, where time-of-flight neutron data differentiate between 3D IC antiferromagnetism

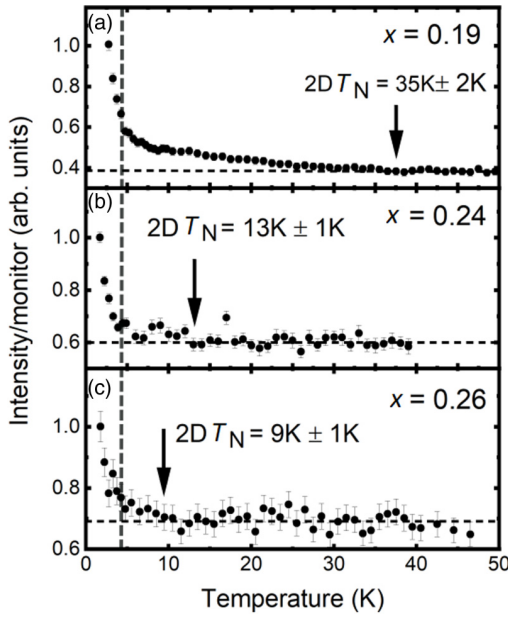


FIG. 2. Elastic temperature scans on one of the four IC AF peaks at $(0.5, 0.64, 0)$. The data were taken upon warming the samples from base temperature ~ 1.5 K up to 50, 40, and 46 K with careful equilibration for each of the $x = 0.19$, 0.24, and 0.26 samples, in (a), (b), and (c), respectively. The vertical dashed line indicates $T = 4$ K, below which a pronounced upturn in all intensities is observed, due to Nd^{3+} - Cu^{2+} coupling. Horizontal dashed lines mark the high-temperature background, and the arrows indicate where the 2D IC AF Bragg scattering signal departs from the background in each sample. The estimated $2D T_N$ for $x = 0.19$ is 35 ± 2 K (a), for $x = 0.24$ it is 13 ± 1 K (b), and for $x = 0.26$ it is 9 ± 1 K (c). The intensity at $T = 1.5$ K has been normalized to 1.

appearing as a Bragg “spot” and 2D magnetic scattering extending into rods of scattering perpendicular to the CuO_2 planes.

In addition, the Cu^{2+} - Nd^{3+} coupling induces a rotation of the $S = 1/2$ Cu^{2+} moments out of the basal plane, so as to be more parallel with the Nd^{3+} moments, which themselves are largely constrained to be along c due to crystal field effects. As c is perpendicular to the $(\frac{1}{2} \pm \delta, \frac{1}{2}, 0)$ and $(\frac{1}{2}, \frac{1}{2} \pm \delta, 0)$ ordering wave vectors, the intensity of the magnetic Bragg scattering also increases as a consequence of the Cu^{2+} moments being more perpendicular to \mathbf{Q} , which results in higher magnetic Bragg intensities due to the polarization dependence of the magnetic neutron scattering cross section.

As the concentration of Nd is the same across this Nd-LSCO series, the same phenomenology is expected at all x . As can be seen from Fig. 2, this is indeed the case with a pronounced factor of ~ 4 enhancement in the strength of the IC AF Bragg scattering at $(\frac{1}{2} \pm \delta, \frac{1}{2}, 0)$ and $(\frac{1}{2}, \frac{1}{2} \pm \delta, 0)$ from $T \sim 4$ K to $T \sim 1.5$ K for all x . Of course, such an enhancement would not occur in the absence of Nd; hence the identification of the IC AF Bragg scattering at low temperatures is considerably easier in Nd-LSCO, as compared with LBCO or LSCO, especially at high doping.

The order parameter measurements also allow us to estimate the onset of the 2D IC antiferromagnetism, $2D T_N$.

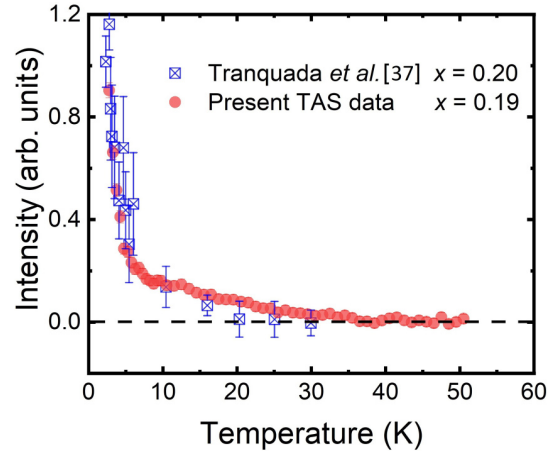


FIG. 3. Comparison of the present TAS data order parameter on the $x = 0.19$ sample and that reported earlier for an $x = 0.20$ sample [37]. The two elastic scattering data sets show very good agreement with each other. However, the present data on the $x = 0.19$ sample have much smaller error bars (smaller than the data points) and much higher temperature point density, aiding in a more accurate estimate of $2D T_N = 35 \pm 2$ K.

From earlier work by Tranquada *et al.* [37] on Nd-LSCO at $x = 0.125$ and 0.15, $2D T_N$ is known to peak at ~ 50 K for $x = 0.125$, where IC charge order is strongest, and the superconducting T_c is a local minimum, ~ 3 K. Our order parameter data in Fig. 2 show $2D T_N$ to correspond to where the 2D IC AF Bragg scattering departs from a high-temperature background. The background employed is $40 < T < 50$ K for $x = 0.19$, $23 < T < 40$ K for $x = 0.24$, and $20 < T < 46$ K for $x = 0.26$. This gives estimates for $2D T_N$ of 35 ± 2 K for $x = 0.19$; 13 ± 1 K for $x = 0.24$; and 9 ± 1 K for $x = 0.26$, as marked by the arrows in Figs. 2(a)–2(c), respectively.

The same earlier work by Tranquada *et al.* [37] on Nd-LSCO also measured the order parameter for an $x = 0.2$ sample, very close in composition to our $x = 0.19$ single crystal. Figure 3 shows these two data sets overlaid on each other, and the raw data are clearly consistent with each other. However, the error bars associated with the neutron intensity and the temperature point density associated with the $x = 0.19$ data are much improved over the preexisting $x = 0.2$ data, allowing us a better estimate of $2D T_N = 35 \pm 2$ K. The earlier estimate of $2D T_N \sim 20$ K had been employed to extrapolate the end of static magnetism in Nd-LSCO at p^* [15]. We employ the $2D T_N \sim 35 \pm 2$ K value for $x = 0.19$ in all subsequent discussions.

TOF elastic neutron scattering data, complementary to the TAS data shown in Fig. 1, are displayed within the $(H, K, -4 < L < 4)$ plane of reciprocal space, for $x = 0.125$, 0.19, and 0.24 single crystals in Fig. 4. The $x = 0.19$ and 0.24 single-crystal samples are the same single-crystal samples used for the TAS measurements in Fig. 1. All three data sets show a difference between $T = 5$ K data and those taken at a temperature equal to or above $2D T_N$ ($T = 60$ K for $x = 0.125$ and $T = 35$ K for each of $x = 0.19$ and 0.24). These data were extracted from four-dimensional (three \mathbf{Q} dimensions, as well as energy) data sets taken with the TOF chopper spectrometer

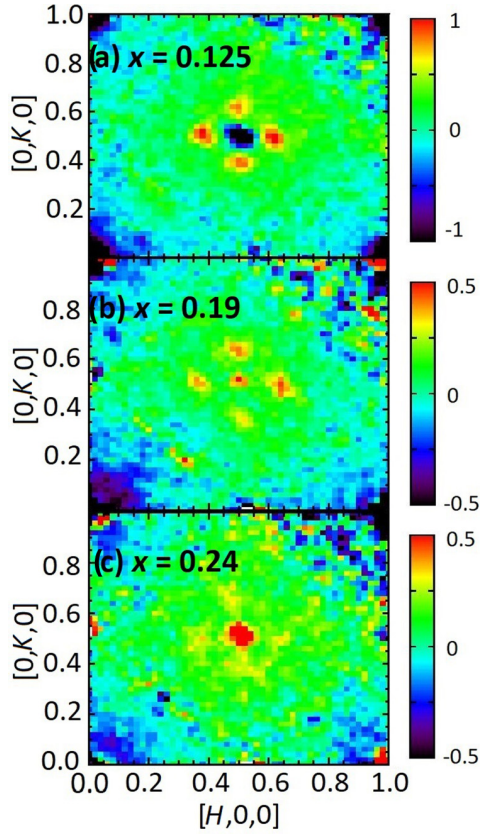


FIG. 4. Elastic time-of-flight (TOF) neutron data from Nd-LSCO with (a) $x = 0.125$, (b) $x = 0.19$, and (c) $x = 0.24$ in the $[H, K, -4 \leq L \leq 4]$ plane; that is with an integration in L from -4 to 4 reciprocal lattice unit (r.l.u.). These results show the subtraction of a high-temperature data set from a low-temperature data set, $5 \text{ K} - 60 \text{ K}$, $5 \text{ K} - 35 \text{ K}$, and $5 \text{ K} - 35 \text{ K}$, respectively. The IC AF magnetic peaks around $[1/2, 1/2, 0]$, arising from 2D parallel stripe order, are sharpest and most intense for $x = 0.125$ in (a) and gradually broaden and weaken with higher doping, 0.19 in (b) and 0.24 in (c). The data have been normalized to a combination of incoherent elastic scattering and that from crystal field excitations of Nd^{3+} for all samples.

SEQUOIA. The elastic scattering data are integrated in energy over the range $-2 < E < 2 \text{ meV}$, which encompasses the $\sim 1.2\text{-meV}$ energy resolution for SEQUOIA measurements employing $E_i = 60 \text{ meV}$. The integration over $-4 < L < 4$ is necessary to capture sufficient 2D IC AF Bragg intensity, which is extended along L at $T = 5 \text{ K}$ and concentrated at relatively low Q , due to the magnetic form factor of Cu^{2+} . Allowed nuclear Bragg peaks occur in these orthorhombic structures at wave vectors such as $(\frac{1}{2}, \frac{1}{2}, L = \pm 1, \pm 2, \pm 3)$, using tetragonal notation. Hence relatively strong nuclear intensity is observed at these positions. These structural zone centers also have low-energy acoustic phonons associated with them, whose intensity increases with increasing temperature, and which, while weak, can be picked up within the energy integration performed here. As a result, the temperature difference plots shown in Fig. 4 have relatively strong positive or negative intensity at the $(\frac{1}{2}, \frac{1}{2}, -4 < L < 4)$ position, due to the subtraction of two relatively large nuclear

intensities. This is an artifact of the subtraction between data sets at two different temperatures.

These measurements were performed on three single crystals of similar size and under very similar conditions. Although a normalization of the strength of the IC AF Bragg intensities is straightforward, and will be carried out below, it is useful to consider the data directly. We can see that the IC AF Bragg intensity at $T = 5 \text{ K}$ is well defined and relatively strong for $x = 0.125$, becoming substantially weaker for $x = 0.19$, and then both weak and broad for $x = 0.24$.

An analysis of the elastic TAS data in Fig. 1, and the elastic TOF data in Fig. 4, was carried out so as to quantitatively estimate the relative strength of the IC AF Bragg scattering as a function of x for our $x = 0.125, 0.19, 0.24$, and 0.26 samples at both $T = 1.5$ and 5 K . The H and K , elastic TAS scans in Fig. 1 were fit to Lorentzian line shapes of the form

$$S(Q, \hbar\omega = 0) = \frac{I_0}{(Q - Q_0)^2 + (\frac{1}{2}\Gamma)^2} \quad (1)$$

(where Γ indicates the full width at half maximum of the function and Q_0 is its center) with the purpose of extracting both the integrated intensity of the IC AF Bragg scattering and its in-plane correlation length. The intensity of the IC AF Bragg scattering was normalized against rocking curve measurements of the intensity of structurally allowed $(1,1,0)$ Bragg peaks, such that the intensities of the IC AF Bragg scattering at $T = 1.5 \text{ K}$ could be quantitatively compared between the $x = 0.19, 0.24$, and 0.26 samples.

A similar normalization protocol was followed for the IC AF Bragg scattering in the $x = 0.125, 0.19$, and 0.24 samples at $T = 5 \text{ K}$, using the TOF data in Fig. 4. As these elastic scattering data are part of much larger inelastic scattering data sets, we can normalize the IC AF integrated Bragg scattering to that of crystalline electric field (CEF) excitations near ~ 12 and 24 meV . A study on these CEF excitations will be reported separately, but their intensity depends primarily on the amount of Nd present in the samples, which is the same in all cases.

These results are summarized in Fig. 5(a) for the integrated intensities and Fig. 5(b) for the correlation lengths. In both cases our results are put into the context of previous measurements on Nd-LSCO single-crystal samples [37,47]. The primary conclusions are that the x dependence of the intensity of the IC AF Bragg peaks, which goes as the square of the sublattice magnetization, $\langle M \rangle^2$, is consistent between our data at $T = 1.5 \text{ K}$ on $x = 0.19, 0.24$, and 0.26 samples and those of Tranquada *et al.* on $x = 0.125, 0.15$, and 0.20 samples [37]. At this low temperature, $T = 1.5 \text{ K}$, the influence of the $\text{Cu}^{2+}\text{-Nd}^{3+}$ coupling is profound, and the scattering has significant 3D correlations. In contrast, our TOF data for $x = 0.125, 0.19$, and 0.24 samples at $T = 5 \text{ K}$ are much more 2D in nature. We can see that this TOF integrated static magnetic intensity also falls off sharply with x from $x = 0.125$ to 0.24 , but at about half the rate seen for the TAS results at $T = 1.5 \text{ K}$. We attribute this difference between the x dependence of the static magnetism at $T = 1.5 \text{ K}$ and that at $T = 5 \text{ K}$, to an x dependence in the nature of the effectiveness of the coupling between Cu^{2+} and Nd^{3+} magnetic moments. We conclude that the coupling is stronger and thus more efficient for smaller x , where more Cu^{2+} moment is present.

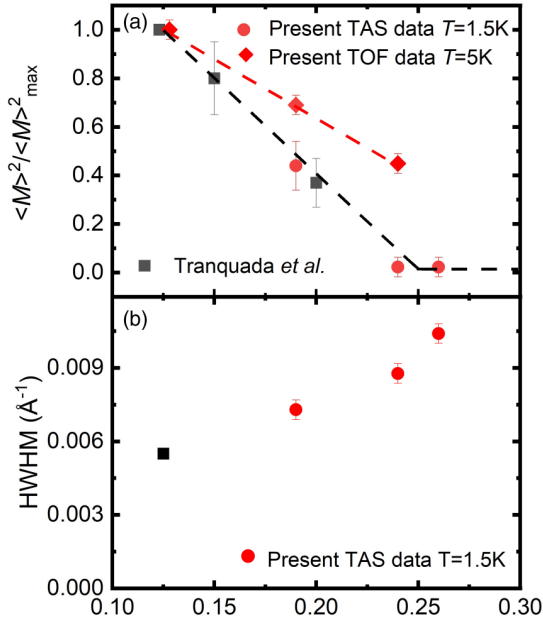


FIG. 5. (a) The square of the sublattice magnetization at 1.5 and 5 K, normalized to $x = 0.12$. The black squares represent preexisting data from Tranquada *et al.* [37]. The red circles represent the current TAS data, which show consistency with the preexisting data. The red diamonds represent the 5-K data taken as the integrated intensities of the IC AF peaks in Fig. 4. Data have been normalized to a combination of incoherent Bragg scattering and crystal field excitation of Nd^{3+} for all samples. (b) The inverse magnetic correlation lengths, which are taken as half-width at half maximum (HWHM), of the current IC AF peaks in $x = 0.19, 0.24,$ and 0.26 are shown, along with preexisting $x = 0.12$ (black square) data from Tranquada *et al.* [47].

Earlier work by Tranquada *et al.* on $x = 0.125$ concluded that the ordered Cu^{2+} moment at low temperatures was $0.1 \pm 0.03 \mu_B$ [48]. Our work then suggests that the ordered Cu^{2+} moment participating in the 2D IC AF structure at $T = 5\text{K}$ in our $x = 0.24$ single-crystal samples is roughly 40% smaller, thus $\sim 0.06 \mu_B$. For context, the ordered Cu^{2+} moment in the ordered state of La_2CuO_4 , as determined by neutron diffraction, is $0.6 \pm 0.05 \mu_B$ [50], while that for Nd_2CuO_4 is $0.46 \pm 0.05 \mu_B$ [50].

The in-plane magnetic correlation lengths at $T = 1.5\text{K}$ are plotted in Fig. 5(b) for our single crystals $x = 0.19, 0.24,$ and 0.26 . Previous studies on IC AF order for $x = 0.125$ had already determined that the relevant magnetic Bragg features had finite in-plane correlation length, in spite of the fact that the IC AF order is at its strongest at this doping level [48]. Our results are consistent with those for $x = 0.125$, in that the sequence of low-temperature in-plane correlation lengths is seen to decrease monotonically with doping (the half-width at half maximum increases monotonically), and the overall trend from $x = 0.125$ to 0.26 is an approximately linear relationship.

B. Low-energy inelastic magnetic scattering

The low-energy spin fluctuations within the static, parallel spin stripe state of Nd-LSCO were also investigated using TAS spectroscopy. Constant- Q measurements were performed

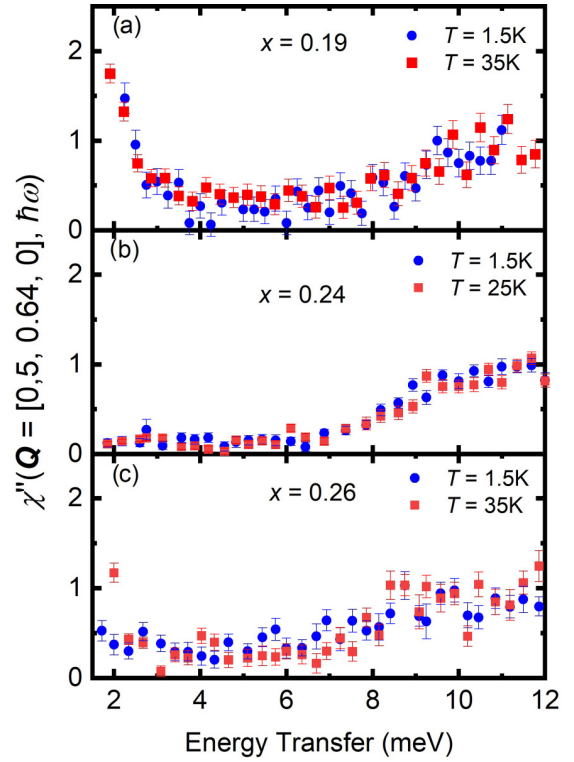


FIG. 6. Energy scans of $\chi''(Q, \hbar\omega)$ taken from TAS constant- Q measurements at $Q = [0.5, 0.64, 0]$: one of the four incommensurate AF peak positions around the $[0.5, 0.5, 0]$ position. Data have been normalized to the intensity of the crystal field excitation from Nd^{3+} around 11 meV.

at the IC AF zone center, $(0.5, 0.64, 0)$, as a function of energy transfer, as shown for $x = 0.19, 0.24,$ and 0.26 in Figs. 6(a)–6(c), respectively. Constant-energy scans were also performed as a function of Q , across an IC AF zone center with scans of the form $(0.5, K, 0)$, as shown in Fig. 7 for the $x = 0.19$ single crystal.

Figures 6–8(a) show the imaginary part of the dynamic susceptibility $\chi''(Q, \hbar\omega)$ as a function of both $\hbar\omega$ and Q , respectively. This quantity is related to the inelastic neutron scattering intensity, the dynamic structure factor $S(Q, \hbar\omega)$, by

$$S(Q, \hbar\omega) = \left[1 - \exp\left(\frac{-\hbar\omega}{k_B T}\right) \right]^{-1} \times \chi''(Q, \hbar\omega). \quad (2)$$

Isolating $\chi''(Q, \hbar\omega)$ from the dynamic structure factor $S(Q, \hbar\omega)$ involves making a robust estimate of the background and then dividing the inelastic neutron scattering signal by the Bose factor, $[1 - \exp(\frac{-\hbar\omega}{k_B T})]^{-1}$. This has been done for the data shown in Figs. 6–8(a), using the scattering away from IC AF Bragg positions, such as $(0.5, 0.68, 0)$, to estimate the background level.

Inspection of the low energy dependence of $\chi''(Q, \hbar\omega)$ at $Q = (0.5, 0.64, 0)$ in Fig. 6 shows that this spectral weight is qualitatively different for the optimally doped $x = 0.19$ sample, with superconducting $T_c \sim 14\text{K}$, as compared with either of the $x = 0.24$ or 0.26 single crystals which lie beyond the pseudogap quantum critical point p^* and close to the end

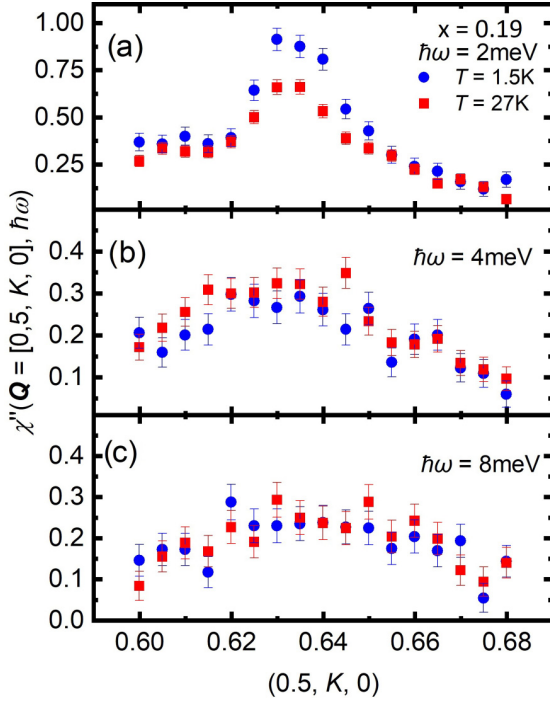


FIG. 7. $\chi''(Q, \hbar\omega)$ for $x = 0.19$ is shown for $Q = [0.5, 0.64, 0]$ and $\hbar\omega = 2, 4,$ and 8 meV in (a), (b), and (c), respectively, from TAS constant-energy-transfer ($\hbar\omega$) scans at both low ($T = 1.5$ K) and high temperatures ($T = 27.5$ K).

of the superconducting dome. While all three samples show pronounced inelastic scattering which peaks near a low-lying CEF excitation at $\sim\hbar\omega = 11$ meV, only the $x = 0.19$ sample shows strong quasielastic scattering which rises up in intensity below ~ 4 meV. For the higher-doped samples, $x = 0.24$ and 0.26 , very little inelastic magnetic spectral weight is obvious at energies less than ~ 4 meV in these measurements.

More detailed constant-energy Q scans show that this low-energy spectral weight is strongly peaked at the IC AF ordering wave vector, as can be seen in Fig. 7 for $x = 0.19$. A strong peak is seen in the $\chi''(Q, \hbar\omega = 2$ meV) data that is not seen in the corresponding data at higher energies, $\hbar\omega = 4$ or 8 meV. At $\hbar\omega = 2$ meV, the strength of $\chi''(Q, \hbar\omega)$ decreases by $\sim 40\%$ on warming from $T = 1.5$ K to $T = 27$ K. $\chi''(Q, \hbar\omega)$ at $\hbar\omega = 4$ or 8 meV remains peaked around the IC AF ordering wave vector, but it is both considerably broader and weaker in intensity than that at 2 meV. As expected, $\chi''(Q, \hbar\omega)$ at $\hbar\omega = 4$ or 8 meV shows little or no temperature dependence to 27 K.

We have measured the temperature dependence of the IC AF inelastic spectral weight at $\hbar\omega = 2$ meV for the $x = 0.19$ sample. This is shown in Fig. 8(a), where $\chi''[Q = (0.5, 0.64, 0), \hbar\omega = 2$ meV] is shown as a function of temperature from $T = 1.5$ K to $T = 30$ K. This temperature dependence is the low-energy, inelastic equivalent of the order parameter, which is the elastic scattering measured at the same IC AF wave vector shown in Figs. 1 and 2. The order parameter for $x = 0.19$, Fig. 2(a), shows that the $2D T_N = 35 \pm 2$ K. Furthermore, it rises sharply with decreasing temperature at low temperatures, due to coupling between the

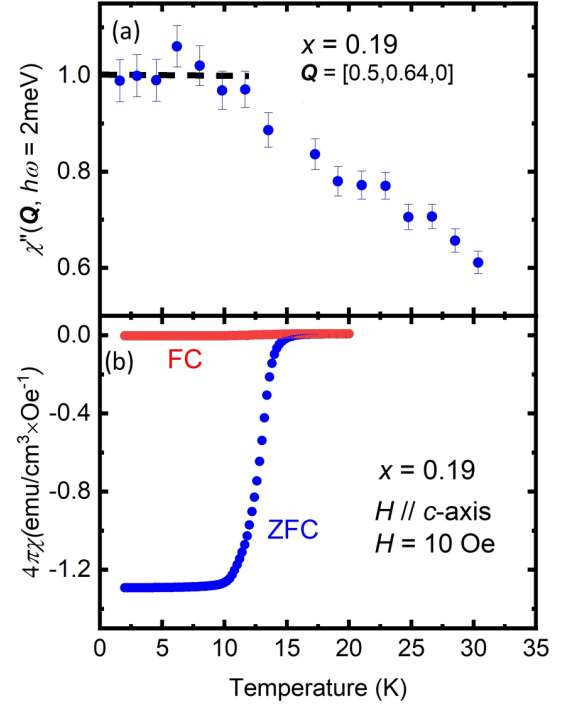


FIG. 8. (a) The temperature dependence of the low-energy spectral weight of the parallel stripe fluctuations, $\chi''(Q, \hbar\omega)$, as a function of temperature for $Q = [0.5, 0.64, 0]$ and $\hbar\omega = 2$ meV is shown for Nd-LSCO with $x = 0.19$. These data were derived from TAS measurements. The horizontal dashed line indicates the plateau behavior for $T \leq T_c \sim 13.5$ K. (b) Field-cooled (FC) and zero-field-cooled (ZFC) magnetic susceptibility measurements on a small single crystal of the $x = 0.19$ Nd-LSCO sample with a magnetic field of 10 Oe applied parallel to the c axis show $T_c \sim 13.5$ K.

Cu^{2+} and Nd^{3+} moments which induces substantial 3D spin correlations [48]. However, the spin fluctuations captured in $\chi''(Q, \hbar\omega = 2$ meV) at the IC AF wave vector rise linearly with decreasing temperature from 30 K to ~ 13 K, before leveling off at low temperatures.

Figure 8 is very interesting as it shows the spectral weight of these low-energy, parallel spin stripe fluctuations in this optimally hole-doped cuprate to saturate at temperatures below the approximate superconducting T_c of this single crystal. In this $x = 0.19$ sample, the temperatures of relevance for 2D magnetic order ($2D T_N \sim 35$ K) and strong 3D correlations (~ 4 K) are well separated from that associated with superconductivity. For ease of reference, the measured magnetic susceptibility of a small piece of the single crystal used in neutron scattering experiments is plotted in Fig. 8(b) directly below the $\chi''(Q, \hbar\omega)$ temperature dependence data for $\hbar\omega = 2$ meV. A strong diamagnetic signal is observed with an onset near $T_c \sim 14.5$ K, but the midpoint on the zero-field-cooled diamagnetic susceptibility curve occurs at ~ 13.5 K, coincident with the start of the plateau in the inelastic, $\hbar\omega = 2$ meV spectral weight at low temperatures. A similar trend in the temperature dependence of $\chi''(Q, \hbar\omega)$ at low energies has been reported for Nd-LSCO with $x = 0.15$ [47], but with a lower temperature point density, making it hard to identify characteristic temperatures.

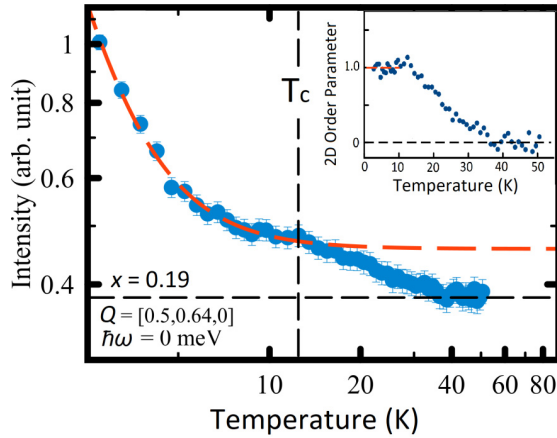


FIG. 9. The order parameter for Nd-LSCO $x = 0.19$ is replotted; this is the same data as in Fig. 2(a), but on a log-log scale. An inflection point in the temperature evolution of the order parameter is clearly observed at superconducting $T_c \sim 13.5$ K (indicated by the vertical dashed fiducial). The inset shows the 2D order parameter (2DOP) for Nd-LSCO $x = 0.19$ derived from the order parameter (OP) measurements shown in the main figure and in Fig. 2(a). 2DOP(T) is obtained from the relation $OP(T) = A(T) \times 2DOP(T)$. The amplification factor $A(T)$ is derived from fitting the $OP(T)$ at $T \leq 12$ K, as shown with the red line in the inset. Like the low-energy spectral weight of the parallel stripe fluctuations, $\chi''(Q = [0.5, 0.64, 0], \hbar\omega = 2 \text{ meV})$ as a function of temperature in Fig. 8, 2DOP displays the onset of its low-temperature plateau coincident with T_c .

Examination of the elastic order parameter for $x = 0.19$ shows evidence for an inflection point at $T_c \sim 13.5$ K. Figure 9 reproduces the order parameter from Fig. 2(a), but now on a log-log scale. The high-temperature background (averaged between 40 and 50 K) is indicated by the horizontal dashed line, while superconducting T_c is indicated by the vertical dashed line. An inflection point at T_c is clear.

In addition, we have modeled the strong upturn in the elastic order parameter for $x = 0.19$ at low temperatures using a phenomenological expression

$$A(T) = a + bT^{-\alpha} \quad (3)$$

for temperatures ≤ 12 K, as shown by the dashed red line in the inset of Fig. 9. We then phenomenologically decompose our measured order parameter (OP) according to

$$OP(T) = A(T) \times 2DOP(T), \quad (4)$$

which gives the two-dimensional order parameter (2DOP) for our $x = 0.19$ sample in the inset of Fig. 9. This decomposition has the interpretation that the effect of the $\text{Cu}^{2+}\text{-Nd}^{3+}$ coupling is to amplify the preexisting 2D Cu^{2+} order parameter at low temperatures. While it is phenomenological, it reproduces in the elastic order parameter similar plateau behavior to that seen in the temperature dependence of $\chi''(Q, \hbar\omega = 2 \text{ meV})$, shown in Fig. 8.

Such intriguing plateaus as a function of decreasing temperature in the magnetic Bragg intensity (the order parameter) and the low-energy spectral weight of the spin fluctuations have been previously observed in several heavy fermion

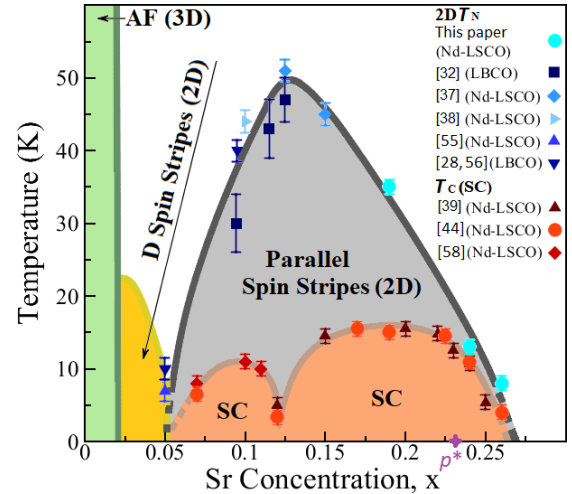


FIG. 10. Phase diagram for quasistatic magnetism in Nd-LSCO as measured by neutron scattering. Combining the current TAS data for $2D T_N$ with preexisting Nd-LSCO data, and complemented with LBCO results for $0.05 \leq x \leq 0.125$, we extend the regime of a 2D parallel spin stripe phase to $0.05 \leq x \leq 0.26$. Such a 2D parallel spin stripe phase is then a prerequisite for superconductivity. All $2D T_N$ parallel spin stripe data come from elastic neutron scattering studies of either Nd-LSCO or LBCO as indicated in the legend. Superconducting T_c for Nd-LSCO are also from references indicated in the legend. p^* indicates the quantum critical point associated with the pseudogap phase [39]. SC, superconductivity.

superconductors, for example, UPt_3 [51,52] and UPd_2Al_3 [53]. Anomalies in the low-energy spectral weight of spin fluctuations have also been observed in the LSCO cuprate system [54]. The coincidence of the plateaus with the superconducting T_c was taken as evidence for strong coupling between magnetism and superconductivity and a key role for AF spin fluctuations in mediating superconductivity in these highly correlated, heavy fermion metals.

IV. PHASE DIAGRAM AND DISCUSSION

Our measurements of $2D T_N$ and the onset of 2D parallel stripes at optimal and high hole-doping levels in Nd-LSCO, with $x = 0.19, 0.24$, and 0.26 , allow us to complete the phase diagram for 2D parallel stripes and to examine their relation to superconductivity. These results extend earlier measurements for Nd-LSCO with $x \leq 0.15$ [37,55]. We have complemented these Nd-LSCO data with corresponding results from LBCO for $0.05 \leq x \leq 0.125$ [28,32,56]. LBCO is a useful proxy for Nd-LSCO at these low doping values, as both LBCO and Nd-LSCO show very pronounced “ $\frac{1}{8}$ anomalies” with superconducting T_c s suppressed to ~ 3 K [57]. In addition, the onset temperature for 2D parallel stripes in both LBCO and Nd-LSCO are maximal at $x = 0.125$, with similar $2D T_N$ s ~ 50 K [32,37].

Figure 10 shows the phase diagram for 2D parallel stripes in Nd-LSCO, superposed with its phase diagram for superconductivity. The superconducting transition temperatures are taken from earlier work [39,44,58] and include data for the four single-crystal samples that were the subject of the present neutron scattering experiments, $x = 0.125, 0.19, 0.24$,

and 0.26 [44]. As previously mentioned, the superconducting phase behavior shows an onset of superconducting ground states at $x = 0.05$, which coincides with the rotation of the 2D diagonal spin stripe structure to the 2D parallel spin stripe structure. Optimal superconducting $T_c \sim 15$ K is reached for Nd-LSCO at $x \sim 0.19$, and the end of the superconducting dome occurs near $x \sim 0.27$ [44].

We can see that the entire region of superconducting ground states for Nd-LSCO is contained within the 2D parallel stripe phase. Superconductivity begins and ends coincident with the beginning and ending of the 2D static parallel stripe phase, as a function of concentration. At a given hole-doping level, superconductivity is entered from a state with static 2D parallel stripe order, as evidenced by quasi-Bragg peaks, and the quasi-Bragg peaks coexist with superconductivity below T_c .

The superconducting T_c vs x relationship in Nd-LSCO is structured over this range of concentrations, $0.05 \leq x \leq 0.27$, due to the $\frac{1}{8}$ anomaly at $x = 0.125$. Hence the strongest 2D parallel spin stripe order, in terms of the highest 2D T_N , appears *anticorrelated* with superconductivity. However, parallel charge stripes have their onset at temperatures higher still than 2D T_N and are intertwined with the parallel spin stripes at and near $x = 0.125$. The charge stripes have been extensively studied in LBCO and to a somewhat lesser extent in Nd-LSCO, but less so still in LSCO—presumably because they are weaker still. The suppression of T_c due to the $\frac{1}{8}$ anomaly in LSCO is itself much less pronounced than in either Nd-LSCO or LBCO. One could therefore argue that the conditions for enhanced superconductivity in these single-layer, hole-doped cuprates is the presence of 2D parallel spin stripes, without, or with less well developed, parallel charge stripes.

V. CONCLUSION

Recent NMR and ultrasound experiments at high magnetic field in LSCO have reported glassy antiferromagnetism existing to higher doping levels than previously believed, up to ~ 0.19 [59]. These measurements require a strong magnetic field to quench superconductivity which would otherwise hide the glassy antiferromagnetism in these experiments. As the enigmatic pseudogap phase in LSCO [15,16,60] itself exists up to $p^* \sim 0.19$, this result implies that strong AF correlations dominate the entire pseudogap phase in LSCO but do not extend beyond p^* .

The pseudogap phase is also well studied in the Nd-LSCO system, and recent work has shown strong thermodynamic evidence for a pseudogap quantum critical point at $p^* \sim 0.23$ [39]. Therefore the corresponding argument in Nd-LSCO would have static AF correlations existing to even higher hole-doping levels than in LSCO, such as $p^* \sim 0.23$ in Nd-LSCO. Such a picture of magnetism being restricted to $p < p^*$ would have been consistent with the previously measured, relatively weak order parameter for Nd-LSCO, $x = 0.20$ [47], shown in Fig. 3. However, it is not consistent with our order parameter results on Nd-LSCO with $x = 0.19, 0.24, \text{ and } 0.26$, all of which clearly show quasi-Bragg peaks due to static parallel spin stripe correlations at low temperatures.

Nonetheless, these NMR and ultrasound results in LSCO [59] are broadly consistent with the present observation of parallel spin stripes existing in Nd-LSCO over the concentration range $0.05 \leq x \leq 0.26$, in that they both show evidence for static parallel spin stripe order to higher doping than previously thought. In addition, while $x = 0.26$ is clearly higher than $p^* \sim 0.23$, elastic neutron scattering measures “static” correlations at much shorter time scales than does NMR (10^{-10} s for neutrons compared with 10^{-6} s for NMR). Consequently, spin correlations on time scales falling between neutron “static” and NMR “static” would appear static to neutrons and dynamic to NMR. One may therefore expect to observe static antiferromagnetism with neutron scattering across a broader range of doping than with NMR.

There remains the question of how the pseudogap quantum critical point at $p^* \sim 0.23$ in Nd-LSCO manifests itself in the 2D static parallel spin stripe magnetism that is the subject of this paper. It is *not* through the nature of the quasistatic spin stripe order, which evolves smoothly across the four Nd-LSCO samples studied here, and therefore smoothly across p^* . Indeed, in and of itself, this is an important result as it decouples quasistatic parallel spin stripe magnetism from the pseudogap’s quantum critical point at p^* . However, as already mentioned, the story for low-energy parallel spin stripe fluctuations is different. Figures 6 and 7 show the spectral weight of the parallel spin stripe fluctuations for $\hbar\omega < 3$ meV at $x = 0.19$ to be qualitatively different from that associated with samples with $x > p^* \sim 0.23$: $x = 0.24$ and 0.26 . These low-energy inelastic parallel spin stripe fluctuations are much stronger and more strongly peaked at the IC ordering wave vector at $x = 0.19$ than at $x = 0.24$ and 0.26 . The temperature scale for the crossover or phase transition associated with the pseudogap phase is itself known to be much higher than either 2D T_N or superconducting T_c in Nd-LSCO [44]. For example, this T^* is ~ 100 K at $x = 0.19$, and it would seem more reasonable to associate the pseudogap with the relatively high energy scale of these parallel spin stripe fluctuations, rather than the low energy scale of the quasistatic parallel spin stripe magnetism.

ACKNOWLEDGMENTS

We thank Louis Taillefer, Amireza Ataie, Takashi Imai, and Graeme Luke for useful and stimulating discussions. We also thank Jianshi Zhou and Zongyao Li for valuable insights into the crystal growth of Nd-LSCO. This work was supported by the Natural Sciences and Engineering Research Council of Canada. We acknowledge the access to neutron infrastructure and supporting technical assistance from the Australian Centre for Neutron Scattering. This research used resources at the Spallation Neutron Source and the High Flux Isotope Reactor, DOE Office of Science User Facilities, operated by the Oak Ridge National Laboratory (ORNL).

Q.M., K.C.R., and B.D.G. performed and analyzed the single-crystal TAS experiment on Nd-LSCO $x = 0.19$ and 0.26 at TAIPAN, ANSTO. Q.M., Z.W.C., S.C., and B.D.G. performed and analyzed the TAS experiment on Nd-LSCO $x = 0.24$ at HB3, HFIR. Q.M., A.I.K., M.B.S., E.M.S., and B.D.G. performed and analyzed the TOF scattering

experiments on Nd-LSCO $x = 0.125, 0.19,$ and 0.24 at SE-QUOIA, SNS. Q.M., M.D., and G.M. carried out the material

synthesis and crystal growth. B.D.G. and Q.M. wrote the manuscript, while B.D.G. conceived and oversaw the project.

- [1] J. G. Bednorz and K. A. Müller, Possible high T_c superconductivity in the Ba-La-Cu-O system, *Z. Phys. B: Condens. Matter* **64**, 189 (1986).
- [2] M. K. Wu, J. R. Ashburn, C. J. Torng, P. H. Hor, R. L. Meng, L. Gao, Z. J. Huang, Y. Q. Wang, and C. W. Chu, Superconductivity at 93 K in a New Mixed-Phase Y-Ba-Cu-O Compound System at Ambient Pressure, *Phys. Rev. Lett.* **58**, 908 (1987).
- [3] P. W. Anderson, The resonating valence bond state in La_2CuO_4 and superconductivity, *Science* **235**, 1196 (1987).
- [4] V. J. Emery, Theory of High- T_c Superconductivity in Oxides, *Phys. Rev. Lett.* **58**, 2794 (1987).
- [5] L. C. Bourne, A. Zettl, T. W. Barbee III, and M. L. Cohen, Complete absence of isotope effect in $\text{YBa}_2\text{Cu}_3\text{O}_7$: Consequences for phonon-mediated superconductivity, *Phys. Rev. B* **36**, 3990 (1987).
- [6] G. Kotliar and J. Liu, Superexchange mechanism and d -wave superconductivity, *Phys. Rev. B* **38**, 5142 (1988).
- [7] J. R. Schrieffer, X.-G. Wen, and S.-C. Zhang, Spin-Bag Mechanism of High-Temperature Superconductivity, *Phys. Rev. Lett.* **60**, 944 (1988).
- [8] F. C. Zhang and T. M. Rice, Effective Hamiltonian for the superconducting Cu oxides, *Phys. Rev. B* **37**, 3759 (1988).
- [9] J. P. Franck, Experimental studies of the isotope effect in high temperature superconductors, in *Physical Properties of High Temperature Superconductors IV*, edited by D. M. Ginsberg (World Scientific, Singapore, 1994), Chap. 4, pp. 189–293.
- [10] V. J. Emery, S. A. Kivelson, and O. Zachar, Spin-gap proximity effect mechanism of high-temperature superconductivity, *Phys. Rev. B* **56**, 6120 (1997).
- [11] M. L. Kulić, Interplay of electron–phonon interaction and strong correlations: the possible way to high-temperature superconductivity, *Phys. Rep.* **338**, 1 (2000).
- [12] P. A. Lee, N. Nagaosa, and X.-G. Wen, Doping a Mott insulator: Physics of high-temperature superconductivity, *Rev. Mod. Phys.* **78**, 17 (2006).
- [13] H. Mukuda, S. Shimizu, A. Iyo, and Y. Kitaoka, High- T_c superconductivity and antiferromagnetism in multilayered copper oxides—a new paradigm of superconducting mechanism—, *J. Phys. Soc. Jpn.* **81**, 011008 (2011).
- [14] D. J. Scalapino, A common thread: The pairing interaction for unconventional superconductors, *Rev. Mod. Phys.* **84**, 1383 (2012).
- [15] L. Taillefer, Scattering and pairing in cuprate superconductors, *Annu. Rev. Condens. Matter Phys.* **1**, 51 (2010).
- [16] C. Proust and L. Taillefer, The remarkable underlying ground states of cuprate superconductors, *Annu. Rev. Condens. Matter Phys.* **10**, 409 (2019).
- [17] B. Keimer, S. A. Kivelson, M. R. Norman, S. Uchida, and J. Zaanen, From quantum matter to high-temperature superconductivity in copper oxides, *Nature (London)* **518**, 179 (2015).
- [18] P. Corboz, T. M. Rice, and M. Troyer, Competing States in the t - J Model: Uniform d -Wave State versus Stripe State, *Phys. Rev. Lett.* **113**, 046402 (2014).
- [19] V. Thampy, M. P. M. Dean, N. B. Christensen, L. Steinke, Z. Islam, M. Oda, M. Ido, N. Momono, S. B. Wilkins, and J. P. Hill, Rotated stripe order and its competition with superconductivity in $\text{La}_{1.88}\text{Sr}_{0.12}\text{CuO}_4$, *Phys. Rev. B* **90**, 100510(R) (2014).
- [20] B. Keimer and J. E. Moore, The physics of quantum materials, *Nat. Phys.* **13**, 1045 (2017).
- [21] M. A. Kastner, R. J. Birgeneau, G. Shirane, and Y. Endoh, Magnetic, transport, and optical properties of monolayer copper oxides, *Rev. Mod. Phys.* **70**, 897 (1998).
- [22] B. Keimer, N. Belk, R. J. Birgeneau, A. Cassanho, C. Y. Chen, M. Greven, M. A. Kastner, A. Aharony, Y. Endoh, R. W. Erwin, and G. Shirane, Magnetic excitations in pure, lightly doped, and weakly metallic La_2CuO_4 , *Phys. Rev. B* **46**, 14034 (1992).
- [23] J. H. Cho, F. C. Chou, and D. C. Johnston, Phase Separation and Finite Size Scaling in $\text{La}_{2-x}\text{Sr}_x\text{CuO}_{(4+\delta)}$ [$0 < (x, \gamma) < 0.03$], *Phys. Rev. Lett.* **70**, 222 (1993).
- [24] F. C. Chou, F. Borsa, J. H. Cho, D. C. Johnston, A. Lascialfari, D. R. Torgeson, and J. Ziolo, Magnetic Phase Diagram of Lightly Doped $\text{La}_{2-x}\text{Sr}_x\text{CuO}_4$ from ^{139}La Nuclear Quadrupole Resonance, *Phys. Rev. Lett.* **71**, 2323 (1993).
- [25] F. Borsa, P. Carretta, J. H. Cho, F. C. Chou, Q. Hu, D. C. Johnston, A. Lascialfari, D. R. Torgeson, R. J. Gooding, N. M. Salem, and K. J. E. Vos, Staggered magnetization in $\text{La}_{2-x}\text{Sr}_x\text{CuO}_4$ from ^{139}La NQR and μSR : Effects of Sr doping in the range $0 < x < 0.02$, *Phys. Rev. B* **52**, 7334 (1995).
- [26] S. Wakimoto, R. J. Birgeneau, M. A. Kastner, Y. S. Lee, R. Erwin, P. M. Gehring, S. H. Lee, M. Fujita, K. Yamada, Y. Endoh, K. Hirota, and G. Shirane, Direct observation of a one-dimensional static spin modulation in insulating $\text{La}_{1.95}\text{Sr}_{0.05}\text{CuO}_4$, *Phys. Rev. B* **61**, 3699 (2000).
- [27] S. Wakimoto, G. Shirane, Y. Endoh, K. Hirota, S. Ueki, K. Yamada, R. J. Birgeneau, M. A. Kastner, Y. S. Lee, P. M. Gehring, and S. H. Lee, Observation of incommensurate magnetic correlations at the lower critical concentration for superconductivity in $\text{La}_{2-x}\text{Sr}_x\text{CuO}_4$ ($x = 0.05$), *Phys. Rev. B* **60**, R769 (1999).
- [28] S. R. Dunsiger, Y. Zhao, B. D. Gaulin, Y. Qiu, P. Bourges, Y. Sidis, J. R. D. Copley, A. Kallin, E. M. Mazurek, and H. A. Dabkowska, Diagonal and collinear incommensurate spin structures in underdoped $\text{La}_{2-x}\text{Ba}_x\text{CuO}_4$, *Phys. Rev. B* **78**, 092507 (2008).
- [29] M. Fujita, H. Goka, K. Yamada, J. M. Tranquada, and L. P. Regnault, Stripe order, depinning, and fluctuations in $\text{La}_{1.875}\text{Ba}_{0.125}\text{CuO}_4$ and $\text{La}_{1.875}\text{Ba}_{0.075}\text{Sr}_{0.050}\text{CuO}_4$, *Phys. Rev. B* **70**, 104517 (2004).
- [30] K. Yamada, C. H. Lee, K. Kurahashi, J. Wada, S. Wakimoto, S. Ueki, H. Kimura, Y. Endoh, S. Hosoya, G. Shirane, R. J. Birgeneau, M. Greven, M. A. Kastner, and Y. J. Kim, Doping dependence of the spatially modulated dynamical spin correlations and the superconducting-transition temperature in $\text{La}_{2-x}\text{Sr}_x\text{CuO}_4$, *Phys. Rev. B* **57**, 6165 (1998).
- [31] M. Kofu, S.-H. Lee, M. Fujita, H.-J. Kang, H. Eisaki, and K. Yamada, Hidden Quantum Spin-Gap State in the Static Stripe

- Phase of High-Temperature $\text{La}_{2-x}\text{Sr}_x\text{CuO}_4$ Superconductors, *Phys. Rev. Lett.* **102**, 047001 (2009).
- [32] M. Hücker, M. v. Zimmermann, G. D. Gu, Z. J. Xu, J. S. Wen, G. Xu, H. J. Kang, A. Zheludev, and J. M. Tranquada, Stripe order in superconducting $\text{La}_{2-x}\text{Ba}_x\text{CuO}_4$ ($0.095 \leq x \leq 0.155$), *Phys. Rev. B* **83**, 104506 (2011).
- [33] B. Nachumi, Y. Fudamoto, A. Keren, K. M. Kojima, M. Larkin, G. M. Luke, J. Merrin, O. Tchernyshyov, Y. J. Uemura, N. Ichikawa, M. Goto, H. Takagi, S. Uchida, M. K. Crawford, E. M. McCarron, D. E. MacLaughlin, and R. H. Heffner, Muon spin relaxation study of the stripe phase order in $\text{La}_{1.6-x}\text{Nd}_{0.4}\text{Sr}_x\text{CuO}_4$ and related 214 cuprates, *Phys. Rev. B* **58**, 8760 (1998).
- [34] P. M. Singer, A. W. Hunt, A. F. Cederström, and T. Imai, Systematic ^{63}Cu NQR Study of the Stripe Phase in $\text{La}_{1.6-x}\text{Nd}_{0.4}\text{Sr}_x\text{CuO}_4$ for $0.07 < x < 0.25$, *Phys. Rev. B* **60**, 15345 (1999).
- [35] A. W. Hunt, P. M. Singer, A. F. Cederström, and T. Imai, Glassy slowing of stripe modulation in $(\text{La}, \text{Eu}, \text{Nd})_{2-x}(\text{Sr}, \text{Ba})_x\text{CuO}_4$: A ^{63}Cu and ^{139}La NQR study down to 350 mK, *Phys. Rev. B* **64**, 134525 (2001).
- [36] J. M. Tranquada, B. J. Sternlieb, J. D. Axe, Y. Nakamura, and S. Uchida, Evidence for stripe correlations of spins and holes in copper oxide superconductors, *Nature (London)* **375**, 561 (1995).
- [37] J. M. Tranquada, J. D. Axe, N. Ichikawa, A. R. Moodenbaugh, Y. Nakamura, and S. Uchida, Coexistence of, and Competition between, Superconductivity and Charge-Stripe Order in $\text{La}_{1.6-x}\text{Nd}_{0.4}\text{Sr}_x\text{CuO}_4$, *Phys. Rev. Lett.* **78**, 338 (1997).
- [38] N. Ichikawa, S. Uchida, J. M. Tranquada, T. Niemöller, P. M. Gehring, S.-H. Lee, and J. R. Schneider, Local Magnetic Order vs Superconductivity in a Layered Cuprate, *Phys. Rev. Lett.* **85**, 1738 (2000).
- [39] B. Michon, C. Girod, S. Badoux, J. Kačmarčík, Q. Ma, M. Dragomir, H. A. Dabkowska, B. D. Gaulin, J.-S. Zhou, S. Pyon, T. Takayama, H. Takagi, S. Verret, N. Doiron-Leyraud, C. Marcenat, L. Taillefer, and T. Klein, Thermodynamic signatures of quantum criticality in cuprate superconductors, *Nature (London)* **567**, 218 (2019).
- [40] H. Takagi, T. Ido, S. Ishibashi, M. Uota, S. Uchida, and Y. Tokura, Superconductor-to-nonsuperconductor transition in $(\text{La}_{1-x}\text{Sr}_x)_2\text{CuO}_4$ as investigated by transport and magnetic measurements, *Phys. Rev. B* **40**, 2254 (1989).
- [41] T. Suzuki, T. Goto, K. Chiba, T. Shinoda, T. Fukase, H. Kimura, K. Yamada, M. Ohashi, and Y. Yamaguchi, Observation of modulated magnetic long-range order in $\text{La}_{1.88}\text{Sr}_{0.12}\text{CuO}_4$, *Phys. Rev. B* **57**, R3229 (1998).
- [42] T. P. Croft, C. Lester, M. S. Senn, A. Bombardi, and S. M. Hayden, Charge density wave fluctuations in $\text{La}_{2-x}\text{Sr}_x\text{CuO}_4$ and their competition with superconductivity, *Phys. Rev. B* **89**, 224513 (2014).
- [43] H. Miao, G. Fabbris, R. J. Koch, D. G. Mazzone, C. S. Nelson, R. Acevedo-Esteves, Y. Li, G. D. Gu, T. Yilmaz, K. Kaznatcheev, E. Vescovo, M. Oda, K. Kurosawa, N. Momono, T. A. Assefa, I. K. Robinson, E. Bozin, J. M. Tranquada, P. D. Johnson, and M. P. M. Dean, Charge density waves in cuprate superconductors beyond the critical doping, *npj Quantum Mater.* **6**, 31 (2021).
- [44] M. Dragomir, Q. Ma, J. P. Clancy, A. Ataei, P. A. Dube, S. Sharma, A. Huq, H. A. Dabkowska, L. Taillefer, and B. D. Gaulin, Materials preparation, single-crystal growth, and the phase diagram of the cuprate high-temperature superconductor $\text{La}_{1.6-x}\text{Nd}_{0.4}\text{Sr}_x\text{CuO}_4$, *Phys. Rev. Material* **4**, 114801 (2020).
- [45] R. Daou, N. Doiron-Leyraud, D. LeBoeuf, S. Y. Li, F. Laliberté, O. Cyr-Choiniere, Y. J. Jo, L. Balicas, J.-Q. Yan, J.-S. Zhou, J. B. Goodenough, and L. Taillefer, Linear temperature dependence of resistivity and change in the Fermi surface at the pseudogap critical point of a high- T_c superconductor, *Nat. Phys.* **5**, 31 (2009).
- [46] G. E. Granroth, A. I. Kolesnikov, T. E. Sherline, J. P. Clancy, K. A. Ross, J. P. C Ruff, B. D. Gaulin, and S. E. Nagler, SE-QUOIA: A newly operating chopper spectrometer at the SNS, *J. Phys.: Conf. Ser.* **251**, 012058 (2010).
- [47] J. M. Tranquada, N. Ichikawa, and S. Uchida, Glassy nature of stripe ordering in $\text{La}_{1.6-x}\text{Nd}_{0.4}\text{Sr}_x\text{CuO}_4$, *Phys. Rev. B* **59**, 14712 (1999).
- [48] J. M. Tranquada, J. D. Axe, N. Ichikawa, Y. Nakamura, S. Uchida, and B. Nachumi, Neutron-scattering study of stripe-phase order of holes and spins in $\text{La}_{1.48}\text{Nd}_{0.4}\text{Sr}_{0.12}\text{CuO}_4$, *Phys. Rev. B* **54**, 7489 (1996).
- [49] J. J. Wagman, G. Van Gastel, K. A. Ross, Z. Yamani, Y. Zhao, Y. Qiu, J. R. D. Copley, A. B. Kallin, E. Mazurek, J. P. Carlo, H. A. Dabkowska, and B. D. Gaulin, Two-dimensional incommensurate and three-dimensional commensurate magnetic order and fluctuations in $\text{La}_{2-x}\text{Ba}_x\text{CuO}_4$, *Phys. Rev. B* **88**, 014412 (2013).
- [50] J. M. Tranquada, Neutron scattering studies of antiferromagnetic correlations in cuprates, in *Handbook of High-Temperature Superconductivity* (Springer, New York, 2007), pp. 257–298..
- [51] G. Aeppli, E. Bucher, C. Broholm, J. K. Kjems, J. Baumann, and J. Hufnagl, Magnetic Order and Fluctuations in Superconducting UPt_3 , *Phys. Rev. Lett.* **60**, 615 (1988).
- [52] E. D. Isaacs, P. Zschack, C. L. Broholm, C. Burns, G. Aeppli, A. P. Ramirez, T. T. M. Palstra, R. W. Erwin, N. Stücheli, and E. Bucher, Antiferromagnetism and its Relation to the Superconducting Phases of UPt_3 , *Phys. Rev. Lett.* **75**, 1178 (1995).
- [53] N. Metoki, Y. Haga, Y. Koike, N. Aso, and Y. Onuki, Coupling between magnetic and superconducting order parameters and evidence for the spin excitation gap in the superconducting state of a heavy fermion superconductor UPd_2Al_3 , *J. Phys. Soc. Jpn.* **66**, 2560 (1997).
- [54] A. T. Rømer, J. Chang, N. B. Christensen, B. M. Andersen, K. Lefmann, L. Mähler, J. Gavilano, R. Gilardi, Ch. Niedermayer, H. M. Rønnow, A. Schneidewind, P. Link, M. Oda, M. Ido, N. Momono, and J. Mesot, Glassy low-energy spin fluctuations and anisotropy gap in $\text{La}_{1.88}\text{Sr}_{0.12}\text{CuO}_4$, *Phys. Rev. B* **87**, 144513 (2013).
- [55] S. Wakimoto, J. M. Tranquada, T. Ono, K. M. Kojima, S. Uchida, S.-H Lee, P. M. Gehring, and R. J. Birgeneau, Diagonal static spin correlation in the low-temperature orthorhombic Pccn phase of $\text{La}_{1.55}\text{Nd}_{0.4}\text{Sr}_{0.05}\text{CuO}_4$, *Phys. Rev. B* **64**, 174505 (2001).
- [56] S. R. Dunsiger, Y. Zhao, Z. Yamani, W. J. L. Buyers, H. A. Dabkowska, and B. D. Gaulin, Incommensurate spin ordering and fluctuations in underdoped $\text{La}_{2-x}\text{Ba}_x\text{CuO}_4$, *Phys. Rev. B* **77**, 224410 (2008).
- [57] J. D. Axe, A. H. Moudden, D. Hohlwein, D. E. Cox, K. M. Mohanty, A. R. Moodenbaugh, and Y. Xu, Structural Phase Transformations and Superconductivity in $\text{La}_{2-x}\text{Ba}_x\text{CuO}_4$, *Phys. Rev. Lett.* **62**, 2751 (1989).

- [58] J. D. Axe and M. K. Crawford, Structural instabilities in lanthanum cuprate superconductors, *J. Low Temp. Phys.* **95**, 271 (1994).
- [59] M. Frachet, I. Vinograd, R. Zhou, S. Benhabib, S. Wu, H. Mayaffre, S. Krämer, S. K. Ramakrishna, A. Reyes, J. Debray, T. Kurosawa, N. Momono, M. Oda, S. Komiya, S. Ono, M. Horio, J. Chang, C. Proust, D. LeBoeuf, and M.-H. Julien, Hidden magnetism at the pseudogap critical point of a cuprate superconductor, *Nat. Phys.* **16**, 1064 (2020).
- [60] P. Giraldo-Gallo, J. A. Galvis, Z. Stegen, K. A. Modic, F. F. Balakirev, J. B. Betts, X. Lian, C. Moir, S. C. Riggs, J. Wu, A. T. Bollinger, X. He, I. Božovi, B. J. Ramshaw, R. D. McDonald, G. S. Boebinger, and A. Shekhter, Scale-invariant magnetoresistance in a cuprate superconductor, *Science* **361**, 479 (2018).

Chapter 6

Parallel Spin Stripe Fluctuations in Optimally and Overdoped Nd-LSCO

6.1 Preface

This chapter examines the dynamic spin fluctuations associated with the parallel spin stripe order, up to 34 meV in Nd-LSCO $x = 0.12, 0.19, 0.24$ and 0.26 as measured using time-of-flight spectroscopy SEQUOIA at ORNL[61]. In the past, the dynamic spin fluctuation spectrum has been studied by Wakimoto *et al* in LSCO $0.25 \leq x \leq 0.30$ from $\omega = 2 - 10$ meV energy range. From this study it was concluded that the maximum spin susceptibility $\chi''(\omega)$ at the incommensurate stripe ordering wavevector decreases linearly with superconducting T_C as shown in Fig.6.1 [72]. They later extended their study up to 120 meV to rule out a possible shift of the spectral weight from low to high energies [73]. However, similar results were observed in both experiments. The conclusion that the intensity diminishes and practically vanishes in heavily overdoped LSCO samples remained the same. This observation suggested a direct linear relationship between the superconducting transition temperature and the dynamic spectral weight of spin fluctuations in LSCO system.

Following Chapter 4, our recent elastic triple-axis neutron scattering study on static parallel spin stripes [30], it was natural to further examine the dynamics

associated with this magnetic order, that is the spin fluctuations associated with parallel spin stripe order.

Four high quality single crystal samples of Nd-LSCO $x = 0.12, 0.19, 0.24$ and 0.26 were determined to be suitable for time-of-flight inelastic neutron scattering experiments using SEQUOIA, ORNL. The three optimal and overdoped samples are the same crystals measured in Chapter 5. All crystals have similar diameter of approx. 6mm and range between 3-5 cm in length, corresponding to masses between 3.5 and 5 grams each. The $x = 0.19$ sample was made up by two co-aligned single crystals with a mosaic spread $< 0.5^\circ$ pre-determined by neutron and Laue measurements. All other samples were checked using a back diffraction Laue instrument for their single crystal nature and alignment. The samples were aligned in the HHL planes and loaded in closed cycle refrigerators with a base temperature of 5 K. The incident neutron energy was set to 60 meV in order to capture a significant fraction of the magnetic and phonon spectral weight, with sufficient Q -resolution, and also the low lying Nd^{3+} crystal electric field excitations in the system. Due to the nature of the time-of-flight neutron scattering experiment, the data set is four dimensional with H, K, L in reciprocal space and an additional dimension in energy transfer between neutrons and the scattering system. To visualize the 4D data, we employ the methods discussed in Chapter 2 by integrating the data in $H\bar{H}$ from -0.1 to 0.1 and L from -4 to 4 and make a slice of, for example, Energy transfer vs HH as a color contour plot. The spin dynamics manifests itself as rod like features centered around $[\pm 1/2, \pm 1/2, L]$ positions in the reciprocal space under this data visualization method. We can also project the data in HK planes with an integration in energy from 5 - 10, 10 - 15, 15 - 20 and 28 - 33 meV, in L from [-4, 4] to produce cuts of segments of the color contour plot for analysis on the incommensurate spin stripe feature in reciprocal space. We combine data produced by these two methods and study the inelastic spectral weight for the spin dynamics in different samples and at different energies. We then performed fitting of the incommensurate spin stripe peaks using both Gaussian and Lorentzian functions on top of a smooth spline background to best simulate the real scattering background.

This Chapter shows clear evidence that the spectral weight of the parallel spin

stipe dynamics below 33 meV remains largely unchanged from $x = 0.12$ to 0.24 in Nd-LSCO and experiences a $\sim 20\%$ drop in the $x = 0.26$ sample. This result appears to be different from that reported in earlier measurements on LSCO data discussed above. Nonetheless, our result is consistent with recent RIXS measurements [27, 28] where high energy "paramagnon" has been consistently observed from low to high doped LSCO samples. The newest theoretical model that connects cuprate superconductors with quantum spin glasses is also consistent with our observation[74], both with regard to the x dependence of the elastic scattering from static parallel spin stripes and the inelastic scattering from parallel spin stripe fluctuations in the Nd-LSCO system.

My role in this project includes, growing and characterizing the single crystal Nd-LSCO samples, conducting a series of time-of-flight experiments and analyzing the associated data. Evan M. Smith, Zachary W. Cronkwright supported the experiments as group members. Mirela Dragomir, Gabrielle Mitchell contributed during the crystal growth. Alexander I. Kolesnikov, Matthew B. Stone were beamline scientists at SEQUOIA, ORNL. Bruce D. Gaulin and I co-wrote the manuscript while Bruce D. Gaulin oversaw the project.

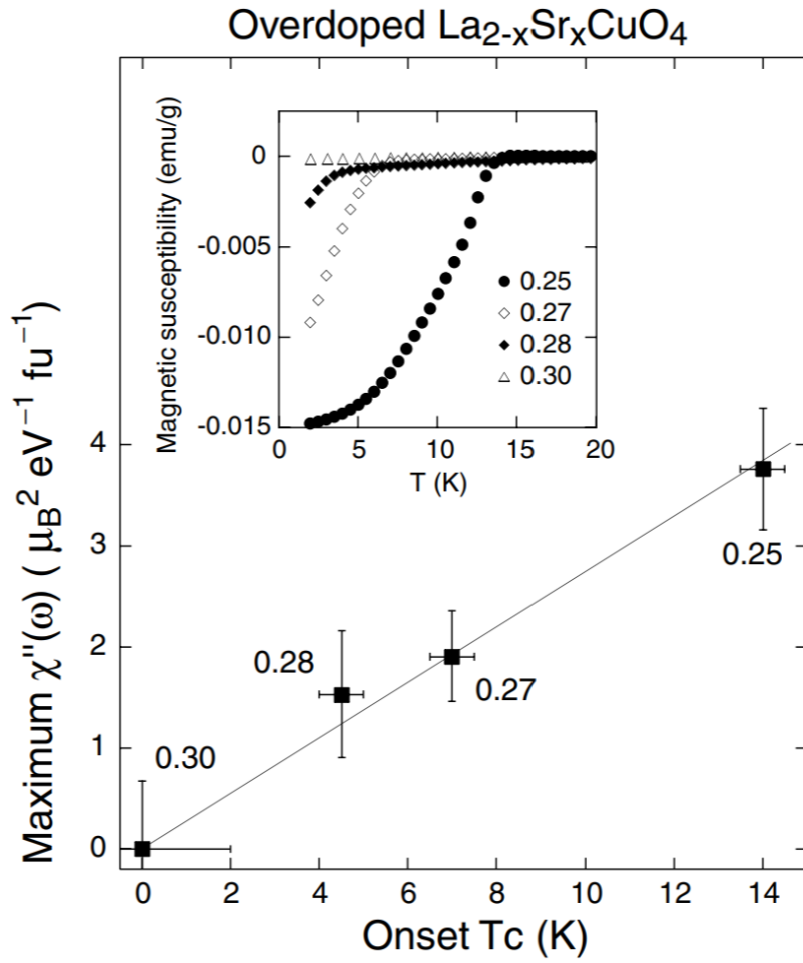


FIGURE 6.1: Summarized maximum $\chi''(\omega)$ vs onsite T_c measured by the magnetic susceptibility for LSCO $x = 0.25, 0.27, 0.28$ and 0.30 . The $\chi''(\omega)$ is taken as maximum from 2-10 meV energy range. Figure reproduced from [72] with permission.

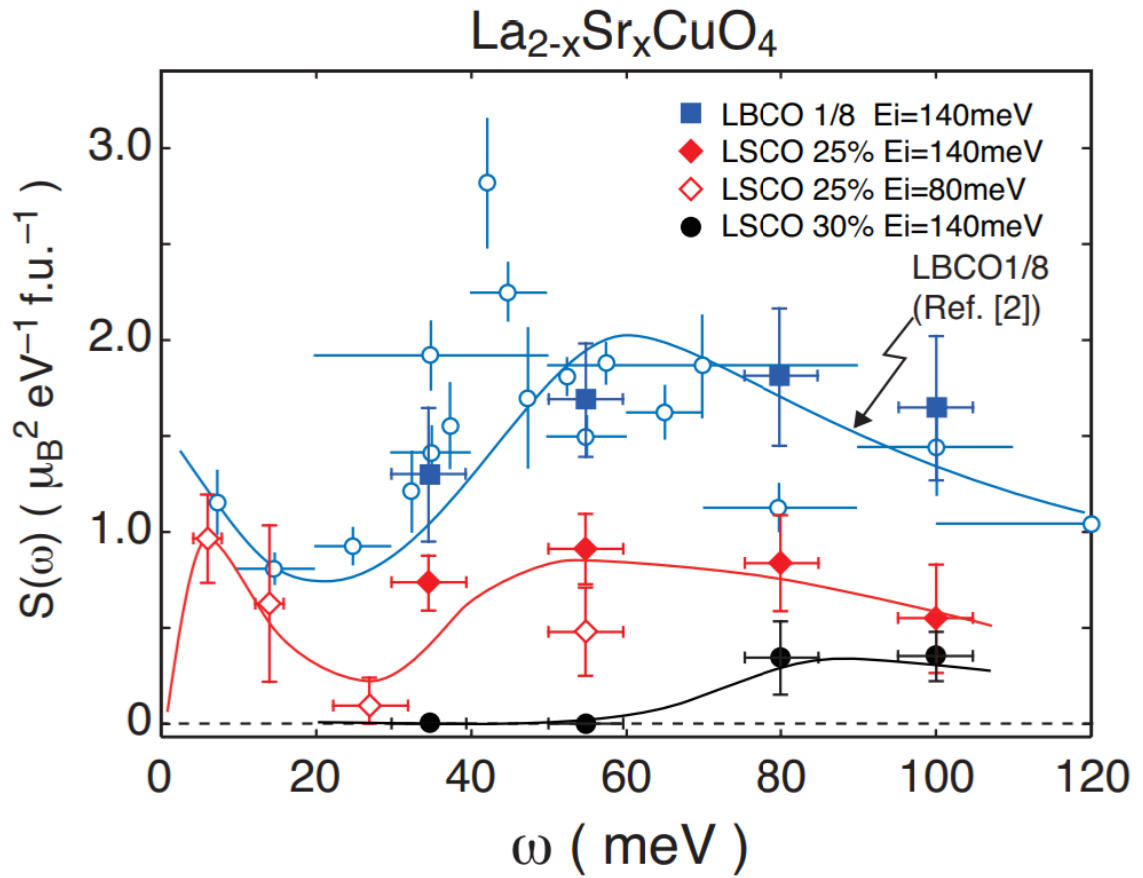


FIGURE 6.2: Integrated intensity of $S(\omega)$ vs ω in meV. Blue square indicates data from LBCO and the rest are LSCO data with Sr concentration $x = 0.25$ and 0.30 . Figure reproduced from [73] with permission.

Dynamic Parallel Spin Stripes from the 1/8 anomaly to the End of Superconductivity in $\text{La}_{1.6-x}\text{Nd}_{0.4}\text{Sr}_x\text{CuO}_4$

Qianli Ma,¹ Evan M. Smith,¹ Zachary W. Cronkwright,¹ Mirela Dragomir,^{2,3} Gabrielle Mitchell,¹ Alexander I. Kolesnikov,⁴ Matthew B. Stone,⁴ and Bruce D. Gaulin^{1,2,5}

¹*Department of Physics and Astronomy, McMaster University, Hamilton, Ontario, L8S 4M1, Canada*

²*Brockhouse Institute for Materials Research, Hamilton, Ontario, L8S 4M1, Canada*

³*Electronic Ceramics Department, Jožef Stefan Institute, 1000 Ljubljana, Slovenia*

⁴*Neutron Scattering Division, Oak Ridge National Laboratory, Oak Ridge, TN 37830, United States*

⁵*Canadian Institute for Advanced Research, MaRS Centre, West Tower 661 University Ave., Suite 505, Toronto, ON, M5G 1M1, Canada*

(Dated: January 27, 2022)

We have carried out new neutron spectroscopic measurements on single crystals of $\text{La}_{1.6-x}\text{Nd}_{0.4}\text{Sr}_x\text{CuO}_4$ from $0.12 \leq x \leq 0.26$ using time-of-flight techniques. These measurements allow us to follow the evolution of parallel spin stripe fluctuations with energies less than ~ 33 meV, from $x=0.12$ to 0.26 . Samples at these hole-doping levels are known to display static (on the neutron scattering time scale) parallel spin stripes at low temperature, with onset temperatures and intensities which decrease rapidly with increasing x . Nonetheless, we report remarkably similar dynamic spectral weight for the corresponding dynamic parallel spin stripes, between 5 meV to 33 meV, from the 1/8 anomaly near $x=0.12$, to optimal doping near $x=0.19$ to the quantum critical point for the pseudogap phase near $x=0.24$, and finally to the approximate end of superconductivity near $x=0.26$. This observed dynamic magnetic spectral weight is structured in energy with a peak near 17 meV at all dopings studied. Earlier neutron and resonant x-ray scattering measurements on related cuprate superconductors have reported both a disappearance with increasing doping of magnetic fluctuations at (π, π) wavevectors characterizing parallel spin stripe structures, and persistent paramagnon scattering away from this wavevector, respectively. Our new results on $\text{La}_{1.6-x}\text{Nd}_{0.4}\text{Sr}_x\text{CuO}_4$ from $0.12 \leq x \leq 0.26$ clearly show persistent parallel spin stripe fluctuations at and around at (π, π) , and across the full range of doping studied. These results are also compared to recent theory. Together with a rapidly declining x -dependence to the static parallel spin stripe order, the persistent parallel spin stripe fluctuations show a remarkable similarity to the expectations of a quantum spin glass, random t-J model, recently introduced to describe strong local correlations in cuprates.

I. INTRODUCTION

High temperature superconductivity in hole-doped cuprates arises from the presence of mobile holes in the quasi-two dimensional CuO_2 layers, introduced by chemical doping. The un-doped parent material for the 214 family of superconductors is La_2CuO_4 , a Mott insulator with three dimensional antiferromagnetic order at ~ 300 K[1, 2]. On doping La^{3+} with Sr^{2+} in either $\text{La}_{2-x}\text{Sr}_x\text{CuO}_4$ (LSCO) or $\text{La}_{1.6-x}\text{Nd}_{0.4}\text{Sr}_x\text{CuO}_4$ (Nd-LSCO), or with Ba^{2+} in $\text{La}_{2-x}\text{Ba}_x\text{CuO}_4$ (LBCO), three dimensional antiferromagnetism is rapidly destroyed, and replaced, by $x \sim 0.02$, with incommensurate, quasi-two dimensional static magnetism which onsets at much lower temperatures[1–5].

Neutron scattering famously sees this quasi-two dimensional, incommensurate spin order as elastic Bragg peaks, with finite reciprocal space widths, or inverse correlation lengths, in the ab basal plane, [6–9], which can be referred to as quasi-Bragg peaks. Using a tetragonal unit cell, for which $a=b=3.88$ Å, diffraction from diagonal spin stripe order is first observed at low doping with quasi-Bragg peaks at four positions split off from the $(\frac{1}{2}, \frac{1}{2}, 0)$, or $(\pi, \pi, 0)$, position in reciprocal space[6]. Wakimoto and collaborators made the remarkable discovery that the incommensurate pattern of quasi-Bragg peaks in LSCO rotates within the a^*-b^* plane of reciprocal space by 45° , to ordering wavevectors of the form $(\frac{1}{2}, \frac{1}{2} \pm \delta, 0)$ and $(\frac{1}{2} \pm \delta, \frac{1}{2}, 0)$, forming parallel spin stripe order, at $x=0.05$, which is also the onset of superconducting ground states in LSCO[10]. A

similar rotation between so-called diagonal and parallel spin stripe magnetism has also been observed in LBCO and Nd-LSCO[11–14].

Recently, much interest has focused on Nd-LSCO as it possesses the full complexity of the hole-doped cuprate phase diagram while exhibiting relatively low superconducting transition temperatures. The low temperature magnetic and superconducting phase diagram for Nd-LSCO is summarized in Fig. 1. The low superconducting T_C 's allow for relatively easy access to normal state properties at low temperatures, as superconductivity can be destroyed with application of relatively modest, and therefore practical, magnetic field strengths. This in turn has allowed detailed studies of both electrical and thermal transport in normal state Nd-LSCO at all doping levels. In particular it allowed recent thermodynamic measurements which reveal a quantum critical point at $p^*=0.23$, signifying the end of the elusive pseudogap phase[15]. Hall effect measurements show that p^* is coincident with an abrupt change in the Hall number, n_H , from being proportional to p , to be proportional to $1+p$, consistent with a dramatic change in Fermi surface coincident with p^* [16–18]. The Nd-LSCO materials system can be grown as high quality, large single crystals, appropriate for neutron scattering measurements, over a relatively large range of hole-doping, $x \leq 0.26$, in $\text{La}_{1.6-x}\text{Nd}_{0.4}\text{Sr}_x\text{CuO}_4$ [19].

Recent elastic neutron scattering measurements have shown static, quasi-two dimensional parallel stripe order in Nd-LSCO single crystals with $x=0.12, 0.19, 0.24$ and 0.26 [14]. This order is not true long range three dimensional order, but cor-

responds to large in-plane correlation lengths in the a - b plane, and short correlation lengths along c , such that well-defined incommensurate quasi-Bragg peaks are easily observed at low temperatures. With finite correlation lengths at all temperatures and spin 1/2 degrees of freedom, such a system also corresponds to a quantum spin glass. The static (on the time scale of the neutron) magnetic moment associated with the parallel stripe order is a small fraction of the $1 \mu_B$ expected for $S=1/2$ Cu^{2+} ions, and the intensity of the quasi-Bragg peaks fall off with increased doping, while the in-plane correlation lengths correspondingly decrease. Nonetheless, they remain observable even at $x=0.26$, which is close to the end of the superconducting dome, and which displays a high temperature tetragonal phase down to at least $T=2$ K. This work is broadly consistent with recent NMR studies on the LSCO where magnetism has been observed at higher doping than previously believed [20].

Resonant elastic x-ray scattering performed on samples cut from the same Nd-LSCO single crystals studied here also show clear evidence for the corresponding static parallel *charge* stripe Bragg peaks, at $x=0.12$ and 0.17 , but not at $x=0.19$ [21] above $T=22$ K. In LSCO, recent scattering have reported both an end to parallel charge stripes, or charge density wave (CDW) scatterings at $x \sim 0.18$, and the observation of CDWs [22] to $x = 0.21$.

Modern time-of-flight (TOF) neutron scattering techniques allow comprehensive four dimensional (4D) measurements, covering three reciprocal space dimensions as well as energy. However, measurements with full 4D sensitivity have only been employed relatively recently. In the past, TOF neutron scattering performed on direct-geometry chopper instruments were often performed with single crystals of cuprate superconductors in a single orientation, with $k_i // c$ -axis. Information on the evolution of the dynamic magnetic spectral weight within a tetragonal basal plane of reciprocal space, a^*b^* , could be obtained, but under these conditions, the energy transfer of the scattering is conflated with the c^* dependence of the scattering. This could be used to good effect provided that there either was no c^* -dependence to the scattering, or that the c^* -dependence of this scattering was well understood. However, the hole-doped cuprates are complex oxides with many atoms per unit cell, and hence with complex phonon spectra, as well as crystalline electric field excitations in the case of Nd-LSCO, in addition to magnetic excitations. Hence a full 4D data set and analysis is preferred.

In this paper, we present comprehensive 4-D TOF neutron scattering data on single crystal Nd-LSCO samples of $x = 0.12, 0.19, 0.24$ and 0.26 , covering the under-doped, optimally-doped and over-doped regions of the phase diagram, as indicated in Fig. 1. Our results clearly show that the dynamic parallel spin stripes persist beyond the quantum critical point at p^* , up to the very end of the superconducting dome with remarkably little decrease in spectral weight until an $\sim 33\%$ drop in intensity is observed at $x=0.26$. We compare our results to preexisting studies of dynamic magnetic spectral weight from both neutron and resonant inelastic x-ray scattering in related 214 cuprates [23–25], as well as to recent theory based on the Hubbard model at optimal and relatively high hole-doping[26],

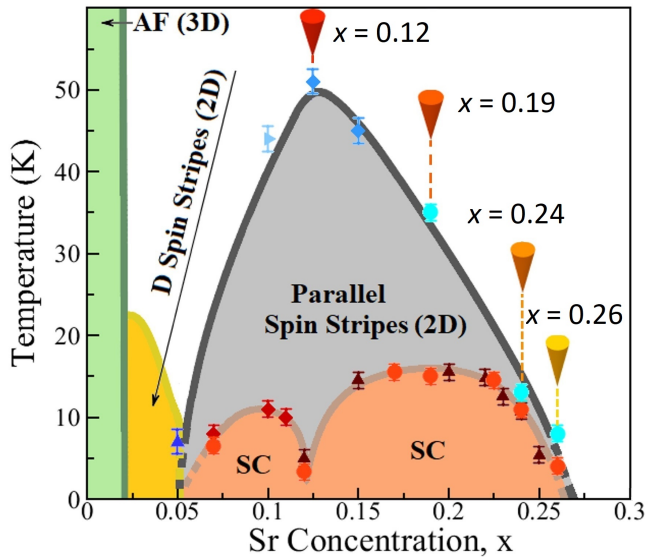


FIG. 1. The magnetic and superconducting phase diagram for Nd-LSCO is shown, with markers indicating the hole-doping level $x = 0.12, 0.19, 0.24$ and 0.26 of the single crystal samples which are the subject of the present inelastic neutron scattering study. This plot is modified from Ref [14], where the references for the magnetic and superconducting transition temperatures are given.

as well as to work on a random t-J model, appropriate to a quantum spin glass[27].

II. SAMPLE PREPARATION & EXPERIMENTAL METHODS

High quality single crystals of Nd-LSCO with $x = 0.12, 0.19, 0.24$ and 0.26 were grown using the traveling solvent floating zone technique at McMaster University. The resulting single crystals were of mass 3.8g, 3.6g, 4.0g, and 3.9g for each of $x=0.12, 0.19, 0.24$ and 0.26 , respectively. The Nd-LSCO sample with $x = 0.19$ was comprised of two co-aligned single crystals each weighs $\sim 1.5\text{g}$ and 2.1g . The single crystals were produced using a four-mirror Crystal Systems Inc. halogen lamp image furnace at approximate growth speeds of 0.68 mm/hr, and growths lasting for approximately 1 week each. The Sr concentration of each single crystal was determined by careful correlation of the structural phase transition temperatures with pre-existing phase diagrams, as described in [19]. Further details regarding the materials preparation and single crystal growth of these samples, as well as determination of their stoichiometry, is reported in [19]. All single crystals were scanned using a back-scattering Laue X-ray instrument to assess their single-crystal nature. Neutron diffraction measurements showed mosaic spreads of less than 0.5° in all crystals, attesting to their high quality, single crystalline nature.

Time-of-flight (TOF) neutron chopper spectrometer measurements were carried out on all four of the $x = 0.12, 0.19, 0.24$ and 0.26 single crystals using the direct-geometry chopper time-of-flight spectrometer, SEQUOIA, at the Spallation

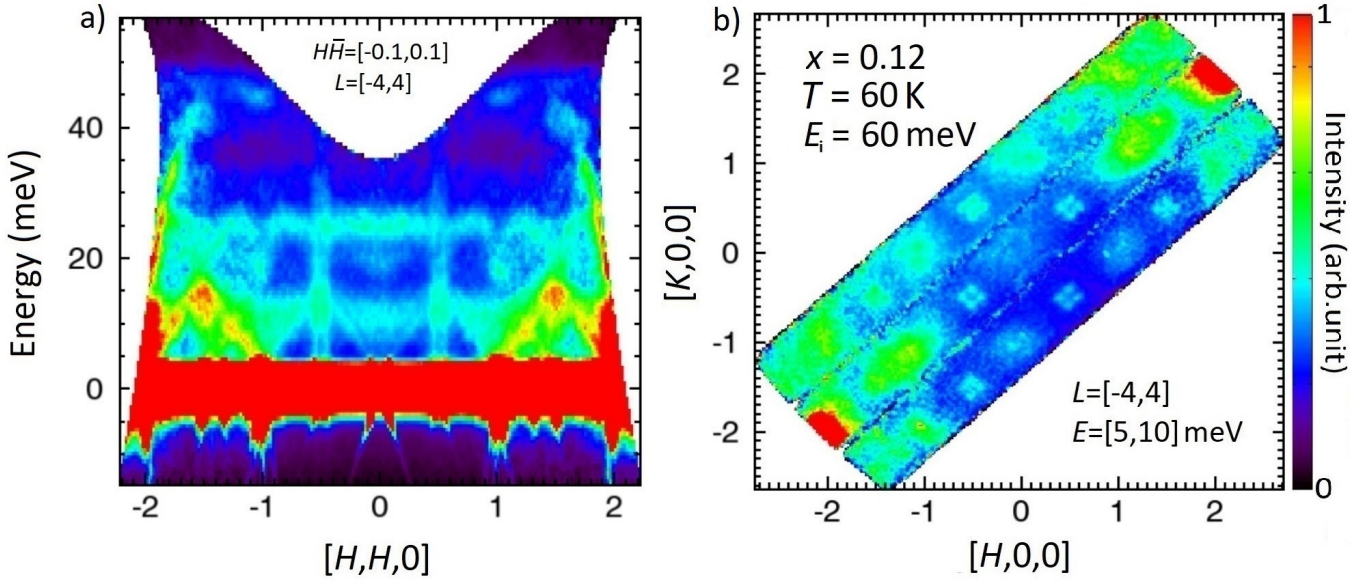


FIG. 2. Typical TOF neutron scattering results for the Nd-LSCO $x = 0.12$ single crystal are shown at $T=60$ K. Panel a) shows an energy vs HH plot, with integrations of $-4 \leq L \leq 4$ and $-0.1 \leq H, \bar{H} \leq 0.1$. Panel b) shows an energy slice for $5 \text{ meV} \leq E \leq 10 \text{ meV}$, within the HK plane of reciprocal space and with an L integration of $-4 \leq L \leq 4$. These data have had an empty sample can, background data set subtracted from it. A hybridization of optical phonon modes and the 25 meV CEF level can be observed in a). The ladder-like features centered around $[\frac{1}{2}, \frac{1}{2}, L]$ and $[-\frac{1}{2}, -\frac{1}{2}, L]$ in a) are the dynamic parallel spin stripes, which are also recognized by the quartet of peaks around $[\frac{1}{2}, \frac{1}{2}, 0]$, $[\frac{3}{2}, \frac{1}{2}, 0]$ and equivalent wavevectors in b).

Neutron Source, Oak Ridge National Laboratory [28]. All measurements were performed using $E_i=60$ meV neutrons, which gave an energy resolution of ~ 1.2 meV at the elastic position. The single crystal samples were loaded in closed cycle refrigerators with a base temperature of 5 K, and aligned with their HHL planes coincident with the horizontal plane. The single crystal samples were rotated through 360° about the vertical axis of the instrument in 1 degree steps during the course of any one measurement, which typically required 24 hours of counting.

III. EXPERIMENTAL RESULTS

A. Inelastic neutron scattering

Typical $E_i=60$ meV time-of-flight (TOF) inelastic neutron scattering data for single crystal Nd-LSCO with $x=0.12$ and $T=60$ K is shown in Fig. 2 a) and b) and in Fig. 3 a) and b). This data comes from a single 4D data set, and presenting it as two-dimensional colour-contour maps, as in both Fig. 2 and Fig. 3 a), requires two integrations. For the data shown in Fig. 2 a) the plot shows E (meV) vs the $H, H, 0$ direction of reciprocal space, with integrations in L between -4 and 4 and in $H, \bar{H}, 0$ between $H=-0.1$ and $H=0.1$. In Fig. 2 b) the plot shows the $0, K, 0$ direction of reciprocal space vs the $H, 0, 0$ direction of reciprocal space, again with integrations in L between -4 and 4 and in energy between 5 and 10 meV. These data sets have had an empty sample cell background

data set subtracted from them, but are otherwise plotted on full intensity scale (ie. no false zero is employed). For the $x=0.12$ sample, measurements were taken at both $T=5$ K and 60 K. There is little qualitative difference between these two data sets, although higher intensity is seen at energies below ~ 10 meV at $T=60$ K, due to the Bose population factor.

Figure 2 shows rich inelastic scattering due to the Cu^{2+} spin excitations near $[1/2, 1/2, 0]$ and equivalent wavevectors; both acoustic (below ~ 14 meV) and optical (above ~ 14 meV) phonons at relatively large H and K ; as well as Nd^{3+} crystalline electric field excitations at ~ 11 meV, 25 meV and 45 meV. These are identified by the \mathbf{Q} dependence of the neutron scattering cross section, which goes like the magnetic form factor squared, $F(\mathbf{Q})^2$, for magnetic scattering and like $(\epsilon \cdot \mathbf{Q})^2$ for phonons, where ϵ is the phonon eigenvector. Nd^{3+} crystal field excitations are expected to be broadly dispersionless, as they are a single ion property, and restricted to small \mathbf{Q} due to the magnetic form factor.

Dynamic parallel spin stripes are clear in both Fig. 2 a) and b). In Fig. 2 b) these are easily recognized as a quartet of peaks around $(1/2, 1/2, 0)$ and equivalent “ (π, π) ” wavevectors, as well as $(3/2, 1/2, 0)$ and equivalent “ $(3\pi, \pi)$ ” wavevectors. These dynamic parallel spin stripe fluctuations are between 5 and 10 meV in energy, and are extended in L , hence two dimensional in nature. Thus integrating this signal in L over the low- \mathbf{Q} range $-4 \leq L \leq 4$ is very effective. A greater L integration allows greater intensity, but also includes more high- \mathbf{Q} scattering originating from phonons, while a smaller L -integration provides less integrated intensity from the quasi-two dimen-

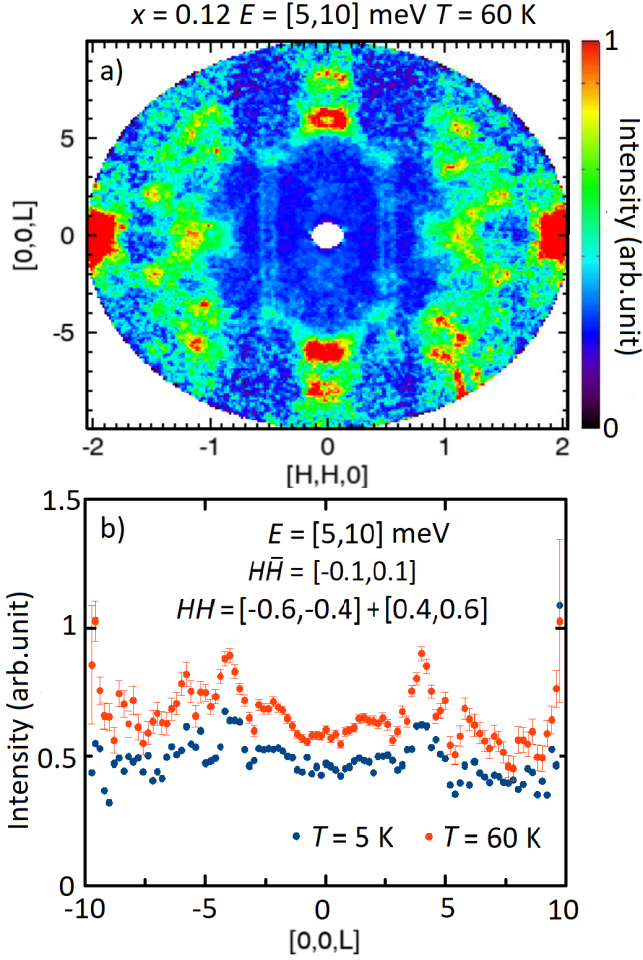


FIG. 3. a) A color contour map of inelastic scattering within the HHL plane of the $x = 0.12$ Nd-LSCO sample, integrated between 5 to 10 meV and $HH = [-0.1, 0.1]$. This data set has had an empty sample can, background data set subtracted from it. The dynamic parallel spin stripes can be seen as “ladder”-like features of scattering along L about the $HH = 0.5$ and -0.5 positions. b) Line scans along L direction from the color contour map in a) for both 5 K and 60 K data set of $x = 0.12$ Nd-LSCO sample. The cuts integrate data centered about both 0.5 and -0.5 in HH . The weak structure at $L=2, 4$ and 6 is attributed to acoustic phonons, with most of the intensity due to two dimensional parallel spin stripes.

sional magnetism. The L -dependence to the inelastic scattering between 5 and 10 meV in energy is explicitly examined below and in Fig. 3.

As shown in Fig. 2 a) these parallel stripe fluctuations are very dispersive, and they appear as approximate ladders around $(1/2, 1/2, 0)$. Work on other 214 families of cuprates shows these excitations to disperse towards zone boundary energies in the 200 meV to 300 meV range[29]; thus they appear to disperse vertically when studied on an energy scale of ~ 45 meV, as is shown here.

Both Fig. 2 a) and b) also show phonon scattering, which is strongest at relatively large Q . Acoustic branches are clear

in Fig. 2 a) as they disperse linearly from zone centres at $1,1,L$ and $2,2,L$ and equivalent zone centres. The acoustic zone boundary energies are observed to be ~ 14 meV. Optic modes are observed above ~ 15 meV. Similar optic phonon scattering was better investigated in earlier studies of the LSCO system [30, 31], and the results presented here are very consistent.

The crystalline electric field excitations associated with Nd^{3+} are also seen in Fig. 2 a) as the almost dispersionless bands that are clear centred on ~ 11 meV and 25 meV. These are associated with neutron (and therefore dipole) induced transitions from the Kramer’s doublet ground state of the $J=9/2$ multiplet appropriate to Nd^{3+} to excited states at these energies. Their presence in the Nd-LSCO system means that there are two relatively low energy windows, in which the very dispersive Cu^{2+} parallel spin stripe fluctuations can be studied with little interference from the Nd^{3+} CEF excitations: these are from the edge of the quasi-elastic nuclear incoherent scattering which extends to ~ 4 meV and the bottom of the 1^{st} excited state CEF scattering at ~ 10 meV, and then from ~ 14 meV to 23 meV, which lies between the scattering from the 1^{st} and 2^{nd} excited states of the Nd^{3+} CEF scheme.

In Fig. 3, we explicitly examine the L -dependence of the inelastic scattering between 5 meV and 10 meV. Fig. 3 a) shows a colour contour map with integrations in energy for $5 \text{ meV} \leq E \leq 10 \text{ meV}$, and in reciprocal space within the basal plane but normal to the HH direction, $-0.1 \leq HH \leq 0.1$, for the $T = 60$ K, $x = 0.12$ data set. The dynamic parallel spin stripes are identified as clear parallel “ladders” of scattering along L and centred about either $HH = -0.5$ or 0.5 . These appear extended in L due to the two dimensional nature of the dynamic parallel spin stripes.

Fig. 3 b) shows L -cuts through the Fig. 3 a) colour contour map, integrating across the HH direction in reciprocal space from -0.6 to -0.4 and from 0.4 to 0.6 , so as to capture all of the dynamic parallel spin stripe scattering. These cuts show higher intensity at $T = 60$ K as compared with $T = 5$ K, which is expected due to the effect of the Bose factor on this inelastic scattering. It also shows weak structure in L , near $L = 2, 4$ and 6 , which we attribute to weak acoustic phonons, emanating from $(1, 0, L=2,4,6)$ zone centres, using orthorhombic notation (these are $(1/2, 1/2, L)$ using tetragonal notation). We thus explicitly see that the dynamic parallel spin stripes have pronounced two dimensional character - no three dimensional correlations are obvious beyond those that can be attributed to weak phonon scattering.

The quality of this data also allows the clear observation of interactions between these various elementary excitations, and particularly between the 2^{nd} excited state Nd^{3+} CEF level and an optic phonon. This can be seen in Fig. 2 a) at $[-1, -1, 0]$, where an optic phonon at ~ 17 meV disrupts the flat dispersion of the CEF excitation. We tentatively identify this as a vibronic bound state, resulting from the entanglement of an optic phonon with the 2^{nd} excited state CEF excitation of Nd^{3+} . Such hybridized bound states are known to exist in other rare earth oxides, such as the spin ices $Ho_2Ti_2O_7$ and related pyrochlores[32]. We also note that earlier TOF neutron scattering studies have also observed evidence for strong coupling between relatively low-lying optic phonons in the 17 meV - 19

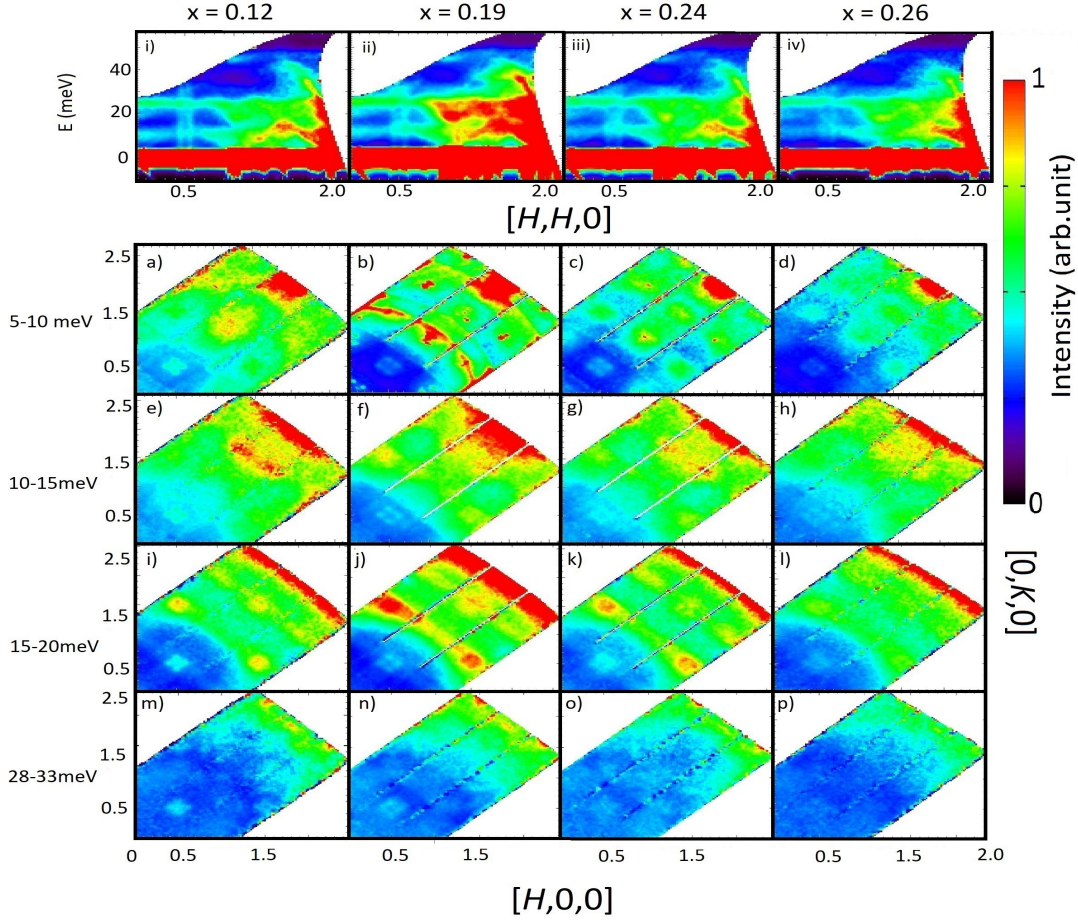


FIG. 4. Top row: Inelastic neutron scattering shown as Energy vs HH for $x = 0.12$ i), 0.19 ii), 0.24 iii) and 0.26 iv). The rod-like feature around $(0.5, 0.5, 0)$ represents the parallel spin stripe fluctuations. Bottom four rows, a) - p): energy cuts through the same data, from 5 to 10 meV (a to d), from 10 to 15 meV (e to h), from 15 to 20 meV (i to l), and from 28 to 33 meV (m to p) in H, K -maps. The incommensurate peaks around $(0.5, 0.5, 0)$ are the same parallel spin stripe fluctuations as the rod-like features in the top row, i) to iv). The data has been normalized to a combination of Nd^{3+} crystal field excitations at ~ 10 and 25 meV.

meV range and again near 30 meV, and dispersive parallel spin stripe fluctuations in underdoped LBCO[30, 31].

TOF inelastic scattering measurements, similar to those presented in Fig. 2 for Nd-LSCO $x=0.12$, were performed on single crystals of Nd-LSCO with $x=0.19, 0.24$ and 0.26 , using SEQUOIA and $E_i=60$ meV. These results, at $T=5$ K, are shown in panels i) - iv) and a) - p) of Fig. 4. The data in Fig. 4 i) - iv) has been symmetrized between $[\bar{H}, \bar{H}, 0]$ and $[H, H, 0]$, while the data in Fig. 4 a) to p) have been symmetrized within a single quadrant of $[H, K, 0]$ reciprocal space. This symmetrization overlays signal in different Brillouin zones, while averaging over any variations in background. The intensity scale for different samples has been normalized by considering the intensity of three scattering features unrelated to Cu^{2+} magnetism: the intensity of acoustic phonons in the vicinity of $[1,1,0]$, the intensity of Nd^{3+} CEF scattering near 10 meV as well as that near 25 meV. All of these are expected to be \sim independent of x for Nd-LSCO with $0.12 \leq x \leq 0.26$. The normalization factors used to set the relative intensities between the samples

differed by $\sim 10\%$, which was consistent with differences in sample masses employed.

Qualitative examination of the dynamic incommensurate spin fluctuations in the Nd-LSCO system, shows that both the “ladder”-like spin excitations, dispersing vertically from around (π, π) wavevectors (that is, around $(0.5, 0.5, 0)$) in Fig. 4 i) - iv), and the quartet of inelastic peaks around $(0.5, 0.5, 0)$ in Fig. 4 a) - p) are present for all values of $0.12 \leq x \leq 0.26$. They are somewhat sharper and easier to visually discriminate at relatively low doping, $x=0.12$, but they are present at all doping levels studied.

We can, of course, make a quantitative statement regarding the relative spectral weight of these parallel stripe fluctuations. In Fig. 5, we present cuts along the $[H, H, 0]$ direction of reciprocal space through the $[H, K, 0]$ maps of inelastic scattering. These cuts integrate over $-4 \leq L \leq 4$ as well as over -0.1 to 0.1 in the $[H, \bar{H}, 0]$ direction, that is normal to the $[H, H, 0]$ direction in reciprocal space and within the basal plane. Projected in this manner, the quartet of incommensurate inelastic magnetic

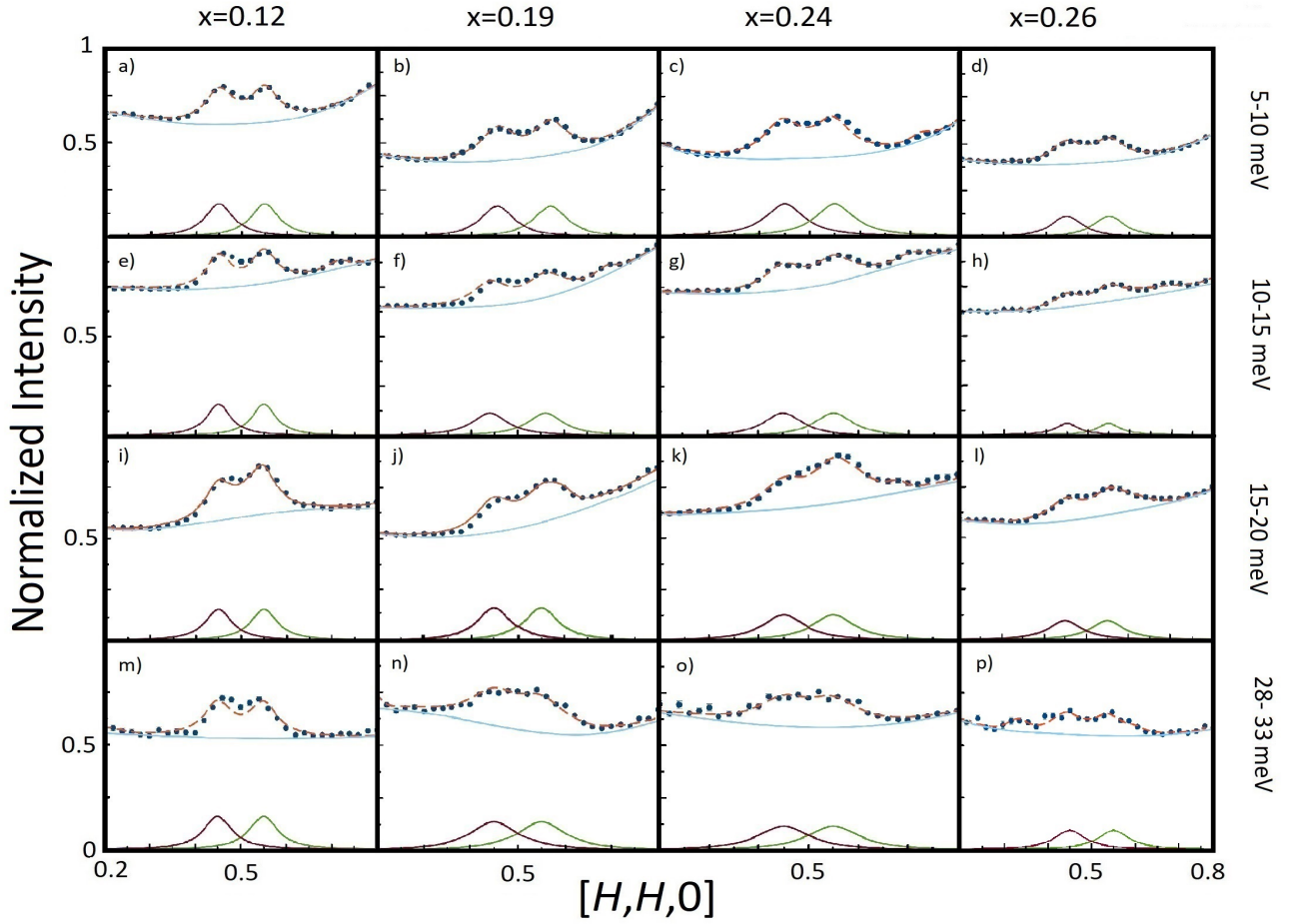


FIG. 5. Diagonal line cuts of the inelastic neutron scattering shown in Fig. 4, along the HH direction in reciprocal space from 5 to 10 meV (a to d), 10 to 15 meV (e to h), 15 to 20 meV (i to l) and 28 to 33 meV (m to p). Such cuts produce two IC peaks, from the 4 IC peaks observed in Fig. 4 a to p. As can be seen, the signal, albeit weak, is clearly observable for all four samples $x = 0.12, 0.19, 0.24$ and 0.26 .

peaks then presents as a pair of peaks symmetrically split off from the $[0.5, 0.5, 0]$ or (π, π) wavevector.

Figure 5 shows such cuts over the energy range 5 meV to 10 meV, in Fig. 5 a) - d), over the range 10 meV to 15 meV in Fig. 5 e) - h), over the 15 meV to 20 meV in Fig. 5 i) - l), and over the range 28 meV to 33 meV in Fig. 5 m) - p). Each of the four panels within these groupings corresponds to the same cut for each of the Nd-LSCO $x=0.12, 0.19, 0.24,$ and 0.26 single crystal samples, as indicated in Fig. 5. The x -dependence of the normalized relative intensity of this dynamic spectral weight is then obtained to fitting the scattering profiles in Fig. 5 to the sum of two Lorentzians symmetrically split off from the $[0.5, 0.5, 0]$ wavevector, with equal intensity and width and a smoothly varying background as indicated by the thin blue lines in Fig. 5. In several cases an additional relatively weak Lorentzian feature was added to the background to account for structure not associated with the parallel spin stripe wavevectors. This occurs primarily for the energy interval 10-15 meV, where the background is relatively high compared with either 5 - 10 meV or 15 - 20 meV, due to overlap with the ~ 10 meV CEF excitation. However a small additional contribution to

the scattering is required in the 15 - 20 meV range, due to optic phonons. Interference with the ~ 25 meV CEF excitation makes reliable fits at higher energies in this data set difficult. The fits to the pair of Lorentzians isolated by this procedure and indicative of the inelastic spectral weight due to Cu^{2+} magnetism are shown in each panel directly below the data plus overall fits.

Figure 6 a) shows the integrated dynamic spectral weight associated with dynamic parallel spin stripes in the four different energy regimes, 5 - 10 meV, 10 - 15 meV, 15 - 20 meV, and 28 - 33 meV, as a function of Sr concentration, x , within $\text{La}_{1.6-x}\text{Nd}_{0.4}\text{Sr}_x\text{CuO}_4$. We observe minimal variation of the spectral weight of these fluctuations for all of $x=0.12, 0.19$ and 0.24 . An $\sim 33\%$ decrease in spectral weight across all energies studied is observed for Nd-LSCO with $x=0.26$, which is close to the end of the superconducting dome, and the only single crystal studied which displays the high temperature tetragonal phase as all temperatures above $T=2\text{K}$. Figure 6 b) shows the x variation in the fitted half width at half maximum (HWHM) of the inelastic Lorentzian peaks, without including the effects of instrumental resolution. This shows a progressive broadening

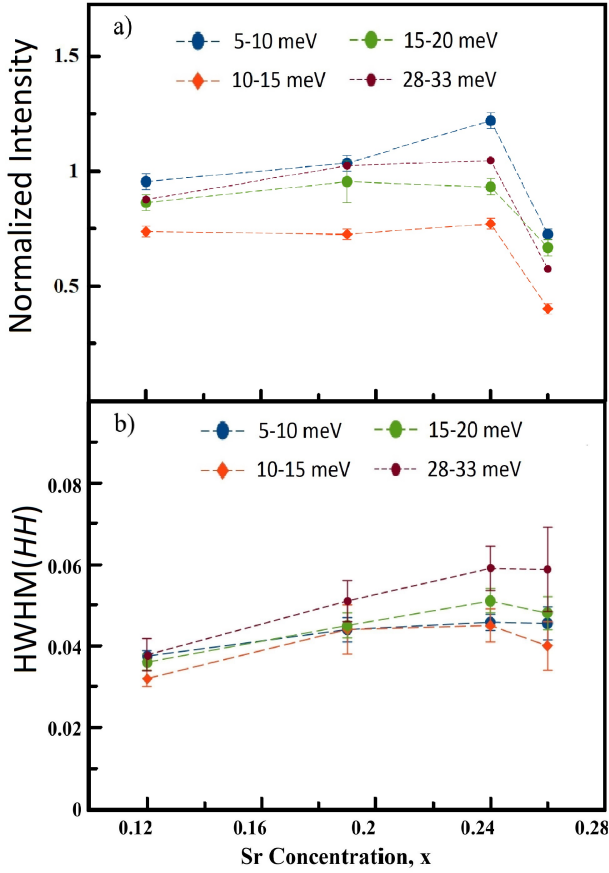


FIG. 6. a) Neutron scattering intensities of the incommensurate peaks near (π, π) wavevectors, presented in Fig. 5, as a function of Sr concentration, x , and integrated in four energy bands: 5 to 10 meV, 10 to 15 meV, 15 to 20 meV and 28 to 33 meV. The normalized intensity evolves little across the phase diagram up to $x=0.24$ then shows a $\sim 35\%$ decrease at $x=0.26$. b) The half width at half maximum (HWHM) from the fit IC peaks widths shown in Fig. 5. Again the HWHM are shown for the same four energy bands as in a) and as a function of Sr concentration, x .

of the inelastic spectral weight in reciprocal space at all energies studied. Given that the integrated dynamic spectral weight is slowly varying with a decrease at the highest hole-doping, x , the dynamic parallel spin stripes are qualitatively harder to see with increasing x , as a survey of Fig. 4 demonstrates. Accounting for the momentum resolution semi-quantitatively, our current measurements are consistent with an $\sim 50\%$ increase in the width of this incommensurate inelastic scattering, consistent with the decrease in correlation length previously reported using elastic triple axis neutron scattering on the same crystals[14].

The energy dependence of the parallel spin stripe fluctuations was investigated for the four Nd-LSCO single crystals, $x=0.12, 0.19, 0.24$ and 0.26 , using the same analysis discussed above, but employing a smaller, 2 meV, energy window so as to obtain finer detail in the energy dependence of $\int S(\mathbf{Q}, \hbar\omega)d\mathbf{Q}$, where the \mathbf{Q} integral is over the incommensurate ordering

wavevectors. Note that $\int S(\mathbf{Q}, \hbar\omega)d\mathbf{Q} = \int \chi''(\mathbf{Q}, \hbar\omega)d\mathbf{Q}$ for the range of energies ($\hbar\omega \geq 6$ meV) and temperatures (5 K) considered here. This is shown in Fig. 7, in 2 meV steps from 6 meV to 22 meV and 30 meV and 32 meV. We observe a consistent form for this dynamic spectral weight at all x , with a maximum in the spectral weight near 17 meV, a fall off beyond 30 meV, and a low-energy upturn near the lowest energies measured (5 meV). This form is largely consistent with that observed in both underdoped LBCO[30, 31] and LSCO at a variety of dopings[33–35], where peaks in $\chi''(\hbar\omega)$ at incommensurate ordering wavevectors are observed near 15 - 17 meV and again just above 30 meV. As discussed for LBCO[30, 31], these energies correspond to crossings of the vertically-dispersing dynamic parallel spin stripe scattering, and both zone boundary acoustic phonons, as well as optic phonons near 18 and 30 meV. This earlier work proposed this structured energy dependence arose from hybridization of these phonons with the parallel spin stripe fluctuations. Independent of its origin, this very distinctive energy dependence appears to be a universal feature of the 214 hole-doped cuprates, from underdoped to optimally and overdoped regimes, and the end of superconductivity.

IV. DISCUSSION

Our present results show clearly that the spectral weight for dynamic parallel spin stripes around (π, π) wavevectors below ~ 33 meV in Nd-LSCO change relatively little with hole doping from the 1/8 anomaly at $x=0.12$, to optimal doping at $x=0.19$, through the pseudogap quantum critical point at $x=0.24$ and $x=0.26$, the latter of which is close to the end of the superconducting dome. This raises at least two important points for consideration: How do these results compare to the results of earlier studies on other 214 cuprate superconductors? How do these results fit into the context of theory and what is known about the evolution of the Fermi surface of these systems at relatively high doping?

Earlier inelastic scattering results from spin fluctuations in 214 cuprate superconductors present an evolving and somewhat incomplete picture[36, 37]. In part, this is because both inelastic neutron scattering and resonant inelastic x-ray scattering (RIXS) capabilities have themselves evolved considerably over the last decade. In part this is also due to the fact that neutron scattering tends to concentrate on wavevectors near (π, π) , where the spectral weight is strongest, while RIXS is limited to relatively small wavevectors and cannot reach in-plane wavevectors as large as (π, π) .

The earliest work examining the hole-doping, x , dependence of the magnetic spectral weight at low energies (≤ 10 meV) and near (π, π) in LSCO showed the maximum $\chi''(\omega)$ to scale with superconducting T_C for $0.25 \leq x \leq 0.3$ [36]. This result implied that the magnetic spectral weight falls off relatively strongly with doping, at least at high doping. Later neutron work extended this to higher energies with a similar conclusion, with a large difference in dynamic spectral weight up to ~ 100 meV reported between LBCO at $x=0.125$ and LSCO at $x=0.25$ and 0.3 [37]. However RIXS measurements on epitaxial thin films, first in the $(H, 0)$ direction of in-plane re-

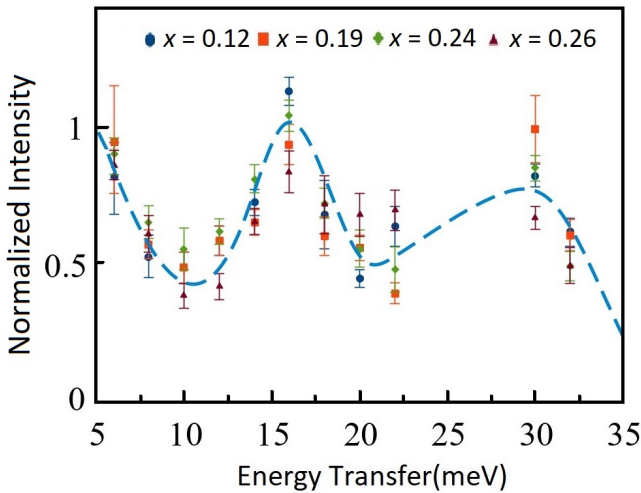


FIG. 7. Summary of the integrated neutron scattering intensity vs energy for all four single crystal samples, and across energy from 6meV to 33 meV. With this relatively small energy binning (2 meV) the spectral weight of the dynamic parallel spin stripes is $\sim x$ -independent. The energy dependence of this spectral weight is structured with a significant peak near ~ 17 meV, consistent with earlier measurements on LBCO and LSCO.

reciprocal space[23, 24], and later in the (H, H) direction[38], both reported high energy “paramagnon” scattering with relatively little x -dependence to its integrated spectral weight over a broad range of hole-doping in LSCO, $0 \leq x \leq 0.4$ for the $(H, 0)$ direction and $0 \leq x \leq 0.26$ for the (H, H) direction. The long wavelength of the incident x -rays employed at the Cu L_3 edge in these RIXS measurements restricted the largest wavevector accessed in the (H, H) direction to be just beyond $(0.3, 0.3)$ and well removed from the (π, π) position, $(0.5, 0.5)$. Work by Wakimoto *et al* in 2015 [39] and Monney *et al* in 2016 [40] showed that while high energy neutron scattering and RIXS scattering covered complementary regions of the Brillouin zone, the “paramagnon” dispersion measured with both techniques was largely consistent, and closely resembled that of the 214 parent material La_2CuO_4 in each of the (H, H) and $(H, 0)$ in-plane directions in reciprocal space. Later RIXS measurements [25] on LSCO single crystals at $x=0, 0.12$ and 0.16 , show an initial increase in “paramagnon” spectral weight at both $(0.25, 0)$ and $(0.25, 0.25)$ and up to ~ 400 meV from $x=0$ to $x=0.12$, with little change between $x=0.12$ and 0.16 .

Our results on the persistence of the spectral weight for dynamic parallel spin stripes, that is magnetic fluctuations near (π, π) wavevectors, and below ~ 33 meV in Nd-LSCO appear inconsistent with earlier neutron results on LSCO, as discussed above. It is possible that the incommensurate magnetism in LSCO and LBCO is simply different than that in Nd-LSCO, although this seems unlikely given the strong similarities between all the 214 cuprate families. The estimate of the normalized intensities of these magnetic excitations becomes progressively more difficult with increasing x , as the widths of these excitations becomes broader, and they are therefore harder to distinguish from both background and other

excitations, such as phonons. Better neutron instrumentation, as is being continuously developed, will no doubt help resolve these issues going forward. However, our measurements showing the persistence of the dynamic parallel spin stripes over this broad range of doping is consistent with the results of all RIXS measurements reported to date on LSCO, at in plane wavevectors both along (HH) and $(H0)$.

Several recent works have focused on theoretical models relevant to the cuprates near optimal and high doping [[26, 27, 41]. Two of these allow for concrete comparisons with the present neutron scattering work on Nd-LSCO.

A recent theoretical study has examined the Hubbard model on a two dimensional square lattice and both near-neighbour and next-near neighbour hopping, as well as an on-site Coulomb interaction[26]. This model can account for both a Lifshitz transition at high doping, and a transition to an electron-like Fermi surface at p^* . As a function of hole doping, this theory shows an evolution in $\int \chi'' d\omega$ from concentrated around (π, π) at $x=0.15$ to more evenly distributed throughout the Brillouin zone at $x=0.25$. At low energies $\chi''(\mathbf{Q}, \hbar\omega)$ shows strong x -dependence at (π, π) , but a much weaker x -dependence at $(\pi, 0)$ and $(0, 0)$.

The work by Shackleton *et al* [27] is particularly interesting. It presents finite-cluster exact diagonalization of a t-J model for $S=1/2$ electrons with random all-to-all hopping, and hence can be thought of as a model for a quantum spin glass. At zero temperature, it shows a spin glass phase with static order out to $p_c \sim 0.33$, similar to the observed behaviour of quasi-Bragg peaks in Nd-LSCO out to at least $x=0.26$, but with dynamic spectral weight which is $\sim x$ -independent over a large range of dopings, similar to that reported here.

One conclusion which seems clear is that the persistence of the dynamic parallel spin stripes which we observe in Nd-LSCO is inconsistent with models of the inelastic incommensurate magnetic scattering arising from nesting of portions of the Fermi surface. Such an origin for the dynamic parallel spin stripes would imply substantial changes in this scattering across $p^*=x^*=0.23$ in Nd-LSCO, as Hall measurements in Nd-LSCO show a pronounced change in the x -dependence of the Hall number, from p to $1+p$, implying a significant change in Fermi surface properties at p^* . ARPES measurements on the Nd-LSCO system by C.E.Matt *et al*[42] have also shown the closing of an antinodal pseudogap at $\sim p^*$. We therefore believe that a local spin nature to the incommensurate spin fluctuations is required to account for such persistence, making them vestiges of the parent insulator. This persistence of the dynamic parallel spin stripes we observe is captured by the quantum spin glass, random t-J model[27], but does not appear to be accounted for in detail within the aforementioned Hubbard model theory[26], which predicts relatively strong reduction in $\chi''(\mathbf{Q}, \hbar\omega)$ at low $\hbar\omega$, and at (π, π) as a function of x . However, the overall x dependence of the calculated $\int \int \chi'' d\omega d\mathbf{Q}$, integrated in \mathbf{Q} over the Brillouin zone, is likely much more modest, and could be more consistent with the conclusions for the persistence of dynamic parallel spin stripes we present here.

V. CONCLUSIONS

We have carried out TOF inelastic neutron scattering measurements on single crystals of Nd-LSCO with hole doping, x , ranging from the 1/8 anomaly at $x=0.12$ to optimal doping at $x=0.19$, to just beyond the pseudogap quantum critical point at $x=0.24$, to the end of the superconducting dome, at $x=0.26$. For all four dopings, we observe structured spectral weight at incommensurate wavevectors around (π, π) , which peaks at ~ 17 meV, consistent with earlier measurements on both LBCO [30, 31] and LSCO [33–35].

Our main conclusion is that this incommensurate magnetic spectral weight near (π, π) , which we refer to as dynamic parallel spin stripes, is \sim independent of hole-doping, x , for $0.12 \leq x \leq 0.24$, and then displays an $\sim 33\%$ drop at $x=0.26$, as superconductivity recedes. This observed persistence of the low energy (< 33 meV) spin fluctuations in Nd-LSCO with doping is consistent with the persistence of relatively high energy “paramagnon” scattering reported in LSCO using RIXS techniques [24].

Recent elastic neutron scattering studies on the same four single crystal Nd-LSCO samples showed “static” parallel spin stripe order in the form of quasi-Bragg peaks to extend out to the end of the superconducting dome, albeit with diminishing ordered moment and in plane correlation lengths [14]. The present inelastic measurements reach a similar conclusion regarding dynamic parallel spin stripe fluctuations: that they persist across the superconducting dome, with largely undiminished spectral weight, until the end of the superconducting dome, and continue to play a role in the physics of superconducting hole-doped cuprates at high doping. Both of these features are reproduced within the recent quantum spin glass, random t - J model [27]. We hope that this study helps to guide future studies, both theory and experiment, such that the intertwined nature of the superconducting and magnetic states of matter as expressed in the cuprates can be fully understood.

VI. ACKNOWLEDGMENTS

We thank Amireza Ataei, Nigel Hussey, Takashi Imai, Hae-Young Kee, Steven Kivelson, Graeme Luke, Subir Sachdev, Louis Taillefer, and John Tranquada for useful and stimulating discussions. This work was supported by the Natural Sciences and Engineering Research Council of Canada. This research used resources at the Spallation Neutron Source, DOE Office of Science User Facilities operated by the Oak Ridge National Laboratory (ORNL).

VII. APPENDIX A: ALTERNATIVE, GAUSSIAN LINESHAPE DESCRIPTION OF THE CONSTANT-ENERGY, $[H, H, 0]$ SCANS OF THE DYNAMIC PARALLEL SPIN STRIPES

In the section III and Fig. 5, we employed a fitting algorithm of constant-energy cuts of the inelastic neutron scattering data which used Lorentzian functions to describe the inelastic, IC

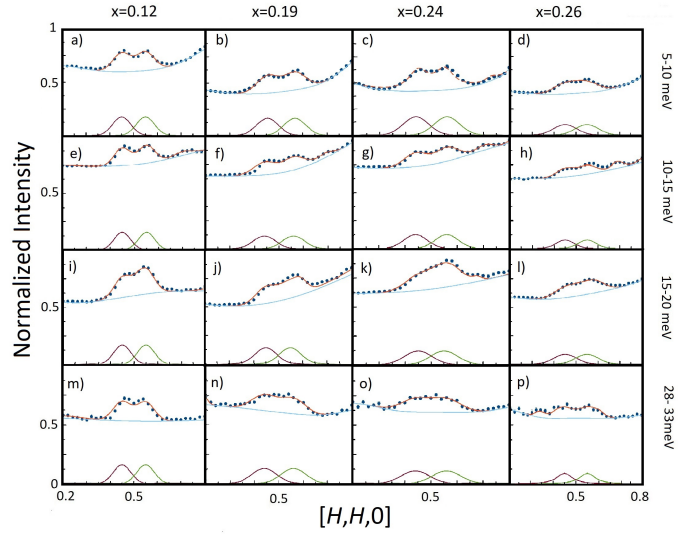


FIG. 8. Diagonal line cuts of the inelastic neutron scattering shown in Fig. 4, along the HH direction in reciprocal space from 5 to 10 meV (a to d), 10 to 15 meV (e to h), 15 to 20 meV (i to l) and 28 to 33 meV (m to p). The IC peaks are now fitted with Gaussian lineshapes, as opposed to the Lorentzian lineshapes employed in Fig. 5.

magnetic peaks near the (π, π) positions in reciprocal space. The resulting normalized intensities and HWHM of the fitted peaks were plotted in Fig. 6 which showed little variation of the IC peak intensities across $x=0.12, 0.19$ and 0.24 , with an $\sim 33\%$ drop in spectral weight for $x=0.26$. In the interest of investigating the sensitivity of these results to the inelastic IC lineshape employed, we repeated the analysis leading to the fittings shown in Fig. 5, but using Gaussian lineshapes, rather than Lorentzian lineshapes to describe the IC inelastic peaks. The primary difference between the two is that the Gaussian lineshapes have much restricted tails, as compared with Lorentzian. The results of this alternative fitting protocol is shown in Fig. 8, which also results in a good quality fit to the data. The resulting x -dependence of the normalized integrated intensities of the fitted IC inelastic scattering, as well as the corresponding HWHM are shown in Fig. 9. As can be seen, the trend of the x -dependence of both the spectral weight and the HWHM are very similar to the results shown in Fig. 6, and we conclude that our results regarding the x -dependence of the inelastic IC spectral weight, that is the persistence of the strength of the dynamic parallel spin stripes across $0.12 \leq x \leq 0.26$ are robust to the details of the choice of function used to describe them.

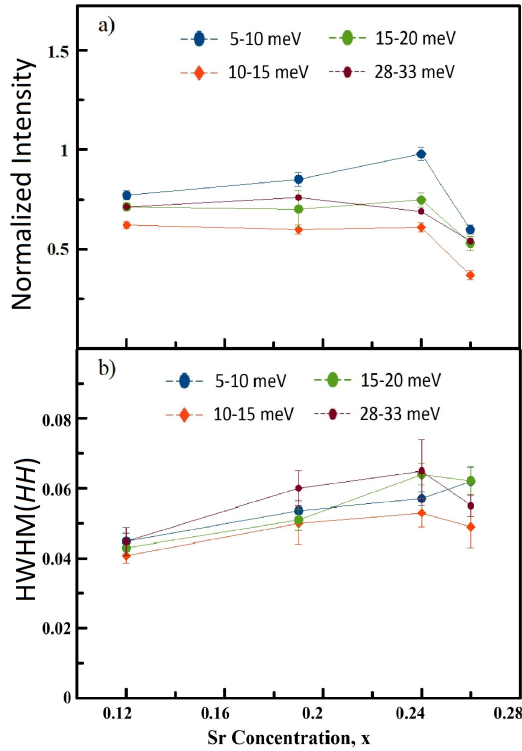


FIG. 9. a) Normalized neutron scattering intensities of the incommensurate peaks near (π, π) wavevectors, presented in Fig. 8, as a function of Sr concentration, x , and integrated in four energy bands b) The half width at half maximum (HWHM) from the fit IC peaks widths shown in Fig. 8. All data are obtained using Gaussian lineshapes, as opposed to the Lorentzian lineshapes employed in Fig. 6.

-
- [1] M. A. Kastner, R. J. Birgeneau, G. Shirane, and Y. Endoh, “Magnetic, transport, and optical properties of monolayer copper oxides,” *Rev. Mod. Phys.* **70**, 897–928 (1998).
- [2] B. Keimer, N. Belk, R.J. Birgeneau, A. Cassanho, C.Y. Chen, M. Greven, M.A. Kastner, A. Aharony, Y. Endoh, R.W. Erwin, and G. Shirane, “Magnetic Excitations in Pure, Lightly Doped, and Weakly Metallic La_2CuO_4 ,” *Physical Review B* **46**, 14034 (1992).
- [3] J. H. Cho, F.C. Chou, and D. C. Johnston, “Phase Separation and Finite Size Scaling in $\text{La}_{2-x}\text{Sr}_x\text{CuO}_{4+\delta}$ [$0 < (x, \gamma) < 0.03$],” *Physical Review Letters* **70**, 222 (1993).
- [4] F.C. Chou, F. Borsa, J.H. Cho, D.C. Johnston, A. Lascialfari, D.R. Torgeson, and J. Ziolo, “Magnetic Phase Diagram of Lightly Doped $\text{La}_{2-x}\text{Sr}_x\text{CuO}_4$ from La-139 Nuclear Quadrupole Resonance,” *Physical Review Letters* **71**, 2323 (1993).
- [5] F. Borsa, P. Carretta, J.H. Cho, F.C. Chou, Q. Hu, D.C. Johnston, A. Lascialfari, D.R. Torgeson, R.J. Gooding, N.M. Salem, and K.J.E. Vos, “Staggered Magnetization in $\text{La}_{2-x}\text{Sr}_x\text{CuO}_4$ from La-139 NQR and μSR : Effects of Sr Doping in the Range $0 < x < 0.02$,” *Physical Review B* **52**, 7334 (1995).
- [6] J.M. Tranquada, B.J. Sternlieb, J.D. Axe, Y. Nakamura, and S. Uchida, “Evidence for Stripe Correlations of Spins and Holes in Copper Oxide Superconductors,” *Nature* **375**, 561–563 (1995).
- [7] J.M. Tranquada, J.D. Axe, N. Ichikawa, A.R. Moodenbaugh, Y. Nakamura, and S. Uchida, “Coexistence of, and competition between, superconductivity and charge-stripe order in $\text{La}_{1.6-x}\text{Nd}_{0.4}\text{Sr}_x\text{CuO}_4$,” *Physical Review Letters* **78**, 338 (1997).
- [8] J.M. Tranquada, N. Ichikawa, and S. Uchida, “Glassy Nature of Stripe Ordering in $\text{La}_{1.6-x}\text{Nd}_{0.4}\text{Sr}_x\text{CuO}_4$,” *Physical Review B* **59**, 14712 (1999).
- [9] J.M. Tranquada, J.D. Axe, N. Ichikawa, Y. Nakamura, S. Uchida, and B. Nachumi, “Neutron-Scattering Study of Stripe-Phase Order of Holes and Spins in $\text{La}_{1.48}\text{Nd}_{0.4}\text{Sr}_{0.12}\text{CuO}_4$,” *Physical Review B* **54**, 7489 (1996).
- [10] S. Wakimoto, G. Shirane, Y. Endoh, K. Hirota, S. Ueki, K. Yamada, R.J. Birgeneau, M.A. Kastner, Y.S. Lee, P.M. Gehring, and S.H. Lee, “Observation of Incommensurate Magnetic Correlations at the Lower Critical Concentration for Superconductivity in $\text{La}_{2-x}\text{Sr}_x\text{CuO}_4$ ($x=0.05$),” *Physical Review B* **60**, R769

- (1999).
- [11] S.R. Dunsiger, Y. Zhao, B.D. Gaulin, Y. Qiu, P. Bourges, Y. Sidis, J.R.D. Copley, A. Kallin, E.M. Mazurek, and H.A. Dabkowska, “Diagonal and Collinear Incommensurate Spin Structures in Underdoped $\text{La}_{2-x}\text{Ba}_x\text{CuO}_4$,” *Physical Review B* **78**, 092507 (2008).
- [12] M. Fujita, H. Goka, K. Yamada, J.M. Tranquada, and L.P. Regnault, “Stripe Order, Depinning, and Fluctuations in $\text{La}_{1.875}\text{Ba}_{0.125}\text{CuO}_4$ and $\text{La}_{1.875}\text{Ba}_{0.075}\text{Sr}_{0.050}\text{CuO}_4$,” *Physical Review B* **70**, 104517 (2004).
- [13] S. Wakimoto, J.M. Tranquada, T. Ono, K.M. Kojima, S. Uchida, S-H Lee, P.M. Gehring, and R.J. Birgeneau, “Diagonal Static Spin Correlation in the Low-Temperature Orthorhombic Pccn Phase of $\text{La}_{1.55}\text{Nd}_{0.45}\text{Sr}_{0.05}\text{CuO}_4$,” *Physical Review B* **64**, 174505 (2001).
- [14] Q. Ma, K. C. Rule, Z. W. Cronkwright, M. Dragomir, G. Mitchell, E. M. Smith, S. Chi, A. I. Kolesnikov, M. B. Stone, and B. D. Gaulin, “Parallel spin stripes and their coexistence with superconducting ground states at optimal and high doping in $\text{La}_{1.6-x}\text{Nd}_{0.4}\text{Sr}_x\text{CuO}_4$,” *Phys. Rev. Research* **3**, 023151 (2021).
- [15] B. Michon, C. Girod, S. Badoux, J. Kačmarčík, Q. Ma, M. Dragomir, H.A. Dabkowska, B.D. Gaulin, J-S Zhou, S. Pyon, Takayaman T., Takagi H., Verret S., Doiron-Leyraud N., Marce-nat C., Taillefer L., and Klein T., “Thermodynamic Signatures of Quantum Criticality in Cuprate Superconductors,” *Nature* **567**, 218–222 (2019).
- [16] S. Badoux, W. Tabis, F. Laliberté, G. Grissonnanche, B. Vignolle, D. Vignolles, J. Béard, D.A. Bonn, W.N. Hardy, R. Liang, Doiron-Leyraud N., Taillefer L., and Proust C., “Change of carrier density at the pseudogap critical point of a cuprate superconductor,” *Nature* **531**, 210–214 (2016).
- [17] C. Collignon, S. Badoux, S. A. Afshar, B. Michon, F. Laliberté, O. Cyr-Choinière, J.-S. Zhou, S. Licciardello, S. Wiedmann, N. Doiron-Leyraud, and Louis Taillefer, “Fermi-surface transformation across the pseudogap critical point of the cuprate superconductor $\text{La}_{1.6-x}\text{Nd}_{0.4}\text{Sr}_x\text{CuO}_4$,” *Phys. Rev. B* **95**, 224517 (2017).
- [18] M Lizaire, A Legros, A Gourgout, S Benhabib, S Badoux, F Laliberté, M-E Boulanger, A Ataei, G Grissonnanche, D LeBoeuf, *et al.*, “Transport signatures of the pseudogap critical point in the cuprate superconductor $\text{Bi}_2\text{Sr}_{2-x}\text{La}_x\text{CuO}_{6+\delta}$,” arXiv preprint arXiv:2008.13692 (2020).
- [19] M. Dragomir, Q. Ma, J. P. Clancy, A. Ataei, P. A. Dube, S. Sharma, A. Huq, H. A. Dabkowska, L. Taillefer, and B. D. Gaulin, “Materials preparation, single-crystal growth, and the phase diagram of the cuprate high-temperature superconductor $\text{La}_{1.6-x}\text{Nd}_{0.4}\text{Sr}_x\text{CuO}_4$,” *Phys. Rev. Materials* **4**, 114801 (2020).
- [20] Mehdi Frachet, Igor Vinograd, Rui Zhou, Siham Benhabib, Shangfei Wu, Hadrien Mayaffre, Steffen Krämer, Sanath K Ramakrishna, Arneil P Reyes, Jérôme Debray, *et al.*, “Hidden magnetism at the pseudogap critical point of a cuprate superconductor,” *Nature Physics* **16**, 1064–1068 (2020).
- [21] N. K Gupta, C McMahon, R Sutarro, T Shi, R Gong, H. I Wei, K.M. Shen, F. He, Q Ma, M Dragomir, B. D. Gaulin, and Hawthorn D.G., “Vanishing nematic order beyond the pseudogap phase in overdoped cuprate superconductors,” *Proceedings of the National Academy of Sciences* **118** (2021).
- [22] H Miao, G Fabbris, RJ Koch, DG Mazzone, CS Nelson, R Acevedo-Esteves, GD Gu, Y Li, T Yilmaz, K Kaznatcheev, *et al.*, “Charge density waves in cuprate superconductors beyond the critical doping,” *npj Quantum Materials* **6**, 1–6 (2021).
- [23] MPM Dean, RS Springell, C Monney, KJ Zhou, J Pereiro, I Božović, Bastien Dalla Piazza, HM Rønnow, E Morenzoni, J Van Den Brink, *et al.*, “Spin excitations in a single La_2CuO_4 layer,” *Nature materials* **11**, 850–854 (2012).
- [24] MPM Dean, Greta Dellea, Ross S Springell, Flora Yakhou-Harris, Kurt Kummer, NB Brookes, X Liu, YJ Sun, J Strle, Thorsten Schmitt, *et al.*, “Persistence of magnetic excitations in $\text{La}_{2-x}\text{Sr}_x\text{CuO}_4$ from the undoped insulator to the heavily overdoped non-superconducting metal,” *Nature materials* **12**, 1019–1023 (2013).
- [25] H. C. Robarts, M. Barthélemy, K. Kummer, M. García-Fernández, J. Li, A. Nag, A. C. Walters, K. J. Zhou, and S. M. Hayden, “Anisotropic damping and wave vector dependent susceptibility of the spin fluctuations in $\text{La}_{2-x}\text{Sr}_x\text{CuO}_4$ studied by resonant inelastic x-ray scattering,” *Phys. Rev. B* **100**, 214510 (2019).
- [26] Thomas A. Maier, Seher Karakuzu, and Douglas J. Scalapino, “Overdoped end of the cuprate phase diagram,” *Phys. Rev. Research* **2**, 033132 (2020).
- [27] Henry Shackleton, Alexander Wietek, Antoine Georges, and Subir Sachdev, “Quantum phase transition at nonzero doping in a random $t-j$ model,” *Phys. Rev. Lett.* **126**, 136602 (2021).
- [28] G.E. Granroth, A.I. Kolesnikov, T.E. Sherline, J.P. Clancy, K.A. Ross, JPC Ruff, B.D. Gaulin, and S.E. Nagler, “SEQUOIA: A Newly Operating Chopper Spectrometer at the SNS,” in *Journal of Physics-Conference Series*, Vol. 251 (2010) p. 012058.
- [29] John M Tranquada, “Spins, stripes, and superconductivity in hole-doped cuprates,” in *AIP Conference Proceedings*, Vol. 1550 (American Institute of Physics, 2013) pp. 114–187.
- [30] J. J. Wagman, J. P. Carlo, J. Gaudet, G. Van Gastel, D. L. Abernathy, M. B. Stone, G. E. Granroth, A. I. Kolesnikov, A. T. Savici, Y. J. Kim, H. Zhang, D. Ellis, Y. Zhao, L. Clark, A. B. Kallin, E. Mazurek, H. A. Dabkowska, and B. D. Gaulin, “Neutron scattering studies of spin-phonon hybridization and superconducting spin gaps in the high-temperature superconductor $\text{La}_{2-x}(\text{Sr}, \text{Ba})_x\text{CuO}_4$,” *Phys. Rev. B* **93**, 094416 (2016).
- [31] J. J. Wagman, D. Parshall, M. B. Stone, A. T. Savici, Y. Zhao, H. A. Dabkowska, and B. D. Gaulin, “Quasi-two-dimensional spin and phonon excitations in $\text{La}_{1.965}\text{Ba}_{0.035}\text{CuO}_4$,” *Phys. Rev. B* **91**, 224404 (2015).
- [32] J. Gaudet, A. M. Hallas, C. R. C. Buhariwalla, G. Sala, M. B. Stone, M. Tachibana, K. Baroudi, R. J. Cava, and B. D. Gaulin, “Magnetoelastically induced vibronic bound state in the spin-ice pyrochlore $\text{Ho}_2\text{Ti}_2\text{O}_7$,” *Phys. Rev. B* **98**, 014419 (2018).
- [33] O. J. Lipscombe, B. Vignolle, T. G. Perring, C. D. Frost, and S. M. Hayden, “Emergence of coherent magnetic excitations in the high temperature underdoped $\text{La}_{2-x}\text{Sr}_x\text{CuO}_4$ superconductor at low temperatures,” *Phys. Rev. Lett.* **102**, 167002 (2009).
- [34] B Vignolle, SM Hayden, DF McMorrow, Henrik M Rønnow, B Lake, CD Frost, and TG Perring, “Two energy scales in the spin excitations of the high-temperature superconductor $\text{La}_{2-x}\text{Sr}_x\text{CuO}_4$,” *Nature Physics* **3**, 163–167 (2007).
- [35] Yangmu Li, Ruidan Zhong, M. B. Stone, A. I. Kolesnikov, G. D. Gu, I. A. Zaliznyak, and J. M. Tranquada, “Low-energy antiferromagnetic spin fluctuations limit the coherent superconducting gap in cuprates,” *Phys. Rev. B* **98**, 224508 (2018).
- [36] S. Wakimoto, H. Zhang, K. Yamada, I. Swainson, Hyunkyung Kim, and R. J. Birgeneau, “Direct relation between the low-energy spin excitations and superconductivity of overdoped high- T_c superconductors,” *Phys. Rev. Lett.* **92**, 217004 (2004).
- [37] S. Wakimoto, K. Yamada, J. M. Tranquada, C. D. Frost, R. J. Birgeneau, and H. Zhang, “Disappearance of antiferromagnetic spin excitations in overdoped $\text{La}_{2-x}\text{Sr}_x\text{CuO}_4$,” *Phys. Rev. Lett.* **98**, 247003 (2007).
- [38] D. Meyers, H. Miao, A. C. Walters, V. Bisogni, R. S. Springell, M. d’Astuto, M. Dantz, J. Pellicciari, H. Y. Huang, J. Okamoto, D. J. Huang, J. P. Hill, X. He, I. Božović, T. Schmitt, and

- M. P. M. Dean, “Doping dependence of the magnetic excitations in $\text{La}_{2-x}\text{Sr}_x\text{CuO}_4$,” *Phys. Rev. B* **95**, 075139 (2017).
- [39] S. Wakimoto, K. Ishii, H. Kimura, M. Fujita, G. Dellea, K. Kummer, L. Braicovich, G. Ghiringhelli, L. M. Debeer-Schmitt, and G. E. Granroth, “High-energy magnetic excitations in overdoped $\text{La}_{2-x}\text{Sr}_x\text{CuO}_4$ studied by neutron and resonant inelastic x-ray scattering,” *Phys. Rev. B* **91**, 184513 (2015).
- [40] C. Monney, T. Schmitt, C. E. Matt, J. Mesot, V. N. Strocov, O. J. Lipscombe, S. M. Hayden, and J. Chang, “Resonant inelastic x-ray scattering study of the spin and charge excitations in the overdoped superconductor $\text{La}_{1.77}\text{Sr}_{0.23}\text{CuO}_4$,” *Phys. Rev. B* **93**, 075103 (2016).
- [41] Zi-Xiang Li, Steven A Kivelson, and Dung-Hai Lee, “Superconductor-to-metal transition in overdoped cuprates,” *npj Quantum Materials* **6**, 1–7 (2021).
- [42] C. E. Matt, C. G. Fatuzzo, Y. Sassa, M. Månsson, S. Fatale, V. Bitetta, X. Shi, S. Pailhès, M. H. Berntsen, T. Kurosawa, M. Oda, N. Momono, O. J. Lipscombe, S. M. Hayden, J.-Q. Yan, J.-S. Zhou, J. B. Goodenough, S. Pyon, T. Takayama, H. Takagi, L. Patthey, A. Bendounan, E. Razzoli, M. Shi, N. C. Plumb, M. Radovic, M. Grioni, J. Mesot, O. Tjernberg, and J. Chang, “Electron scattering, charge order, and pseudogap physics in $\text{La}_{1.6-x}\text{Nd}_{0.4}\text{Sr}_x\text{CuO}_4$: An angle-resolved photoemission spectroscopy study,” *Phys. Rev. B* **92**, 134524 (2015).

Chapter 7

Conclusion

7.1 Materials Synthesis, Crystal Growth and the Phase diagram of Nd-LSCO

Chapter 4 provided a comprehensive description of the procedures of material synthesis and single crystal growth that we employed to produce samples of $\text{La}_{1.6-x}\text{Nd}_{0.4}\text{Sr}_x\text{CuO}_4$ (Nd-LSCO), across the entire phase diagram from $x=0.01$ to 0.4 ($x = 0.07$ to 0.26 as single crystal). It is now well known that there are several established families of cuprate superconductors, all of which are based on hole or electron doping of CuO_2 layers. These structures can be organized into single layer structures, bi-layer structures, and more complicated stackings of this two dimensional structure. Therefore much activity has been devoted to the study of phenomena in a range of cuprate superconductors, including YBCO, LSCO, Bi-2212, LBCO etc, which have structures made up of different stackings and which are doped by different mechanisms (Sr^{2+} replacing La^{3+} , oxygen stoichiometry etc) [20, 75–79].

A common feature of these families of cuprate superconductors is that a form of magnetic and charge order is often found at low temperatures and these appear to be intertwined with both the pseudogap phase and superconductivity. The La-214 family of materials are single layered copper oxides, and on doping, these exhibit incommensurate magnetic and charge ordered structures. Particular interest in Nd-LSCO has gained momentum as it displays all the complexity of hole-doped cuprate superconductors, but has relatively low superconducting T_C 's. Therefore

the application of a practical lab-based magnetic field can allow Nd-LSCO to remain in its normal state down to the lowest temperatures, even for optimal doping. Transport studies of the pseudogap phase in Nd-LSCO has benefited greatly from this characteristic. Before we started work in this area, the overdoped region of the phase diagram of Nd-LSCO ($x > 0.21$) was not explored very well due to the lack of availability of high quality single crystals. The work in this chapter was intended to improve this situation and document the crystal growth procedures and accompanying characterization of the synthesized materials, so as to open up this research area to greater experimental scrutiny.

In order to acquire a quantitative understanding of the rich structure of the Nd-LSCO family, we conducted neutron powder diffraction experiments, as well as x-ray powder diffraction experiments on all of our powder Nd-LSCO samples. Our results showed that all of the powder samples are phase pure, with no detectable contaminating phases. The unit cell crystallographic parameters and unit cell volumes are systematic and consistent across this series of materials.

The Nd-LSCO single crystals were grown using traveling solvent floating zone technique. High resolution X-Ray diffraction experiments were conducted on Nd-LSCO single crystals with $x = 0.12, 0.17, 0.19, 0.24$ and 0.26 . The change in the structure, from tetragonal to orthorhombic symmetry, alters the peak profiles for certain Bragg peaks. The $(3,3,0)_{HTT}$ Bragg peak, for example, were tracked at different temperatures in this study. At room temperature, the $x = 0.12$ sample resides in LTO1 structure and it persists all the way down to $\sim 68\text{K}$ within this structure. It then undergoes a phase transition into the LTO2 structure, with a corresponding set of peak splittings. The $x = 0.24$ sample was studied by the same procedure, and two structural phase transitions were found. The $x = 0.24$ sample first experiences a second order phase transition where the $(3,3,0)_{HTT}$ Bragg peak experience a continuous split into two peaks at 150K , indicating the onset of the LTO1 phase, which is associated with a tilting of the CuO_6 octahedra. A first order phase transition to LTT was observed at lower temperatures, $\sim 65\text{K}$. The $(3,3,0)_{HTT}$ Bragg peak is broadened in LTT structure comparing with that in HTT, consistent with the fact that the LTT structure is actually pseudo-tetragonal. The

behaviour of the $x = 0.26$ single crystal sample showed distinctively different behaviour, as no phase transition was observed down to the lowest temperature measured, $\sim 4\text{K}$, confirming that the $x = 0.26$ sample remains in the HTT structure at all temperatures ($> 4\text{ K}$) below room temperature.

Magnetic susceptibility data for the single crystals $x = 0.07, 0.12, 0.17, 0.19, 0.225, 0.24$ and 0.26 was acquired using an RF SQUID by applying either a 10 Oe or a 100 Oe field parallel to the c -axis in all samples. The onset of the superconducting transition temperature was estimated by comparing the field-cooled with zero-field-cooled data, and noting the temperature where a splitting between the two was observed. The estimation of the superconducting T_C in this way, was in good agreement with transport measurements provided by Ref.[33]. By taking advantage of the rich structural transitions in Nd-LSCO combined with the superconducting transition temperature data, the Sr concentration in each of the single crystal samples can be determined by cross referencing the pre-existing structural transition and superconducting temperature data from Ref.[33, 80]. We answer one of the remaining questions originally posed in [80], regarding at which concentration the HTT structure terminates. We estimate the boundary of the HTT structure occurs at $p_{LTT} = 0.255 \pm 0.005$ in Nd-LSCO. We also compare the phase diagram of Nd-LSCO with that in LSCO and conclude that the quantum critical point p^* of both materials occurs well below p_{LTT} .

7.2 Parallel Spin Stripes and their co-existence with Superconductivity in Nd-LSCO

Chapter 5 presents mostly elastic neutron scattering data on the static parallel spin stripe magnetic structure in the optimal and overdoped region of the Nd-LSCO, by looking at $x = 0.19, 0.24$ and 0.26 single crystal samples using triple axis spectrometer. The spin stripe order in the underdoped region has been extensively studied and linked with superconductivity as both the diagonal spin stripe phase and superconducting ground states onset at the same Sr x concentration, $x \sim 0.05$. However the evolution of spin (and charge) stripe order into the overdoped region of the phase diagram was much more poorly understood. Previous neutron

scattering data, much of it more than 20 years old, had been interpreted as having the onset temperature for parallel spin stripe order ending close to p^* [12, 59].

Chapter 5 shows that the static parallel stripe orders, albeit weak, exists beyond the quantum critical point $p^* \sim 0.235 \pm 0.005$ [33] and appears to persist until the end of the superconducting dome at $x \sim 0.26$ in the Nd-LSCO systems. This elastic scattering data has been normalized to put it on the same scale with pre-existing measurements [12] to show the relative intensities between different samples. This revealed that the intensity associated with the static spin stripe decreases by as much as an order of magnitude in $x=0.24$ Nd-LSCO compared with $x=0.19$ Nd-LSCO, while the peak width increases by $\sim 50\%$ making it difficult to accurately determine the transition temperature. In the hindsight, the combination of better neutron scattering instrumentation and larger single crystals meant that revisiting the original study in the $x=0.19$ regime would be useful, and indeed our new estimate for the onset of parallel spin stripe order in the $x=0.19$ single crystal exceeds the original estimate for $x=0.2$ by ~ 15 K.

One major question Chapter 5 raises is what role does the antiferromagnetic spin stripe order plays in a broader picture of the pseudogap phase in 214 cuprate superconductors. Various measurements have indicated that the carrier density changes from p to $1+p$ at the quantum critical point p^* . This was tentatively explained by an abrupt change in the Fermi surface from electron-like to hole-like across p^* [43, 81]. Antiferromagnetism has been linked with the Fermi surface reconstruction as a symmetry breaking mechanism that increases the original lattice periodicity. It creates an additional Fermi surface at (π, π) positions that intercepts with the original Fermi surfaces to create hole and electron pockets as demonstrated in Fig.7.1 panel b) and c). One of the supporting pieces of evidence for this hypothesis was that prior neutron scattering was interpreted in terms of magnetic order at $x = 0.20$ fading quickly with increasing doping[12]. This was used to extrapolate the phase boundary of spin stripes to the end of p^* as mentioned before. Such picture then implies static spin stripe order should not exist beyond the quantum critical point p^* . Clearly this is not what we observe as Chapter 5 reports the observation of static (on the time scale of the neutron) parallel spin stripe order in $x = 0.26$ Nd-LSCO.

Finally we conclude that the static parallel spin stripe order exists from $x = 0.19$ to 0.26 beyond p^* . Earlier work had established parallel spin stripe order from the onset of superconductivity at $x=0.05$ to 0.2 . We then proposed a new phase diagram suggesting that static parallel spin stripe is a precursor to a superconducting ground state. Therefore it remains an open question as to what produces the reconstructed the Fermi surface in Nd-LSCO.

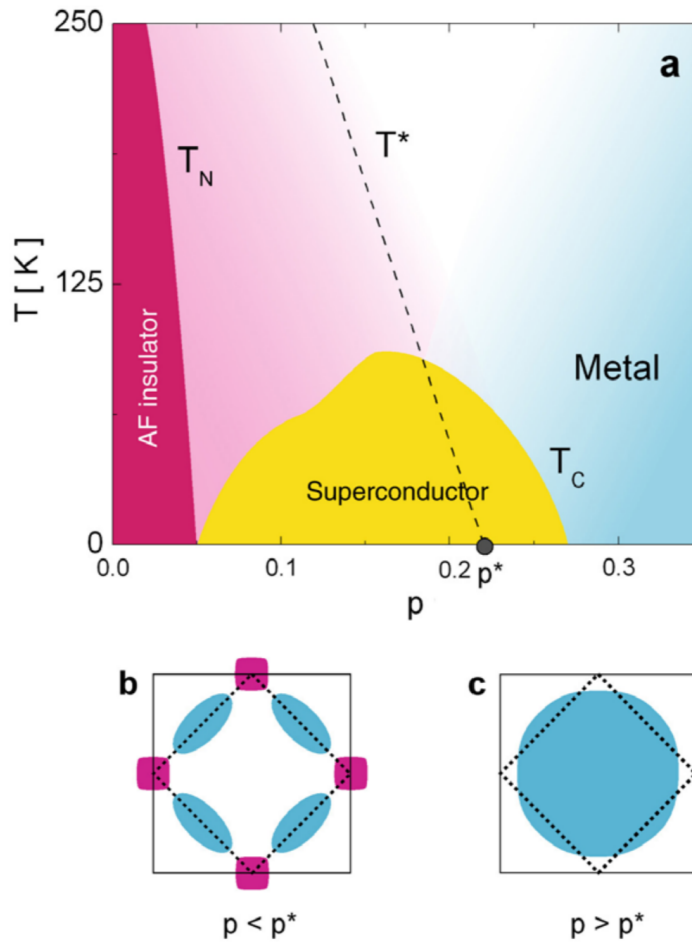


FIGURE 7.1: a) Schematic phase diagram of antiferromagnetic insulating state, superconducting dome, Fermi metal and the pseudogap characterized by the linear T resistivity T^* . b),c) Schematic drawing of the electron like Fermi surface and reconstructed Fermi surface as a result of an order with (π, π) wavevector. Reproduced from [81] with permission.

7.3 The Persistence of Parallel Spin Spin Fluctuations Across the Phase Diagram of Nd-LSCO

The figures of merit associated with neutron scattering using spallation neutron sources have improved by factors of ~ 50 to 100 over the past two decades and this has been combined with the advances in both position and time-sensitive neutron detectors and associated computer and visualization technology, it has become viable to sample very large volumes of reciprocal space and to make sense of this data in a timely fashion. Chapter 6 illustrates how these advances in neutron and related technology can project data from a large four dimensional data set, and that captures the weak inelastic neutron scattering signal of the dynamic spin fluctuations in Nd-LSCO systems.

Chapter 5 showed the static parallel spin stripes are more robust than previously thought, at least in the Nd-LSCO systems. Looking beyond the elastic channel, the inelastic neutron scattering measures parallel spin stripe fluctuations, or dynamic spin stripes, in the form of incommensurate inelastic scattering around (π, π) and symmetry related positions. The origins of this incommensurate inelastic scattering has been argued to arise from: 1. the vestiges of antiferromagnetism from the undoped parent compound La_2CuO_4 ; and 2. arising from neutron-induced transitions between portions of nested Fermi surfaces. ARPES has measured the Fermi surface of LSCO [82] and Nd-LSCO [35] systems. Z.X. Shen and co-workers measured the Fermi surface of LSCO $x = 0.063$, as shown in Fig.7.2 [83]. The antiferromagnetic zone boundary intercepts with the Fermi surface and creates 8 hot spots. From Shen's paper, it was proposed that the incoming neutrons cause a pair of electrons at the hot spots associated with two parallel antinodal segments to be scattered to the opposite sides on the Fermi surface and flip their spins in the process. This could give rise to the the incommensurate peaks around (π, π) positions measured by inelastic neutron scattering.

However, as we have already discussed, thermodynamic measurements on the Nd-LSCO system have revealed a quantum critical point at $p^* = 0.23$. The Hall

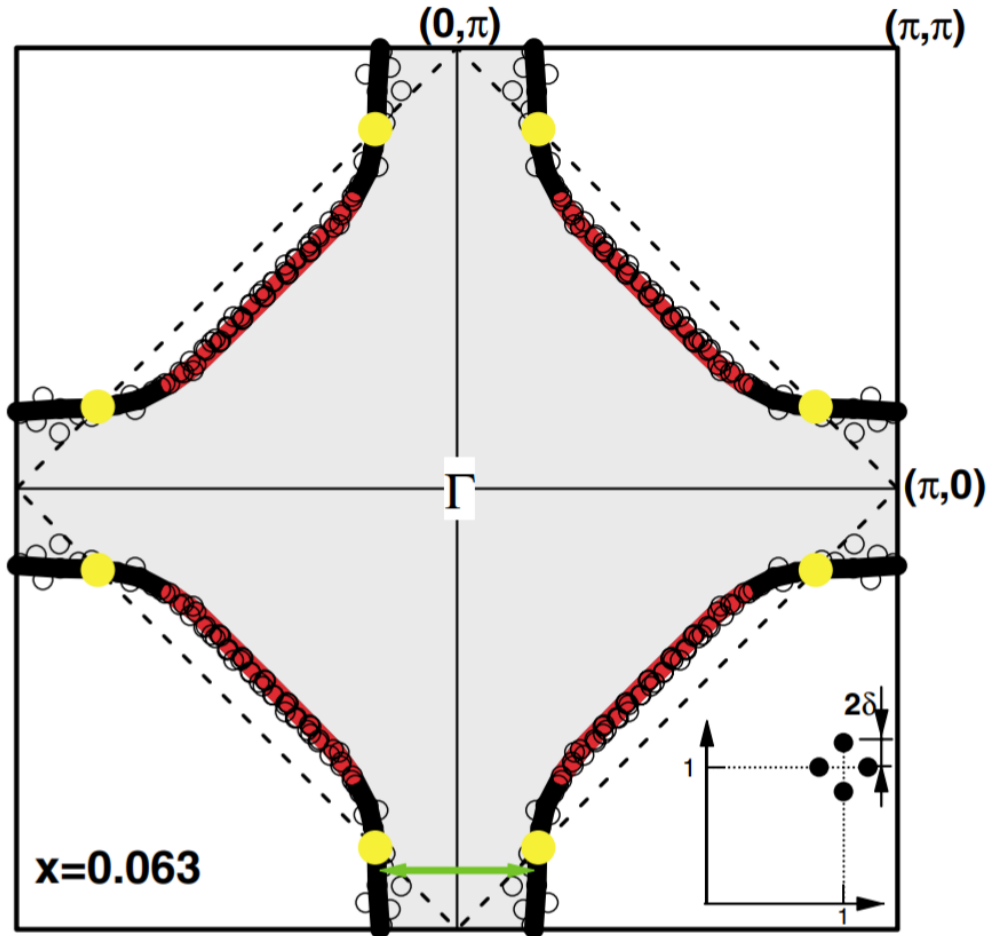


FIGURE 7.2: Fermi surface of LSCO $x = 0.063$. Black solid lines and red open circles are sketched Fermi surface and measured data points. The dotted lines represent the antiferromagnetic zone boundary. There are eight yellow dots marks the intercepts between the AF zone boundary and the Fermi surface. The double headed green arrow is the nesting vector. The inset demonstrates the incommensurate peaks measured by neutron scattering. Reproduced from [83] with permission.

number abruptly changes from being proportional to p to $1+p$ [36, 43, 84] at p^* , suggesting that significant changes to the Fermi surface occur around p^* . A Fermi surface reconstruction would be expected to alter the nested portions of the original Fermi surface. This would then be expected to correspond to a significant change in neutron scattering response for Nd-LSCO doping levels around p^* . The results of Chapter 5 support the "vestiges" picture and are not consistent with the nested Fermi surface picture, as we observe little or no change in the inelastic scattering associated with dynamic parallel spin stripes across p^* .

Previous scattering studies of dynamic magnetism in LSCO have produced a somewhat confusing picture. Previous measurements on LSCO [72, 73] suggested the dynamic spin spectral weight decreases with increased Sr doping up to 120meV from $x = 0.25$ to 0.30 in LSCO. However recent Resonant Inelastic X-ray Scattering (RIXS) on epitaxial thin films measured in two different directions [27, 28, 85] reported persistent "paramagnon" scattering at high energy with little doping dependence in LSCO from $x = 0$ to 0.4 for the $(H, 0)$ direction and from $x = 0$ to 0.26 in the (H, H) direction respectively. Neutron scattering and RIXS cover complementary regions of the reciprocal space and the recent neutron scattering work have shown that the two methods are consistent with each other such that the magnetism has little variance across the LSCO phase diagram [86, 87].

Relating to latest theoretical work, the persistence of the dynamic spin stripe order appears inconsistent with recent Hubbard model studies, which can account for both a Lifshitz transition and a transition to an electron-like Fermi surface at p^* [88]. However recent work by Shackleton *et al.* [74] proposed a new theoretical picture connecting cuprate magnetism to that of a quantum spin glass. It employed finite-cluster exact diagonalization technique to calculate a random t-J model for spin-1/2 electrons. Some of this study's results are shown in Fig. 7.3, where a spin glass phase is linked with quasi static peaks in the spectral weight at low ω . We relate our static spin stripe order as peaks in the quasi elastic region in Fig.7.3 with decreased intensity as x increases up to 0.26 in our case and up to 0.33 in the theoretical paper. The calculated dynamic spectral weight appears to be \sim independent of x over a large range of doping, very similar to our results in Chapter 6.

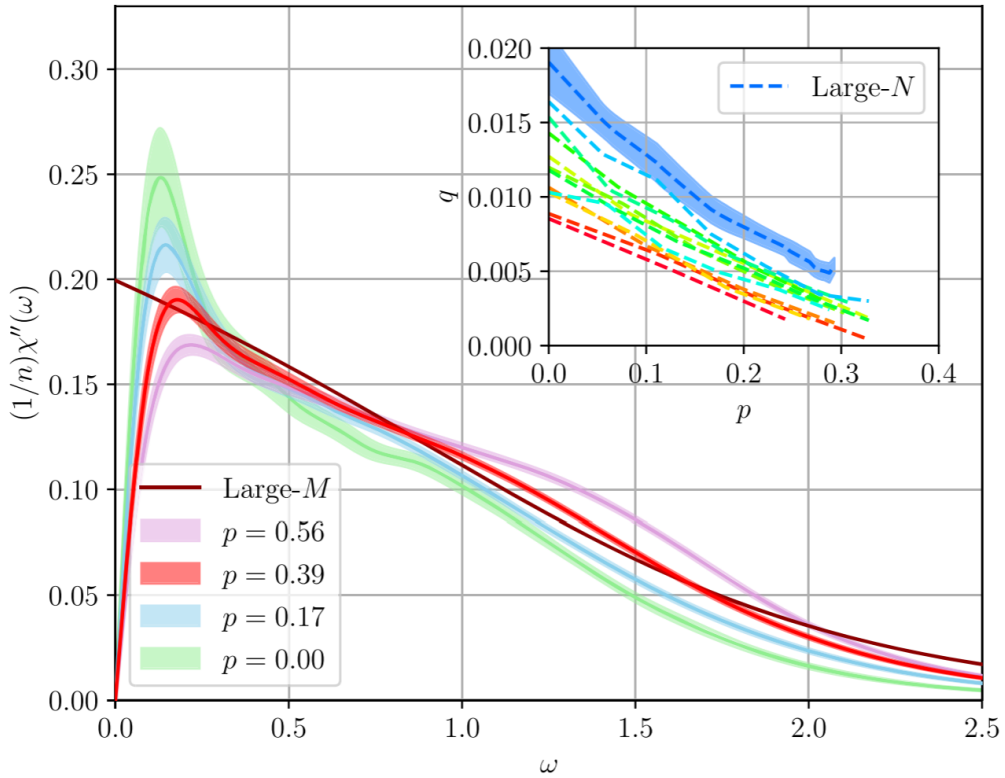


FIGURE 7.3: The spectral function $\chi''(\omega)$ calculated from random t-J model averaged over 100 disorder realizations on an 18-site cluster. We interpret the peaks at $\omega \sim 0.1$ with our quasi-elastic neutron scattering data on the static parallel spin strip order up to $x = 0.26$. We also associate the region where $\omega > 0.5$ with our inelastic neutron scattering results suggesting the intensity at different energies do not show strong x - dependence. Reproduced from [74] with permission.

7.4 Main Conclusions and Future Considerations

In general, this thesis reported on the material synthesis and single crystal growth of $\text{La}_{1.6-x}\text{Nd}_{0.4}\text{Sr}_x\text{CuO}_4$, up to $x = 0.26$ in single crystal form, and up to $x = 0.4$ in polycrystalline form. A series of characterization measurements were performed on these samples, including neutron and x-ray powder diffraction, high resolution single crystal x-ray diffraction, and magnetic susceptibility measurements, which were used to benchmark the precise Sr doping across the phase diagram. Four relatively large and high quality Nd-LSCO single crystals of $x = 0.12, 0.19, 0.24$ and 0.26 were chosen as good candidates to conduct neutron scattering experiments on. The elastic triple axis scattering results observed static (on the time scale of the neutron) parallel spin stripes up to $x = 0.26$, beyond the putative quantum critical point $p^* = 0.235$. The direct geometry time-of-flight chopper spectrometer, SE-QUOIA, was employed to investigate the dynamic spin fluctuations in Nd-LSCO. The results showed little variance in the dynamic spectral weight for energies below ~ 35 meV, over a large doping concentration range, from $x = 0.12$ to 0.24 and a $\sim 33\%$ drop at $x = 0.26$, close to the end of superconducting dome. We propose that the static parallel spin stripes are a precursor to superconductivity in this system, and have updated its phase diagram. Our results are broadly consistent with the most recent RIXS results on LSCO and also with leading theoretical work that connects cuprate systems with quantum spin glasses.

Work presented in the thesis challenged some of the well ingrained perceptions regarding magnetism in 214 cuprate systems. It also shows more work is needed to improve our understanding of different phases and how they could be related to superconductivity in copper oxide systems. One limitation of the studies contained in this thesis is that they could not address how magnetic order evolves beyond superconductivity, due to difficulties associated with single crystal growth of Nd-LSCO beyond $x=0.26$. Future work could be focused on producing large and high quality Nd-LSCO single crystals of $x > 0.27$ and to continue to study the fascinating properties of this family of high T_C superconductors beyond superconductivity - and perhaps beyond ordered magnetism.

To conclude the thesis, I would like to re-produce and slightly modify a useful

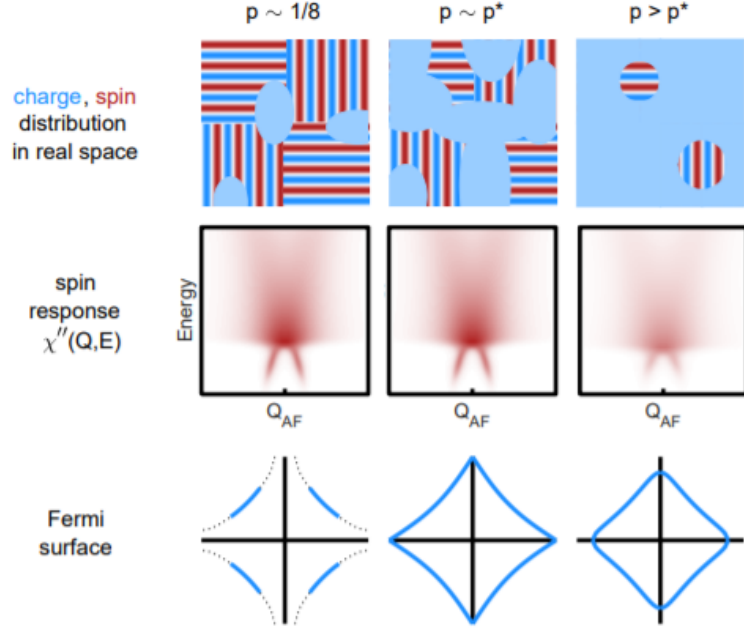


FIGURE 7.4: Illustrations of different properties of the spin and charge dynamics in Nd-LSCO. Top row shows static spin and charge distribution in real space. Middle row shows the dynamic spin fluctuations and the bottom row shows the Fermi surfaces at different doping. Reproduced from [89] with modification.

figure, taken from Ref.[89] that summarizes the magnetism, spin dynamics and Fermi surface in Fig.7.4. The work in this thesis is certainly consistent with the schematic picture of static spin and charge stripe distributions as a function of hole-doping, as shown in the top row in Fig.7.4. However, the static spin order appears strongest at $p=1/8$ but dramatically reduced at $p > p^*$ (although not eliminated). The spin susceptibility remains largely unchanged across the phase diagram, as indicated in the middle row of 7.4. I hope that the work carried out in this thesis will provide modest additional insights and help to guide future theoretical and experimental studies on how magnetic order and fluctuations interacts with the pseudogap state and superconducting ground states in cuprate-based high temperature superconductors.

Bibliography

- [1] J. G. Bednorz and K. A. Müller Possible High T_c Superconductivity in the Ba-La-Cu-O System *Zeitschrift für Physik B, Condensed Matter* 64.(2) (1986), 189–193.
- [2] M. K. Wu, J. R. Ashburn, C. J. Torng, P. H. Hor, R. L. Meng, L. Gao, Z. J. Huang, Y. Q. Wang, and C. W. Chu Superconductivity at 93 K in a new mixed-phase Y-Ba-Cu-O compound system at ambient pressure *Phys. Rev. Lett.* 58 (9 Mar. 1987), 908–910.
- [3] P. W. Anderson The Resonating Valence Bond State in La_2CuO_4 and Superconductivity *science* 235.(4793) (1987), 1196–1198.
- [4] W. Li, J. Zhao, L. Cao, Z. Hu, Q. Huang, X. Wang, Y. Liu, G. Zhao, J. Zhang, Q. Liu, et al. Superconductivity in a unique type of copper oxide *Proceedings of the National Academy of Sciences* 116.(25) (2019), 12156–12160.
- [5] J. Bardeen, L. N. Cooper, and J. R. Schrieffer Theory of Superconductivity *Phys. Rev.* 108 (5 Dec. 1957), 1175–1204.
- [6] H. Kamerlingh Onnes The resistance of pure mercury at helium temperatures *Commun. Phys. Lab. Univ. Leiden, b* 120 (1911).
- [7] M. L. Cohen and P. Anderson Comments on the maximum superconducting transition temperature in: *AIP Conference Proceedings* vol. 4 1 American Institute of Physics 1972, 17–27.
- [8] J. Nagamatsu, N. Nakagawa, T. Muranaka, Y. Zenitani, and J. Akimitsu Superconductivity at 39 K in magnesium diboride *nature* 410.(6824) (2001), 63–64.
- [9] C. M. Varma, P. B. Littlewood, S. Schmitt-Rink, E. Abrahams, and A. E. Ruckenstein Phenomenology of the normal state of Cu-O high-temperature superconductors *Phys. Rev. Lett.* 63 (18 Oct. 1989), 1996–1999.
- [10] B. Keimer, S. A. Kivelson, M. R. Norman, S. Uchida, and J. Zaanen From Quantum Matter to High-Temperature Superconductivity in Copper Oxides *Nature* 518.(7538) (2015), 179–186.

Bibliography

- [11] J. Tranquada, B. Sternlieb, J. Axe, Y. Nakamura, and S. Uchida Evidence for Stripe Correlations of Spins and Holes in Copper Oxide Superconductors *Nature* 375.(6532) (1995), 561–563.
- [12] J. Tranquada, J. Axe, N. Ichikawa, A. Moodenbaugh, Y. Nakamura, and S. Uchida Coexistence of, and Competition between, Superconductivity and Charge-Stripe Order in $\text{La}_{1.6-x}\text{Nd}_{0.4}\text{Sr}_x\text{CuO}_4$ *Physical Review Letters* 78.(2) (1997), 338.
- [13] J. Tranquada, N. Ichikawa, and S. Uchida Glassy Nature of Stripe Ordering in $\text{La}_{1.6-x}\text{Nd}_{0.4}\text{Sr}_x\text{CuO}_4$ *Physical Review B* 59.(22) (1999), 14712.
- [14] S. Dunsiger, Y. Zhao, B. Gaulin, Y. Qiu, P. Bourges, Y. Sidis, J. Copley, A. Kallin, E. Mazurek, and H. Dabkowska Diagonal and Collinear Incommensurate Spin Structures in Underdoped $\text{La}_{2-x}\text{Ba}_x\text{CuO}_4$ *Physical Review B* 78.(9) (2008), 092507.
- [15] S. Dunsiger, Y. Zhao, Z. Yamani, W. Buyers, H. Dabkowska, and B. Gaulin Incommensurate Spin Ordering and Fluctuations in Underdoped $\text{La}_{2-x}\text{Ba}_x\text{CuO}_4$ *Physical Review B* 77.(22) (2008), 224410.
- [16] M. Fujita, H. Goka, K. Yamada, J. M. Tranquada, and L. P. Regnault Stripe order, depinning, and fluctuations in $\text{La}_{1.875}\text{Ba}_{0.125}\text{CuO}_4$ and $\text{La}_{1.875}\text{Ba}_{0.075}\text{Sr}_{0.050}\text{CuO}_4$ *Phys. Rev. B* 70 (10 Sept. 2004), 104517.
- [17] J. J. Wagman, J. P. Carlo, J. Gaudet, G. Van Gastel, D. L. Abernathy, M. B. Stone, G. E. Granroth, A. I. Kolesnikov, A. T. Savici, Y. J. Kim, H. Zhang, D. Ellis, Y. Zhao, L. Clark, A. B. Kallin, E. Mazurek, H. A. Dabkowska, and B. D. Gaulin Neutron scattering studies of spin-phonon hybridization and superconducting spin gaps in the high-temperature superconductor $\text{La}_{2-x}(\text{Sr}, \text{Ba})_x\text{CuO}_4$ *Phys. Rev. B* 93 (9 Mar. 2016), 094416.
- [18] J. J. Wagman, D. Parshall, M. B. Stone, A. T. Savici, Y. Zhao, H. A. Dabkowska, and B. D. Gaulin Quasi-two-dimensional spin and phonon excitations in $\text{La}_{1.965}\text{Ba}_{0.035}\text{CuO}_4$ *Phys. Rev. B* 91 (22 June 2015), 224404.
- [19] B. Vignolle, S. Hayden, D. McMorrow, H. M. Rønnow, B. Lake, C. Frost, and T. Perring Two energy scales in the spin excitations of the high-temperature superconductor $\text{La}_{2-x}\text{Sr}_x\text{CuO}_4$ *Nature Physics* 3.(3) (2007), 163–167.
- [20] Z.-X. Shen, D. S. Dessau, B. O. Wells, D. M. King, W. E. Spicer, A. J. Arko, D. Marshall, L. W. Lombardo, A. Kapitulnik, P. Dickinson, S. Doniach, J. DiCarlo, T. Loeser, and C. H. Park Anomalously large gap anisotropy in the a-b plane of $\text{Bi}_2\text{Sr}_2\text{CaCu}_2\text{O}_{8+\delta}$ *Phys. Rev. Lett.* 70 (10 Mar. 1993), 1553–1556.

Bibliography

- [21] A. Lanzara, P. Bogdanov, X. Zhou, S. Kellar, D. Feng, E. Lu, T. Yoshida, H. Eisaki, A. Fujimori, K. Kishio, et al. Evidence for ubiquitous strong electron-phonon coupling in high-temperature superconductors *Nature* 412.(6846) (2001), 510–514.
- [22] A. Damascelli, Z. Hussain, and Z.-X. Shen Angle-resolved photoemission studies of the cuprate superconductors *Rev. Mod. Phys.* 75 (2 Apr. 2003), 473–541.
- [23] T. Yoshida, W. Malaeb, S. Ideta, D. Lu, R. Moor, Z.-X. Shen, M. Okawa, T. Kiss, K. Ishizaka, S. Shin, et al. Coexistence of a pseudogap and a superconducting gap for the high- T_c superconductor $\text{La}_{2-x}\text{Sr}_x\text{CuO}_4$ studied by angle-resolved photoemission spectroscopy *Physical Review B* 93.(1) (2016), 014513.
- [24] Z. Chen, Y. Wang, S. N. Rebec, T. Jia, M. Hashimoto, D. Lu, B. Moritz, R. G. Moore, T. P. Devereaux, and Z.-X. Shen Anomalously strong near-neighbor attraction in doped 1D cuprate chains *Science* 373.(6560) (2021), 1235–1239.
- [25] P. Abbamonte, L. Venema, A. Rusydi, G. Sawatzky, G. Logvenov, and I. Bozovic A structural probe of the doped holes in cuprate superconductors *Science* 297.(5581) (2002), 581–584.
- [26] P. Abbamonte, A. Rusydi, S. Smadici, G. Gu, G. Sawatzky, and D. Feng Spatially modulated 'mottness' in $\text{La}_{2-x}\text{Ba}_x\text{CuO}_4$ *Nature Physics* 1.(3) (2005), 155–158.
- [27] M. Dean, R. Springell, C. Monney, K. Zhou, J. Pereiro, I. Božović, B. Dalla Piazza, H. Rønnow, E. Morenzoni, J. Van Den Brink, et al. Spin excitations in a single La_2CuO_4 layer *Nature materials* 11.(10) (2012), 850–854.
- [28] M. Dean, G. Dellea, R. S. Springell, F. Yakhou-Harris, K. Kummer, N. Brookes, X. Liu, Y. Sun, J. Strle, T. Schmitt, et al. Persistence of magnetic excitations in $\text{La}_{2-x}\text{Sr}_x\text{CuO}_4$ from the undoped insulator to the heavily overdoped non-superconducting metal *Nature materials* 12.(11) (2013), 1019–1023.
- [29] M. Dragomir, Q. Ma, J. P. Clancy, A. Ataei, P. A. Dube, S. Sharma, A. Huq, H. A. Dabkowska, L. Taillefer, and B. D. Gaulin Materials preparation, single-crystal growth, and the phase diagram of the cuprate high-temperature superconductor $\text{La}_{1.6-x}\text{Nd}_{0.4}\text{Sr}_x\text{CuO}_4$ *Phys. Rev. Materials* 4 (11 Nov. 2020), 114801.

Bibliography

- [30] Q. Ma, K. C. Rule, Z. W. Cronkwright, M. Dragomir, G. Mitchell, E. M. Smith, S. Chi, A. I. Kolesnikov, M. B. Stone, and B. D. Gaulin Parallel spin stripes and their coexistence with superconducting ground states at optimal and high doping in $\text{La}_{1.6-x}\text{Nd}_{0.4}\text{Sr}_x\text{CuO}_4$ *Phys. Rev. Research* 3 (2 May 2021), 023151.
- [31] H. Eskes and G. A. Sawatzky Tendency towards Local Spin Compensation of Holes in the High- T_c Copper Compounds *Phys. Rev. Lett.* 61 (12 Sept. 1988), 1415–1418.
- [32] F. C. Zhang and T. M. Rice Effective Hamiltonian for the superconducting Cu oxides *Phys. Rev. B* 37 (7 Mar. 1988), 3759–3761.
- [33] B. Michon, C. Girod, S. Badoux, J. Kačmarčík, Q. Ma, M. Dragomir, H. Dabkowska, B. Gaulin, J.-S. Zhou, S. Pyon, T. T., T. H., V. S., D.-L. N., M. C., T. L., and K. T. Thermodynamic Signatures of Quantum Criticality in Cuprate Superconductors *Nature* 567.(7747) (2019), 218–222.
- [34] H. Alloul, T. Ohno, and P. Mendels ^{89}Y NMR evidence for a fermi-liquid behavior in $\text{YBa}_2\text{Cu}_3\text{O}_{6+x}$ *Phys. Rev. Lett.* 63 (16 Oct. 1989), 1700–1703.
- [35] C. E. Matt, C. G. Fatuzzo, Y. Sassa, M. Månsson, S. Fatale, V. Bitetta, X. Shi, S. Pailhès, M. H. Berntsen, T. Kurosawa, M. Oda, N. Momono, O. J. Lipscombe, S. M. Hayden, J.-Q. Yan, J.-S. Zhou, J. B. Goodenough, S. Pyon, T. Takayama, H. Takagi, L. Patthey, A. Bendounan, E. Razzoli, M. Shi, N. C. Plumb, M. Radovic, M. Grioni, J. Mesot, O. Tjernberg, and J. Chang Electron scattering, charge order, and pseudogap physics in $\text{La}_{1.6-x}\text{Nd}_{0.4}\text{Sr}_x\text{CuO}_4$: An angle-resolved photoemission spectroscopy study *Phys. Rev. B* 92 (13 Oct. 2015), 134524.
- [36] S. Badoux, W. Tabis, F. Laliberté, G. Grissonnanche, B. Vignolle, D. Vignolles, J. Béard, D. Bonn, W. Hardy, R. Liang, D.-L. N., T. L., and P. C. Change of carrier density at the pseudogap critical point of a cuprate superconductor *Nature* 531.(7593) (2016), 210–214.
- [37] Y. Ando, G. S. Boebinger, A. Passner, T. Kimura, and K. Kishio Logarithmic Divergence of both In-Plane and Out-of-Plane Normal-State Resistivities of Superconducting $\text{La}_{2-x}\text{Sr}_x\text{CuO}_4$ in the Zero-Temperature Limit *Phys. Rev. Lett.* 75 (25 Dec. 1995), 4662–4665.
- [38] G. S. Boebinger, Y. Ando, A. Passner, T. Kimura, M. Okuya, J. Shimoyama, K. Kishio, K. Tamasaku, N. Ichikawa, and S. Uchida Insulator-to-Metal Crossover in the Normal State of $\text{La}_{2-x}\text{Sr}_x\text{CuO}_4$ Near Optimum Doping *Phys. Rev. Lett.* 77 (27 Dec. 1996), 5417–5420.

- [39] R. Cooper, Y. Wang, B. Vignolle, O. Lipscombe, S. Hayden, Y. Tanabe, T. Adachi, Y. Koike, M. Nohara, H. Takagi, et al. Anomalous Criticality in the Electrical Resistivity of $\text{La}_{2-x}\text{Sr}_x\text{CuO}_4$ *Science* 323.(5914) (2009), 603–607.
- [40] P. Giraldo-Gallo, J. Galvis, Z. Stegen, K. A. Modic, F. Balakirev, J. Betts, X. Lian, C. Moir, S. Riggs, J. Wu, et al. Scale-Invariant Magnetoresistance in a Cuprate Superconductor *Science* 361.(6401) (2018), 479–481.
- [41] R. Daou, N. Doiron-Leyraud, D. LeBoeuf, S. Li, F. Laliberté, O. Cyr-Choiniere, Y. Jo, L. Balicas, J.-Q. Yan, J.-S. Zhou, et al. Linear Temperature Dependence of Resistivity and Change in the Fermi Surface at the Pseudogap Critical Point of a High- T_c Superconductor *Nature Physics* 5.(1) (2009), 31–34.
- [42] R. Daou, O. Cyr-Choinière, F. Laliberté, D. LeBoeuf, N. Doiron-Leyraud, J.-Q. Yan, J.-S. Zhou, J. B. Goodenough, and L. Taillefer Thermopower across the stripe critical point of $\text{La}_{1.6-x}\text{Nd}_{0.4}\text{Sr}_x\text{CuO}_4$: Evidence for a quantum critical point in a hole-doped high- T_c superconductor *Phys. Rev. B* 79 (18 May 2009), 180505.
- [43] C. Collignon, S. Badoux, S. A. A. Afshar, B. Michon, F. Laliberté, O. Cyr-Choinière, J.-S. Zhou, S. Licciardello, S. Wiedmann, N. Doiron-Leyraud, and L. Taillefer Fermi-surface transformation across the pseudogap critical point of the cuprate superconductor $\text{La}_{1.6-x}\text{Nd}_{0.4}\text{Sr}_x\text{CuO}_4$ *Phys. Rev. B* 95 (22 June 2017), 224517.
- [44] J. M. Luttinger and J. C. Ward Ground-State Energy of a Many-Fermion System. II *Phys. Rev.* 118 (5 June 1960), 1417–1427.
- [45] J. M. Luttinger Fermi Surface and Some Simple Equilibrium Properties of a System of Interacting Fermions *Phys. Rev.* 119 (4 Aug. 1960), 1153–1163.
- [46] K. Yamada, C. Lee, K. Kurahashi, J. Wada, S. Wakimoto, S. Ueki, H. Kimura, Y. Endoh, S. Hosoya, G. Shirane, R. J. Birgeneau, M. Greven, M. A. Kastner, and Y. J. Kim Doping Dependence of the Spatially Modulated Dynamical Spin Correlations and the Superconducting-Transition Temperature in $\text{La}_{2-x}\text{Sr}_x\text{CuO}_4$ *Physical Review B* 57.(10) (1998), 6165.
- [47] H. v. Löhneysen, A. Rosch, M. Vojta, and P. Wölfle Fermi-liquid instabilities at magnetic quantum phase transitions *Rev. Mod. Phys.* 79 (3 Aug. 2007), 1015–1075.
- [48] H. v. Löhneysen, T. Pietrus, G. Portisch, H. G. Schlager, A. Schröder, M. Sieck, and T. Trappmann Non-Fermi-liquid behavior in a heavy-fermion alloy at a magnetic instability *Phys. Rev. Lett.* 72 (20 May 1994), 3262–3265.

Bibliography

- [49] S. A. Kivelson, I. P. Bindloss, E. Fradkin, V. Oganesyan, J. M. Tranquada, A. Kapitulnik, and C. Howald How to detect fluctuating stripes in the high-temperature superconductors *Rev. Mod. Phys.* 75 (4 Oct. 2003), 1201–1241.
- [50] P. Corboz, T. M. Rice, and M. Troyer Competing States in the t-J Model: Uniform d-Wave State versus Stripe State *Phys. Rev. Lett.* 113 (4 July 2014), 046402.
- [51] D. Scalapino and S. White Stripe structures in the t-t'-J model *Physica C: Superconductivity* 481 (2012), 146–152.
- [52] T. Wu, H. Mayaffre, S. Kramer, M. Horvatic, C. Berthier, W. Hardy, R. Liang, D. Bonn, and M.-H. Julien Magnetic-field-induced charge-stripe order in the high-temperature superconductor $\text{YBa}_2\text{Cu}_3\text{O}_y$ *Nature* 477.(7363) (2011), 191–194.
- [53] E. H. da Silva Neto, P. Aynajian, A. Frano, R. Comin, E. Schierle, E. Weschke, A. Gyenis, J. Wen, J. Schneeloch, Z. Xu, et al. Ubiquitous interplay between charge ordering and high-temperature superconductivity in cuprates *Science* 343.(6169) (2014), 393–396.
- [54] R. Comin, A. Frano, M. M. Yee, Y. Yoshida, H. Eisaki, E. Schierle, E. Weschke, R. Sutarto, F. He, A. Soumyanarayanan, et al. Charge order driven by Fermi-arc instability in $\text{Bi}_2\text{Sr}_{2-x}\text{La}_x\text{CuO}_{6+\delta}$ *Science* 343.(6169) (2014), 390–392.
- [55] J. Chang, E. Blackburn, A. Holmes, N. B. Christensen, J. Larsen, J. Mesot, R. Liang, D. Bonn, W. Hardy, A. Watenphul, et al. Direct observation of competition between superconductivity and charge density wave order in $\text{YBa}_2\text{Cu}_3\text{O}_{6.67}$ *Nature Physics* 8.(12) (2012), 871–876.
- [56] N. K. Gupta, C. McMahan, R. Sutarto, T. Shi, R. Gong, H. I. Wei, K. Shen, F. He, Q. Ma, M. Dragomir, B. D. Gaulin, and H. D.G. Vanishing nematic order beyond the pseudogap phase in overdoped cuprate superconductors *Proceedings of the National Academy of Sciences* 118.(34) (2021).
- [57] P. M. Singer, A. W. Hunt, A. F. Cederström, and T. Imai Systematic ^{63}Cu NQR study of the stripe phase in $\text{La}_{1.6-x}\text{Nd}_{0.4}\text{Sr}_x\text{CuO}_4$ for $0.07 < x < 0.25$ *Phys. Rev. B* 60 (22 Dec. 1999), 15345–15355.
- [58] H. Miao, G. Fabbris, R. Koch, D. Mazzone, C. Nelson, R. Acevedo-Esteves, G. Gu, Y. Li, T. Yilmaz, K. Kaznatcheev, et al. Charge density waves in cuprate superconductors beyond the critical doping *npj Quantum Materials* 6.(1) (2021), 1–6.
- [59] L. Taillefer Scattering and Pairing in Cuprate Superconductors *Annu. Rev. Condens. Matter Phys.* 1.(1) (2010), 51–70.

Bibliography

- [60] G. L. Squires *Introduction to the Theory of Thermal Neutron Scattering* Courier Corporation, 1996.
- [61] G. Granroth, A. Kolesnikov, T. Sherline, J. Clancy, K. Ross, J. Ruff, B. Gaulin, and S. Nagler SEQUOIA: A Newly Operating Chopper Spectrometer at the SNS in: *Journal of Physics-Conference Series* vol. 251 1 2010, 012058.
- [62] M. A. Kastner, R. J. Birgeneau, G. Shirane, and Y. Endoh Magnetic, transport, and optical properties of monolayer copper oxides *Rev. Mod. Phys.* 70 (3 July 1998), 897–928.
- [63] B. Keimer, N. Belk, R. Birgeneau, A. Cassanho, C. Chen, M. Greven, M. Kastner, A. Aharony, Y. Endoh, R. Erwin, and G. Shirane Magnetic Excitations in Pure, Lightly Doped, and Weakly Metallic La_2CuO_4 *Physical Review B* 46.(21) (1992), 14034.
- [64] J. H. Cho, F. Chou, and D. C. Johnston Phase Separation and Finite Size Scaling in $\text{La}_{2-x}\text{Sr}_x\text{CuO}_{(4+\delta)}$ [$0 < (x, \gamma) < 0.03$] *Physical Review Letters* 70.(2) (1993), 222.
- [65] F. Chou, F. Borsa, J. Cho, D. Johnston, A. Lascialfari, D. Torgeson, and J. Ziolo Magnetic Phase Diagram of Lightly Doped $\text{La}_{2-x}\text{Sr}_x\text{CuO}_4$ from La-139 Nuclear Quadrupole Resonance *Physical Review Letters* 71.(14) (1993), 2323.
- [66] F. Borsa, P. Carretta, J. Cho, F. Chou, Q. Hu, D. Johnston, A. Lascialfari, D. Torgeson, R. Gooding, N. Salem, and K. Vos Staggered Magnetization in $\text{La}_{2-x}\text{Sr}_x\text{CuO}_4$ from La-139 NQR and μSR : Effects of Sr Doping in the Range $0 < x < 0.02$ *Physical Review B* 52.(10) (1995), 7334.
- [67] S. Wakimoto, G. Shirane, Y. Endoh, K. Hirota, S. Ueki, K. Yamada, R. Birgeneau, M. Kastner, Y. Lee, P. Gehring, and S. Lee Observation of Incommensurate Magnetic Correlations at the Lower Critical Concentration for Superconductivity in $\text{La}_{2-x}\text{Sr}_x\text{CuO}_4$ ($x=0.05$) *Physical Review B* 60.(2) (1999), R769.
- [68] A. Damascelli, Z. Hussain, and Z.-X. Shen Angle-Resolved Photoemission Studies of the Cuprate Superconductors *Rev. Mod. Phys.* 75 (2 Apr. 2003), 473–541.
- [69] M. Frachet, I. Vinograd, R. Zhou, S. Benhabib, S. Wu, H. Mayaffre, S. Krämer, S. K. Ramakrishna, A. Reyes, J. Debray, et al. Hidden Magnetism at the Pseudogap Critical point of a High Temperature Superconductor *arXiv preprint arXiv:1909.10258* (2019).
- [70] E. D. Isaacs, P. Zschack, C. L. Broholm, C. Burns, G. Aeppli, A. P. Ramirez, T. T. M. Palstra, R. W. Erwin, N. Stücheli, and E. Bucher Antiferromagnetism and Its Relation to the Superconducting Phases of UPt_3 *Phys. Rev. Lett.* 75 (6 Aug. 1995), 1178–1181.

Bibliography

- [71] G. Aeppli, E. Bucher, C. Broholm, J. Kjems, J. Baumann, and J. Hufnagl Magnetic Order and Fluctuations in Superconducting UPt_3 *Physical Review Letters* 60.(7) (1988), 615.
- [72] S. Wakimoto, H. Zhang, K. Yamada, I. Swainson, H. Kim, and R. J. Birgeneau Direct Relation between the Low-Energy Spin Excitations and Superconductivity of Overdoped High T_c Superconductors *Phys. Rev. Lett.* 92 (21 May 2004), 217004.
- [73] S. Wakimoto, K. Yamada, J. M. Tranquada, C. D. Frost, R. J. Birgeneau, and H. Zhang Disappearance of Antiferromagnetic Spin Excitations in Overdoped $\text{La}_{2-x}\text{Sr}_x\text{CuO}_4$ *Phys. Rev. Lett.* 98 (24 June 2007), 247003.
- [74] H. Shackleton, A. Wietek, A. Georges, and S. Sachdev Quantum Phase Transition at Nonzero Doping in a Random t-J Model *Phys. Rev. Lett.* 126 (13 Mar. 2021), 136602.
- [75] J. M. Tranquada, D. E. Cox, W. Kunmann, H. Moudden, G. Shirane, M. Suenaga, P. Zolliker, D. Vaknin, S. K. Sinha, M. S. Alvarez, A. J. Jacobson, and D. C. Johnston Neutron-Diffraction Determination of Antiferromagnetic Structure of Cu Ions in $\text{YBa}_2\text{Cu}_3\text{O}_{6+x}$ with $x = 0.0$ and 0.15 *Phys. Rev. Lett.* 60 (2 Jan. 1988), 156–159.
- [76] I. A. Zaliznyak, J. P. Hill, J. M. Tranquada, R. Erwin, and Y. Moritomo Independent Freezing of Charge and Spin Dynamics in $\text{La}_{1.5}\text{Sr}_{0.5}\text{CoO}_4$ *Phys. Rev. Lett.* 85 (20 Nov. 2000), 4353–4356.
- [77] J. M. Tranquada, C. H. Lee, K. Yamada, Y. S. Lee, L. P. Regnault, and H. M. Rønnow Evidence for an incommensurate magnetic resonance in $\text{La}_{2-x}\text{Sr}_x\text{CuO}_4$ *Phys. Rev. B* 69 (17 May 2004), 174507.
- [78] D. S. Marshall, D. S. Dessau, A. G. Loeser, C.-H. Park, A. Y. Matsuura, J. N. Eckstein, I. Bozovic, P. Fournier, A. Kapitulnik, W. E. Spicer, and Z.-X. Shen Unconventional Electronic Structure Evolution with Hole Doping in $\text{Bi}_2\text{Sr}_2\text{CaCu}_2\text{O}_{8+\delta}$: Angle-Resolved Photoemission Results *Phys. Rev. Lett.* 76 (25 June 1996), 4841–4844.
- [79] P. M. Lozano, G. D. Gu, J. M. Tranquada, and Q. Li Experimental evidence that zinc impurities pin pair-density-wave order in $\text{La}_{2-x}\text{Ba}_x\text{CuO}_4$ *Phys. Rev. B* 103 (2 Jan. 2021), L020502.
- [80] J. Axe and M. Crawford Structural Instabilities in Lanthanum Cuprate Superconductors *Journal of Low Temperature Physics* 95.(1-2) (1994), 271–284.
- [81] L. Taillefer Fermi surface reconstruction in high- T_c superconductors *Journal of Physics: Condensed Matter* 21.(16) (2009), 164212.

Bibliography

- [82] T. Yoshida, X. J. Zhou, K. Tanaka, W. L. Yang, Z. Hussain, Z.-X. Shen, A. Fujimori, S. Sahrakorpi, M. Lindroos, R. S. Markiewicz, A. Bansil, S. Komiya, Y. Ando, H. Eisaki, T. Kakeshita, and S. Uchida Systematic doping evolution of the underlying Fermi surface of $\text{La}_{2-x}\text{Sr}_x\text{CuO}_4$ *Phys. Rev. B* 74 (22 Dec. 2006), 224510.
- [83] X. J. Zhou, T. Yoshida, D.-H. Lee, W. L. Yang, V. Brouet, F. Zhou, W. X. Ti, J. W. Xiong, Z. X. Zhao, T. Sasagawa, T. Kakeshita, H. Eisaki, S. Uchida, A. Fujimori, Z. Hussain, and Z.-X. Shen Dichotomy between Nodal and Antinodal Quasiparticles in Underdoped $(\text{La}_{2-x}\text{Sr}_x)\text{CuO}_4$ Superconductors *Phys. Rev. Lett.* 92 (18 May 2004), 187001.
- [84] M. Lizaire, A. Legros, A. Gourgout, S. Benhabib, S. Badoux, F. Laliberté, M.-E. Boulanger, A. Ataei, G. Grissonnanche, D. LeBoeuf, et al. Transport signatures of the pseudogap critical point in the cuprate superconductor $\text{Bi}_2\text{Sr}_{2-x}\text{La}_x\text{CuO}_{6+\delta}$ *arXiv preprint arXiv:2008.13692* (2020).
- [85] D. Meyers, H. Miao, A. C. Walters, V. Bisogni, R. S. Springell, M. d’Astuto, M. Dantz, J. Pelliciari, H. Y. Huang, J. Okamoto, D. J. Huang, J. P. Hill, X. He, I. Božović, T. Schmitt, and M. Dean Doping dependence of the magnetic excitations in $\text{La}_{2-x}\text{Sr}_x\text{CuO}_4$ *Phys. Rev. B* 95 (7 Feb. 2017), 075139.
- [86] S. Wakimoto, K. Ishii, H. Kimura, M. Fujita, G. Della, K. Kummer, L. Braicovich, G. Ghiringhelli, L. M. Debeer-Schmitt, and G. E. Granroth High-energy magnetic excitations in overdoped $\text{La}_{2-x}\text{Sr}_x\text{CuO}_4$ studied by neutron and resonant inelastic x-ray scattering *Phys. Rev. B* 91 (18 May 2015), 184513.
- [87] C. Monney, T. Schmitt, C. E. Matt, J. Mesot, V. N. Strocov, O. J. Lipscombe, S. M. Hayden, and J. Chang Resonant inelastic x-ray scattering study of the spin and charge excitations in the overdoped superconductor $\text{La}_{1.77}\text{Sr}_{0.23}\text{CuO}_4$ *Phys. Rev. B* 93 (7 Feb. 2016), 075103.
- [88] T. A. Maier, S. Karakuzu, and D. J. Scalapino Overdoped end of the cuprate phase diagram *Phys. Rev. Research* 2 (3 July 2020), 033132.
- [89] J. M. Tranquada Cuprate Superconductors as Viewed Through a Striped lens *Advances in Physics* 69.(4) (2020), 437–509.